

REPORT DOCUMENTATION PAGE			Form Approved OMB No. 0704-0188	
Public reporting burden for this collection of information is estimated to average 1 hour per response, including the time for reviewing instructions, searching existing data sources, gathering and maintaining the data needed, and completing and reviewing the collection of information. Send comments regarding this burden estimate or any other aspect of this collection of information, including suggestions for reducing this burden to Washington Headquarters Services, Directorate for Information Operations and Reports, 1215 Jefferson Davis Highway, Suite 1204, Arlington, VA 22202-4302, and to the Office of Management and Budget, Paperwork Reduction Project (0704-0188), Washington, DC 20503.				
1. AGENCY USE ONLY (Leave blank)	2. REPORT DATE  1994	3. REPORT TYPE AND DATES COVERED  Final Report		
4. TITLE AND SUBTITLE  Flow Patterns and Heat Exchange in Supersonic Vortex		5. FUNDING NUMBERS  F6170893W0614		
6. AUTHOR(S)  Prof V. Ya. Borovoy				
7. PERFORMING ORGANIZATION NAME(S) AND ADDRESS(ES)  Central Aerohydrodynamics Institute (TsAGI) 140160 Zhukovsky Moscow, Russia		8. PERFORMING ORGANIZATION REPORT NUMBER  SPC-93-4045		
9. SPONSORING/MONITORING AGENCY NAME(S) AND ADDRESS(ES)  EOARD PSC 802 BOX 14 FPO 09499-0200		10. SPONSORING/MONITORING AGENCY REPORT NUMBER  SPC-93-4045		
11. SUPPLEMENTARY NOTES				
12a. DISTRIBUTION/AVAILABILITY STATEMENT  Approved for public release; distribution is unlimited.		12b. DISTRIBUTION CODE  A		
13. ABSTRACT (Maximum 200 words)  In many cases vortices are being generated on the aircraft surface: on the upper wing and body surfaces, in the vicinity of the deflected fins. They can essentially influence pressure distribution and heat transfer. The vortex generated on the upper surface of a body or a wing can encounter the shock wave in front of the fin, located downstream. Another example is: interaction of the vortex, generated by a canard, a strake or a nose flap intended for aircraft trimming with the wing or fin shock wave. A case important for practical purposes is described in: interaction between the vortex and inlet shock waves qualitatively changes the inlet entry flow pattern. A similar phenomenon can be observed in the case of interaction of the vortex generated in the inlet with the pylon of the air-breathing jet combustion chamber. In this context, it is worthwhile to investigate the vortex structure and its interaction with the streamlined body.  <div style="text-align: right;">DTIC QUALITY INSPECTED 3</div>				
14. SUBJECT TERMS		15. NUMBER OF PAGES  202		
		16. PRICE CODE		
17. SECURITY CLASSIFICATION OF REPORT  UNCLASSIFIED	18. SECURITY CLASSIFICATION OF THIS PAGE  UNCLASSIFIED	19. SECURITY CLASSIFICATION OF ABSTRACT  UNCLASSIFIED	20. LIMITATION OF ABSTRACT  UL	

# DISCLAIMER NOTICE



**THIS DOCUMENT IS BEST  
QUALITY AVAILABLE. THE  
COPY FURNISHED TO DTIC  
CONTAINED A SIGNIFICANT  
NUMBER OF PAGES WHICH DO  
NOT REPRODUCE LEGIBLY.**

SPC-93-4045

# **FLOW PATTERNS AND HEAT EXCHANGE IN SUPERSONIC VORTEX**

**Final Report**

19970506 088

**Zhukovsky  
1994**

SPC-93-4045

# **FLOW PATTERNS AND HEAT EXCHANGE IN SUPERSONIC VORTEX**

**Project manager**

**V.Ya.Borovoy**



**Executors**

V.Ya. Borovoy  
V.S. Naumov  
R.A. Kazanskiy  
T.V. Kubyshina  
A.A. Shamshurin

A.S. Skuratov  
V.N. Trigub  
L.V. Yakovleva  
V.V. Zhdanov  
Yu.V. Zhilin

**Zhukovsky**

**1994**

## Contents

	Page
Introduction	5
Nomenclature for the part A	8
<b>A. Experimental investigation of vortex structure and its interaction with a sphere</b>	10
<b>1. Experimental facility</b>	10
1.1. Description of the T-33 wind tunnel	10
1.2. Vortex generators	11
1.3. Total pressure and stagnation temperature probes and device for their positioning	13
1.4. Models of sphere	14
1.5. Heat flux sensors. Method of heat flux measurument	15
1.6. Flow visualization method	17
<b>2. Investigation results and their analysis</b>	18
2.1. Free stream flow parameters	18
2.2. Flow pattern past vortex generators	18
2.2.1. Flow pattern	18
2.2.2. Vortex dimensions	20
2.2.3. Pressure and stagnation temperature profiles	21
2.3. Vortex-sphere interaction	25
2.3.1. Gas flow pattern in front of sphere	25
2.3.2. Heat transfer on sphere surface	29
Nomenclature for the part B	34
<b>B. Analitical and numerical study of vortex development</b>	36
<b>1. Problem formulation</b>	36
1.1. Governing equations	36
1.2. Inviscid axisymmetric steady flow	38

1.3. Small perturbations of the cylindrical flow _ _ _ _ _	44
1.4. Quasi-cylindrical approximation _ _ _ _ _	53
2. The structure of flow at the initial region of vortex _ _ _ _ _	58
2.1. Representation of the solution in the penetration layer _ _ _ _ _	58
2.2. Numerical study of the flow at the initial region _ _ _ _ _	67
3. Numerical solution of the quasi-cylindrical approximation system for compressible flow _ _ _	70
3.1. Problem statement. Numerical method _ _ _	70
3.2. Numerical results _ _ _ _ _	73
4. Solutions describing the flow far down- stream from initial section _ _ _ _ _	76
4.1. Generalization of the Batchelor's expantion _ _ _ _ _	76
4.2. Comparison of the numerical results with asymptotic solutions _ _ _ _ _	81
5. Comparison of the numerical results with experimental data _ _ _ _ _	82
Conclusions _ _ _ _ _	86
References _ _ _ _ _	90
Appendix. Tables of the measurements results _ _ _	94

## Introduction

In many cases vortices are being generated on the aircraft surface: on the upper wing and body surfaces, in the vicinity of the deflected fins. They can essentially influence pressure distribution and heat transfer. The vortex generated on the upper surface of a body or a wing can encounter the shock wave in front of the fin, located downstream (Fig.1a). Another example is: interaction of the vortex, generated by a canard [1], a strake or a nose flap intended for aircraft trimming with the wing or fin shock wave (Fig.1b). A case important for practical purpose is described in [2] (Fig.1c): interaction between the vortex and inlet shock waves qualitatively changes the inlet entry flow pattern. A similar phenomenon can be observed in the case of interaction of the vortex generated in the inlet with the pylon of the air-breathing jet combustion chamber (Fig.1d). In this context it is worthwhile to investigate the vortex structure and its interaction with the streamlined body.

Wing flow at an angle of attack, followed by a flow separation and vortices formation, have been investigated in many studies. In some papers vortices structure is investigated in detail. Most works deal with flows of incompressible fluid. A vortex layer, shedding from a wing surface, rolls up into a spiral. Its shape and velocity distribution are approximately described by the equations of motion for incompressible fluid [3,4]. At high Reynolds numbers the experimental [5,6] and theoretical results are in good agreement. However velocity tangential discontinuity on the spiral surface typical for an incompressible fluid flow are smoothed due to the influence of viscous diffusion [5,6]. The influence of viscosity is still greater in the internal vortex core. It was discovered by the experiment [5] and investigated theoretically for a laminar flow in works [7,8].

A survey of these investigations is given in [9]. In 1957 Peckham and Atkinson discovered a vortex burst [10]. They observed it in the flow field in the vicinity of the wing in the region of a positive pressure gradient. The vortex burst is also observed in the swirling nozzles and diffusers flows. After the discovery of the vortex burst a great variety of theoretical investigations of this phenomenon was carried out.

A supersonic vortex structure was thoroughly investigated in the work [1]. Using modern measurement techniques the researchers obtained the data concerning the influence of the swirl strength and pressure gradient on the velocity and gas pressure in the vortex at Mach numbers from 1.6 to 2.28.

In 1975 research [2] discovered a vortex breakdown in front of the inlet due to the influence of a strong shock wave. The investigation was carried out at Mach number from 1.4 to 3.0. It was shown that a vortex breakdown is followed by formation a dead region which induces a cone shock. The inclination angle of the dead region borderline and pressure increase in it are close to similar values for a separation region of the turbulent boundary layer. The formation of the dead region reduces the pressure recovery coefficient in the supersonic inlet. This investigation was continued in works [1,11,12].

Paper [1] determines the parameters, influencing the vortex burst when interacting with the normal shock: vortex strength and Mach number (shock pressure difference). The vortex breakdown conditions are specified for Mach number up to 2.5. In this paper on the basis of the Euler equations are also theoretically determined the conditions under which the vortex breakdown occurs. The calculation results and the experimental data are in good agreement. In paper [11] similar analysis of interaction between a vortex and an oblique

shock past which a supersonic flow is retained was carried out at Mach numbers of 2.28 and 5.0. In calculations a vortex breakdown was not obtained. In paper [2] it is shown that at Mach numbers from 2.5 to 4.0 a vortex breakdown occurs at a rather high angle of attack of the wing generating a vortex (at  $\alpha > 5-10^\circ$ ). In paper [12] a vortex burst was also observed during interaction between a vortex and a central shock in the under-expanded jet. It occurred at angles of attack of the wing-vortex generator greater than  $8^\circ$ .

In the known papers a stagnation temperature distribution in a supersonic vortex was not investigated. At the same time measurements performed at subsonic speeds in the Ranque tube indicate that vortex temperature can essentially change [13]. This property of vortex flows is applied in the simplest refrigerators.

None of the studies familiar to the authors deals with the investigations of the vortex influence on the heat exchange on the frontal surfaces of a body. At the same time the obtained data about the vortex breakdown indicate that this influence can be essential.

The aim of this paper is as follows:

- 1) To obtain additional data about the vortex structure in supersonic flow by means of experiment and theoretical investigations.
- 2) To obtain experimental data about the vortex influence on the heat transfer on the frontal surface of the blunted body.

# Nomenclature for the part A

- a = thermodiffusion coefficient,
- b = chord of vortex generator,
- c = heat capacity,
- d = vortex diameter,
- d<sub>r</sub> = reference vortex diameter (at the begin of the vortex's straight portion),
- D = sphere diameter,
- Fo =  $a\tau/\delta^2$ , Fourier number,
- h =  $q/(T_0 - T_w)$ , heat transfer coefficient,
- i = enthalpy,
- l = length of separation region in front of sphere,
- M = Mach number,
- p = pressure,
- q = heat flux,
- q<sub>0</sub> = theoretical value of the heat flux in the stagnation point of the sphere,
- R = D/2, sphere radius,
- Re =  $\rho_\infty u_\infty D / \mu_\infty$ , Reynolds number,
- Re<sub>1</sub> =  $\rho_\infty u_\infty / \mu_\infty$ , unit Reynolds number (per 1 m),
- s = distance along sphere surface from its center,
- t = temperature,
- T = temperature,
- u = velocity,
- x = coordinate in free stream direction,
- x<sub>s</sub> = distance from trailing edge of vortex generator to sphere,
- y, z = coordinates in the directions perpendicular to a free stream,
- $\alpha$  = angle of attack of a vortex generator,
- $\beta$  = inclination angle of shock wave,
- $\gamma$  = azimuthal angle,
- $\delta$  = model wall thickness,
- $\theta$  = angle of borderline inclination of separation region,

$\lambda$  = thermal conductivity coefficient,  
 $\mu$  = viscosity coefficient,  
 $\rho$  = density,  
 $\tau$  = time,  
 $\varphi$  = angle between the x-axis and the probe axis.

#### Subscripts

$\infty$  = free stream conditions,  
0 = wind tunnel settling chamber,  
i = initial conditions,  
m = maximum value,  
s = stagnation point past normal shock wave,  
w = on the model surface.

## A. Experimental investigation of the vortex structure and its interaction with a sphere

### 1. Experimental facility

#### 1.1. Description of the T-33 wind tunnel

The T-33 facility is an intermittent, blowdown wind tunnel (Fig.2). It is often used at TsAGI for investigation of heat transfer and pressure distribution on the bodies surface in supersonic gas flows as well as for flow visualization. This wind tunnel was being used for similar investigations in the subsonic flow.

The scheme of the T-33 wind tunnel is shown in Fig.3. In the majority of experiments an electrical resistance heater (1) is used for air heating. Its power is up to 1000 kW. When the experiment purpose is a flow visualizaton another heater is used wherein heating occurs due to combustion of kerosene. It represents a modified combustion chamber of the turbojet engine.

The maximum temperature of the air in both heaters is about 500°C. However in the majority of experiments the temperature doesnot exceed 200°C. In settling chamber (2) the flow is straightened by a honeycomb and a system of grids. The maximum pressure in the settling chamber reaches  $8 \cdot 10^5$  Pa. For developing a supersonic flow axisymmetric nozzles (3) contoured to produce uniform Mach 3, 4 or 5 flow are used. There is also a convergent nozzle generating a subsonic flow. In this investigation the nozzle intended for Mach number of 3 was used. The nozzle exit section diameter is 304.5 mm.

The wind tunnel test section (4) (see Figs. 3 and 4) presents itself the Eiffel chamber. Its diameter is 800 mm, the distance between the nozzle and the diffuser is 550 mm. In

the walls of the test section there are 5 windows for illumination and observation of models. For fixing the models there are 2 supporting mechanisms in the wind tunnel test section (above and below). They can inject a model and a measuring unit or two parts of a compound model into the flow simultaneously or one after the other. The lower supporting device can be moved in the axial direction during the experiment. Furthermore it is possible to change the model angle of attack during the experiment.

Below on the test section wall a thermostatic chamber is mounted. During the heat transfer investigations this chamber prevents the model installed on the lower supporting mechanism from heating at the period when the flow becomes steady. After obtaining a prescribed steady regime a flap of the thermostatic chamber is moved aside and the model is quickly injected into the flow. A maximum model length is 350 mm.

For obtaining the required air rarefaction in the test section a two-stage supersonic ejector is applied.

A great number of investigations of heat transfer by means of thermosensitive coatings and discrete thermocouples was carried out in the T-33 wind tunnel. Furthermore, a flow visualization by a shadowgraph technique, a laser knife and a calibrated oil points is often performed in the tunnel. Some results obtained in the T-33 wind tunnel are presented in papers [14,15].

### 1.2. Vortex generators

Different ways of vortex generation are known. In a number of works for generation of a vortex a swept or a straight wing at an angle of attack is used. Delery [1] used for vortex generation in subsonic flow a wing-type generator along

with a vane-type generator. The vane-type generator presented itself an axisymmetric body on which two vanes were installed at a certain angle of attack. In Ref.[16], a vortex produced also by swirl-vanes being placed into axisymmetric casing, is described. The investigation [1] has shown that the velocities distributions in the vortices produced by a wing and swirl-vanes differ substantially. In a supersonic flow vanes without external casing evidently were not used up till now.

In the current investigation three generators of both type were used: 2 generators in the form of a rectangular wing and one generator of a vane type. In designing the wing-type generator the investigation results of Ref.[17] were used. In this paper information about vortex dimensions and its position at different wing angles of attack was obtained. Figures 5, 6 and 7 show the schemes of the generators which were used. Generators 1 and 2 have an rectangular shape. The leading and lower edges are sharp and the trailing edge is blunt. Over a greater part of the wing span a cross section profile has a triangular shape. Generators 1 and 2 differ only by the chord length. The wing chord of generator 1 is almost 3 times greater than that of generator 2. Generator 1 is designed mainly for investigating a total pressure and total temperature distribution in a vortex and generator 2 - mainly for investigating a vortex development and its interaction with a sphere.

Generator 3 (Fig.7) presents itself an axisymmetric body with a diameter of 6 mm, on which 4 rectangular vanes are fixed at an angle of attack of  $30^{\circ}$  (there are also generators with the vane setting angles of  $10^{\circ}$  and  $20^{\circ}$  but they were not used). A potential advantage of generator 3 as compared with two other generators consists in a less flow perturbation because the plate on which the generator is mounted is installed at a zero angle of attack.

### 1.3. Total pressure and stagnation temperature probes and device for their positioning

A stagnation pressure probe (Fig.8a) presents itself a capillary tube fabricated from a stainless steel with an external and internal diameters 0.8 and 0.48 mm respectively. A capillary with a straight section length 12 mm was bent in a manner as shown in Fig.8a and went through a positioning device rod. The end of the capillary was connected with a miniature pressure probe with a measuring range from 0 to 10 bar, by means of a flexible pipe. The inertia of the total pressure probe did not exceed 0.1 s.

A stagnation temperature probe (Fig.8b) presented itself a tube made of a stainless steel with external and internal diameters 2 and 1.5 mm respectively and straight section length 20 mm. Inside this tube a thermocouple junction from chromel-copel alloys with a wire thickness of 0.1 mm was placed. The rear end of the tube had a plug and there were 2 holes 0.5 mm in diameter in the side surface behind the thermocouple junction. A signal from the thermocouple was recorded by a data acquisition processing system. A temperature recovery coefficient of this probe design at specified flow parameters according to literature data was estimated

$$\zeta = \frac{T_s - T}{T_0 - T} \approx 0.965 \pm 0.025$$

The real values of the recovery coefficient were estimated in the tests.

For moving the probes a positioning device was developed and fabricated (Figs.9,10). Probe 1 is fixed inside the rod 2 (Fig.9). Miniature cooled engines 4 and 10 move the rod in

the vertical direction and rotate it relative to the axis. The positioning device is mounted on the lower supporting mechanism of the T-33 tunnel and can be moved along the tunnel axis.

The positioning device allows the probe to be moved along the y-axis (in vertical direction) at the distance up-to 120 mm with the minimum spacing of 0.05 mm. At every specified station along the y-axis the positioning device can stop the probe and rotate it up to the angle  $\pm 90^\circ$  with the minimum setting  $0.5^\circ$ .

The positioning device is controlled by a computer. A control code allows to change movement and rotation steps  $\Delta y$  and  $\Delta \varphi$ , respectively, as well as duration of maintaining the probe in stop position necessary for conducting reliable measurements. For the current investigation the code was developed in such a way in order to obtain maximum information about flow characteristics in the vortex region during minimum wind tunnel running time.

#### 1.4. Models of sphere

For investigating a vortex blunt body interaction two spheres with a diameter  $D=60$  mm were fabricated. One sphere was made of steel and intended for a flow visualization. Another sphere was made of glass-fibre plastic and intended for investigation of heat transfer. 43 heat flux sensors were mounted on it (Fig.11a). A scheme of sensors location is shown in Fig.11b.

### 1.5. Heat flux sensors. Method of heat flux measurement

In this investigation the surface thermocouples were used as heat flux sensors [18]. They are fabricated from chromel-copel alloys. A diameter of thermocouple wires is 0.1 mm. In the measurement position they are being rolled-off into the ribbons of 0.02 mm thickness, 0.2 mm width and 4.0 mm long. The ribbons are bonded flush with the model surface. The thermocouples ends are brought into the model through drillings.

Estimation of a heat flux from a surface temperature is a problem of the boundary condition conversation. This problem may be considered as a limited inverse heat conduction problem which occurs in processing temperature data measured on the body surface. In such formulation the inverse heat conduction problem is correct.

As the model wall thickness  $\delta$  is sufficiently large, the thermal conductivity coefficient and testing time are small (i.e. the Fourier number  $Fo \ll 1$ ), the semi-infinite body model can be used for investigating a process of heat transfer. In this case the boundary inverse heat conduction problem may be formulated as follows: using the known solution  $T(0, \tau) = f(\tau)$  of the heat conduction equation

$$\frac{\partial T(z, \tau)}{\partial \tau} = a \frac{\partial^2 T(z, \tau)}{\partial z^2}, \quad \tau < 0, \quad z > 0$$

(here  $z$  is the coordinate directed inside the body perpendicular to the surface)

with the boundary conditions

$$\frac{\delta T(\infty, \tau)}{\delta z} = 0; \quad T(\infty, \tau) = T_1$$

and the initial condition

$$T(z, 0) = T_1$$

to determine a heat flux to the heated surface

$$q(\tau) = - \lambda \frac{\delta T(0, \tau)}{\delta z}$$

The problem solution takes the following form [19]:

$$q(\tau) = \frac{\sqrt{\lambda c \rho}}{\sqrt{\pi}} \frac{d}{dz} \int_0^\tau \frac{f(t) dt}{\sqrt{\tau-t}} = \frac{\sqrt{\lambda c \rho}}{\sqrt{\pi}} \int_0^\tau \frac{f'(t) dt}{\sqrt{\tau-t}}$$

For smoothing and functional presentation of heating curves K-spline approximation by the least squares method is applied [20].

The thermal activity coefficient value  $\sqrt{\lambda \rho c}$  incoming into the above expression was specified for every sensor at a special calibration setup (Fig.12a) wherein an air jet of 2.0 mm diameter, producing a known heat flux is directed to the sensor perpendicularly to the model surface. The heat flux action period is approximately the same as in the wind tunnel model tests. Using the measured surface temperature and known heat flux value one can estimate the value of  $\sqrt{\lambda \rho c}$  using the solution of one-dimensional heat conduction prob-

lem for a semi-infinite body. The typical calibration curve is shown in Fig.12b.

#### 1.6. Flow visualization methods

For flow visualization a laser knife method [15,17] was used along with a shadowgraph technique. This method is similar to a vapour screen method and allows to observe a flow cross section. For flow visualization by the laser knife method kerosene was burned up in the T-33 wind tunnel heater. Carbon dioxide and water vapour containing in the combustion products transit to a solid phase during air expansion in the nozzle. In addition there are particles of soot in the combustion products. Laser with a power of 6 W and a wavelength of 5150 Å was used as a light source. A plane light sheet 2 mm thickness was formed by means of cylindrical optics. This light sheet crossed the gas flow in the perpendicular direction to the free stream flow. The flow pattern pictures were taken by a camera located behind the laser knife plane. Prior to the experiment, pictures of a template located in the laser knife plane were taken. By means of this template image scales along the x and y-axes were determined. During the experiment a vortex generator moved relative to the laser knife plane and in this way a flow visualization at the different distances from the generator was carried out.

For flow visualization on the sphere surface oil paint was used. The paint was applied on the surface in the form of discrete points [15,21]. Under the influence of a hot air flow the paint is being softened and carried away by the flow. The lines appearing on the model surface are useful in visualization of the flow direction and viscous stress value.

## 2. Investigation results and their analysis

### 2.1. Free stream flow parameters

The investigation was conducted at a Mach number 3. The total pressure was the same  $p_0 = 5 \cdot 10^5$  Pa in all experiments, and the temperature was different: in one part of the experiment air was heated up to  $T_0 = 410$  K (by flow visualization, by investigation of heat transfer), in another part of the experiment the stagnation temperature was close to normal  $T_0 = 280$  K (by measuring pressure and stagnation temperature distribution). In the first case the unit Reynolds number was  $Re_1 = 1.1 \cdot 10^7$  1/m, in the second case -  $Re_1 = 3.7 \cdot 10^7$  1/m.

### 2.2. Flow pattern past vortex generator

#### 2.2.1. Flow pattern

At first let us consider a flow past wing-type generators and then past a vane-type generator. Figures 13 and 14 show pictures of vortex cross sections past generator 1 at angles of attack  $\alpha = 10^\circ$  and  $20^\circ$ . The image scale was 2:1 relative to the real one. Origin of the x-coordinate coincides with the rear generator edge. When analysing the pictures obtained by a laser knife method it should be taken into consideration that in the flow regions corresponding to slightly curved streamlines brightness of the images is proportional to gas density. It is confirmed by comparison measuring results of the image density and stagnation pressure in the Prandtl-Mayer flow region [17]. Due to this one can see shock waves, rarefaction areas, and a wing wake in these pictures. The results of digital processing of the pictures are presented in Fig.15. This processing was carried out to obtain more comprehensive information about the gas density

distribution in the flow field. At the bottom of Fig.15 a gray scale is shown. Every gradation on the scale corresponds to a certain gas density. In the region with a large curvature of the streamlines and particularly in the vortex, these pictures are not useful for visualization of the density distribution: due to the large curvature of the streamlines, solid and liquid particles flow away from the vortex region under the influence of centrifugal forces. So these vortices are seen as black spots in the pictures. Similar materials about the vortex formed by generator 2 are presented in Figs. 16-19.

Figures 20 and 21 present a flow visualization past generator 3 which has the four-vanes form. The vanes present themselves rectangular finite span wings. Each vane produces two tip vortices. Altogether 8 vortices are formed: 4 vortices in the vicinity of the axis of symmetry and 4 vortices in the periphery. All eight vortices and covering them shock waves are clearly seen directly past the generator (Fig.20,  $x = 20$  mm, Fig.21a). Four central vortices are joined into one central vortex at the distance  $x \approx 100$  mm and four peripheral ones are retained throughout the whole region available for observation ( $x_{\max} = 160$  mm). Further, for the investigations only the wing-type generators were used because they produce only one concentrated vortex.

Let us address to the analysis of the flow past the wing-type vortex generators. In papers [14,17] a scheme of the flow in the vicinity of the rectangular wing is presented. It is reproduced in slightly distinguished form in Fig.22a. Elements of this scheme are seen also in Fig.14,  $x=2$  mm (1 - bow shock wave, 2 - internal shock wave, 3 - vortex, 4 - Prandtl-Mayer flow). In the vicinity of the wing the vortex has a cone shape. A cone angle of the vortex is close by its order of magnitude to the wing angle of attack. There is an expansion of the vortex in the wing region due to the inflow

of the inviscid gas into the rotation region. The flow past the wing is shown in a schematic presentation in Fig.22b and c. Past the wing the flow expands only due to the viscous dissipation. A vortex expansion angle is not high (see below). A free vortex 5 induces a weak conical compression wave 6 (Fig. 22c). It is seen in the picture at a large distance from the generator (Fig.13b,  $x=135$  mm; Fig.14b,  $x=100$  mm). Analysis of the pictures show that far from the tip section past the wing a viscous weak expanding wake 7 is formed. It also induces a weak compression wave 8 (Fig.22b). Analysis of the pictures taken at different distances from the generator shows that the M-lines (Fig.22b) and the N-lines (Fig.22c) are approximately linear and located at the same angle relative to a free stream flow direction. It is close to the value of  $\arcsin 1/M$  at  $M=3$ . This confirms that lines 6 and 8 observed in the laser pictures are weak compression waves.

### 2.2.2. Vortex dimensions

Let us continue the analysis of the laser pictures. The vortex axis past the wing is curved, the vortex centre is displaced towards the windward generator surface (in the positive direction along  $z$ -axis) by the distance up to  $0.4 b$  at the angle of attack up to  $20-30$  deg. The curved portion length of the vortex axis is about  $1.5 b$ . At a larger distance from the generator the vortex axis is approximately parallel to a free stream flow direction.

Figure 23 shows variation of the vortex diameter versus the distance from the generator. Linear dimensions are related to the wing chord. The vortex has a spiral shape. It is clearly seen in Fig.18 as well as in some pictures of Fig.24. The vortex core has an oval shape and its axes are rotated with increase of the distance from the generator (Fig.24).

The core boundaries become gradually blurred and the core itself becomes not so black. This is due to deceleration of rotation and increase of gas density in the core. Because of insufficient sharpness of the core boundaries its dimensions can be determined only approximately by means of the pictures. In Fig.23 dimensions of the vortex cross section in the y and z directions ( $d_y$ ,  $d_z$ ) are shown. At  $\alpha = 10^\circ$  and  $30^\circ$  vortex dimensions change according to the linear law throughout the range and at  $\alpha = 20^\circ$  only when  $x > 1.5 b$ . The relative vortex diameter value  $d/b$  practically does not depend on the wing dimensions: the experimental points obtained with generators 1 and 2 are on the general curve when the angle of attack growth. The vortex diameter  $d = 1/2(d_y + d_z)$  sharply increases (Fig.25).

When analysing vortex dissipation it is reasonable to neglect the generator dimensions. So in Fig.26 linear dimensions are related to some conditional reference vortex diameter  $d_r$ . For each experiment value  $d_r = 1/2(d_y + d_z)$  was determined at the distance  $x = 1.5 b$ , where a transitional curvilinear vortex portion ends and its straight portion starts. From Fig.26, it can be seen that at  $\alpha \leq 20^\circ$  all experimental data regardless to a generator dimension and angle of attack are described by a general function: the vortex linearly expands. An expansion vortex angle is about 1 deg. At  $\alpha = 30^\circ$  this angle increases up to  $3^\circ$ .

### 2.2.3. Pressure and stagnation temperature profiles

Pressure and temperature were measured past generator 1 ( $b = 58$  mm) at angle of attack  $\alpha = 20^\circ$  in two transverse sections  $x_1 = 2$  mm and  $x_2 = 110$  mm as shown in Fig.27. The laser pictures evidence that the vortex centre in section 1 is displaced relative to the plane  $z = 0$  towards the leeward surface by 13 mm. Besides, the generator is bent under the inf-

fluence of aerodynamic force and the vortex centre is additionally displaced in the direction of the negative z-axis approximately by 5 mm. Taking into account the data obtained in the preliminary experiments the probes axes were set at a certain angle to the direction of the y-axis (Fig.27a). In section one this angle was about  $5^\circ$  and in section two  $4^\circ$ .

The total pressure probe was rotated in the plane  $y=\text{const}$  in the angle range of  $\varphi = \pm 45^\circ$  in increments of  $15^\circ$ . Rotating was carried out relative to the probe entry, i.e., the probe entry position did not change during probe rotations (Fig.27c). At each position the probe was kept for 1-2 s, that provided a sufficient measurement accuracy. The results of all pressure measurements are presented in Tables 1 and 2.

In Fig. 28, as an example measurements results of the stagnation pressure in section 1 and 2 at different distances from the vortex centre are shown. In a free stream flow ( $y'=20$  mm for section 1 and  $y'=15$  mm for section 2) as expected the probe indications are approximately symmetric to the flow direction. The probe is practically insensitive to a flow deflection up to the angle  $\varphi \approx 15^\circ$ , this agrees with literature data [22]. In the region of the vortex influence the flow is swirled in the clockwise direction: above the vortex axis ( $y'=107$  mm in section 1 and  $y'=118$  mm in section 2) the flow is displaced in the direction of the positive z-axis and below the vortex axis ( $y'=96$  mm in section 1 and  $y'=93$  mm in section 2) in the opposite direction. Judging by the stagnation pressure measurements angle of flow swirl in section 2 is significantly less than in section 1.

The influence of the rotation angle of the stagnation temperature probe on its indications can be seen in Fig. 29 and tables 3 and 4. The stagnation temperature probe indications are practically insensitive to a flow deflection also in the

range  $\pm 15^\circ$  (Fig.29,  $y'=15$  mm). The stagnation temperature measurements confirm the presence of the flow swirl in a clockwise direction if to consider it in the flow direction. At each probe position  $y=\text{const}$  from all results of measuring pressure or temperature at different rotation angles of the probe  $\varphi$  the maximum value was chosen (it is marked by an asterisk in tables 1-4). It was assumed that this indication gives the stagnation pressure value ( $p_s=p_*$ ) and the stagnation temperature value ( $T_s=T_*$ ) past a shock wave.

In Fig.30 a, b and c the stagnation pressure measurement results are presented. At the bottom of Fig.30 a and b, pictures of the vortex cross section, with denoted the shock wave  $S_1$ ,  $S_2$  and the vortex boundaries  $V_1$  and  $V_2$ , are presented. It is seen that the stagnation pressure measurement results are adequate to the flow pattern presented in the corresponding picture of the flow cross section. In fact, in a free stream flow the stagnation pressure is approximately constant; it sharply increases in the point S when crossing a bow shock wave of the generator. Then it gradually decreases while approaching to the generator, that agrees with the results of the digital pictures processing, Fig.15. This stagnation pressure decrease continuously transit to a pressure drop induced by a flow swirl. So the measurement results presented in Fig.30 do not allow to determine the vortex boundary. It can be determined by the value of a flow deflection: outside the vortex dependence of the pressure  $p$  on the angle  $\varphi$  is approximately symmetric to the free stream direction. In section 1 the vortex boundaries are in the points  $y=95-96$  mm and  $y = 106-107$  mm. This agrees with the boundaries determined by the pictures and proves the use of laser pictures for investigating a vortex development. In Fig.30c it is also can be seen that directly past the generator (in section 1) the stagnation pressure at the vortex axis is 16 times less of that in the free stream flow. In section 2 these values differ only by 2-3 times (in Fig.30c

the points corresponding to the minimum pressure values are superposed). Hence, with growth of the distance from the generator the vortex diameter increases slowly but the flow swirl decreases sharply and the vortex core is filled up with a significantly denser gas.

In Fig.31 a and b the stagnation temperature measurement results are presented. The shock wave, as expected, unlike stagnation pressure, does not cause increase of stagnation temperature. However, in the region of rotational motion the stagnation temperature significantly decreases. At the vortex axis this decrease was  $18^{\circ}$  in section 1 and approximately  $3^{\circ}$  in section 2 as compared to the stagnation temperature in front of the shock wave. The noted decrease of temperatures difference is caused by deceleration of gas rotation in the vortex.

In the book by Gupta [13] the measurement results of air temperature in the Ranque tube, described in paper [23] are presented. In this experimental setup air swirl is produced by a tangential air jet injection into a cylindrical chamber at one its end. The minimum air temperature was in the vicinity of the chamber axis at the same end, where air jet injection is performed. The minimum air temperature in paper [23] was by  $25^{\circ}$  lower than the injection air temperature, this agrees with the results of the current experiment. In the book [23] gas cooling at the vortex axis is explained by energy transfer due to turbulent fluctuations. In this investigation the air flow was laminar. Apparently, air cooling in the vortex can be explained in the following way: at first in the vicinity of the wing a vortex with high circumferential speeds is formed and herein speed increases while approaching to the axis, except low vicinity of the axis. The internal fast rotational layers due to gas viscosity (molecular or turbulent) transfer a moment of momentum to the external layers and increase their circumferential spe-

ed. This leads to decrease of the internal layers temperature and increase of the external gas layers temperature. As the internal layers mass is less than the external layers mass involved into the accelerated rotation, temperature decrease of the internal layers is essentially higher than the temperature increase of the external layers. Local temperature increase of the external layer is seen in Fig.31a in the vicinity of the vortex boundaries  $V_1$  and  $V_2$  and in Fig.31b in the vicinity of the vortex boundary  $V_1$ .

In Fig.32 the measured stagnation temperature  $T_s$  is related to the settling chamber temperature  $T_0$  ( $T_0 = 275-280$  K). The vortex centres in sections 1 and 2 (Fig.32) are conditionally superposed. The maximum stagnation temperature drop directly past the generator constitutes only 11%. As a first approximation one can neglect the influence of stagnation temperature variation on gas density and heat transfer.

### 2.3. Vortex-sphere interaction

#### 2.3.1. Gas flow pattern in front of sphere

For investigating vortex-sphere interaction a sphere with the diameter  $D=60$  mm was located past generator 2 ( $b=20$  mm) at the different distances  $x_s$  from its trailing edge. The sphere centre was situated approximately along the vortex axis. The investigation was carried out at the total pressure  $P_0 = 5 \cdot 10^5$  Pa and stagnation temperature  $T_0 = 410$  K. For flow visualization a kerosene heater was used.

Figure 33a shows a picture of the sphere in the absence of a vortex generator. This picture as well as the other is obtained by a straight shadowgraph method. Dimensions in the picture coincide with the real ones if not to take into account small distortions due to the light rays deviation. In

Fig.33b a picture of the flow past the generator installed at the angle of attack  $\alpha = 20^\circ$  is presented. Throughout the region available for observation the flow remains laminar and the vortex diameter weakly changes, as noted in the previous chapter.

Figures 34 and 35 present shadow pictures of the vortex cord interaction with the sphere at the generator angle of attack  $\alpha = 10^\circ$  and  $20^\circ$  ( $\bar{x}_s = x_s/D$ ). Analysis of these pictures shows the following. At some distance in front of the sphere a vortex breakdown occurs, i.e., the vortex sharply expands and in front of the sphere "a liquid cone" is formed, which generates a cone shock wave. Similar effect was observed earlier by interaction of the vortex with the inlet shock wave [2], with the shock wave in front of the cone and the barrel shock wave in the under-expanded jet [12], with the shock wave in front of two-dimensional wedge [24].

Figure 36 shows a supposed flow pattern. The gas involved into rotational motion in the vortex has a lower stagnation pressure  $p_s$  than the gas in the external flow outside the vortex. Still a greater difference is observed in the corresponding values of the axial momentum component. The gas with low value of the axial momentum component can not penetrate into the high pressure region past the bow shock wave. So during flow formation gas accumulation occurs in front of the sphere, followed by a vortex expansion i.e., a vortex breakdown. The flow region which can be conditionally called as a dead zone because in the significant part of this area (in the vicinity of the symmetry axis) gas speeds are low, is formed in front of the sphere. The dead zone is a region of approximately constant pressure. So it should have a conical shape. In the point of intersection of the shear layer separating the dead zone from the flow past the shock wave with the sphere surface a closing shock wave is formed. The dead zone length should be sufficiently large in

order the axial momentum component in the vortex flow can grow due to the momentum transfer from the external flow to the level which is sufficient for gas penetration into the high pressure region past the closing shock wave.

The described concept is confirmed not only by analysis of the pictures and also by results of calculations based on the Euler equations [1]. Certainly, such calculations do not allow the liquid cone formation to be described. However, they allow to determine the critical relation of the flow swirl and pressure ratio in the shock wave under which a vortex breakdown occurs.

The sphere shock wave-vortex interaction is similar to the interaction of the sphere shock wave with the boundary layer of the pin installed on the sphere [25]. In the case with the pin the boundary layer is separated from the pin surface in front of the bow shock wave and displaced from the axial direction to periphery in front of the bow sphere shock wave. In the case with the vortex a solid surface is absent but streamlines are also displaced to periphery in front of the bow shock. Having reached the sphere surface a portion of gas is deviated inside the dead zone and forms a slow reverse flow and the rest portion continues moving in the main direction. On the sphere surface the attachment line R is formed (Fig.37). In Fig.37 departure from the axial symmetry attracts attention: the separation point S is displaced relative to the sphere centre O to the right side. This is due to eccentricity of the sphere relative to the vortex axis. At the same time the attachment line R has approximately a shape of circle with the centre at the sphere axis (in the point O). It also attracts attention such a fact that the flow rotation in the periphery and in the centre of the sphere is weakly expressed.

Analysis of Figs.34 and 35 indicates to a turbulent flow be-

haviour in the larger part of the dead zone: in the pictures (exposure about 5 mcs) large vortices are seen as well as compression waves exited by them. The separation shock wave is an envelope of these waves. Location of the laminar-turbulent transition along the x-axis changes depending on the angle of attack and accidental factors. The transition occurs either inside the dead zone or at the beginning of the dead zone. In the first case the dead zone boundary is a broken line (Fig.36 b), through to this point the boundary is inclined at the angle about  $6^\circ$  relative to the flow axis and past it at the angle about  $20^\circ$ . In the second case the boundary is at the angle of  $17^\circ$ . At  $\alpha = 20^\circ$  a laminar-turbulent transition probably occurs in the vortex before the breakdown point. It is displayed in vortex expansion. From the transition point a weak compression wave spreads (see e.g. Fig.35 b). Evidently, disturbances from the dead zone are transferred upstream over the vortex core. Due to a complex character of the vortex-shock wave interaction the interpretation of the pictures is rather difficult and the above considerations about location of the laminar-turbulent transition should be verified.

The separation shock angle induced by the dead zone is approximately  $25^\circ$ . It is close to the calculated cone shock angle  $\beta = 23^\circ$ , formed in flow over a circular cone with the apex angle  $\theta = 12^\circ$  at Mach number of 3.

At a small distance between the sphere and generator the dead zone can appear between the leading and trailing edges of the generator as shown in Fig.34 a, in the other cases it appears past the vortex generator. In some cases it is difficult to determine unambiguously the dead zone length because of its complex shape. It can be assumed that at  $X_s/D \gg 1.15$  the dead zone length was approximately the same and constituted  $1.05 D$  in all experiments.

### 2.3.2. Heat transfer on the sphere surface

Heat transfer measurements on the sphere surface were carried out at  $x_s = 70$  mm ( $x_s/D=1.17$ ) and three angles of attack of the vortex generator 2:  $\alpha = 10^\circ$ ,  $20^\circ$  and  $30^\circ$ . The measurements on the sphere surface were also carried out without a vortex generator. The experiments were performed at  $T_0 \approx 400$  K. An electrical air heater was used.

The sphere was located in the wind tunnel test section in such a way that the generatrix with thermocouples 1-34 was in the plane  $z=0$ , and the generatrix with thermocouples 35-43 - in the plane  $y=0$ . The experiments were performed in the following way. During the period of setting a flow regime in the wind tunnel the model was in the thermostatic chamber and was separated from the flow by a special flap. Airflow over the model surface was performed by a cool air through the pipe, situated near the frontal surface. After setting a prescribed flow regime the model was injected into the flow by means of the fast-acting mechanism. The model has been in the flow for 3 seconds. During this period recording of thermocouples signals was carried out with sampling rate of 100 1/s, then the model was took out from the flow and the wind tunnel operation was stopped.

The results of the measurements are presented in Tables 5-8. The following parameters are presented in the tables: the generator angle of attack  $\alpha$ , the Mach number  $M$ , the Reynolds number  $Re$ , the stagnation temperature  $T_0$ , the total pressure  $P_0$ . The time  $\tau = 1$  s is also presented there, for this time the obtained data processing was being carried out. The chosen time is essentially larger than the period of injection of the model into the flow and it is quite small to avoid of noticeable heat spreading in the region of the maximum heat transfer on the sphere surface. In the first column of the

tables the thermocouple number is pointed out, in the second one - its coordinate  $s/R$ , further - the actual surface temperature  $T$  at  $\tau = 1$  s, the smoothed temperature  $T_{sm0}$ , the heat flux  $q$ , the calculated value of a heat flux in the stagnation sphere point  $q_0$  at the temperature  $T$  and the relation  $q/q_0$ .

The heat flux in the stagnation sphere point was calculated from the Fay-Riddell formula [26] which for the perfect gas takes form

$$q_0 = 0.94(\rho_w \mu_w)^{0.1} (\rho_s \mu_s)^{0.4} (i_0 - cT_w) R^{-0.5} (\delta u / \delta s)^{0.5}$$

In hypersonic flow over the sphere for calculation of the velocity gradient in the stagnation point we can use the formula obtained under condition of the Newton pressure distribution on the surface

$$\delta u / \delta s = 1/R(2(p_s - p_\infty)/\rho_s)^{0.5} \quad (1)$$

In the current paper for improving accuracy of the pressure gradient calculation at  $M=3$ , calculation results for inviscous flow over the sphere were used [27]. The difference in the value  $\delta u / \delta s$  as compared to formula (1) was 7.5 %.

Distribution of the relative heat flux  $q/q_0$  over the sphere surface in the case with a laminar flow was calculated by the equation [28]

$$q/q_0 = g_0 + g_1 \cos(\omega\eta) + g_2 \cos(2\omega\eta) + g_3 \cos(3\omega\eta)$$

Here  $\eta = \Re^n(s/s_*)$ ,  $s_*$  is a sonic point coordinate;  $n=0.5$ ;  $\omega=1$ ;  $g_0=0.452$ ;  $g_1=0.499$ ;  $g_2=0.049$ ;  $g_3=0$ ;  $\Re=1.4$ . Due to account for the influence of the Mach number on the sonic point location this formula gives a higher accuracy than a simple and often used equation

$$q/q_0 = 0.55 + 0.45\cos(2s/R)$$

In this paper a sonic point coordinate was determined by the tables [27].

In Fig.38 calculated and experimental heat flux distributions over the sphere surface in the absence of a vortex generator are compared. The heat flux values are presented for the surface temperature  $T_w=290K$ . It is seen that under these conditions a laminar flow over the whole sphere surfaces was retained. Some divergence of the heat flux values at the different generatrices of the sphere as well as the difference of a calculated and experimental values in the vicinity of the stagnation point are due to the experimental error. Furthermore, excess of the experimental value over the calculated one in the vicinity of the stagnation point can be associated with incoming flow turbulence: according to the measurements carried out by a laser Doppler Velocity Measurement System (DLA) the flow turbulence in the T-33 wind tunnel constitutes approximately 1%.

Figure 39 shows the influence of the vortex cord-bow wave interaction on the heat flux distribution over the sphere surface. In Fig.39 both calculated and experimental heat flux values are related to the calculated heat flux in the stagnation point of the sphere. The vortex causes a qualitative variation of the heat flux distribution: in the vicinity of the sphere axis the heat flux is substantially less than on the isolated sphere. In the vicinity of the attachment line R the heat flux in the presence of a vortex essentially increases not only as compared to the heat flux in the same point and in comparison with the heat flux in the stagnation point of the isolated sphere (Fig.39b,  $\alpha=20^\circ$ ). Such a significant heat flux increase can be explained by two things:

1) subsequent gas compression in the oblique and normal shock waves leads to a greater pressure increase at the attachment line R than the gas compression in the normal shock in the vicinity of the stagnation point of the isolated sphere;  
2) vortex-bow wave interaction leads to a flow turbulation in the vicinity of the sphere. The flow turbulence also leads to a significant increase of the heat transfer downstream of the line R on the cylindrical part of the model (compare  $q/q_0$  at  $s/R \approx 2.5$ , Fig. 38b and 39b). As a result of the vortex influence, an integral heat flux to the blunt body surface increases as well.

The heat flux distribution on the sphere interacting with a vortex is similar to the heat flux distribution on the spiked sphere [25]: in case two the heat flux in the vicinity of the symmetry line also decreases and increases at the attachment line and behind it.

From Fig. 39 it is seen that the heat flux distribution over the sphere surface interacting with a vortex was asymmetrical at all investigated values of the generator angles of attack. Probably, it is associated with that fact that the vortex and sphere are not coaxial. Judging by Fig. 39 at all angles of attack the vortex was essentially displaced relative to the sphere axis in the vertical plane: at  $\gamma = 180^\circ$  the heat flux maximum is substantially less and displaced by a greater distance from the axis of symmetry than at  $\gamma = 0$  (Fig. 39). It can be the consequence of that fact that the vortex axis goes below the sphere axis.

In Fig. 40 the heat flux distributions at different angles of attack of the generator are compared for each sphere generator. The maximum relative heat flux values  $q_m/q_0$  versus the generator angle of attack are presented in Fig. 41. From Figs. 40 and 41 it is seen that  $q_m/q_0$  changes against the angle in nonmonotonous manner: at  $\alpha < 20^\circ$  the value  $q_m/q_0$

grows with increase of the angle and at a higher angle of attack it decreases. However, this effect can not be unambiguously associated either with the flow swirl increase or the vortex diameter increase against the angle of attack. Apparently, the value  $q_m/q_0$  was greatly influenced by the vortex axis displacement relative to the sphere axis. At  $\alpha=20^\circ$  the eccentricity was the least one (coincidence of heat flux distributions at  $\gamma=0$  and  $\gamma=90^\circ$  is an evidence of this). Probably, it was the reason that the maximum relative heat flux value was obtained at  $\alpha=20^\circ$ .

For quantitative comparison of heat transfer on the sphere interacting with the vortex and on the sphere with the pin on the ordinate axis of Fig. 41, the maximum value from the paper by Crawford described in [25] is presented. The maximum values obtained in this investigation are close to Crawford results.

Thus, the measurements have shown that due to the vortex influence the flow over the blunt body is being reconstructed and on its surface a significant heat transfer increase is observed, that is very important for practical applications.

# Nomenclature for the part B

- a = speed of sound,
- $c_p$  = specific heat at constant pressure,
- $c_v$  = specific heat at constant volume,
- g = velocity circulation in axisymmetric flow,
- h =  $\gamma p / ((\gamma - 1) / \rho)$ , enthalpy per unit mass,
- $h_0$  =  $h + (u^2 + v^2 + w^2) / 2$ , total enthalpy per unit mass,
- M = Mach number,
- p = pressure,
- r = radial coordinate,
- R =  $\rho_\infty u_\infty \delta / \mu_\infty$ , Reynolds number,
- S = entropy per unit mass,
- T = absolute temperature,
- u, v, w = axial, radial and azimuthal components of velocity,
- v =  $v \cdot r$ ,
- x = coordinate along free stream direction,
- y =  $r^2 / 2$ ,
- $\gamma$  =  $c_p / c_v$ , ratio of specific heats,
- $\delta$  = vacuum core scale,
- $\delta_u$ ,  $\delta$  = effective vortex thicknesses
- $\eta$  =  $r^2 / (4x)$ ,
- $\mu$  = viscosity coefficient,
- $\mu_2$  = second viscosity coefficient,
- $\xi$  =  $x^{(1-\gamma)/\gamma} (r^2 - 1) / 2$ ,
- $\rho$  = density,
- $\delta$  = Prandtl number,
- $\tau$  = time,
- $\varphi$  = swirl angle,
- $\psi$  = stream function,
- $\bar{g}, \bar{h}$ ,
- $\bar{p}, \bar{T}$  = circulation, enthalpy, pressure, temperature scaled by external values at  $r \rightarrow \infty$ ,

$T_0$  = total temperature.

subscripts

- $\infty$  = free stream conditions,
- 1 = first term in asymptotic expansion,
- 2 = second term in asymptotic expansion,
- d = dimensional values,
- e = external flow,
- i = initial conditions,
- s = stagnation point past normal shock wave.

## B. Analitical and numerical study of vortex development

### 1. Problem formulation

The main theoretical approaches used for description of the vortex development and breakdown in incompressible fluid [30-41] are generalized here to include compressibility. The quasi-cylindrical approximation is derived as asymptotic approach for the slender, smoothly developing vortex. Small perturbations of the cylindrical flow are considered to generalize a well-known classification of the vortex flows on subcritical and supercritical [30].

#### 1.1. Governing equations

Axisymmetric compressible flow of perfect gas having axial, radial and azimuthal components of velocity is considered. The viscosity  $\mu$  and the bulk viscosity  $\mu_2$  are the functions of temperature, the Prandtl number  $\delta$  and  $\gamma = C_p/C_v$  are constants. The Navier-Stokes equations for axial, radial and azimuthal momentums and the mass-conservation equation are represented correspondently as:

$$\rho \frac{du}{dt} = - \frac{\delta p}{\delta x} + \mu \nabla^2 u + \frac{1}{3} (\mu + 2\mu_2) \frac{\delta D}{\delta x} +$$

$$+ \frac{\delta \mu}{\delta x} \left( 2 \frac{\delta u}{\delta x} - \frac{2}{3} D \right) + \frac{\delta \mu}{\delta r} \left( \frac{\delta v}{\delta x} + \frac{\delta u}{\delta r} \right) + \frac{2}{3} \frac{\delta \mu_2}{\delta x} D , \quad (1.1.1)$$

$$\rho \left( \frac{dv}{d\tau} - \frac{w^2}{r} \right) = - \frac{\delta p}{\delta r} + \mu \left( \nabla^2 v - \frac{v}{r^2} \right) + \frac{1}{3} (\mu + 2\mu_2) \frac{\delta D}{\delta r} + \quad (1.1.2)$$

$$+ \frac{\delta \mu}{\delta x} \left( \frac{\delta v}{\delta x} + \frac{\delta u}{\delta r} \right) + \frac{\delta \mu}{\delta r} \left( 2 \frac{\delta w}{\delta r} - D \right) + \frac{2}{3} \frac{\delta \mu_2}{\delta r} D ,$$

$$\rho \left( \frac{dw}{d\tau} + v \frac{w}{r} \right) = \mu \left( \nabla^2 w - \frac{w}{r^2} \right) + \frac{\delta \mu}{\delta x} \frac{\delta w}{\delta x} + \frac{\delta \mu}{\delta r} \left( \frac{\delta w}{\delta r} - \frac{w}{r} \right) , \quad (1.1.3)$$

$$\frac{d\rho}{d\tau} + \rho D = 0 , \quad (1.1.4)$$

where  $x, r$  - cylindrical axial and radial coordinates;  $u, v, w$  - axial, radial and azimuthal components of velocity;  $p$  - pressure;  $\rho$  - density,

$$\frac{d}{d\tau} \equiv \frac{\delta}{\delta \tau} + u \frac{\delta}{\delta x} + v \frac{\delta}{\delta r} ,$$

$$D \equiv \text{div } V = \frac{\delta u}{\delta x} + \frac{1}{r} \frac{\delta}{\delta r} (vr) ,$$

$$\nabla^2 = \frac{\delta^2}{\delta x^2} + \frac{\delta^2}{\delta r^2} + \frac{1}{r} \frac{\delta}{\delta r} .$$

We reproduce here also equations for enthalpy  $h = \gamma p / ((\gamma - 1)\rho)$  and pressure:

$$\rho \frac{dh}{d\tau} = \frac{dp}{d\tau} + \operatorname{div} \left( \frac{\mu}{\delta} \nabla h \right) + N, \quad (1.1.5)$$

$$\frac{dp}{d\tau} = -\gamma p D + (\gamma - 1) \operatorname{div} \left( \frac{\mu}{\delta} \nabla h \right) + (\gamma - 1) N, \quad (1.1.6)$$

$$N = \mu \left[ 2 \left( \frac{\delta u}{\delta x} \right)^2 + 2 \left( \frac{\delta v}{\delta r} \right)^2 + 2 \frac{v^2}{r^2} + \left( \frac{\delta w}{\delta x} \right)^2 + \right. \\ \left. + \left( \frac{\delta v}{\delta x} + \frac{\delta u}{\delta r} \right)^2 + \left( \frac{\delta w}{\delta r} - \frac{w}{r} \right)^2 \right] - \frac{2}{3} (\mu - \mu_2) D^2.$$

The equations (1.1.1)-(1.1.4) together with any of equations (1.1.5), (1.1.6) and with stated functions  $\mu(h)$ ,  $\mu_2(h)$  compose the complete system which is to be analyzed.

## 1.2 Inviscid axisymmetric steady flow

The inviscid counterparts of the equations considered above are obtained setting  $\mu=0$ ,  $\mu_2=0$ . Then, the well-known consequences of the equations are:

$$u \frac{\delta h_0}{\delta x} + v \frac{\delta h_0}{\delta r} = 0,$$

$$u \frac{\delta S}{\delta x} + v \frac{\delta S}{\delta r} = 0, \quad (1.2.1)$$

$$u \frac{\delta g}{\delta x} + v \frac{\delta g}{\delta r} = 0,$$

where  $h_0 = h + (u^2 + v^2 + w^2)/2$  - total enthalpy;  $S = S_0 + c_v \ln(p/\rho^\gamma)$  - entropy;  $g = wr$  - circulation. The mass-conservation equation (1.1.4) is integrated by introducing of the stream function  $\psi$ :

$$\rho u r = \frac{\delta \psi}{\delta r}, \quad (1.2.2)$$

$$\rho v r = - \frac{\delta \psi}{\delta x}.$$

The equations (1.2.1)-(1.2.2) demonstrate that the functions  $h_0$ ,  $S$ ,  $g$  are convected along streamsurfaces. Therefore, three integrals exist for the inviscid axisymmetric steady flow:  $h_0 = h_0(\psi)$ ,  $S = S(\psi)$ ,  $g = g(\psi)$ .

We notice, that entropy is always convected together with gas particles, total enthalpy is convected along the streamlines only in steady flows. The circulation in arbitrary three-dimensional flow is described by following equation

$$\frac{d\Gamma}{dt} = \int (\nabla T \times \nabla S) \cdot n \, dA,$$

where  $\Gamma$  - circulation along a closed curve formed by moving particles,  $T$ -temperature,  $dA$  - area element of the surface based on this closed curve,  $\vec{n}$  - unit vector normal to this element. Therefore, in contrast to incompressible flow, the circulation is conserved, and the conservation equation (1.2.1) is a consequence of axisymmetry.

Using the momentum equation represented in the Lamb's form

$$\nabla\left(\frac{V^2}{2}\right) + (\text{rot } V) \times V = - \frac{1}{\rho} \nabla p,$$

and the thermodynamic correlation  $T \nabla S = \nabla h - \frac{1}{\rho} \nabla p$ , the following relation is found:

$$V \times \text{rot } V = \nabla h_0 - T \nabla S, \quad (1.2.3)$$

The right-hand side vector in (1.2.3) is normal to the stream surfaces. Therefore, the vorticity  $\Omega = \text{rot } V$  has zero component in this normal direction, its component along the meridian section of the stream surface  $\Omega_r = \rho q \delta(wr) / \delta\psi$ ,  $q = (u^2 + v^2)^{1/2}$ , and azimuthal component  $\Omega_\varphi = \delta v / \delta x - \delta u / \delta r$ . The velocity vector is decomposed as  $V_r = q$ ,  $V_n = 0$ ,  $V_\varphi = w$ . Using these coordinates, (1.2.3) is represented as:

$$\frac{\delta v}{\delta x} - \frac{\delta u}{\delta r} = \rho r \left( T \frac{ds}{d\psi} - \frac{dh_0}{d\psi} + \frac{1}{2r^2} \frac{dw^2}{d\psi} \right) \quad (1.2.4)$$

We use the following identities to transform the left-hand part of (1.2.4) into adapted form:

$$\rho \left( \frac{\delta v}{\delta x} - \frac{\delta u}{\delta r} \right) = \frac{\delta(\rho v)}{\delta x} - \frac{\delta(\rho u)}{\delta r} - \left( v \frac{\delta \rho}{\delta x} - u \frac{\delta \rho}{\delta r} \right),$$

$$v \frac{\delta \rho}{\delta x} - u \frac{\delta \rho}{\delta r} = \frac{1}{a^2} \left( v \frac{\delta p}{\delta x} - u \frac{\delta p}{\delta r} \right) + \frac{1}{c_p r} \frac{ds}{d\psi} \left[ \left( \frac{\delta \psi}{\delta x} \right)^2 + \left( \frac{\delta \psi}{\delta r} \right)^2 \right].$$

Using the conservative form of the momentum equation we found

$$v \frac{\delta p}{\delta x} - u \frac{\delta p}{\delta r} = - \frac{1}{r} \left[ u^2 \frac{\delta^2 \psi}{\delta x^2} + 2uv \frac{\delta^2 \psi}{\delta x \delta r} + v^2 \frac{\delta^2 \psi}{\delta r^2} + \rho u v^2 \right].$$

Finally, the equation (1.2.4) is represented as

$$\left( 1 - \frac{u^2}{a^2} \right) \frac{\delta^2 \psi}{\delta x^2} - \frac{2uv}{a^2} \frac{\delta^2 \psi}{\delta x \delta r} + \left( 1 - \frac{v^2}{a^2} \right) \frac{\delta^2 \psi}{\delta r^2} - \frac{1}{r} \frac{\delta \psi}{\delta r} = \quad (1.2.5)$$

$$= \rho^2 r^2 \left[ \frac{dh_0}{d\psi} - \frac{1}{2r^2} \frac{dg^2}{d\psi} - T \frac{ds}{d\psi} \left( 1 + (\gamma - 1) \frac{u^2 + v^2}{a^2} \right) \right] + \frac{\rho u g^2}{a^2 r^2}.$$

Three arbitrary functions  $h_0(\psi)$ ,  $S(\psi)$ ,  $g(\psi)$  must be determined on all stream surfaces entering the region of interest. Then,  $u$ ,  $v$ ,  $\rho$ ,  $p$ ,  $a$ ,  $T$  are expressed as functions of  $\psi$ ,  $r$ ,  $\delta\psi/\delta r$ ,  $\delta\psi/\delta x$  using the relations (1.2.2) and

$$h_0(\psi) = \frac{\gamma}{\gamma - 1} \frac{p}{\rho} + \frac{u^2 + v^2}{2} + \frac{g^2}{2r^2},$$

$$S(\psi) = S_0 + c_v \ln \frac{p}{\rho^\gamma}, \quad (1.2.6)$$

$$a^2 = \frac{p}{\rho^\gamma}, \quad T = a^2 / [(\gamma-1)c_p].$$

Therefore, the inviscid axisymmetric compressible steady flow is described by single quasilinear second-order equation (1.2.5). As far as the shocks may be formed in the flow, the equations must be supplemented by the conditions on the shock. We do not concern this question here and only note, that the functions  $h_0(\psi)$ ,  $g(\psi)$  do not change through the shock, while  $S(\psi)$  has a jump.

The simplest application of equations (1.2.5), (1.2.2), (1.2.6) is the investigation of the cylindrical vortex response on the changes of the external pressure.

Let the axial scale is large compared with the radial one and  $v \ll u$ . The small terms are discarded in (1.2.5) and the second-order ordinary differential equation is obtained:

$$\begin{aligned} r \frac{d}{dr} \left( - \frac{1}{r} \frac{d\psi}{dr} \right) = \rho^2 r^2 \left[ \frac{dh_0}{d\psi}(\psi) - \frac{1}{2r^2} \frac{dg^2(\psi)}{d\psi} - \right. \\ \left. - T \frac{dS(\psi)}{d\psi} (1 + (\gamma-1) \frac{u^2}{a^2}) \right] + \frac{\rho u g^2(\psi)}{a^2 r^2}. \end{aligned} \quad (1.2.7)$$

Let the initial profiles  $u_1(r) > 0$ ,  $g_1(r)$ ,  $\rho_1(r)$ , and the pressure at infinity  $p_1(\infty)$  are determined at some section. The pressure and stream-function are found by integration:

$$p_1(r) = p_1(\infty) - \int_r^{\infty} \frac{\rho_1 g_1^2}{r^3} dr, \quad (1.2.8.)$$

$$\psi(r) = \int_0^r \rho_1 u_1 r dr.$$

Then, the inverse function  $r(\psi)$  is obtained and the functions

$$g(\psi) = g_1(r(\psi)),$$

$$S(\psi) = S_0 + c_v \ln \left. \frac{p_1}{\rho_1^\gamma} \right|_{r=r(\psi)}, \quad (1.2.9)$$

$$h_0(\psi) = \left( \frac{\gamma}{\gamma-1} \frac{p_1}{\rho_1} + \frac{u_1^2}{2} + \frac{g_1^2(\psi)}{2r^2} \right) \Big|_{r=r(\psi)}$$

are determined.

The profiles  $\rho$ ,  $u$ ,  $p$ ,  $T$  are found at  $v=0$  from (1.2.2), (1.2.6), like it was mentioned above, and are the functions of  $\psi$ ,  $r$ ,  $d\psi/dr$ .

The profiles  $g$ ,  $S$ ,  $h_0$  are considered tending to constants as  $\psi \rightarrow \infty$ , i.e. the vortex is surrounded by potential flow. Let the external pressure changes from  $p_1(\infty)$  to  $p(\infty)$ . Then, the velocity and density at infinity are obtained from

$$u^2(\infty) = u_1^2(\infty) + 2 \frac{\gamma p_1(\infty)}{\gamma-1 \rho_1(\infty)} \left[ 1 - \frac{p(\infty)}{p_1(\infty)} \right]^{(\gamma-1)/\gamma},$$

$$\rho(\infty) = \rho_1(\infty) \left[ \frac{p(\infty)}{p_1(\infty)} \right]^{1/\gamma}. \quad (1.2.10)$$

The response of the vortex on this external pressure change is found by solving of (1.2.7) at boundary conditions

$$\psi(0) = 0, \quad \frac{1}{r} \frac{\delta \psi}{\delta r} \rightarrow \rho(\infty) u(\infty) \quad \text{at} \quad r \rightarrow \infty.$$

It is easy to show that the profile  $\psi(r)$  found from (1.2.8) is a solution of (1.2.7) for boundary conditions

$$\psi(0) = 0, \quad \frac{1}{r} \frac{\delta \psi}{\delta r} \rightarrow \rho_1(\infty) u_1(\infty) \quad \text{at} \quad r \rightarrow \infty.$$

Do other solutions of (1.2.7) exist at the same boundary conditions? Such solutions were found in incompressible flows and were called "conjugate" to the basic one [30]. The existence of conjugate flows allows spontaneous jumps between them which were treated as vortex breakdown.

### 1.3 Small perturbations of the cylindrical flow

The analysis of steady small perturbations of the cylindrical vortex performed for incompressible flow resulted in an important division of the vortex flow on subcritical and

supercritical. We generalize this analysis for the compressible vortex.

The governing equation may be derived from (1.2.5). However, it is useful to perform the derivation directly from the Euler equations:

$$\rho \left( u \frac{\delta u}{\delta x} + v \frac{\delta u}{\delta r} \right) = - \frac{\delta p}{\delta x} ,$$

$$u \frac{\delta g}{\delta x} + v \frac{\delta g}{\delta r} = 0 ,$$

$$u \frac{\delta p}{\delta x} + v \frac{\delta p}{\delta r} = - \gamma p \left( \frac{\delta u}{\delta x} + \frac{1}{r} \frac{\delta(vr)}{\delta r} \right) , \quad (1.3.1)$$

$$\frac{\delta(\rho u)}{\delta x} + \frac{1}{r} \frac{\delta(\rho v r)}{\delta r} = 0 ,$$

$$\rho \left( u \frac{\delta(vr)}{\delta x} + v \frac{\delta(vr)}{\delta r} - \frac{g^2 + v^2 r^2}{r^2} \right) = - r \frac{\delta p}{\delta r} .$$

The small perturbations of the basic cylindrical flow are considered:

$$u = u_0(y) + \varepsilon u_1(x, y) + \dots ,$$

$$g = g_0(y) + \varepsilon g_1(x, y) + \dots ,$$

$$p = p_0(y) + \varepsilon p_1(x, y) + \dots , \quad (1.3.2)$$

$$\rho = \rho_0(y) + \varepsilon \rho_1(x, y) + \dots ,$$

$$V = \varepsilon V_1(x, y) + \dots ,$$

where  $\varepsilon \rightarrow 0$ ,  $V = vr$ ,  $y = r^2/2$  and the base cylindrical profiles are correlated by the equation

$$\frac{d\rho_0}{dy} = \frac{\rho_0 g_0^2}{4y^2} . \quad (1.3.3)$$

The equations for perturbations are:

$$\rho_0 \left( u_0 \frac{\delta u_1}{\delta x} + V_1 u_0' \right) = - \frac{\delta p_1}{\delta x} ,$$

$$u_0 \frac{\delta g_1}{\delta x} + V_1 g_0' = 0 ,$$

$$\rho_0 \frac{\delta u_1}{\delta x} + u_0 \frac{\delta \rho_1}{\delta x} + \rho_0 \frac{\delta V_1}{\delta y} + V_1 \rho_0' = 0 , \quad (1.3.4)$$

$$u_0 \frac{\delta p_1}{\delta x} + V_1 p_0' = -\gamma p_0 \left( \frac{\delta u_1}{\delta x} + \frac{\delta V_1}{\delta y} \right) ,$$

$$-\rho_1 \frac{g_0^2}{2y} + \rho_0 \left( u_0 \frac{\delta V_1}{\delta x} - \frac{g_0 g_1}{y} \right) = -2y \frac{\delta p_1}{\delta y} ,$$

where the prime means the y-derivative.

The axial derivatives of the perturbations are found from

the former four equations of (1.3.4):

$$\frac{1}{\rho_0 u_0^2} \frac{\delta p_1}{\delta x} = \left( \frac{p_0'}{\gamma p_0} f + f' \right) / (1 - M_0^2) ,$$

$$\frac{1}{u_0} \frac{\delta u_1}{\delta x} = - \frac{u_0'}{u_0} f - \left( \frac{p_0'}{\gamma p_0} f + f' \right) / (1 - M_0^2) ,$$

$$\frac{\delta g_1}{\delta x} = - g_0' f ,$$
(1.3.5)

$$\frac{1}{\rho_0} \frac{\delta \rho_1}{\delta x} = - \frac{\rho_0'}{\rho_0} f - f' + \left( \frac{p_0'}{\gamma p_0} f + f' \right) / (1 - M_0^2) ,$$

where  $f = V_1/u_0$ ,  $M_0^2 = \rho_0 u_0^2 / (\gamma p_0)$ .

Using (1.3.5) and the last equation of (1.3.4), the following second-order linear equation is obtained:

$$\left( \frac{\rho_0 u_0^2 f'}{1 - M_0^2} \right) + \frac{\rho_0 u_0^2}{2y} \frac{\delta^2 f}{\delta x^2} + \left[ \left( \frac{p_0'}{1 - M_0^2} \right) + \frac{2}{y} p_0' - \frac{p_0'^2}{\gamma p_0 (1 - M_0^2)} \right] f = 0.$$
(1.3.6)

The ordinary differential equation is found for the perturbations having a form  $f = \exp(\alpha x) F(y)$ :

$$\left(\frac{\rho_0 u_0^2}{1-M_0^2} F'\right)' + \left[\frac{\rho_0 u_0^2}{2y} \alpha^2 + \left(\frac{p_0'}{1-M_0^2}\right) + \frac{2}{y} p_0' - \frac{p_0'^2}{\gamma p_0 (1-M_0^2)}\right] F = 0. \quad (1.3.7)$$

The sonic point  $M_0=1$  is a singular point of equation (1.3.7). We must investigate this singularity, especially taking into account that the term  $(1-M_0^2)$  is a denominator in (1.3.5).

Let  $M_0=1$  at  $y=y_0$  and  $\vartheta=y-y_0$ . The equation (1.3.7) is represented near  $\vartheta=0$  as

$$\vartheta(1+A\vartheta+\dots)F'' - (1+B\vartheta+\dots)F' + (C+D\vartheta+\dots)F = 0,$$

$$A = \frac{M_0'^2}{M_0^2},$$

$$B = -\frac{3}{2}A - \frac{p_0'}{p_0} - (M_0'^2)', \quad (1.3.8)$$

$$C = -\frac{p_0'}{\gamma p_0},$$

$$D = (\gamma-1)C^2 - C\left(-\frac{3}{2}A - (M_0'^2)'\right),$$

where the coefficients A,B,C,D are calculated at  $\vartheta=0$ .

According to the method of Frobenius, two linearly indepen-

dent solutions of (1.3.7) near  $\tilde{\vartheta} = 0$  have the form:

$$F_1 = \vartheta^2 \sum_{n=0}^{\infty} a_n \vartheta^n ,$$

$$F_2 = QF_1 \ln|\vartheta| + \sum_{n=0}^{\infty} b_n \vartheta^n ,$$

where coefficients  $a_n$ ,  $b_n$ ,  $Q$  are determined from (1.3.7):

$$a_0 = 1, \quad a_1 = -\frac{1}{3}(2(A-B)+C), \quad \dots ,$$

$$b_0 = 1, \quad b_1 = C, \quad \dots ,$$

$$Q = -\frac{1}{2}[D+(B-C)b_1] .$$

In general case, the solution has infinite second derivative at  $\tilde{\vartheta}=0$ . However, direct calculation showed that  $Q \equiv 0$ , and all derivatives are finite. Moreover, the generally singular term  $(fp_0' / \gamma p_0 + f') / (1-M_0^2)$  is regular.

An arbitrary jump of the second derivative is allowed by the equation (1.3.7) at  $y=y_0$ . But in this case, the functions  $u_1$ ,  $p_1$ ,  $\rho_1$  would have a jump too, and we exclude this possibility. This requirement makes the problem closed.

The another question is the asymptotic behaviour of the solutions of (1.3.7) at  $y \rightarrow \infty$ . For this purpose we must know more details about structure of the basic cylindrical flow. We consider the vortex surrounded by potential flow with  $h_0 = \text{const}$ ,  $S = \text{const}$ ,  $g = \text{const}$ . The deflexion of these functions from constants is caused inside the vortex by diffusion and

is usually exponentially small far from the vortex core. The potential vortex has its own dimensional scale

$$r_* = \frac{g_\infty}{a_\infty} \left[ \frac{\gamma-1}{2} \right]^{1/2}, \quad y_* = \frac{r_*^2}{2},$$

where  $a_\infty$  - the sound velocity far from the core. The solution is easily found from (1.3.3) and the conditions  $h_0 = \text{const}$ ,  $S = \text{const}$ ,  $g = \text{const}$ :

$$u_0 = u_\infty,$$

$$M_0^2 = M_\infty^2 / (1 - y_*/y),$$

$$\frac{a_0^2}{a_\infty^2} = 1 - \frac{y_*}{y}, \quad (1.3.9)$$

$$\frac{p_0}{p_\infty} = \left[ 1 - \frac{y_*}{y} \right]^{\gamma/(\gamma-1)},$$

$$\frac{\rho_0}{\rho_\infty} = \left[ 1 - \frac{y_*}{y} \right]^{1/(\gamma-1)}.$$

This solution represents a vortex having the vacuum core at  $y = y_*$ ,  $M_0 \rightarrow \infty$  as  $y \rightarrow y_*$ . The solution has not counterparts in incompressible fluid (a rather remote analogue is the vortex with cavitation). The expansion of the solution (1.3.9) at  $y \gg y_*$  is the general representation of the flow around a compressible vortex. Using this representation, the asymptotic behaviour of the solutions of (1.3.7) at  $y \rightarrow \infty$  is found:

$$F = (2y)^{1/2} \exp(6\sqrt{2y}) [1 - c(2y)^{-1/2} + o(y^{-1})] ,$$

$$\beta = \pm (\alpha^2 (M_\infty^2 - 1))^{1/2} , \quad (1.3.10)$$

$$c = - \left[ \frac{3}{8\beta} + \beta y_* \left( \frac{2}{\gamma-1} - \frac{M_\infty^2}{1-M_\infty^2} \right) \right] .$$

Two signs in (1.3.10) correspond to two different linearly independent solutions. The positive eigenvalues  $\alpha^2 > 0$  describe the upstream influence of the profile perturbed at some position, while  $\alpha^2 < 0$  describe the standing waves. In two cases:  $\alpha^2 > 0$ ,  $M_\infty > 1$  and  $\alpha^2 < 0$ ,  $M_\infty < 1$ , one of two functions increases exponentially as  $y \rightarrow \infty$  and obviously must be excluded.

The following physical examination is useful for understanding of possible solutions of (1.3.7). We consider the vortex confined into finite cylinder ( $0 < y < y_R$ ). The boundary conditions for (1.3.7) in this case are:  $F(0)=0$ ,  $F(y_R)=0$ . Only monotonous profiles of  $M_0$  are considered. The assertions are not rigorously proved and are obtained from asymptotic analysis of the solutions for  $|\alpha^2| \gg 1$ .

1. In the case  $M_0^2 < 1$  the infinite discrete spectrum exists such that  $\alpha_0^2 < \alpha_1^2 < \alpha_2^2 < \dots$ . The positive  $\alpha_n^2 > 0$  are condensed into continuous spectrum as  $y_R \rightarrow \infty$ . In this limit only a finite number of discrete eigenvalues  $\alpha_n^2 < 0$  may exist. If at least one  $\alpha^2 < 0$  exist - the flow supports standing waves and is called "subcritical", in opposite case - "supercritical". This is direct generalization of the classification adopted for incompressible flows.

2. In the case  $M_0^2 > 1$  the infinite discrete spectrum is ordered as  $\alpha_0^2 > \alpha_1^2 > \alpha_2^2 > \dots$ . The standing waves are always supported in the confined supersonic flow. They are caused simply by reflection from the boundaries. For physical rea-

sons all  $\alpha^2$  are negative (however, we did not prove it directly for the equation (1.3.7)). All negative eigenvalues are condensed into continuous spectrum as  $y_R \rightarrow \infty$ . Is there a positive eigenvalue possible ?

3. In the case  $M_\infty > 1$ ,  $M_0(0) < 1$ , the discrete spectrum covers whole real axis:  $\dots < \alpha_{-1}^2 < \alpha_0^2 < \alpha_1^2 < \dots$ . Its negative part is condensed into continuous spectrum as  $y_R \rightarrow \infty$ . The infinite discrete positive spectrum always exists for unbounded flow. From this spectrum we can determine how the profile perturbations propagate upstream.

4. In the case  $M_\infty < 1$ ,  $M_0(0) > 1$  the discrete spectrum covers whole real axis too. Its positive part is condensed, however infinite discrete negative spectrum remains as  $y_R \rightarrow \infty$ . Such unbounded flow always supports standing waves attributed to the reflection inside the inner supersonic part.

Therefore, two problem statements concerning discrete spectra in unbounded flow are formulated: if  $M_\infty < 1$  - to find all  $\alpha^2 < 0$ , and if  $M_\infty > 1$  - to find all  $\alpha^2 > 0$ , such that the equation (1.3.7) and boundary conditions  $F(0) = 0$ ,  $F'(\infty) = 0$  are satisfied.

The most important finding possible during the discrete spectra analysis is the detection of an eigenvalue which tends to zero as some profile parameter changes. The existence of the eigenvalue close to zero means that the perturbations propagate far upstream.

The asymptotic behaviour of the solutions at  $\alpha^2 = 0$ ,  $y \rightarrow \infty$  differs from (1.3.10). Two linearly independent solutions have the form:

$$F_1 = 1 + \frac{a_1}{y} + O\left(\frac{1}{y^2}\right),$$

$$F_2 = y + b_1 \ln y + O\left(\frac{\ln y}{y}\right),$$

(1.3.11)

$$a_1 = \frac{\gamma p_\infty M_\infty^2}{(\gamma - 1)(1 - M_\infty^2)} y_*,$$

$$b_1 = -2a_1 - \left(\frac{M_\infty^2}{1 - M_\infty^2} - \frac{1}{\gamma - 1}\right) y_*.$$

#### 1.4 Quasi-cylindrical approximation

The quasi-cylindrical approximation is an asymptotic approach for description of the slender vortex smoothly regrouping under the action of viscosity or pressure gradient. It is similar in its nature to the boundary-layer approach.

Let the vortex has a radial scale  $\delta$  in its initial section. Nondimensional variables are introduced by the scaling:  $r_d = \delta r$ ,  $x_d = R_\delta \delta x$ ,  $u_d = u_\infty u$ ,  $v_d = (u_\infty / R_\delta) v$ ,  $w_d = u_\infty w$ ,  $\rho_d = \rho_\infty \rho$ ,  $p_d = \rho_\infty u_\infty^2 p$ ,  $\mu_d = \mu_\infty \mu$ . The index "d" corresponds to dimensional variables, index " $\infty$ " - to the flow in the initial section at  $r \rightarrow \infty$ ,  $R_\delta = \rho_\infty u_\infty \delta / \mu_\infty$  is the Reynolds number. The analysis of the Navier-Stokes equations at the limit  $R_\delta \rightarrow \infty$ ,  $r=O(1)$ ,  $x=O(1)$  allows to find the first-approximation equations:

$$\rho \left( u \frac{\partial u}{\partial x} + v \frac{\partial u}{\partial r} \right) = - \frac{\partial p}{\partial x} + \frac{1}{r} \frac{\partial}{\partial r} \left( \mu r \frac{\partial u}{\partial r} \right),$$

$$\rho \left( u \frac{\delta g}{\delta x} + v \frac{\delta g}{\delta r} \right) = r \frac{\delta}{\delta r} \left( \mu \frac{1}{r} \frac{\delta g}{\delta r} \right) - \frac{2}{r} \frac{\delta \mu}{\delta r} g ,$$

$$\frac{\delta(\rho u)}{\delta x} + \frac{1}{r} \frac{\delta(\rho v r)}{\delta r} = 0 ,$$

$$\frac{1}{r} \frac{\delta p}{\delta r} = \rho \frac{g^2}{r^4} , \quad (1.4.1)$$

$$\begin{aligned} \rho \left( u \frac{\delta h}{\delta x} + v \frac{\delta h}{\delta r} \right) &= u \frac{\delta p}{\delta x} + v \frac{\delta p}{\delta r} + \frac{1}{r} \frac{\delta}{\delta r} \left( \mu \frac{\delta h}{\delta r} \right) + \\ &+ \mu \left[ \left( \frac{\delta u}{\delta r} \right)^2 + \left( \frac{1}{r} \frac{\delta g}{\delta r} - \frac{g}{r^2} \right)^2 \right] , \end{aligned}$$

$$h = \frac{\gamma}{\gamma-1} \frac{p}{\rho} , \quad \mu = \mu(h) ,$$

where  $g=wr$ .

The equation for  $h$  may be changed by the equation for  $p$ :

$$\begin{aligned} u \frac{\delta p}{\delta x} + v \frac{\delta p}{\delta r} &= - \gamma p \left( \frac{\delta u}{\delta x} + \frac{1}{r} \frac{\delta(vr)}{\delta r} \right) + (\gamma-1) \frac{1}{r} \frac{\delta}{\delta r} \left( \mu \frac{\delta h}{\delta r} \right) + \\ &+ (\gamma-1) \mu \left[ \left( \frac{\delta u}{\delta r} \right)^2 + \left( \frac{1}{r} \frac{\delta g}{\delta r} - \frac{g}{r^2} \right)^2 \right] . \end{aligned} \quad (1.4.2)$$

The system (1.4.1) is a nonlinear parabolic system. We formulate the problem statement for the vortex surrounded by potential flow.

Let the initial profiles  $u_1$ ,  $g_1$ ,  $h_1$  are determined at the section  $x=0$  ( $u_1(\infty)=1$ ,  $g_1(\infty)=g_\infty$ ,  $h_1(\infty)=1/(\gamma-1)M_\infty^2$ ). The pressure profile  $p_1(r)$  is restored by integration with the boundary condition  $p_1(\infty)=1/\gamma M_\infty^2$ . If the external pressure distribution  $p(x,\infty)=p_e(x)$  is determined, the axial velocity and enthalpy at infinity are found:

$$h(x,\infty) \equiv h_e(x) = \frac{1}{(\gamma-1)M_\infty^2} \left[ \gamma M_\infty^2 p_e \right]^{(\gamma-1)/\gamma} \quad (1.4.3)$$

$$u^2(x,\infty) \equiv u_e^2(x) = 1 + \frac{1}{(\gamma-1)M_\infty^2} \left[ 1 - (\gamma M_\infty^2 p_e)^{(\gamma-1)/\gamma} \right]$$

Then, the boundary conditions are formulated as follows:

$$u(0,r) = u_1(r), \quad g(0,r) = g_1(r), \quad h(0,r) = h_1(r);$$

$$u(x,\infty) = u_e(x), \quad g(x,\infty) = g_\infty, \quad h(x,\infty) = h_e(x); \quad (1.4.4)$$

$$g(x,0) = 0, \quad |u(x,0)| < \infty, \quad |h(x,0)| < \infty, \quad v(x,0) = 0.$$

An interesting example of the problem is the development of the potential vortex (1.3.9) caused by viscous effects. The choice  $\delta = r_*$  results in the following boundary conditions:

$$u_1(r) = 1, \quad g_1(r) = g_\infty = \frac{1}{M_\infty} \left[ \frac{2}{\gamma-1} \right]^{1/2},$$

$$h_1(r) = h_\infty(1 - \frac{1}{r^2}), \quad p_1(r) = p_\infty \left[ 1 - \frac{1}{r^2} \right]^{\gamma/(\gamma-1)}, \quad r \gg 1, \quad (1.4.5)$$

$$u_e(x)=1, \quad h_e(x)=\text{const}, \quad p_e(x)=\text{const}.$$

The problem at fixed gas model ( $\gamma, \delta, \mu$ ) contains the only parameter -  $M_\infty$ . However, this problem has a singular inner boundary - the vacuum core, and requires special treatment.

The equations (1.4.1) may be represented in the form resolved relatively  $x$  - derivatives. The procedure is similar to those used in derivation of (1.3.5), (1.3.7) results in:

$$\left[ \frac{\rho u^2}{1-M^2} f' \right]' + \left[ \left( \frac{p'}{1-M^2} \right)' + \frac{2p'}{y} - \frac{p'^2}{\gamma p(1-M^2)} \right] f = D_0, \quad (1.4.6)$$

$$\frac{1}{u} \frac{\delta u}{\delta x} = - \frac{f'}{f} - \frac{p'}{\gamma p} - \frac{(f' + f)/(1-M^2)}{\gamma p(1-M^2)} + \frac{D_3/u - D_1}{\gamma p(1-M^2)},$$

$$\frac{1}{\rho} \frac{\delta \rho}{\delta x} = - \frac{f'}{f} - f' + \frac{(f' + f)/(1-M^2)}{\gamma p} - \frac{D_3/u - D_1}{\gamma p(1-M^2)},$$

$$\frac{1}{\rho u^2} \frac{\delta p}{\delta x} = \frac{p'}{\gamma p} + \frac{(f' + f)/(1-M^2)}{\gamma p(1-M^2)} + \frac{D_1/M^2 - D_3/u}{\gamma p(1-M^2)}, \quad (1.4.7)$$

$$\frac{1}{g} \frac{\delta g}{\delta x} = - \frac{g'}{g} + \frac{D_2}{ug},$$

$$D_1 = \frac{\delta}{\delta y} \frac{\delta u}{\delta y}, \quad D_2 = \frac{1}{\rho} \left[ \frac{\delta}{2y} \frac{\delta g}{\delta y} - \frac{\delta \mu}{2} \frac{g}{\delta y} \right],$$

$$D_3 = \frac{\delta}{\delta y} \frac{\mu}{6} \frac{\delta h}{\delta y} + (\gamma-1)\mu \left[ 2y \left( \frac{\delta u}{\delta y} \right)^2 + \left( \frac{\delta g}{\delta y} - \frac{g}{y} \right)^2 \right],$$

$$D_0 = \left[ \frac{M^2 (D_3/u) - D_1}{1-M^2} \right]' - \frac{p'}{\gamma p} \left[ \frac{D_3/u - D_1}{1-M^2} \right] + \frac{\rho g D_2}{2y^2 u},$$

where  $f=(vr)/u$ ,  $y=r^2/2$  and the primes denote the  $y$ -derivatives. The boundary conditions for the first equation are:  $f(x,0)=0$ ,

$$f'(x,\infty) = (1-M_e^2) \frac{dp_e}{dx} / (\rho_e u_e^2).$$

If the profiles  $u$ ,  $g$ ,  $h$ ,  $p$  are known at some section, the coefficients of (1.4.6) are determined. The problem for (1.4.6) is inhomogeneous and coincide at  $f'(\infty)=0$ ,  $D_0=0$  with the problem (1.3.7) at  $\alpha=0$ . Therefore, if the spectrum of the problem (1.3.7) does not contain  $\alpha=0$ , the problem (1.4.6) has unique solution, the right-hand sides of (1.4.7) can be calculated and the profiles may be continued on. In opposite case, the problem has singularity or bifurcation at the section and the solution either can not be continued on at all, or may be continued in various ways.

At presence of sonic point  $M=1$ , the special correlations must be satisfied in it to avoid the singularity in the diffusion terms. In this case, the equations (1.4.6), (1.4.7) may be found unsuitable for numerical implementation, and

the original statement (1.4.1), (1.4.4) with implicit method of integration is to be used.

The equations (1.4.7) may be also used for description of the inviscid vortex development under the action of the external pressure changes. In this case, the axial scaling is determined by the scale of the external pressure  $p_e$  and all diffusion terms are to be discarded. This approach is equivalent to the solving of the nonlinear problem (1.2.7) step-by-step from the initial section.

## 2. The structure of flow at the initial region of vortex

Expressions (1.4.5) cannot be used directly as initial conditions for numerical integration of equations (1.4.1.) because of presence of the singular vacuum core at  $0 < r < 1$ . Near it's boundary relation  $\rho u/\mu$  decreases so that effects of viscous forces are significant at small distance from the initial section. Hence singular layer appears near the cylindrical surface at  $r=1$ . This layer reveals essential properties of the classical mixing layer but in our case it is more properly to name it "penetration layer".

### 2.1. Representation of the solution in the penetration layer

Let us consider the flow in the neighbourhood of the vacuum core and introduce new variable:

$$\xi = x^{(1-\gamma)/\gamma} \frac{r^2-1}{2} . \quad (2.1.1)$$

Expansions of the solutions are represented as

$$\begin{aligned}
 u &= 1 + x^{(\gamma^{-1})/\gamma} u_1(\xi) + \dots, \\
 g &= g_\infty + x^{(\gamma^{-1})/\gamma} g_1(\xi) + \dots, \\
 h &= x^{(\gamma^{-1})/\gamma} h_1(\xi) + \dots, \\
 p &= x p_1(\xi) + \dots, \\
 \rho &= x^{1/\gamma} \rho_1(\xi) + \dots, \\
 vr &= x^{-1/\gamma} v_1(\xi) + \dots, \\
 \mu &= x^{(\gamma^{-1})/\gamma} h_\infty^{-1} h_1 + \dots,
 \end{aligned}
 \tag{2.1.2.}$$

where the dots denote higher terms.

Substituting (2.1.2) in the equations (1.4.1) and performing the limit  $x \rightarrow 0$ , we obtain

$$\rho_1 \left[ \frac{\gamma-1}{\gamma} (u_1 - \xi_1 u_1') + v_1 u_1' \right] = -p_1 + \frac{\gamma-1}{\gamma} \xi p_1' + h_\infty^{-1} (h_1 u_1')',$$

$$\rho_1 \left[ \frac{\gamma-1}{\gamma} (g_1 - \xi g_1') + v_1 g_1' \right] = h_\infty^{-1} ((h_1 g_1')' - 2h_1' g_1),$$

$$\rho_1 \left[ \frac{\gamma-1}{\gamma} (h_1 - \xi h_1') + V_1 h_1' \right] = p_1 - \frac{\gamma-1}{\gamma} \xi p_1' + V_1 p_1' +$$

$$+ \frac{1}{6} h_\infty^{-1} (h_1 h_1')',$$

(2.1.3)

$$\frac{1}{\gamma} \rho_1 - \frac{\gamma-1}{\gamma} \xi \rho_1' + (\rho_1 V_1)' = 0,$$

$$p_1' = \rho_1 g_\infty^2, \quad \rho_1 h_1 = \frac{\gamma}{\gamma-1} p_1,$$

where the prime denotes derivatives on variable  $\xi$ .

System (2.1.3) is the system of ordinary differential equations with boundary conditions obtained from matching with the functions in the exterior,  $\xi \rightarrow +\infty$ , and interior,  $\xi \rightarrow -\infty$ , fields. We suppose that  $\rho_1(\xi)$  tends to zero as  $\xi \rightarrow -\infty$  more quickly than  $1/\xi$ , i.e.  $\rho_1 \xi \rightarrow 0$ ,  $\xi \rightarrow -\infty$ . Then, from the latter three equations (2.1.3) we obtain

$$\rho_1 V_1 = p_1 \left( \frac{\xi}{h_1} - \frac{1}{g_\infty^2} \right).$$

(2.1.4)

Using (2.1.4) we see that (2.1.3) may be written as

$$(h_1 h_1')' + \frac{6}{2} p_1 (h_1' - g_\infty^2) = 0,$$

$$h_1 p_1' - \frac{\gamma}{\gamma-1} g_\infty^2 p_1 = 0, \quad (2.1.5)$$

$$(h_1 u_1')' + h_1 u_1' - \frac{g_\infty^2}{2} p_1 \left( \frac{u_1}{h_1} + 1 - \frac{u_1'}{g_\infty^2} - g_\infty^2 \frac{\xi}{h_1} \right) = 0,$$

$$(h_1 g_1') + h_1' (g_1' - 2g_\infty) - \frac{g_\infty^2}{2} p_1 \left( \frac{g_1}{h_1} - \frac{1}{g_\infty^2} g_1' \right) = 0.$$

The solution of the first and second equations in (2.1.5) is found by means of confluent hypergeometric functions M, U [42]:

$$\begin{aligned} h_1 = \exp \left[ -\frac{6}{2} \frac{\gamma-1}{\gamma} \frac{1}{g_\infty^2} p_1 \right] & \left( C_1 M \left( \frac{2\gamma-1}{\gamma}, 1, \frac{6}{2} \frac{\gamma-1}{\gamma} \frac{p_1}{g_\infty^2} \right) + \right. \\ & \left. + C_2 U \left( \frac{2\gamma-1}{\gamma}, 1, \frac{6}{2} \frac{\gamma-1}{\gamma} \frac{p_1}{g_\infty^2} \right) \right), \end{aligned} \quad (2.1.6)$$

where  $C_1$  and  $C_2$  are arbitrary constants.

We consider that  $p_1 \rightarrow 0$  at  $\xi \rightarrow -\infty$ . Therefore, for small values of  $p_1$  from (2.1.6.) we obtain

$$h_1 = C_1 \left( 1 + \frac{6}{2} \frac{\gamma-1}{\gamma} \left( \frac{1}{g_\infty^2} \right)^2 p_1 + O(p_1^2) \right) -$$

$$-\frac{C_2}{\Gamma((2\gamma-1)/\gamma)} \left[ \ln\left(\frac{\delta}{2} \frac{\gamma-1}{\gamma} \frac{1}{g_\infty^2} p_1\right) + o(1) \right], \quad (2.1.7)$$

where  $\Gamma$  is the Gamma function.

If  $C_2 \neq 0$ , expression (2.1.7) contains logarithmic singularity:

$$h_1 \approx \frac{-C_2}{\Gamma((2\gamma-1)/\gamma)} \ln\left(\frac{\delta}{2} \frac{\gamma-1}{\gamma} \frac{1}{g_\infty^2} p_1\right) + \dots,$$

and hence the asymptotic behavior of the solutions of first and second equations in (2.1.5) at  $\xi \rightarrow -\infty$  is

$$p_1 \approx \frac{2}{\delta} \frac{\gamma}{\gamma-1} g_\infty^2 \exp\left[g_\infty \left(2\Gamma\left(\frac{\gamma-1}{\gamma}\right) \frac{\xi - \xi_0}{C_2}\right)^{1/2}\right], \quad (2.1.8)$$

$$h_1 \approx \frac{C_2}{\Gamma((2\gamma-1)/\gamma)} g_\infty \left(2\Gamma\left(\frac{\gamma-1}{\gamma}\right) \frac{\xi - \xi_0}{C_2}\right)^{1/2},$$

where  $\xi_0$  is the constant of integration. From (2.1.8) we find that  $h_1 \rightarrow +\infty$  at  $\xi \rightarrow -\infty$ , so that heat flux

$$\mu \frac{1}{r} \frac{\delta h}{\delta r} = \frac{1}{h} h_1 h_1' \approx 2C_2 \left(\frac{\gamma}{\gamma-1}\right) \frac{1}{\Gamma((\gamma-1)/\gamma)}$$

tends to the constant value.

The absence of the heat flux inside the vacuum core means

that in (2.1.6.) it is necessary to assume  $C_2=0$ . In this case at  $\xi \rightarrow -\infty$  the main terms in asymptotic expansions for  $h_1$ ,  $p_1$  are

$$h_1 \approx C_1 \left( 1 + \frac{6}{2} \frac{\gamma-1}{\gamma} \frac{1}{g_\infty^2} p_1 \right), \quad (2.1.9)$$

$$p_1 \approx \exp \left[ \frac{\gamma}{\gamma-1} g_\infty^2 \frac{\xi - \xi_0}{C_1} \right].$$

Let us investigate the behavior of the function  $g_1(\xi)$  at  $\xi \rightarrow -\infty$ . After considerable manipulation we obtain from (2.1.5) the equation

$$p_1 \frac{d^2 g_1}{dp_1^2} + \left( 1 + \frac{1}{2g_\infty^2} \frac{\gamma-1}{\gamma} p_1 \right) \frac{dg_1}{dp_1} - \frac{1}{2g_\infty^2} \left( \frac{\gamma-1}{\gamma} \right)^2 g_1 = - \frac{2}{g_\infty} \frac{\gamma-1}{\gamma} \frac{dh_1}{dp_1}. \quad (2.1.10)$$

The general solution of (2.1.10) is represented in the form:

$$g_1 = \sum_{k=0}^{\infty} A_k p_1^k + \ln p_1 \sum_{k=0}^{\infty} B_k p_1^k, \quad (2.1.11)$$

where  $A_k$ ,  $B_k$  are constants to be found.

If  $B_0=0$  in (2.1.11), the solution of the equation (2.1.10) tends to constant at  $p_1 \rightarrow 0$ :

$$g_1 \rightarrow - C_1 \frac{26}{g_\infty} \frac{\gamma-1}{\gamma}.$$

This asymptotic behavior of circulation does not match with boundary condition at  $r=0$ .

The second solution of (2.1.10) has a logarithmic singularity

$$g_1 \approx B_0 \ln p_1 ,$$

that, using (2.1.9), reduces to linear dependence

$$g_1 \approx B_0 g_\infty^2 \frac{\gamma}{\gamma-1} \frac{\xi}{C_1} ; \quad (2.1.12)$$

Substituting (2.1.12) into the expansion (2.1.1), (2.1.2) we find

$$\begin{aligned} g(x,r) &= g_\infty + x^{(\gamma-1)/\gamma} g_1 (x^{(1-\gamma)/\gamma})^{\frac{r^2-1}{2}} \approx \\ &\approx g_\infty + B_0 g_\infty^2 \frac{\gamma}{\gamma-1} \frac{r^2-1}{2C_1} . \end{aligned}$$

Boundary condition  $g(x,0) = 0$  determines the coefficient  $B_0$ :

$$B_0 = \frac{2C_1}{g_\infty} \frac{\gamma-1}{\gamma} .$$

Therefore, the circulation distribution in the initial section of the vacuum core is following

$$g(0,r) = g_\infty r^2 , \quad \text{at } 0 \leq r \leq 1 \quad (2.1.13)$$

Indeed, such circulation means that the vacuum core is spinning around the vortex axis like a solid body. Its angular velocity of rotation is

$$\frac{\delta w_d}{\delta r_d} = \frac{1}{M_\infty} \left( \frac{2}{\gamma-1} \right)^{1/2} \frac{u_{d\infty}}{r_d^*}$$

Function  $u_1(\xi)$  satisfies the equation that may be obtained from (2.1.5):

$$\begin{aligned} p_1 \frac{d^2 u_1}{dp_1^2} + \left( 1 + \frac{1}{2g_\infty^2} \frac{\gamma-1}{\gamma} p_1 \right) \frac{du_1}{dp_1} - \frac{1}{2g_\infty^2} \left( \frac{\gamma-1}{\gamma} \right)^2 u_1 = \\ = \frac{1}{2g_\infty^2} \left( \frac{\gamma-1}{\gamma} \right)^2 (h_1 - g_\infty^2 \xi) \quad (2.1.14) \end{aligned}$$

Left hand-side in (2.1.14) is similar to that in (2.1.10). The solution of (2.1.14) at  $p_1 \rightarrow \infty$  is expanded as a series:

$$u_1 = \sum_{k=0}^{\infty} D_k p_1^k + \ln p_1 \sum_{k=0}^{\infty} E_k p_1^k \quad (2.1.15)$$

Absence of an infinite term in (2.1.15),  $E_0 = 0$ , means that in the whole region  $0 \leq r \leq 1$  the axial velocity slightly differs from the initial value. The difference between them tends to zero as  $x \rightarrow 0$ :  $u(0,r) - u(x,r) = O(x^{(\gamma-1)/\gamma})$ . In this case the total enthalpy  $h_0(0,r)$  in the initial section of core is a parabolic function of  $r$ :

$$h_0(0,r) = 1/2 + h_\infty r^2, \quad \text{at } 0 \leq r \leq 1. \quad (2.1.16)$$

In contrast to this, if the vortex generator does not produce considerable changes of the total enthalpy, we must take into account the initial axial velocity profiles different

from constant. At constant initial total enthalpy profile condition and with circulation distribution obtained (2.1.13) the axial velocity profile is completely determined:

$$u(0,r) = (1 + 2h_{\infty}(1 - r^2))^{1/2}, \quad 0 \leq r \leq 1. \quad (2.1.17)$$

Matching (2.1.17) with (2.1.15) yields

$$E_0 = -C_1 \frac{\gamma-1}{\gamma}. \quad (2.1.18)$$

The unknown constants  $C_1$ ,  $\xi_0$  in (2.1.9), (2.1.12), (2.1.18) are determined from matching the solutions of (2.1.3) with functions in inviscid external flow region (1.4.5). For this purpose we use the expansion of hypergeometric function  $M((2\gamma-1)/\gamma, 1, 6(\gamma-1)p_1/(2\gamma g_{\infty}^2))$  at  $p_1 \rightarrow \infty$  [42]. Then, from (2.1.6) we find:

$$h_1 \approx \frac{C_1}{\Gamma((2\gamma-1)/\gamma)} \left[ -\frac{6\gamma-1}{2\gamma} \frac{1}{g_{\infty}^2} p_1 \right] \frac{(\gamma-1)/\gamma}{\gamma} \quad (2.1.19)$$

Substituting (2.1.19) into the second equation (2.1.5), we obtain

$$p_1 \approx \frac{2\gamma}{6\gamma-1} g_{\infty}^2 \left[ \frac{g^2}{C_1} \frac{2\gamma-1}{\gamma} \right] \frac{\gamma/(\gamma-1)}{(\xi-\xi_1)^{\gamma/(\gamma-1)}}, \quad (2.1.20)$$

where  $\xi_1$  is arbitrary constant.

From (1.4.5), (2.1.1), (2.1.4), (2.1.19) and (2.1.20) constants  $C_1$  and  $\xi_1$  are determined:

$$c_1 = h_\infty \Gamma \left( \frac{\gamma-1}{\gamma} \right) \left[ \frac{\gamma-1}{\gamma} \right]^{(2-\gamma)/\gamma} \gamma \left[ \frac{4}{6} \right]^{(\gamma-1)/\gamma}, \quad (2.1.21)$$

$$\xi_1 = 0.$$

As a result, at  $\xi \rightarrow \infty$  we have:

$$h_1 \approx 2h_\infty \xi, \quad p_1 \approx g_\infty^2 \frac{\gamma-1}{\gamma} \frac{1}{\xi}, \quad (2.1.22)$$

$$\rho_1 \approx 2 \frac{1}{\xi} \frac{1}{(\gamma-1)}.$$

## 2.2 Numerical study of the flow at the initial region

The finite difference method was used for integration equations in (2.1.5) to calculate vortex development at the initial region of flow. The independent variable  $\xi$  was considered in the range  $-3.5 < \xi < 3.5$ . The second order method of Keller was used to approximate derivatives. At the first stage the Caushe problem for the first and second equations in (2.1.5) was solved with initial conditions (2.1.9) stated at  $\xi = -3.5$ . The form of equations (2.1.5) does not change if an arbitrary constant is added to independent variable. Therefore, constant  $\xi_0$  in (2.1.9) may be chosen so that  $\xi_1 = 0$  in (2.1.20). On each step of the iteration procedure constant  $\xi_1$  was being found from (2.1.20) by solving the Caushe problem with given value  $\xi_0$ . Then the value of  $\xi_0$  was changed to provide the condition  $\xi_1 = 0$ . The process was finished when appropriate accuracy was reached. It is clear that such iteration procedure is necessary because of disagree-

ment between asymptotic character of expansions (2.1.9), (2.1.22) and the finite interval for independent variable.

As soon as functions  $p_1(\xi)$  and  $h_1(\xi)$  are found, the latter two equations in (2.1.5) are solved. These equations are linear with respect to  $u_1$  and  $g_1$ , and no iteration procedure is required to satisfy the boundary conditions. On the right boundary of interval conditions  $u_1 = 0$ ,  $g_1 = 0$  were considered. On the left boundary the derivative  $g'$  was given:  $g_1' = g_\infty$ . Function  $u(\xi)$  was calculated in two cases corresponding to two boundary conditions on the left boundary of the interval

$$u_1' = 0 \quad (2.2.1)$$

and

$$u_1' = -g_\infty^2. \quad (2.2.2)$$

The results of the calculations of functions  $h_1(\xi)$ ,  $p_1(\xi)$ ,  $\rho_1(\xi)$ ,  $g_1(\xi)$  at  $\delta = 0.7$ ,  $M_\infty = 3$ ,  $\gamma = 1.4$  are presented in Figures 42-45 respectively.

Solution  $u_{11}(\xi)$  satisfying the condition (2.2.1) is represented in Fig.46. The solution  $u_{12}(\xi)$  for condition (2.2.2) is shown in Fig.47.

Representations (2.1.1), (2.1.2) and functions  $h_1(\xi)$ ,  $p_1(\xi)$ ,  $g_1(\xi)$ ,  $u_1(\xi)$  obtained above determine behavior of the flow in the initial region of vortex. Thus, pressure, density and enthalpy increase monotonously inside the vortex as axial coordinate  $x$  increases.

The enthalpy on the vortex axis has non-zero value:

$$h(x,0) \approx x^{(\gamma-1)/\gamma} c_1 =$$

$$= x^{(\gamma-1)/\gamma} h_{\infty} \Gamma\left(\frac{\gamma-1}{\gamma}\right) \left(\frac{\gamma-1}{\gamma}\right)^{(2-\gamma)/\gamma} \left(\frac{4}{6}\right)^{(\gamma-1)/\gamma} \quad (2.2.3)$$

Returning to dimensional variables we obtain from (2.2.3) the following correlation of vortex parameters:

$$\frac{h_d(x_d/(R_\delta \delta), 0)}{h_{d\infty}} \left[ \frac{x_d}{\delta} \right]^{(1-\gamma)/\gamma} = \left[ \frac{4}{6R_\delta} \right]^{(\gamma-1)/\gamma} \frac{1}{(\gamma-1)M_\infty^2} \Gamma\left(\frac{\gamma-1}{\gamma}\right) \left[ \frac{\gamma-1}{\gamma} \right]^{(2-\gamma)/\gamma} \quad (2.2.4)$$

Particularly, at  $\gamma = 1.4$ ,  $\delta = 0.7$ , (2.2.4) reduces to

$$\frac{h_d(x_d/(R \delta), 0)}{h_{d\infty}} = \frac{7.56}{M_\infty^2} (x_d/R_\delta \delta)^{0.29}.$$

In the case when the initial axial velocity profile is constant condition (2.2.1) results in negative values for function  $u_{11}(\xi)$  (see Fig.46). Therefore, the flow is retarded at least for that distance from the initial section where expansion (2.1.2) is valid.

If the initial total enthalpy profile is constant, i.e. the initial velocity distribution is given by (2.1.7), the retardation of the flow is less significant and velocity on the axis stays constant in the first approximation:

$$u(x,0) = (1 + 2h_{\infty})^{1/2}.$$

From expansions (2.1.2) and calculated functions  $h_1$ ,  $p_1$ ,  $g_1$  and  $u_1$  all initial profiles required for the numerical procedure may be found.

### 3. Numerical solution of the quasi-cylindrical approximation system for compressible flow

System (1.4.1) is non-linear parabolic, just as the system of boundary layer equations. Effective numerical methods to solve such equations with given initial and boundary conditions are known. All programming and computing was performed using VAX-780 computer.

#### 3.1. Problem statement. Numerical method

The system (1.4.1) was solved numerically using variables  $x$ ,  $y = r^2/2$  inside the region  $x > 0$ ,  $0 < r \leq r_{\max}$ . The upper boundary condition was stated at point  $r_{\max} = 10$ . To avoid the errors caused by finite region of calculation the following asymptotic expansions were used:

$$\begin{aligned} h(0, r_{\max}) &= h_e \left(1 - \frac{1}{r_{\max}^2}\right), \\ p(0, r_{\max}) &= p_e \left(1 - \frac{1}{r_{\max}^2}\right)^{\gamma/(\gamma-1)}, \\ u(0, r_{\max}) &= u_e, \quad g(0, r_{\max}) = g_{\infty}. \end{aligned} \tag{3.1.1}$$

The solution must be bounded on the axis and it results in conditions [43]:

$$\mu r \frac{\delta u}{\delta r} \rightarrow 0, \quad \mu r \frac{\delta h}{\delta r} \rightarrow 0, \quad r \rightarrow 0. \quad (3.1.2)$$

From the equations (1.4.1) with conditions (3.1.2) the following correlation of functions  $u$  and  $h$  on the axis is found:

$$\left. \frac{d}{dx} [p h^{-\gamma/(\gamma-1)}] + \frac{2}{6u} h^{-\gamma/(\gamma-1)} \mu \frac{1}{r} \frac{\delta h}{\delta r} \right|_{r=0} = 0, \quad (3.1.3)$$

$$\left. \rho \frac{d}{dx} \left[ \frac{u^2}{2} + h \right] - 2\mu \left[ \frac{1}{6r} \frac{\delta h}{\delta r} + \frac{1}{r} \frac{\delta u}{\delta r} \right] \right|_{r=0} = 0.$$

In addition to the conditions (3.1.1), (3.1.3) the conditions for  $v$  and  $y$  on the axis

$$v(x,0) = g(x,0) = 0 \quad (3.1.4)$$

are satisfied.

Initial profiles  $u(0,r)$ ,  $h(0,r)$ ,  $p(0,r)$ ,  $g(0,r)$  must be specified for correct problem statement. We consider two types of initial profiles  $u(0,r)$  corresponding to different conditions of vortex generation

$$u(0,r) = 1, \quad 0 \leq r < \infty \quad (3.1.5)$$

and

$$u(0,r) = 1, \quad r \geq 1,$$

$$u(0,r) = [1 + 2h_{\infty}(1-r^2)]^{1/2}, \quad 0 \leq r < 1. \quad (3.1.6)$$

Initial profiles of  $h$ ,  $p$ ,  $g$  are the same in both cases considered:

$$p(0,r) = h(0,r) = 0,$$

$$g(0,r) = g_{\infty} r^2$$

$$\text{at } 0 \leq r < 1,$$

(3.1.7)

$$p(0,r) = p_{\infty} \left(1 - \frac{1}{r^2}\right)^{\gamma/(\gamma-1)},$$

$$h(0,r) = h_{\infty} \left(1 - \frac{1}{r^2}\right),$$

$$g(0,r) = g_{\infty}$$

at  $r \geq 1$ .

The absolutely stable finite-difference method with second-order approximation of the radial derivatives and variable grid size in radial direction was used for numerical solution of equations (1.4.1). A second order implicit scheme was used for approximation in axial direction.

### 3.2 Numerical results

The initial profiles were found using asymptotic expansions (2.1.1), (2.1.2). The profiles of functions  $\bar{h}(x_1, r) = h(x_1, r)/h_\infty$ ,  $\bar{g}(x_1, r) = g(x_1, r)/g_\infty$ ,  $\bar{p}(x_1, r) = p(x_1, r)/p_\infty$ ,  $\bar{\rho}(x_1, r)$  are demonstrated in figures 48-51 respectively at  $\delta = 0.7$ ,  $\gamma = 1.4$ ,  $M_\infty = 3$ ,  $x_1 = 4.4 \cdot 10^{-4}$ . The profile of total enthalpy scaled by the value  $(1/2 + h_\infty)$ :  $\bar{h}_0(x_1, r) = h_0(x_1, r)/(1/2 + h_\infty)$  is shown in figure 52 at the same values of  $\delta$ ,  $\gamma$ ,  $M_\infty$ ,  $x_1$ . This profile corresponds to the case of constant initial axial velocity. The distribution of axial velocity in the case of constant initial total enthalpy is demonstrated in figure 53.

The subsequent development of the profiles downstream from the initial section was calculated at  $M_\infty = 3$ ,  $\gamma = 1.4$ ,  $\delta = 0.7$  and constant external pressure  $p_e = p_\infty$ . The viscosity  $\mu$  was considered as a linear function of the temperature.

The numerical results obtained are shown in figures 54-64. Each curve in figures 54-64 has the number which indicates the correspondent axial position. The correspondence between the numbers and axial positions is shown in the Table below. For comparison with experimental data the Table contains also the ratio  $x_d/\delta$  of the axial position to the vortex radius at Reynolds number  $R_\delta = 2 \cdot 10^5$ .

Table

N	1	2	3	4	5
x	$2.5 \cdot 10^{-2}$	$5.5 \cdot 10^{-2}$	$9.5 \cdot 10^{-2}$	0.18	0.29
$x_d/\delta$	$5.2 \cdot 10^3$	$1.1 \cdot 10^4$	$2.0 \cdot 10^4$	$3.5 \cdot 10^4$	$6.0 \cdot 10^4$

N	6	7	8
x	0.43	0.73	1.1
$x_d/\delta$	$8.9 \cdot 10^4$	$1.5 \cdot 10^5$	$2.4 \cdot 10^5$

The profiles  $\bar{h}$ ,  $\bar{p}$ ,  $\rho$ ,  $\bar{g}$ ,  $u$ ,  $\bar{h}_0$  at various axial positions are demonstrated in figures 54-59. The profile of the total pressure  $p_s$  calculated taking into account the local Mach number is shown in figure 60. All these functions are scaled by their values in the external flow at  $r \rightarrow \infty$ . Radial and azimuthal components of velocity ( $v, w$ ) and local Mach number  $M$  are represented in figures 61-63. Swirl angle  $\varphi = \arctg(w/u)$  between velocity vector and the axis of the vortex is shown in figure 64 ( $\varphi$  is measured in degrees).

The numerical results represented in figures 54-64 were obtained at initial conditions correspondent to constant axial velocity at the initial section. The results demonstrate that the axial velocity inside the vortex is reduced near the initial section. This tendency is obvious in figure 65 (curve 1), where the axial velocity on the axis is shown. The retardation of the axial flow is caused by increase of

pressure downstream from the initial section. The reason of this pressure increase is diffusion of gas having small azimuthal velocity towards the vortex core resulted in reducing of the radial pressure overfall. The distribution of the total pressure on the axis is represented in figure 67.

Numerical calculations were performed also for the case of constant total enthalpy in the initial section. It was found that the distributions of  $h$ ,  $p$ ,  $g$  are quite close to those obtained at constant axial velocity in the initial section. Significant difference is observed only for axial velocity and total enthalpy on the relatively small distance downstream of the initial position. The distributions of axial velocity  $u(x,0)$ , scaled total enthalpy  $\bar{h}_0(x,0)$  and total pressure  $\bar{p}_s(x,0)$ , Mach number  $M(x,0)$  along the vortex axis are shown in figures 65-68. The curves 1 correspond to the case of constant axial velocity in the initial section and curves 2 - to the case of constant total enthalpy. It could be seen that distributions of the total pressure in both cases almost coincide. The retardation of the flow inside the vortex found in the first case was observed in the second case too. However, the difference between the flows caused by different initial conditions decreases quickly downstream from the initial section. It is interesting that in the second case the total enthalpy quickly drops almost to the values found in the first case. Moreover, positions of minimal axial velocity and total enthalpy on the axis are rather close in both cases.

It may be concluded that development of the vortex downstream from the initial position is caused by two diffusion processes. The first process is spreading of the gas towards the vortex core. This process determines the profiles at relatively small distance from the initial section. The second process is regrouping of the profiles under action of viscosity. This process is relatively slow and determines profiles

at large distance from the initial section. Two functions which characterize radial size of the vortex were considered. The size  $\delta_u$  was determined as the radial position where axial velocity  $u=0.99$ . The second size  $\delta_\phi$  was determined as the radial position where the swirl angle  $\phi$  is maximal (figure 64).

Distributions of these values along the vortex is demonstrated in figure 69. It could be concluded that the vortex develops smoothly and its radial size monotonously increases.

#### 4. Solutions describing the flow far downstream from initial section

The asymptotic expansion for dissipating incompressible trailing vortex far from aircraft was obtained in Batchelor's work [29]. It was shown by Batchelor that an arbitrary constant appears in his asymptotic expansion. We extended the expansions and found terms which contain two arbitrary constants else.

##### 4.1. Generalization of the Batchelor's expansion

Let us introduce a new independent variable:

$$\eta = r^2 / (4x) . \quad (4.1.1)$$

The asymptotic expansions of the solution are:

$$u = 1 + \frac{\ln x}{x} u_1(\eta) + \frac{1}{x} u_2(\eta) + \dots ,$$

$$g/g_{\infty} = 1 - \exp(-\eta) + \frac{\ln x}{x} g_1(\eta) + \frac{1}{x} g_2(\eta) + \dots,$$

$$h/h_{\infty} = 1 + \frac{\ln x}{x} h_1(\eta) + \frac{1}{x} h_2(\eta) + \dots,$$

$$p/p_{\infty} = 1 + \frac{\ln x}{x} p_1(\eta) + \frac{1}{x} p_2(\eta) + \dots, \quad (4.1.2)$$

$$\rho = 1 + \frac{\ln x}{x} \rho_1(\eta) + \frac{1}{x} \rho_2(\eta) + \dots,$$

$$v \cdot r = \frac{\ln x}{x} v_1(\eta) + \frac{1}{x} v_2(\eta) + \dots,$$

$$\mu = 1 + \frac{d\mu}{dh} \bigg|_{h=h_{\infty}} \cdot \left( \frac{\ln x}{x} h_1 + \frac{1}{x} h_2 + \dots \right),$$

where the dots denote terms which have the form  $O(x^k (\ln x)^l)$ , for all  $k, l$ .

After substitution (4.1.1), (4.1.2) into equations (1.4.1) in the first approximation as a result of matching we find:

$$u_1 = - \frac{1}{8} g_{\infty}^2 \exp(-\eta),$$

$$g_1 = -\frac{1}{8} \eta \exp(-\eta) [g_\infty^2 \delta \mu'_\infty (G_{12}(0) - G_{11}(\eta)) + g_\infty^2 / 2 + 4\delta / (1-\delta)],$$

$$h_1 = -\frac{1}{4} \delta \exp(-\delta \eta), \quad (4.1.3)$$

$$p_1 = 0, \quad \rho_1 = -\frac{1}{4} \delta \exp(-\delta \eta),$$

$$v_1 = -\frac{1}{2} \eta [\delta \exp(-\delta \eta) + \frac{1}{2} g_\infty^2 \exp(-\eta)],$$

where

$$\mu'_\infty \equiv \left. \frac{d\mu}{dh} \right|_{h=h_\infty}$$

and

$$G_{11}(\eta) = \int_0^\eta \exp(-\delta \eta) [\exp(\eta) - \eta - 1] \frac{d\eta}{\eta^2},$$

$$G_{12}(\eta) = \int_\eta^\infty \eta G_{11}(\eta) \exp(-\eta) d\eta.$$

Arbitrary constants  $C_u$ ,  $C_g$ ,  $C_h$  appear in the second terms:

$$u_2 = - \frac{1}{8} g_{\infty}^2 \exp(-6\eta) [U(\eta) + C_u] ,$$

$$g_2 = - \frac{1}{8} \eta \exp(-\eta) [\delta \mu'_{\infty} (g_{\infty}^2 G_{21}(\eta) + 4C_h G_{11}(\eta)) + (g_{\infty}^2/2 + 46/(1 + \delta)) G_{22}(\eta) + C_g] , \quad (4.1.4)$$

$$h_2 = - \frac{1}{2} \delta \exp(-6\eta) [H(\eta) + C_h] ,$$

$$p_2 = - \frac{1}{4} \frac{\gamma}{\gamma-1} P(\eta) ,$$

$$\rho_2 = - \frac{1}{4} \frac{\gamma}{\gamma-1} P(\eta) - \frac{1}{2} \delta \exp(-6\eta) [H(\eta) + 2C_h/g_{\infty}^2] ,$$

$$V_2 = - \frac{1}{4} g_{\infty}^2 [1 - \exp(-\eta)] + \frac{1}{2} [1 - \exp(-6\eta)] +$$

$$+ \frac{1}{4} g_{\infty}^2 \eta \exp(-\eta) [U(\eta) + C_u] -$$

$$- \delta \eta \exp(-6\eta) [H(\eta) + 2C_h/g_{\infty}^2] - \frac{1}{2} \frac{\gamma}{\gamma-1} \eta P(\eta) ,$$

where

$$P(\eta) = \int_{\eta}^{\infty} [1 - \exp(-\eta)]^2 \frac{d\eta}{\eta^2},$$

$$U(\eta) = \int_0^{\eta} (\eta P(\eta) - 1 + \exp(-\eta)) \exp(\eta) \frac{d\eta}{\eta},$$

$$H(\eta) = - \frac{1}{2} \int_0^{\eta} [\exp(-2\eta) - \exp(-6\eta) - \eta P(\eta) +$$

$$+ 2(1 - \exp(-\eta))^2 / \eta] \exp(6\eta) \frac{d\eta}{\eta},$$

$$G_{21}(\eta) = \int_0^{\eta} [2H(\eta)(\exp(\eta) - 1 - \eta)\exp(-6\eta) +$$

$$+ G_{12}(0)(1 + \eta) - G_{12}(\eta)\exp(\eta)] \frac{d\eta}{\eta^2},$$

$$G_{22}(\eta) = \int_0^{\eta} [\exp(-\eta) + \eta - 1] \frac{d\eta}{\eta^2}.$$

Using the exponential integral  $Ei(\eta)$  [42] we may produce some calculations:

$$P(0) = 2\ln 2,$$

$$G_{12}(0) = 6/(1+6) + (1-6)\ln((1+6)/6),$$

in order to obtain correlations

$$h(x,0) \approx h_{\infty} \left( 1 + \frac{6 \ln x}{4x} + \frac{6}{2x} C_h \right),$$

$$u(x,0) \approx 1 - \frac{g_{\infty}^2}{8x} (\ln x - C_u), \quad (4.1.5)$$

$$p(x,0) \approx p_{\infty} \left( 1 - \frac{\gamma \ln 2}{\gamma - 1} \frac{1}{2x} \right),$$

$$\begin{aligned} \left. \frac{1}{r} \frac{\delta g(x,r)}{\delta r} \right|_{r=0} &\approx \frac{g_{\infty}}{2x} \left[ 1 - \frac{\ln x}{8x} (\mu_0^2 g_{\infty}^2 \left( \frac{6}{1+\delta} + \right. \right. \\ &\quad \left. \left. + (1-\delta) \ln \frac{1+\delta}{6} + \frac{g_{\infty}^2}{26} + \frac{4}{1-\delta} \right) + \frac{1}{8x} C_g \right]. \end{aligned}$$

#### 4.2 Comparison of the numerical results with asymptotic solutions

To perform comparison with asymptotic solutions it is necessary to determine constants  $C_u$ ,  $C_h$ ,  $C_g$ . Correlations (4.1.5) at large enough values of  $x$  were used for this purpose so as numerical and asymptotic solutions of  $u(x,0)$ ,  $h(x,0)$  and  $\delta g(x,0)/(r\delta r)$  were coincide at  $x=10$ .

Results are demonstrated in figures 70-78. The profiles of function  $\bar{h}=h/h_{\infty}$ ,  $u$ ,  $\bar{g}=g/g_{\infty}$ ,  $\bar{p}=p/p_{\infty}$ , are shown in figures 70-73 at various axial positions. Solid curves correspond to

numerical profiles, dashed curves correspond to the first approximation (4.1.3) and dashed curves with symbols correspond to expansions including both first (4.1.3) and second (4.1.4) terms.

We remind that the first approximation does not depend on constants  $C_u$ ,  $C_h$ ,  $C_g$ .

Distributions of axial velocity  $u(x,0)$ , scaled enthalpy  $\bar{h}(x,0)$  and pressure  $\bar{p}(x,0)$  along the vortex axis are represented in figures 74-76 respectively.

The distributions of total enthalpy  $\bar{h}_0(x,0)$  and Mach number  $M(x,0)$  along the vortex axis are shown in figures 77-78, where the total enthalpy scaled by value in the external flow. Numerical and asymptotic solutions are shown by solid and dashed lines correspondently.

A good agreement between numerical and asymptotic results is observed at large values of  $x$ .

## 5. Comparison of the numerical results with experimental data

The comparison was performed using profiles of the total pressure and stagnation temperature measured experimentally in two radial section of the vortex. At the first step numerical and experimental profiles were correlated in the downstream section. The ratio of the total pressure on the axis ( $Y=113\text{mm}$ ) to the total pressure on the conventional boundary  $P_{se}$  ( $Y=83\text{mm}$ ) was found from the Table 2, and then the numerical data from figure 67 were used to determine position  $x$  where this ratio is close to its numerical prediction. The radius of the vortex was approximately determined using photographs taken in experiment. Thorough adjustment of parame-

ters was performed visually on the display of computer to reach good correspondence between numerical and experimental profiles. Two parameters were adjusted: reference total pressure and initial radius of the vortex vacuum core  $\delta$ . Final result was found taken into account possible deflection of the probe from real position of the vortex axis. The result is represented in figure 79. The total pressure obtained numerically and referenced to its value in external flow is shown by solid line and experimental data - by crosses. The following values of parameters were found: initial radius of the vacuum core  $\delta=5.5\text{mm}$ , the ratio of the total pressure on the vortex boundary to the total pressure in external flow  $p_{se}/p_0=0.273$ , position of the vortex axis  $Y=114\text{mm}$ , and position of the section considered  $x=1.1$ .

Additional information about the flow in this section may be obtained from figures 54-64 (curve 8). In particular, the dependence of the swirl angle  $\varphi$  shown in figure 64 indicates that maximum of the angle is observed at radial position  $r\approx 3$  from the axis. Analysis of the experimental data (Table 2) results in rather close value of  $\varphi$  and radius ( $r_d\approx 16\text{mm}$ ) where the measured total pressure is maximal.

The parameters found were used also for comparison of the numerical and experimental profiles of the stagnation temperature. Both profiles shown by solid line and crosses correspondently are represented in figure 80. The stagnation temperature decreases toward the axis and qualitative agreement between numerical and experimental results is observed.

Significant discrepancy is probably caused by relatively large size of the probe, resulting in space averaging of the experimental data. Furthermore, both profiles are rather close to unity and relative discrepancy is small.

Using values of the parameters found, the Reynolds number  $Re_\delta$

$\approx 2 \cdot 10^5$  and dimensionless coordinate  $x$ . Correspondent to the first section where the profiles were measured are determined. However, the dimensionless distance  $\Delta x$  between the first and second sections turned out so small that the total pressure practically does not change ( $\Delta x = 4 \cdot 10^{-6}$ ). On the other hand, the experimental data reveal rather appreciable change of the total pressure between two sections (Table 1,2). Therefore, strong disagreement between the theoretical model and experimental data is observed. The experimental data indicate that radial diffusion is really more intensive than those caused by molecular viscosity.

Two reasons may be considered to explain this disagreement:

a: Rather high level of acoustical and vortical fluctuations is observed in the work-section of the wind-tunnel. The disturbances will obviously increase the diffusion of the averaged flow. These fluctuations may be taken into account by additional "eddy viscosity" using some kind of turbulence model. The level of the eddy viscosity will be evaluated below.

b: Additional diffusion may be caused by spiral tangential discontinuities in the vortex which were not taken into account within axisymmetrical model considered. However, radial distance between the discontinuities in this case must be very small ( $\Delta r < 0.1 \text{ mm}$ ). Experimental measurements result in spatial averaging of the profiles on much bigger distance. We think, the discontinuities can not completely explain high diffusion, because the averaged profiles again will regroup slowly.

Diffusion coefficient was estimated by comparison of numerical and experimental profiles of the total pressure in two sections. Numerical and experimental values of the total pressure on the axis coincide if the first section is situa-

ted at  $x=0.115$ .

Numerical and experimental profiles of the total pressure in the first section are shown in figure 81. The parameters  $\delta$ ,  $p_{se}/p_0$  were not adjusted and were taken the same as in figure 79. Therefore, only value  $x$  was specially chosen and this is equivalent to choice of the diffusion coefficient. The agreement is not so good as in the second section. Indeed, the first section is situated very close to the wing and the flow can not be considered as quasicylindrical. The profiles of the stagnation temperature at  $X=0.115$  are shown in figure 82.

Taking into account that  $\Delta x = 1.1 - 0.115 \approx 1$ , effective Reynolds number may be evaluated:  $Re^{eff} \approx 110\text{mm}/5.5\text{mm} = 20$ . Correspondent diffusion coefficient  $\mu_T$  turned out very high in comparison with molecular viscosity:  $\mu_T \sim 10^4 \mu$ .

## Conclusions

In the course of the research the devices and models necessary for vortex investigation and its interaction with different bodies were developed. The vortex investigation and its interaction with a spherical blunt body at Mach number 3 and Reynolds numbers from 1.1 to  $3.7 \cdot 10^7$  1/m was carried out. The experimental investigation has shown the following:

1. From the two types of the investigated vortex generators (rectangular wing-type and 4-vanes-type generators) the first type of the generator was chosen for the experiment. The rectangular wing produces one vortex in the investigated part of the flow. The vane-type generator produces four pairs of vortices (one vortex at the internal and external ends of each vane). The internal vortices situated close to each other flow together into one vortex while the four external vortices stay apart even at a large distance from the generator.
2. Variation of the vortex diameter with the increase of the distance from the generator is described by a common function  $d/d_r = f(x/d_r)$  (where  $d_r$  is the reference vortex diameter) regardless to the value  $d_r$  and degree of the flow swirl (the generator angle of attack  $\alpha$ ) in the range  $\alpha \leq 20^\circ$ . The vortex diameter increases linearly along the x-axis. At  $\alpha \leq 20^\circ$  the vortex expansion angle is about  $1^\circ$ . At  $\alpha = 30^\circ$  this angle increases up to  $3^\circ$ .
3. The expanding vortex induces in a supersonic flow a weak compression wave as well as an expanding viscous wake past the wing (vortex generator).
4. The measurements carried out at  $\alpha = 20^\circ$  have shown that

in the initial cross section of the vortex in the vicinity of the vortex axis a region of the low stagnation pressure  $p_s$  is formed. The minimum value  $p_s/p_0$  is approximately 0.06 of the free stream value. At a distance about  $40d_r$  from the initial section the value  $p_s/p_0$  at the vortex axis increases up to 0.35. The laser knife pictures also show the fast increase of density in the vortex core.

5. The stagnation temperature in the vortex also changes. In the initial vortex cross section the stagnation temperature at the vortex axis is lower approximately by 20 degrees than in the free stream. However, the relative value of the stagnation temperature  $T_s/T_0$  at the vortex axis in the initial section is about 0.90. A still weaker influence of the flow swirl on the relative stagnation temperature is observed in the remote section. Such a decrease of the relative stagnation temperature cannot produce a great influence on heat transfer.

6. By interaction of the vortex with the spherical blunt body a vortex breakdown occurs. The vortex breakdown is followed by its expansion, formation of a dead zone in front of the blunt body and flow turbulation. This flow is similar to the flow in front of a spiked body.

7. The vortex which is coaxial with the spherical blunt body causes a heat flux decrease in the vicinity of the symmetry axis. At the end of the dead zone in the vicinity of the attachment line the heat flux increases almost doubles as compared with the heat flux in the stagnation point of the sphere in the absence of the vortex. This effect should be taken into account in analysis of heating bodies interacting with the vortex.

8. Taking into account the drastic influence of the vortex on the heat transfer it is reasonable to investigate the in-

teraction of the vortex with a cylinder and a plate at different angles between the vortex axis and the streamlined body surface.

9. The theoretical model describing viscous diffusion of the axisymmetric trailing vortex in compressible flow was suggested and developed. The main problem of the model concerns correlation of the profiles in the initial section. The profiles of axial velocity, temperature and circulation were chosen on the basis of the classical model of the vortex in compressible gas: the flow was considered as isoenergetic and isoentropic with constant circulation. At these conditions the vortex contains vacuum core in the initial section. The experimental results demonstrate that the vortices in supersonic flow really contain strongly decompressed cores.

10. Under action of viscous diffusion the vacuum core is filled by gas downstream of the initial section. This process was thoroughly analyzed and self-similar solutions near the boundary of the vacuum core were obtained. Two types of solutions were found: the solution with constant axial velocity and another one with constant total enthalpy in the initial section. Numerical calculations demonstrated strong influence of the layer on the flow inside the vortex.

11. The asymptotic expansions of the solutions far downstream from the initial section were also found. These solutions are a generalization for compressible gas of well known solution obtained by Batchelor (1964) for the vortex in incompressible fluid. The asymptotic and numerical results were compared and good agreement between them was demonstrated.

12. Systematic numerical calculations of the vortices regrouping under action of viscosity in supersonic flow were performed on the basis of the suggested theoretical model. Qua-

litative agreement of the numerical and experimental results was demonstrated for profiles of the total pressure and stagnation temperature.

13. Strong change of the total pressure between initial and downstream section observed in the experiment cannot be explained as action of molecular viscous forces. Experimental data indicate very high level of diffusion in radial direction.

14. Two factors might strongly increase the diffusion of the averaged profiles:

- a) High level of acoustical and vortical fluctuations in the wind tunnel produces additional "eddy viscosity".
- b) Additional diffusion may be produced by spiral tangential discontinuity in the vortex which was not taken into account within axisymmetrical model considered.

15. Taking into account the discrepancy between theoretical and experimental results it is worthfull to perform additional experimental study of the vortex structure and include measurements of fluctuations. This study will allow to evaluate turbulent diffusion and develop further the theoretical model of the vortex in supersonic flow.

### References

1. Delery J., Horowitz E., Leuchter Q. and Solignac J-L., Etudes Fondamentales sur les ecoulements tourbillonnaires (in French), La Recherche Aerospatiale, No.2, 1984, pp.81-104.
2. Zatoloka V.V., Ivanyushkin A.K. and Nikolaev A.V., Vortex Interference with Inlet Shock Waves. Vortex Breakdown (in Russian), Uchenye Zapiski TsAGI, Vol.6, No.2, 1975, pp. 134-138.
3. Kucheman D., Weber J., Vortex Motions, ZAMM 45, 457, 1965.
4. Mangler K.W., Weber J., The Flow Field Near the Centre of a Rolled-up Vortex Sheet, JEM 30, 177, 1967.
5. Earnshaw P.B., An Experimental Investigation of the Structure of a Leading Edge Vortex, RAE TN Aero 2740, 1961. ARC R & M 3281.
6. Earnshaw P.B., Measurements of Vortex-Breakdown Position at Low Speed on a Series of Sharp-Edged Symmetrical Models, RAE TR 64047, 1964. ARC CP 828.
7. Hall M.G., A Numerical Method for Solving the Equations for a Vortex Core, RAE TR 65106, 1965. ARC R & M 3467.
8. Stewartson K. and Hall M.G., The Inner Viscous Solution for the Core of a Leading-Edge Vortex, JFM 15, 306, 1963.
9. Kucheman D., The Aerodynamic Design of Aircraft, Pergamon Press, Oxford-New York-Toronto-Sydney-Paris-Frankfurt.
10. Peckham D.H. and Atkinson S.A., Preliminary Results of Low Speed Wind Tunnel Test on a Gothic Wing of Aspect Ratio 1.0, RAE TN Aero 2504, 1957, ARC CP 508.
11. Corpening G. and Anderson J., Numerical Solution to Three-Dimensional Shock Wave/Vortex Interaction at Hypersonic Speeds, AIAA Paper 89-0674, Reno, Nevada, 1989.
12. Glotov G.F., Vortex Cord Shock Wave Interference in Free Stream and Nonisobar Jets (in Russian), Uchenye Zapiski TsAGI, Vol.20, No.5, 1989, pp.21-32.
13. Gupta A.K., Lilley D.G. and Syred N., Swirl Flows, Abacus Press, 1984.

14. Borovoy V.Ya., Gas Flow and Heat Transfer in Zones of Shock Wave-Boundary Layer Interference (in Russian), Mashinostroyeniye, Moscow, 1983.
15. Borovoy V.Ya., Brazhko V.N., Maikapar G.I., Skuratov A.S. and Struminskaya I.V., Heat Trasfer Peculiarities in Supersonic Flows, Journal of Aircraft, Vol.29, No.6, 1992, pp. 969-977.
16. Metwally O. and Settles G., An Experimental Study of Shock Wave/Vortex Interaction, AIAA Paper, 89-0082, Reno, Nevada, 1989.
17. Borovoy V.Ya. and Kharchenko V.N., Experimental investigation of Flow over Rectangular Wing in Supersonic Gas Flow (in Russian), Uchenye Zapiski TsAGI, Vol.6, No.5, 1975, pp.71-80.
18. Borovoy V.Ya. and Kolochinsky Yu.Yu., Surface Thermocouples as an Investigation Means of Heat Transfer on Models Tested in Intermittent Wind Tunnels (in Russian), Trudy TsAGI, Issue 2340, 1987, pp.148-155.
19. Beck J.V., Blackwell B. and Clair C.R., Inverse Heat Conduction- Post Problems, A Wiley-Interscience Publication, New-York, Chrichester, Brisbane, Toronto, Singoporo, 1985.
20. Bor de C.A., Practical Guide to Spline, Springer Verlag, 1978, New York-Heidelberg-Berlin.
21. Brazhko V.N., Method of Visualization of Streamlines on Models Surface in Wind Tunnels (in Russian), Trudy TsAGI, Issue 1749, 1976, pp.241-256.
22. Petunin A.N., Methods and Technique for Gas Flow Parameters Measuring (in Russian), Mashinostroyeniye, Moscow, 1972.
23. Brunn H.H., J. Mech. Eng. Sci., 11, 1969, p.567.
24. Kalkhoran I.M., Vortex Distortion During Vortex-Surface Interaction in a Mach 3 Stream, AIAA J., Vol.32, No.1, 1994, pp.123-129.
25. Chang P.K., Separation of Flow, Pergamon Press, 1970, Oxford-London-Edinburgh-New York-Toronto-Sydney-Paris- Braunschweig.

26. Fay J.A. and Riddell F.R. Theory of Stagnation Point Heat Transfer in Dissociated Air., J. of Aeronautical Sciences, Vol.25, No.2, 1958.
27. Lyubimov A.N. and Rusanov V.V., Gas Flow over Blunt Bodies (in Russian), Nauka, Moscow, Vol.2, 1970.
28. Golovachyev Yu.P. and Timofeyev E.P., Determination of Pressure and Heat Flux on the Frontal Surface of Smooth Blunt Bodies, Uchenye Zapiski TsAGI, Vol.19, No.6, 1988, pp.106-109.
29. Batchelor G.K., Axial Flow in Trailing Line Vortices, J.Fluid Mech., 20, 1964, pp.645-658.
30. Benjamin T.B., Theory of the Vortex Breakdown Phenomenon, J.Fluid Mech., 14, 1962, pp.593-629.
31. Gartshore I.S., Some Numerical Solutions for the Viscous Core of an Irrotational Vortex, NRC Can. Aero. Rep., LR-378, 1963.
32. Hall M.G., A New Approach to Vortex Breakdown, Proc. 1967 Heat Transfer Fluid Mech. Inst. Stanford Univ. Press, pp.319-340.
33. Hall M.G., Vortex Breakdown, Annual Review of Fluid Mech., 4, 1972, pp.195-218.
34. Leibovich S., Weakly Nonlinear Waves in Rotating Fluids, J.Fluid Mech., 42, 1970, pp.803-822.
35. Leibovich S., The Structure of Vortex Breakdown, Annual Review of Fluid Mech., 10, 1978, pp.221-246.
36. Leibovich S., Vortex Stability and Breakdown: Survey and Extension, AIAA J., Vol.22, No.9, 1984, pp.1192-1206.
37. Mager A., Dissipation and Breakdown of a Wing-Tip Vortex, J.Fluid Mech., 55, 1972, pp.609-628.
38. Trigub V.N., The Problem of the Vortex Breakdown., Prikladnaja Matem. i Mech., No.2, 1985, pp.220-226.
39. Trigub V.N., The Problem of the Vortex Breakdown in Inviscid Fluid, Uchenye Zap. TsAGI, No.3, 1985, pp.100-104.

40. Trigub V.N., An Analysis of the Flow Near the Stagnation Point in an Axisymmetrical Wake, Izv.Akad.Nauk SSSR, Mech. Zhid. i Gaza, No.2, 1986, pp.53-59.
41. Trigub V.N., Asymptotic Theory of the Origination of Recirculation Zones in an Axisymmetrical Wake, Izv. Akad. Nauk SSSR, Mech. Zhid. i Gaza, No.5, 1987, pp.54-60.
42. Handbook of Mathematical Functions, Edited by M.Abramowitz and I.Stegun, National Bureau of Standards, 1964.
43. Tikhonov A.N. and Samarsky A.A., Equations of the Mathematical Physics (in Russian), Nauka, Moscow, 1972.

## Appendix

Tables of the measurements results

Table 1

Run N37

Generator N1,  $\alpha = 20^\circ$ ,  $P_s/P_o = f(\Phi, Y)$  $X = 2\text{ mm}$ 

$\Phi$ , degr.	Y, mm						
	0	20	40	60	72	76	80
-45	0.232	0.226	0.228	0.237	0.314	0.305	0.285
-30	0.263	0.26	0.261	0.272	0.355	0.338	0.318
-15	0.271	* 0.268	* 0.27	0.28	0.37	0.352	0.325
0	* 0.272	0.267	0.269	* 0.281	* 0.372	* 0.355	* 0.328
15	0.271	0.266	0.268	0.28	0.369	0.35	0.323
30	0.253	0.241	0.245	0.255	0.339	0.32	0.291
45	0.191	0.18	0.177	0.187	0.248	0.229	0.202
	90	95	96	97	98	99	100
-45	0.163	0.087	0.06	* 0.034	0.02	0.016	0.015
-30	0.173	0.088	* 0.06	0.032	0.02	0.02	0.017
-15	* 0.179	* 0.088	0.057	0.029	0.02	0.019	0.017
0	0.177	0.085	0.052	0.028	* 0.021	* 0.019	* 0.017
15	0.174	0.077	0.045	0.022	0.021	0.018	0.016
30	0.147	0.057	0.03	0.019	0.02	0.017	0.015
45	0.093	0.034	0.019	0.014	0.016	0.015	0.013
	102	103	104	105	106	107	
-45	0.01	0.01	0.012	0.017	0.024	0.031	
-30	0.013	0.013	0.017	0.027	0.042	0.054	
-15	0.016	0.019	0.03	0.051	0.075	0.091	
0	0.019	0.026	0.045	0.072	0.095	0.118	
15	0.019	0.029	0.05	0.075	0.102	* 0.124	
30	0.021	0.032	* 0.054	0.079	0.099	0.122	
45	* 0.022	* 0.033	0.053	* 0.081	* 0.107	0.123	
	110	117	120				
-45	0.039	0.03	0.031				
-30	0.068	0.051	0.055				
-15	0.109	0.079	0.082				
0	0.137	0.091	0.091				
15	* 0.142	* 0.093	* 0.093				
30	0.138	0.093	0.092				
45	0.138	0.091	0.093				

Table 2

Run N36

Generator N1,  $\alpha = 20^\circ$ ,  $P_s/P_o = f(\Phi, Y)$  $X = 110\text{mm}$ 

Phi, degr.	Y, mm							
	0	15	19	23	27	31	35	
-45	0.237	0.225						
-30	0.27	0.26						
-15	* 0.277	* 0.266						
0	0.273	0.266	0.267	0.283	0.328	0.324	0.321	
15	0.272	0.265						
30	0.256	0.244						
45	0.194	0.175						
	39	43	45	47	48	49	51	
0	0.313	0.299	0.293	0.289	0.283	0.276	0.274	
	52	58	61	68	73	78	83	88
0	0.271	0.253	0.245	0.234	0.234	0.24	0.254	0.241
	93	98	103	108	113	118	120	
-45	0.206	0.183	0.154	0.114	0.081	0.105	0.138	
-30	* 0.223	0.194	0.164	0.127	0.11	0.162	0.202	
-15	0.218	* 0.195	0.166	* 0.133	0.118	0.178	0.226	
0	0.222	0.195	* 0.167	0.132	* 0.119	* 0.187	0.24	
15	0.219	0.189	0.157	0.128	0.118	0.184	0.236	
30	0.188	0.16	0.131	0.116	0.11	0.174	* 0.246	
45	0.126	0.105	0.086	0.081	0.101	0.17	0.229	

Table 3

Run N38

Generator N1,  $\alpha = 20^\circ$ ,  $t_0 = f(\Phi, Y)$ , degrees C. $\lambda = 2\text{mm}$ 

X=2mm		Y, mm									
φ, degr		0	20	40	60	80	90				
-45		4.47	2.51	-1.37	-1.84	0.01	-4.07				
-30		7.56	-0.54	4.33	3.26	3.76	1.36				
-15		8.47	5.11	5.49	4.89	4.76	2.53				
0	*	8.64	*	6.71	5.61	* 5.33	* 5.09	*	3.3		
15		8.26		6.41	* 5.63	5.16	4.64		3.07		
30		7.06		5.24	4.33	3.96	3.21		2.14		
45		2.51		-0.34	-1.37	-1.67	-0.73		-1.46		
		91	92	94	95	96	97	98			
-45		-2.3	-2.04	-0.91	-1.3	-1.29	-1.07	-0.83			
-30		1.59	1.04	0.84	0.53	0.3	0.34	0.34			
-15		2.33	2.04	1.76	1.39	1.43	* 1.47	* 1.84			
0	*	3.21	* 3.29	* 2.46	* 2.29	* 1.89	1.24	1.61			
15		2.59	2.24	1.17	0.93	0.59	0.11	0.53			
30		1.31	0.69	-1.29	-1.24	-1.81	-3.29	-3.2			
45		-2.19	-2.41	-4.26	-5.87	-6.8	-6.99	-4.86			
		99	100	101	102	103	104	105			
-45		-0.16	-0.63	* -3.9	-9.6	-10.66	-12.71	-14.66			
-30		0.53	-1.4	-5.51	-9.29	-11.97	-14.2	-15.57			
-15	*	2.57	* 0.07	-5.23	-7.03	-10.29	-13.63	-15.64			
0		2.51	-0.8	-4.97	* -5.49	-10.39	-15.17	-15.93			
15		1.6	-1.84	-5.6	-6.37	-11.17	-15.39	-16.6			
30		-2.83	-5	-7.44	-6.04	* -9.01	-12.64	-12.24			
45		-4.69	-7.73	-9.91	-7.89	-10.3	* -12.23	* -10.2			
		106	107	109	110	112	114	116	118	120	
-45		-14.43	-11.93	-3.59	-1.8	-4.16	-7.41	-8.34	-7.36	-7.6571	
-30		-14.41	-11.21	-3.76	-5.26	-15.77	-11.94	-10.94	-8.33	-13.014	
-15		-14.07	-11.5	-5.71	-5.71	-5.94	-5.24	-3.56	-3.69	-7.3286	
0		-14.83	-12.83	-3.19	-1.37	-1.23	-0.51	-0.06	-1.54	-1.9143	
15		-16.31	-14.36	-0.33	1.49	-0.06	0.26	0.46	*	-0.01	-0.3571
30		-11.24	-5.84	* 3.04	* 1.97	* 0.56	* 0.74	* 0.79	-0.34	*	-0.2571
45	*	-7.24	* -2.59	1.76	0.9	0.24	0.44	0.44	-0.71		-0.6

Table 4

Run N41

 $t_0 = f(\text{Phi}, Y)$ , degrees C

X = 110mm

		Y, mm					
Phi, degr.		0	15	30	45	60	75
-45		-2.67	-5.09	-3.59	-2.96	-3.11	-3.51
-30		2.01	1.03	1.09	0.87	0.71	0.49
-15		2.91	2.07	1.89	1.89	1.60	1.54
0	*	3.21	* 2.39	* 2.16	* 1.97	* 1.73	* 1.74
15		2.87	2.16	1.90	1.60	1.49	1.40
30		1.54	1.06	0.81	0.37	-0.11	-0.36
45		-3.19	-4.89	-5.36	-6.23	-7.11	-7.50
		80	82	84	86	88	90
-45		-3.60	-3.57	-3.27	-3.26	-3.47	-3.87
-30		0.26	0.16	0.06	0.01	0.00	-0.16
-15		1.16	1.09	0.94	0.89	0.77	0.67
0	*	1.3	* 1.24	* 1.06	* 1	* 0.87	* 0.73
15		0.97	0.86	0.77	0.76	0.56	0.39
30		-0.90	-0.96	-0.77	-1.20	-1.51	-1.91
45		-8.00	-8.01	-7.96	-8.24	-8.50	-8.83
		92	94	96	98	100	
-45		-4.04	-4.76	-4.24	-4.16	-3.81	
-30		-0.37	-0.37	-0.50	-0.51	-0.80	
-15		0.40	0.34	* 0.27	0.14	0.20	
0	*	0.44	* 0.4	* 0.23	* 0.2	* 0.26	
15		0.21	0.07	-0.07	-0.23	-0.33	
30		-2.13	-2.93	-2.00	-2.33	-1.87	
45		-9.30	-8.01	-8.23	-7.56	-7.74	
		102	104	106	108	110	
-45		-3.90	-5.20	-5.50	-7.20	-9.01	
-30		-0.74	-1.40	-1.53	-2.40	-3.77	
-15		0.13	-0.03	* -0.23	* -0.67	-1.46	
0	*	0.19	* 0.03	-0.29	-0.70	* -0.9	
15		-0.50	-0.73	-1.30	-1.39	-1.49	
30		-2.16	-2.14	-2.79	-2.90	-2.84	
45		-7.00	-6.69	-7.66	-6.43	-5.39	
		110	112	114	116	118	120
-45		-9.01	-9.71	-10.01	-10.30	-9.17	-11.47
-30		-3.77	-4.57	-4.71	-6.70	-8.34	-5.14
-15		-1.46	-1.59	-2.03	-2.77	-3.26	-1.89
0	*	-0.9	* -1.22	* -1.22	-1.67	-1.56	* -0.49
15		-1.49	-1.50	-1.57	* -1.39	* -1.17	-0.61
30		-2.84	-2.66	-2.63	-2.16	-1.76	-1.64
45		-5.39	-4.00	-3.41	-3.30	-3.10	-2.60

Table 5

Sphere

Run 28

 $M=3.0$   $Re=6.70 \times 10^5$   $T_0 = 413 \text{ K}$   $P_0=4.834 \times 10^5 \text{ Pa}$   $t=1.0 \text{ s}$ 

Thermo-couple	S/R	T K	$T_{smo}$ K	$q$ , kW/m <sup>2</sup>	$q_0$ , kW/m <sup>2</sup>	$q/q_0$
1	1.508	301.7	301.7	7.595	76.95	0.0987
2	1.340	306.3	306.2	14.44	73.79	0.1957
3	1.173	309.4	309.3	21.54	71.63	0.3007
4	1.005	313.7	313.7	29.32	68.63	0.4272
5	0.838	319.5	319.5	37.19	64.62	0.5755
6	0.670	325.6	325.6	45.94	60.39	0.7607
7	0.503	331.4	331.3	50.09	56.41	0.8879
8	0.335	336.0	336.0	50.83	53.19	0.9556
9	0.168	338.2	338.3	55.36	51.57	1.0735
10	0.000	340.8	340.9	52.59	49.76	1.0569
11	0.084	339.8	339.9	56.29	50.44	1.1160
12	0.168	337.6	337.7	56.86	52.02	1.0932
13	0.251	333.9	334.0	57.60	54.58	1.0552
14	0.335	333.0	333.0	55.81	55.22	1.0107
15	0.419	332.1	332.2	51.80	55.82	0.9279
16	0.503	327.7	327.8	52.32	58.85	0.8891
17	0.586	326.2	326.2	49.82	59.93	0.8312
18	0.670	322.1	322.1	50.59	62.78	0.8058
19	0.754	317.6	317.6	44.19	65.88	0.6707
20	0.838	315.0	315.0	38.90	67.69	0.5748
21	0.922	312.7	312.8	35.17	69.26	0.5077
22	1.005	307.8	308.0	30.41	72.59	0.4190
23	1.089	308.2	308.3	26.29	72.36	0.3633
24	1.173	306.0	306.0	22.86	73.96	0.3091
25	1.257	302.4	302.3	17.87	76.48	0.2337
26	1.340	300.5	300.6	13.84	77.71	0.1781
27	1.424	299.7	299.6	11.32	78.37	0.1445
28	1.508	298.6	298.6	8.158	79.04	0.1032
29	1.591	299.0	299.0	5.534	78.80	0.0702
30	1.758	297.8	297.8	4.710	79.63	0.0592
31	1.925	298.1	298.1	4.404	79.42	0.0555
32	2.091	299.0	299.0	4.139	78.78	0.0525
33	2.258	299.9	299.9	4.124	78.17	0.0528
34	2.425	301.0	301.0	4.128	77.42	0.0533
35	0.168	338.4	338.5	54.14	51.44	1.0524
36	0.335	330.7	330.8	56.78	56.77	1.0002
37	0.503	330.9	330.8	50.72	56.73	0.8940
38	0.670	325.9	325.9	46.34	60.16	0.7703
39	0.838	314.6	314.6	41.28	68.02	0.6069
40	1.005	309.7	309.7	32.77	71.38	0.4590
41	1.173	303.9	303.9	25.99	75.42	0.3446
42	1.340	297.9	297.8	16.09	79.63	0.2020
43	1.508	292.0	292.0	11.33	83.63	0.1354

Table 6

Sphere with vortex generator  $\alpha=20^\circ$ 

Run 29

 $M=3.0$   $Re=6.86 \times 10^5$   $T_0 = 410 \text{ K}$   $P_0 = 4.889 \times 10^5 \text{ Pa}$   $t=1.0 \text{ s}$ 

Thermo-couple	S/R	T K	$T_{smo}$ K	$q$ , kW/m <sup>2</sup>	$q_0$ , kW/m <sup>2</sup>	$q/q_0$
1	1.508	311.8	311.8	11.94	68.07	0.1755
2	1.340	320.3	320.3	23.21	62.14	0.3736
3	1.173	329.7	329.7	34.13	55.60	0.6139
4	1.005	339.3	339.4	43.72	48.82	0.8956
5	0.838	347.3	347.4	52.62	43.30	1.2152
6	0.670	354.3	354.3	66.13	38.51	1.7171
7	0.503	351.3	350.9	72.61	40.84	1.7780
8	0.335	338.4	338.2	56.54	49.68	1.1382
9	0.168	331.9	331.9	43.67	54.04	0.8081
10	0.000	335.1	335.0	39.06	51.88	0.7528
11	0.084	335.2	335.0	42.97	51.92	0.8277
12	0.168	335.4	335.5	48.31	51.54	0.9373
13	0.251	335.8	336.0	59.03	51.21	1.1527
14	0.335	339.6	340.1	68.64	48.39	1.4186
15	0.419	346.1	346.5	70.24	43.91	1.5997
16	0.503	345.9	346.3	79.17	44.09	1.7956
17	0.586	346.2	346.6	77.46	43.84	1.7669
18	0.670	343.2	343.5	80.06	45.99	1.7406
19	0.754	339.4	339.8	69.69	48.59	1.4344
20	0.838	336.4	336.7	61.13	50.69	1.2059
21	0.922	332.7	333.0	53.48	53.29	1.0035
22	1.005	328.9	329.1	45.95	55.98	0.8209
23	1.089	326.8	326.9	38.77	57.50	0.6742
24	1.173	321.8	322.0	33.51	60.95	0.5498
25	1.257	317.2	317.2	25.73	64.30	0.4002
26	1.340	313.5	313.6	19.35	66.80	0.2897
27	1.424	310.5	310.5	15.46	68.92	0.2243
28	1.508	308.0	308.0	10.42	70.69	0.1474
29	1.591	306.8	306.8	6.367	71.52	0.0890
30	1.758	306.1	306.1	5.322	72.00	0.0739
31	1.925	306.9	307.0	6.207	71.40	0.0869
32	2.091	308.9	309.0	7.951	70.02	0.1136
33	2.258	310.9	311.0	9.814	68.63	0.1430
34	2.425	312.6	312.7	11.03	67.44	0.1635
35	0.168	332.4	332.5	37.61	53.65	0.7010
36	0.335	326.0	326.0	41.17	58.16	0.7079
37	0.503	324.3	324.3	41.68	59.31	0.7027
38	0.670	321.0	321.1	44.99	61.59	0.7305
39	0.838	314.0	314.3	51.10	66.33	0.7704
40	1.005	310.3	310.4	47.29	68.99	0.6855
41	1.173	305.3	305.5	39.27	72.46	0.5420
42	1.340	301.6	301.7	24.13	75.05	0.3215
43	1.508	297.2	297.4	17.13	78.09	0.2193

Table 7

Sphere with vortex generator  $\alpha=10^\circ$ 

Run 30

 $M=3.0$   $Re=6.69 \times 10^5$   $T_0 = 415 \text{ K}$   $P_0=4.858 \times 10^5 \text{ Pa}$   $\tau=1.0 \text{ s}$ 

Thermo-couple	S/R	T K	$T_{smo}$ K	$q$ , kW/m <sup>2</sup>	$q_0$ , kW/m <sup>2</sup>	$q/q_0$
1	1.508	304.6	304.7	7.761	76.55	0.1014
2	1.340	311.9	312.0	16.25	71.48	0.2274
3	1.173	318.7	318.9	24.84	66.69	0.3725
4	1.005	326.5	326.7	33.05	61.27	0.5394
5	0.838	332.3	332.6	41.96	57.16	0.7341
6	0.670	337.3	337.7	54.31	53.62	1.0128
7	0.503	335.8	336.1	60.06	54.76	1.0968
8	0.335	327.9	327.4	49.41	60.76	0.8132
9	0.168	322.4	322.1	41.73	64.48	0.6472
10	0.000	325.3	324.9	35.54	62.54	0.5683
11	0.084	325.4	324.9	38.77	62.51	0.6203
12	0.168	326.3	325.8	46.03	61.87	0.7441
13	0.251	328.8	328.3	57.15	60.15	0.9501
14	0.335	335.9	335.5	64.88	55.18	1.1758
15	0.419	342.5	342.4	66.37	50.39	1.3173
16	0.503	342.9	343.1	71.42	49.90	1.4314
17	0.586	343.2	343.1	67.68	49.84	1.3579
18	0.670	339.9	339.9	67.51	52.10	1.2958
19	0.754	334.6	334.6	57.30	55.80	1.0270
20	0.838	331.7	331.7	50.21	57.77	0.8690
21	0.922	328.9	329.0	43.84	59.67	0.7347
22	1.005	324.4	324.5	38.00	62.81	0.6050
23	1.089	321.9	321.9	31.68	64.56	0.4907
24	1.173	317.8	317.9	26.81	67.39	0.3979
25	1.257	312.0	312.0	19.94	71.48	0.2789
26	1.340	308.7	308.7	14.27	73.75	0.1934
27	1.424	305.4	305.5	10.49	76.03	0.1380
28	1.508	302.7	302.7	6.350	77.94	0.0815
29	1.591	302.2	302.2	3.311	78.28	0.0423
30	1.758	301.1	301.1	2.456	79.06	0.0311
31	1.925	300.9	300.9	2.802	79.22	0.0354
32	2.091	303.2	303.2	4.210	77.57	0.0543
33	2.258	304.6	304.6	6.607	76.60	0.0863
34	2.425	306.9	306.9	8.728	75.00	0.1164
35	0.168	321.9	321.8	33.63	64.63	0.5203
36	0.335	316.2	316.0	35.50	68.66	0.5169
37	0.503	313.0	312.9	37.03	70.85	0.5227
38	0.670	309.4	309.4	39.52	73.30	0.5392
39	0.838	303.5	303.6	42.49	77.34	0.5494
40	1.005	302.7	302.9	34.75	77.79	0.4467
41	1.173	300.1	300.3	26.25	79.62	0.3297
42	1.340	296.8	297.0	14.74	81.88	0.1801
43	1.508	294.4	294.5	9.301	83.64	0.1112

Table 8

Sphere with vortex generator  $\alpha=30^\circ$ 

Run 43

 $M=3.0$   $Re=6.76 \times 10^5$   $T_0 = 414 \text{ K}$   $P_0 = 4.891 \times 10^5 \text{ Pa}$   $\tau = 1.0 \text{ s}$ 

Thermo-couple	S/R	T K	$T_{smo}$ K	$q$ , kW/m <sup>2</sup>	$q_0$ , kW/m <sup>2</sup>	$q/q_0$
1	1.508	299.9	299.8	6.333	79.54	0.0796
2	1.340	304.5	304.5	11.72	76.30	0.1536
3	1.173	309.0	309.0	16.97	73.16	0.2320
4	1.005	312.9	312.8	22.22	70.51	0.3152
5	0.838	317.6	317.5	27.82	67.21	0.4139
6	0.670	322.2	322.1	33.70	64.05	0.5262
7	0.503	324.4	324.1	35.98	62.61	0.5747
8	0.335	329.3	329.3	35.91	58.99	0.6087
9	0.168	327.4	327.2	38.27	60.44	0.6332
10	0.000	330.1	330.0	35.72	58.55	0.6102
11	0.084	328.4	328.4	36.88	59.62	0.6185
12	0.168	327.7	327.6	35.38	60.21	0.5875
13	0.251	326.7	326.5	35.39	60.93	0.5809
14	0.335	323.2	323.2	35.26	63.28	0.5571
15	0.419	320.3	320.3	33.26	65.25	0.5097
16	0.503	318.7	318.8	34.65	66.35	0.5222
17	0.586	316.8	316.7	33.55	67.75	0.4952
18	0.670	314.3	314.3	33.97	69.48	0.4889
19	0.754	306.9	306.8	29.65	74.67	0.3971
20	0.838	307.2	307.2	26.17	74.41	0.3516
21	0.922	306.3	306.2	23.36	75.10	0.3110
22	1.005	301.7	301.7	20.11	78.24	0.2570
23	1.089	303.8	303.7	17.33	76.82	0.2256
24	1.173	300.6	300.5	15.05	79.08	0.1903
25	1.257	298.7	298.6	12.04	80.38	0.1498
26	1.340	297.9	297.8	9.569	81.00	0.1181
27	1.424	299.9	299.8	7.845	79.55	0.0986
28	1.508	296.5	296.4	5.914	81.93	0.0722
29	1.591	298.1	298.0	4.154	80.81	0.0514
30	1.758	299.6	299.5	3.943	79.79	0.0494
31	1.925	302.4	302.2	4.645	77.90	0.0596
32	2.091	303.5	303.3	5.570	77.11	0.0722
33	2.258	306.6	306.4	6.679	74.98	0.0891
34	2.425	306.0	305.8	7.315	75.37	0.0971
35	0.168	329.0	328.3	34.49	59.72	0.5774
36	0.335	335.2	333.5	52.51	56.07	0.9365
37	0.503	333.2	333.0	52.36	56.43	0.9279
38	0.670	318.3	318.5	39.51	66.50	0.5942
39	0.838	304.5	304.7	24.78	76.18	0.3253
40	1.005	305.8	305.5	22.82	75.62	0.3018
41	1.173	309.8	309.5	27.75	72.78	0.3813
42	1.340	308.5	308.4	20.64	73.58	0.2805
43	1.508	300.4	300.4	16.59	79.18	0.2095

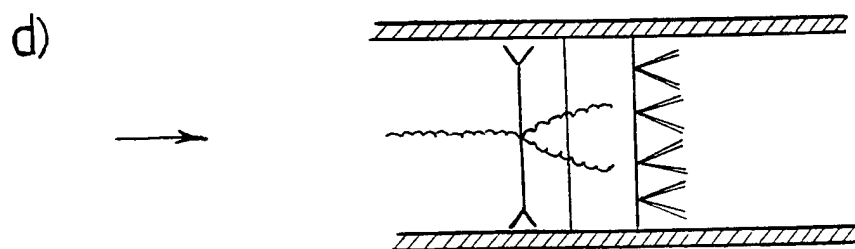
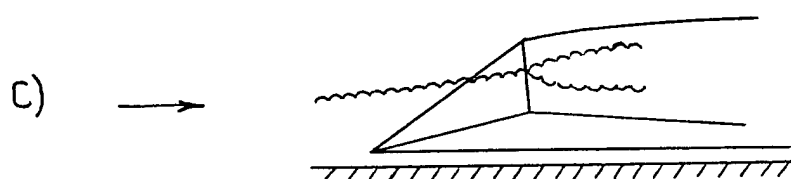
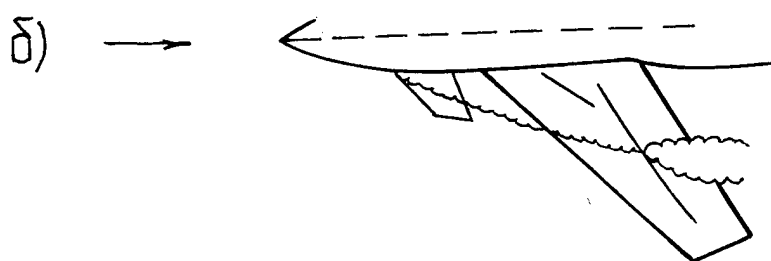
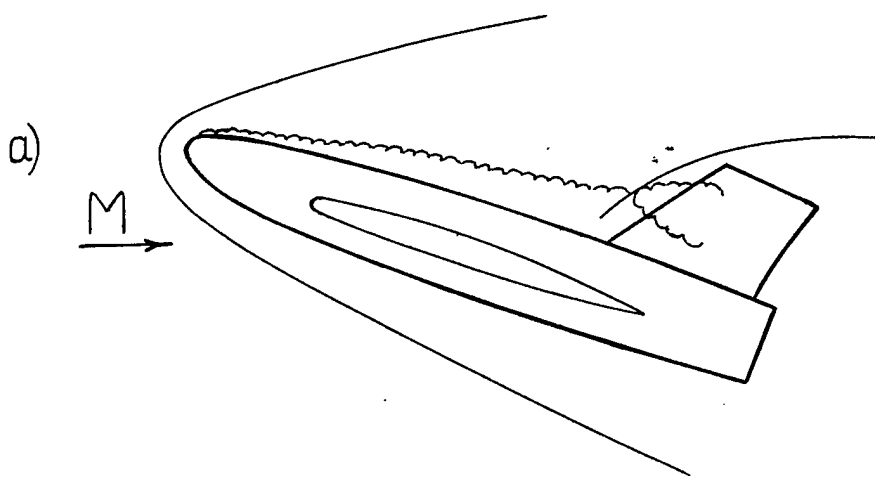


Fig. 1

# T-33 WIND TUNNEL

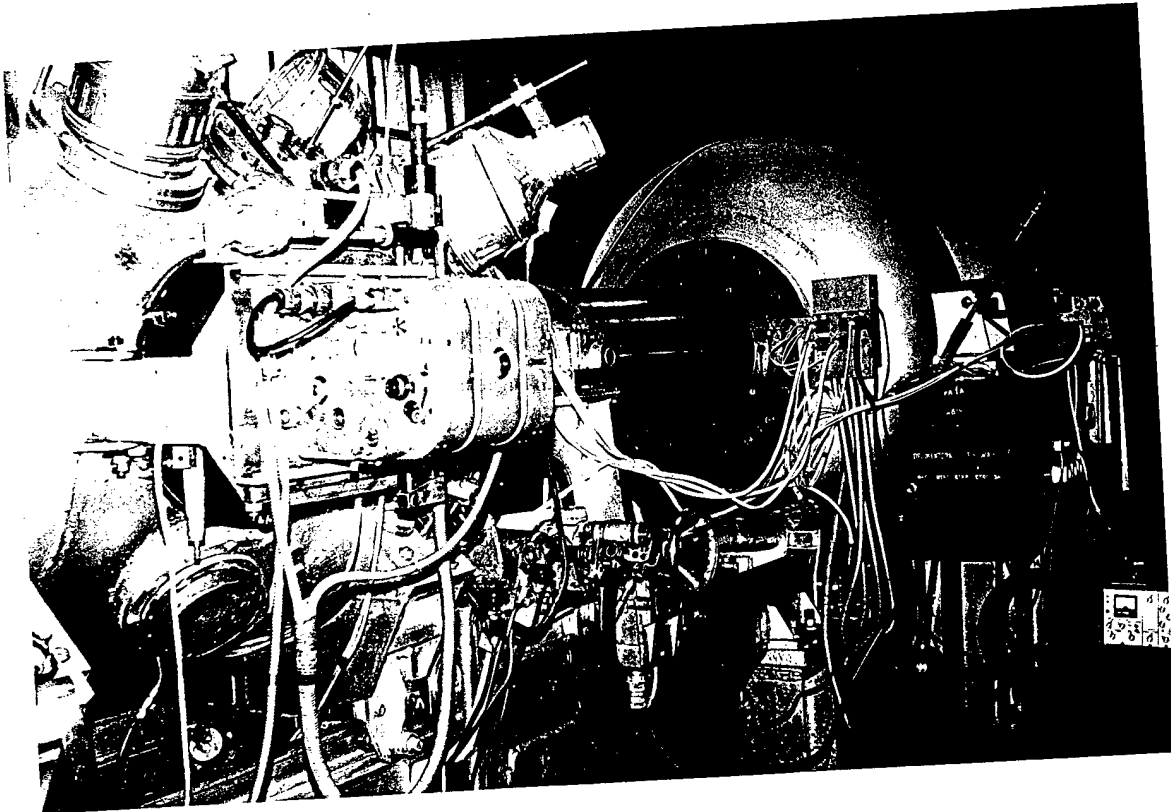


Fig. 2

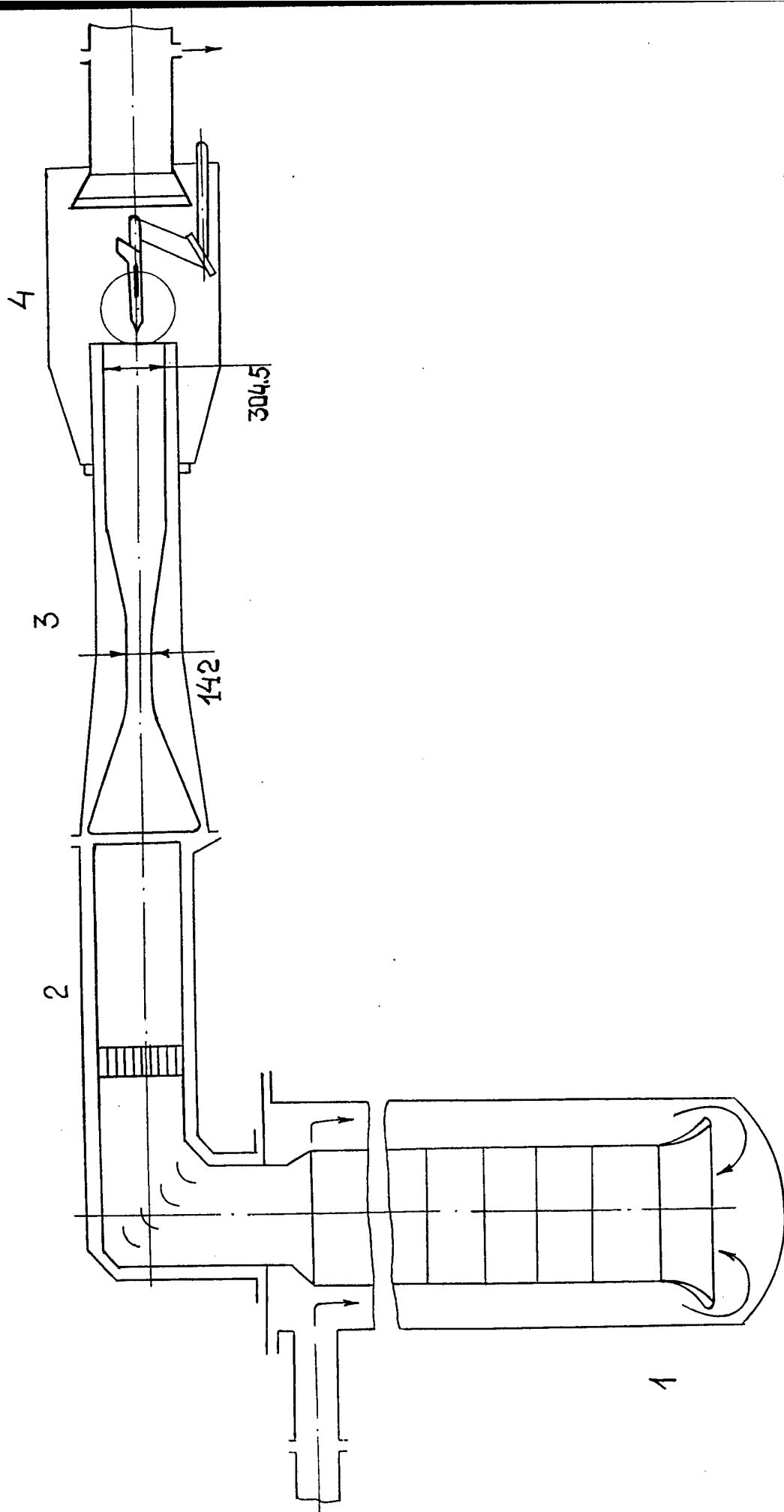
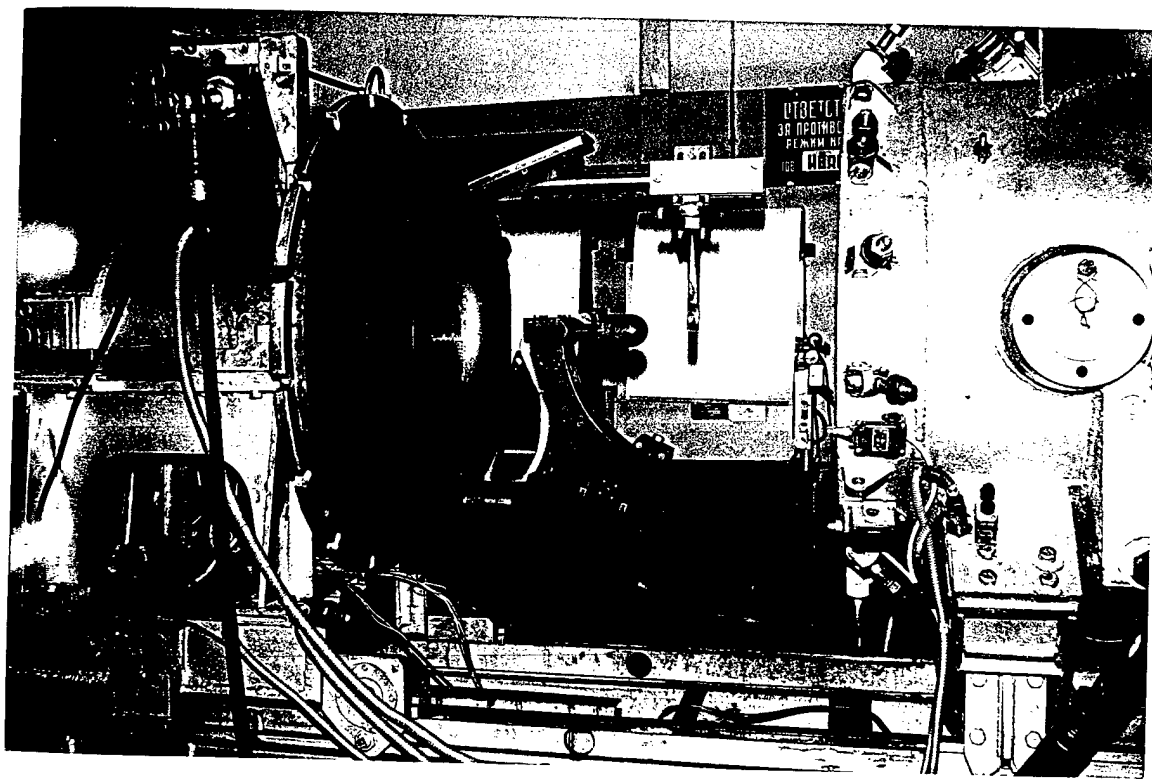


Fig. 3

T-33 TEST SECTION



Generator N1

Scale 1:2

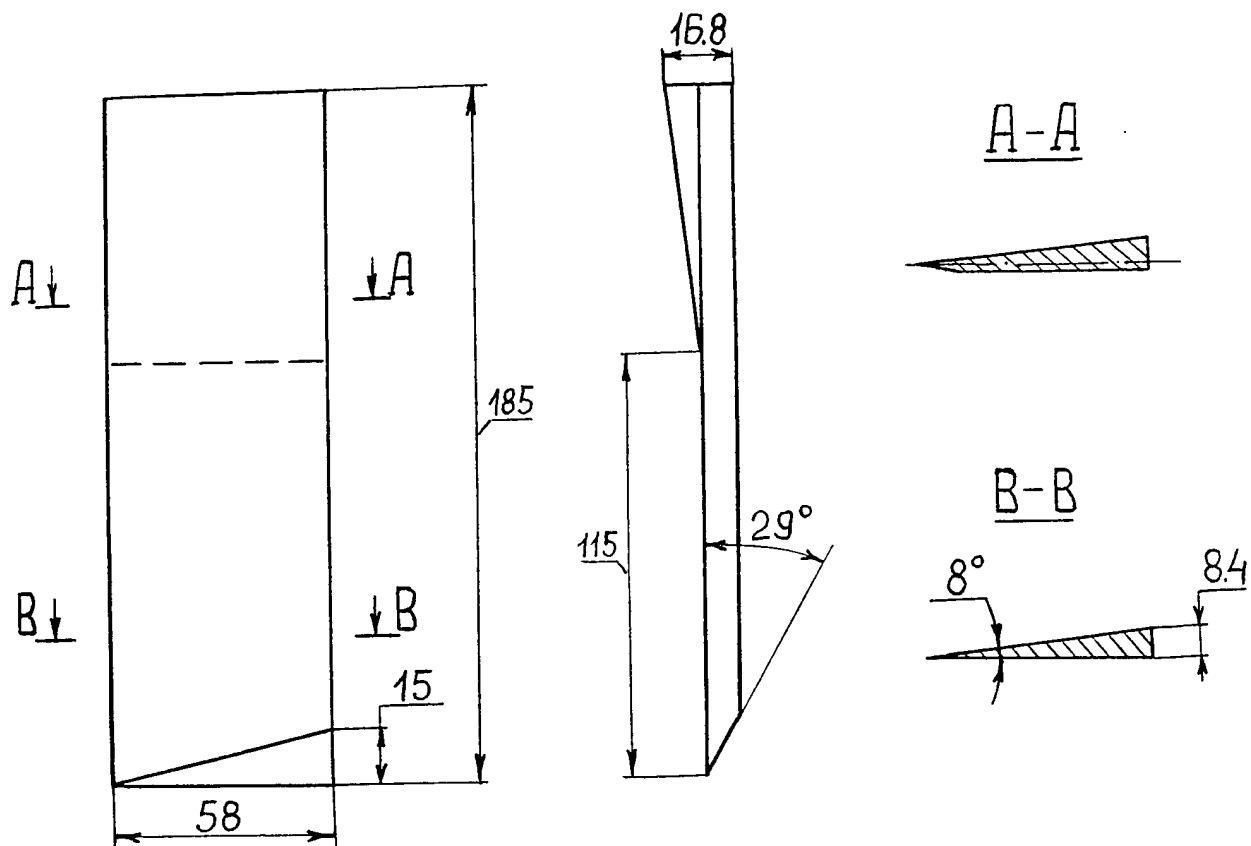


Fig. 5

# Generator N2

Scale 1:2

Scale 1:1

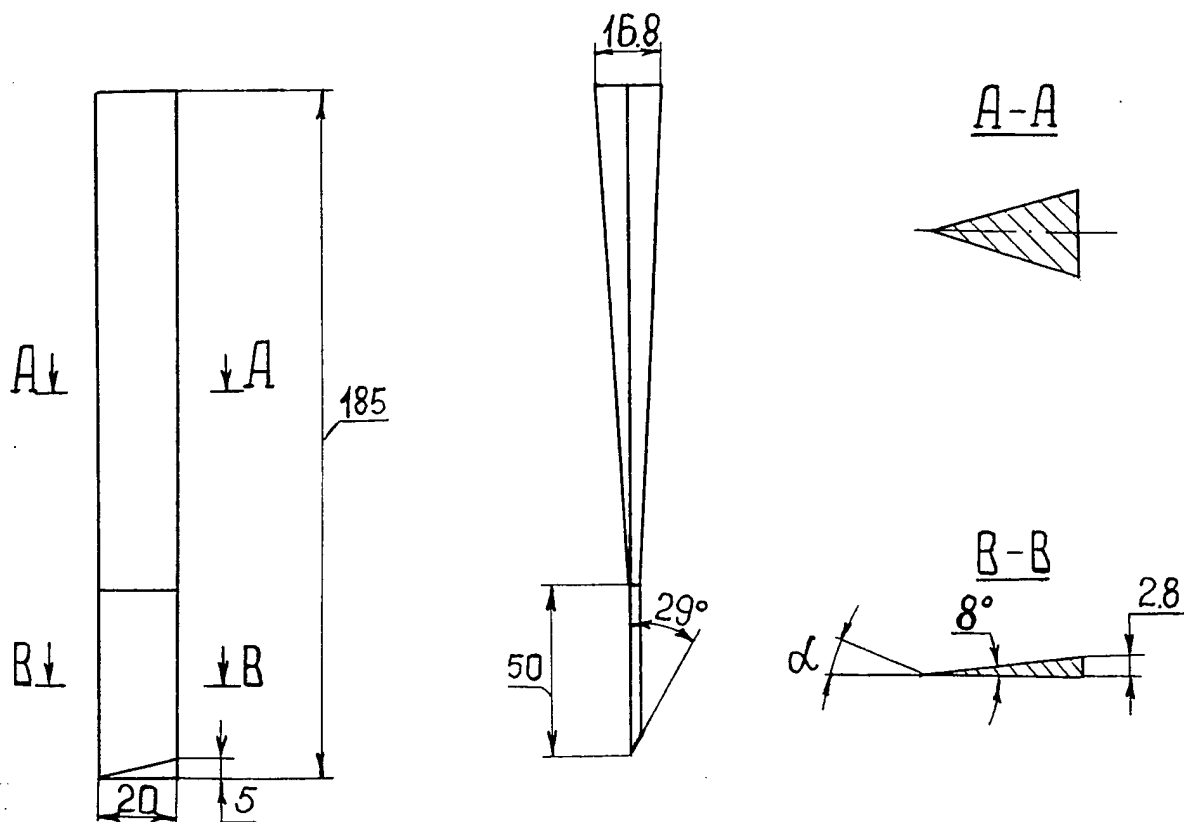


Fig. 6

Generator N3

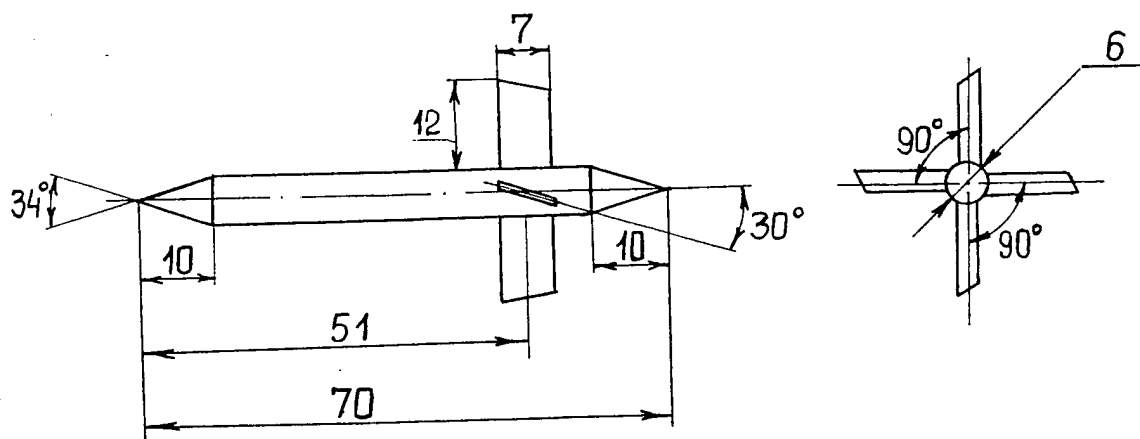


Fig. 7

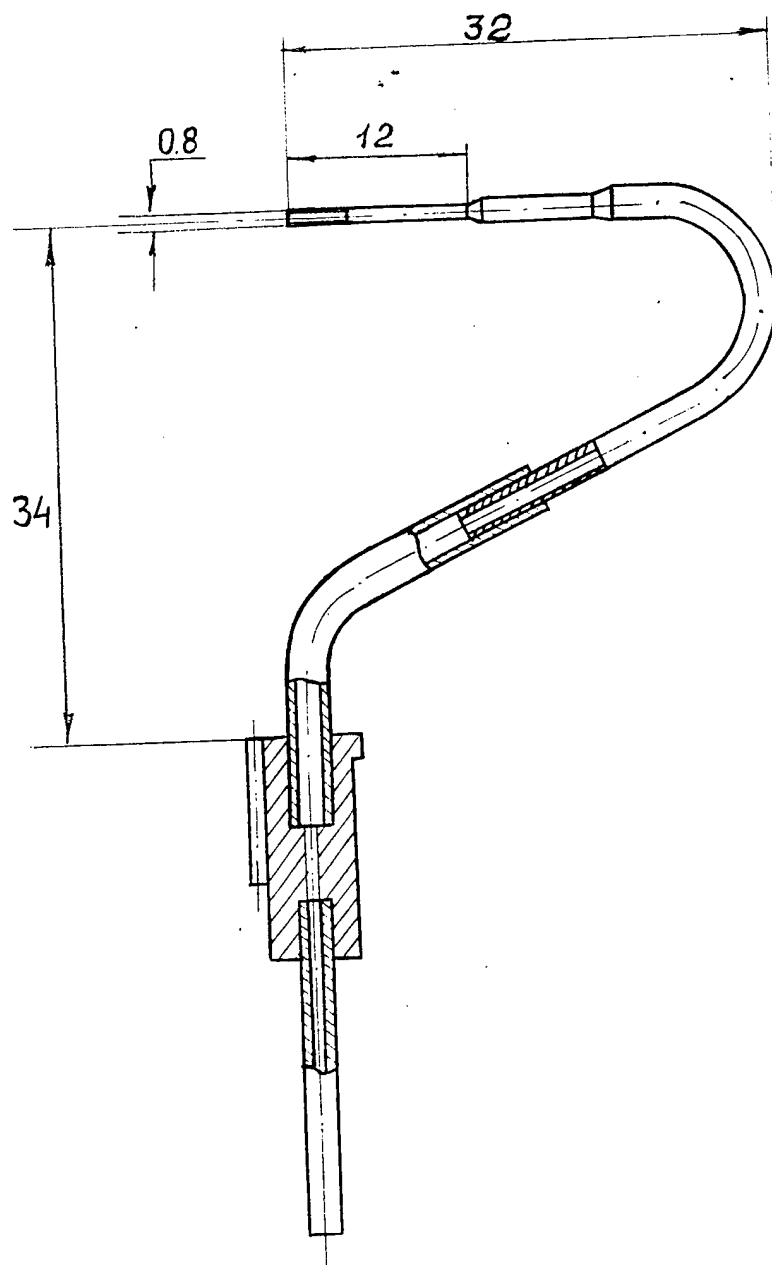


Fig. 8a

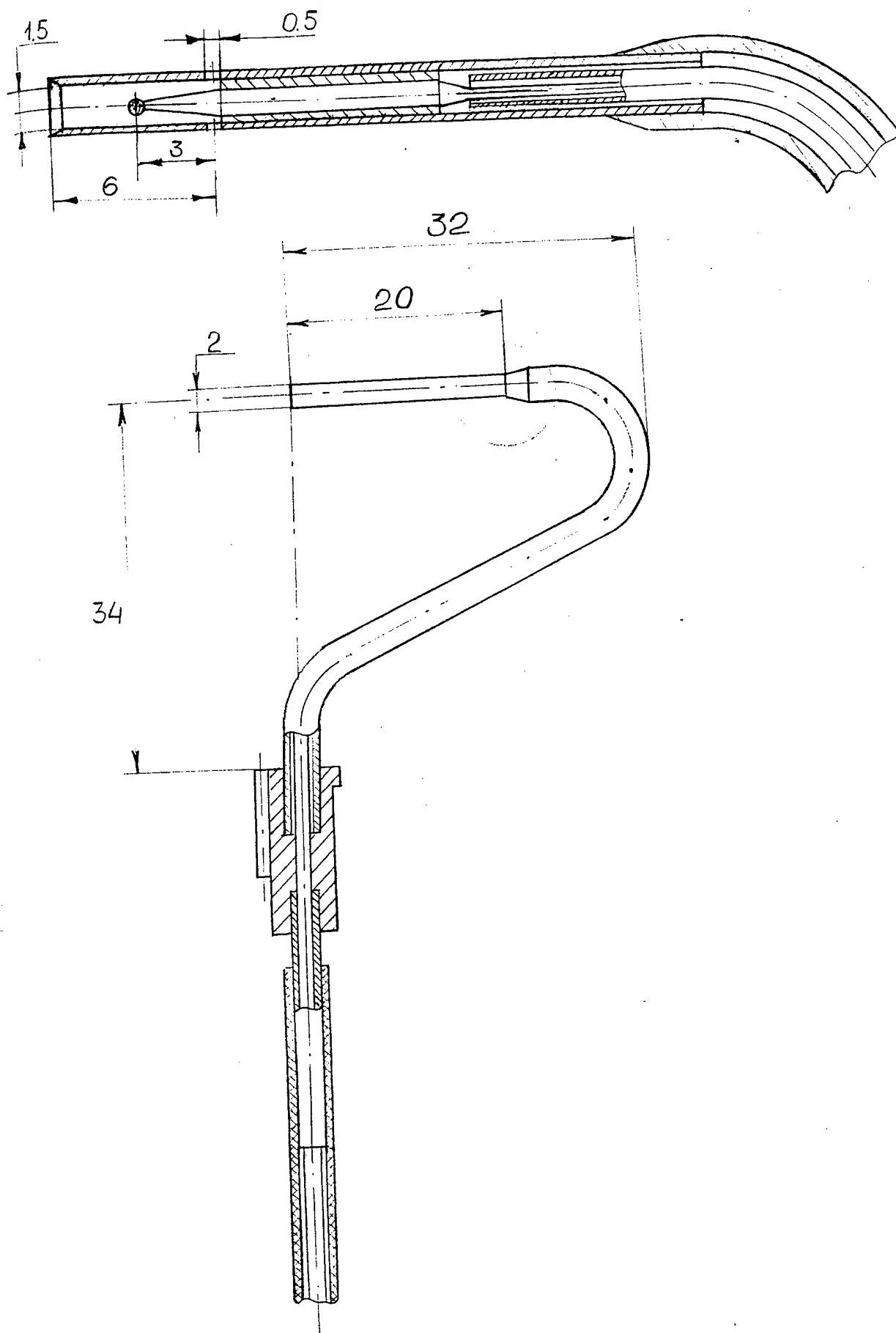


Fig. 8b

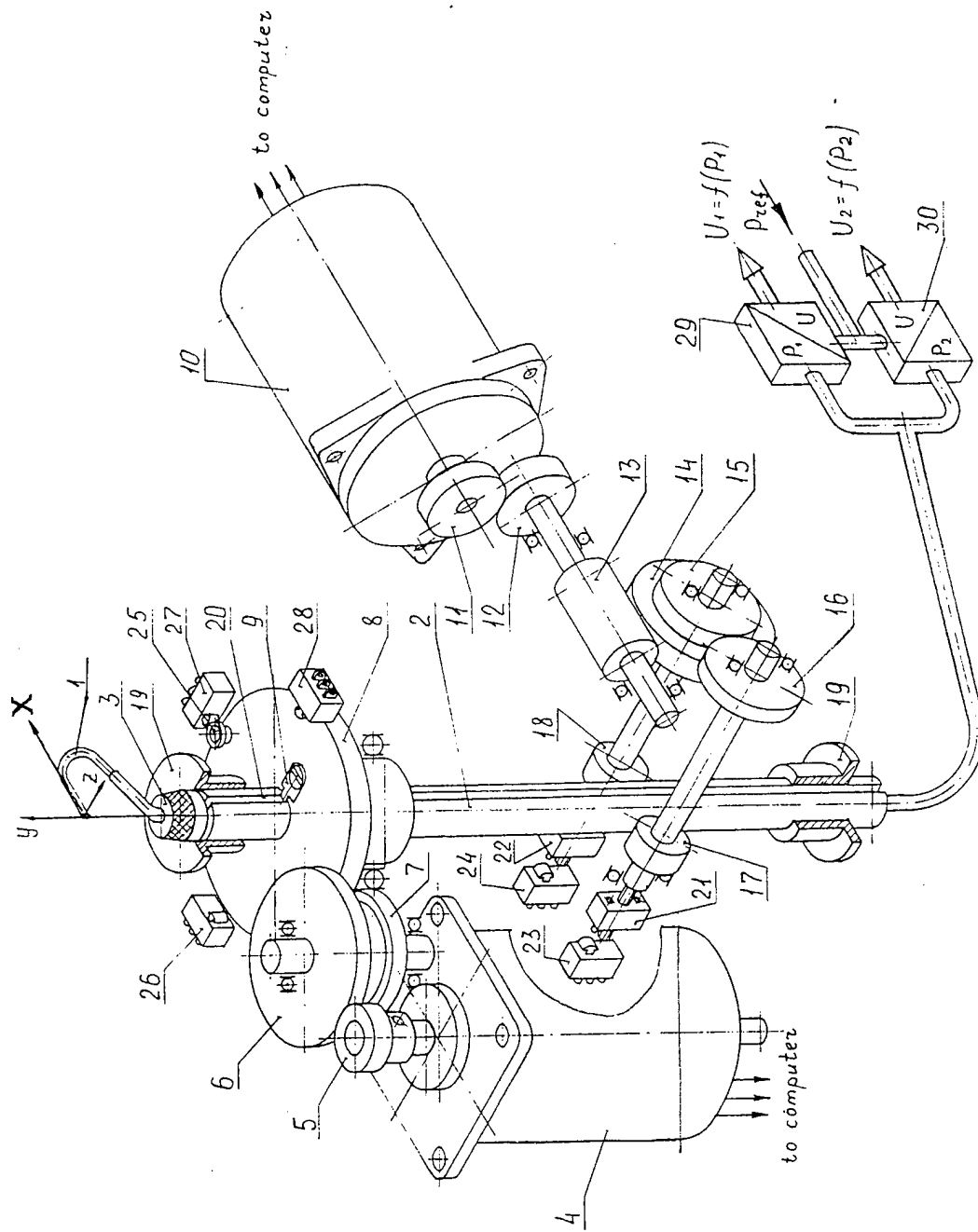


Fig.

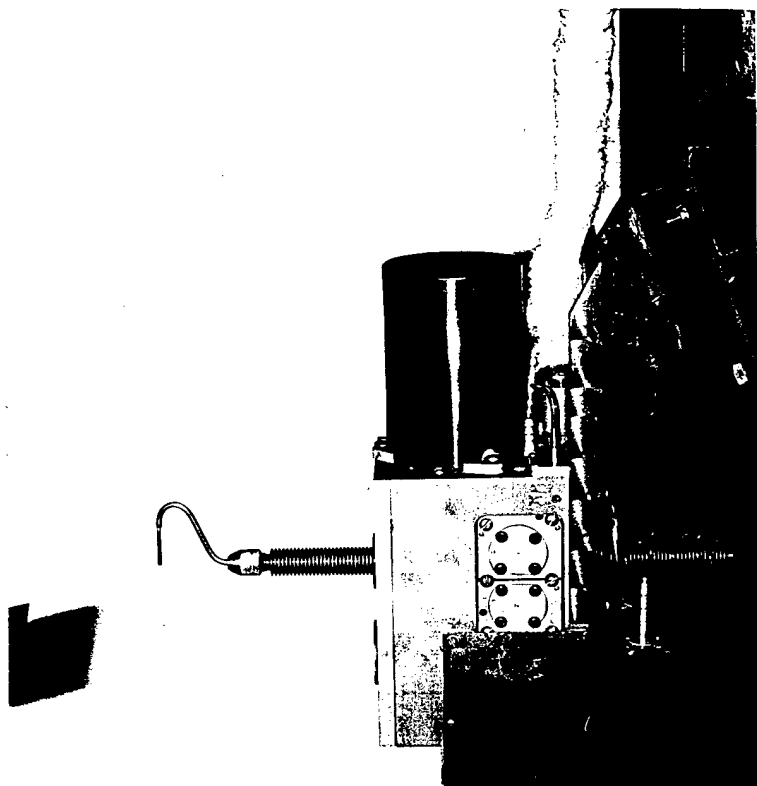
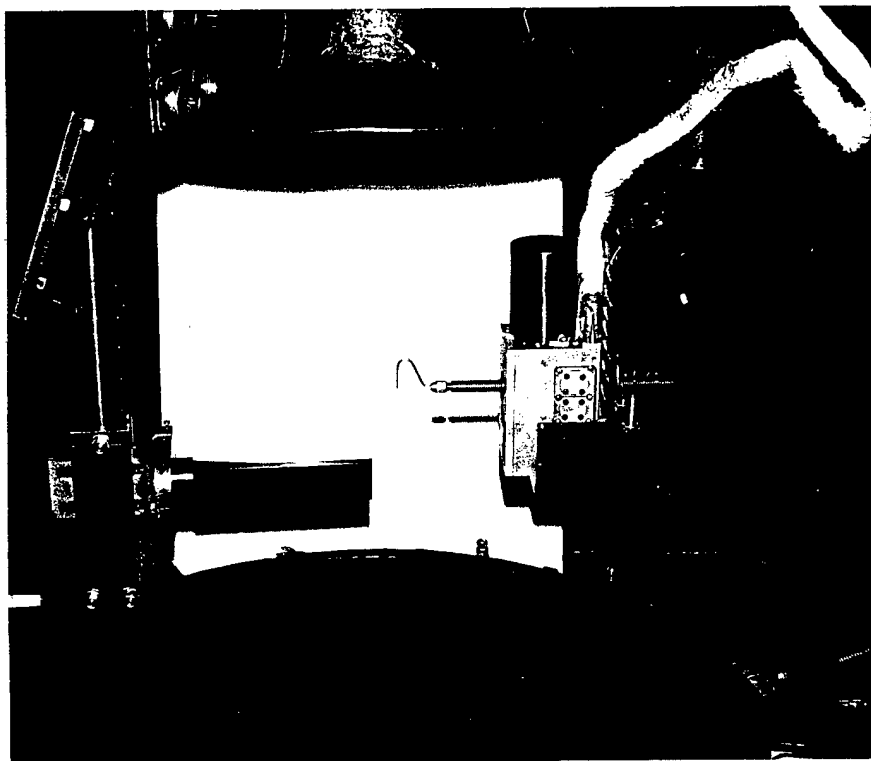


Fig. 10

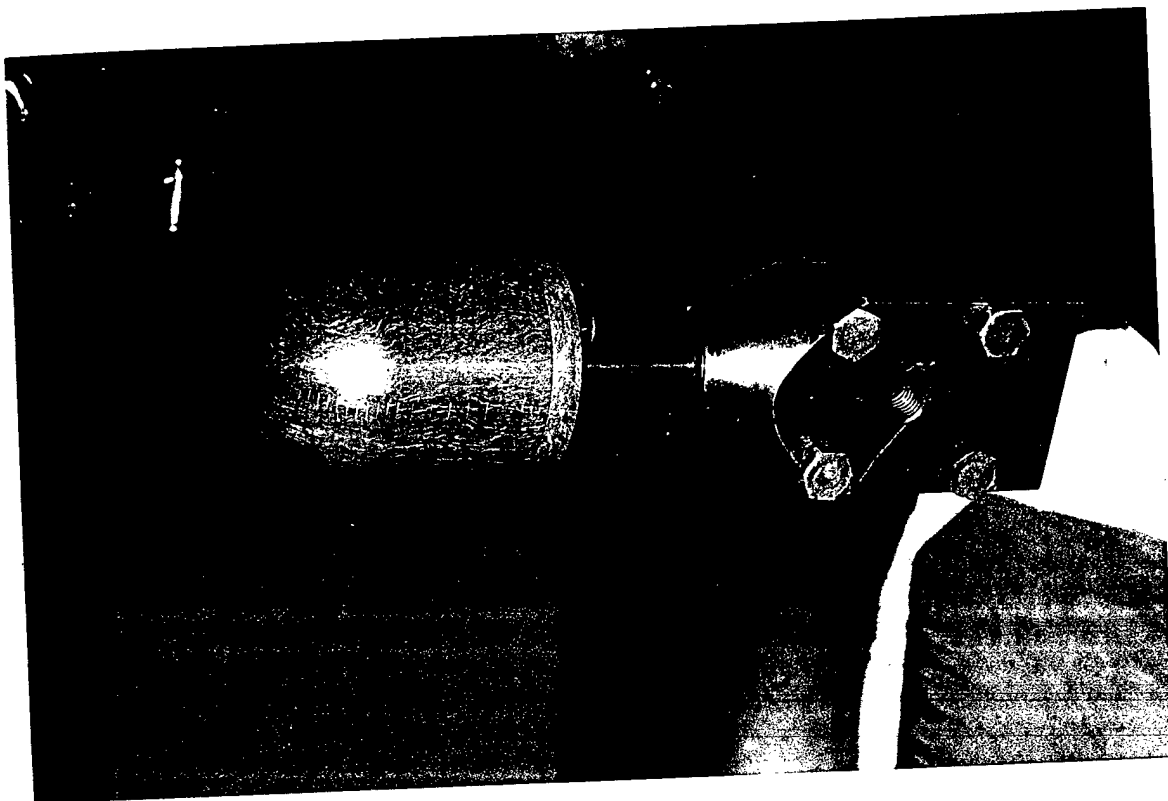
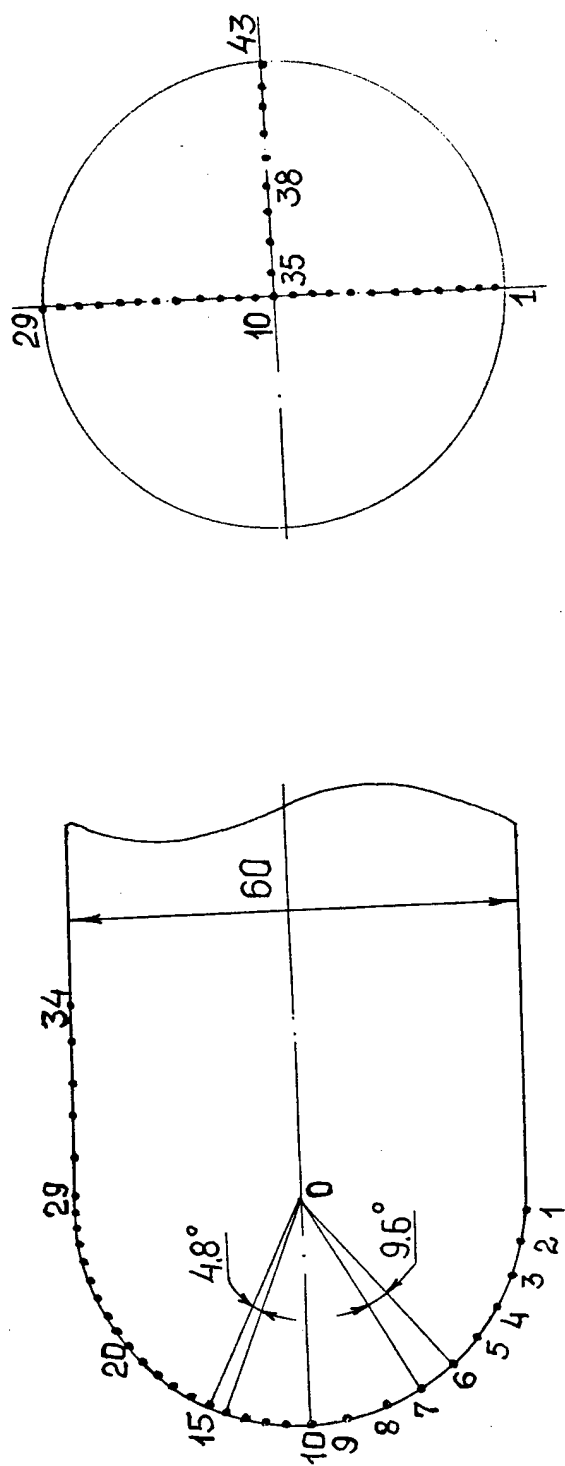


Fig. 11a



SURFACE THERMOCOUPLES LOCATION ON THE SEMISPHERE MODEL

Thermocouples 1-10 over 9.6° or  $\Delta S=5.0$  mm  
 10-29 over 4.8° or  $\Delta S=2.5$  mm  
 29-34 over 9.6° or  $\Delta S=5.0$  mm  
 10-43 over 9.6° or  $\Delta S=5.0$  mm

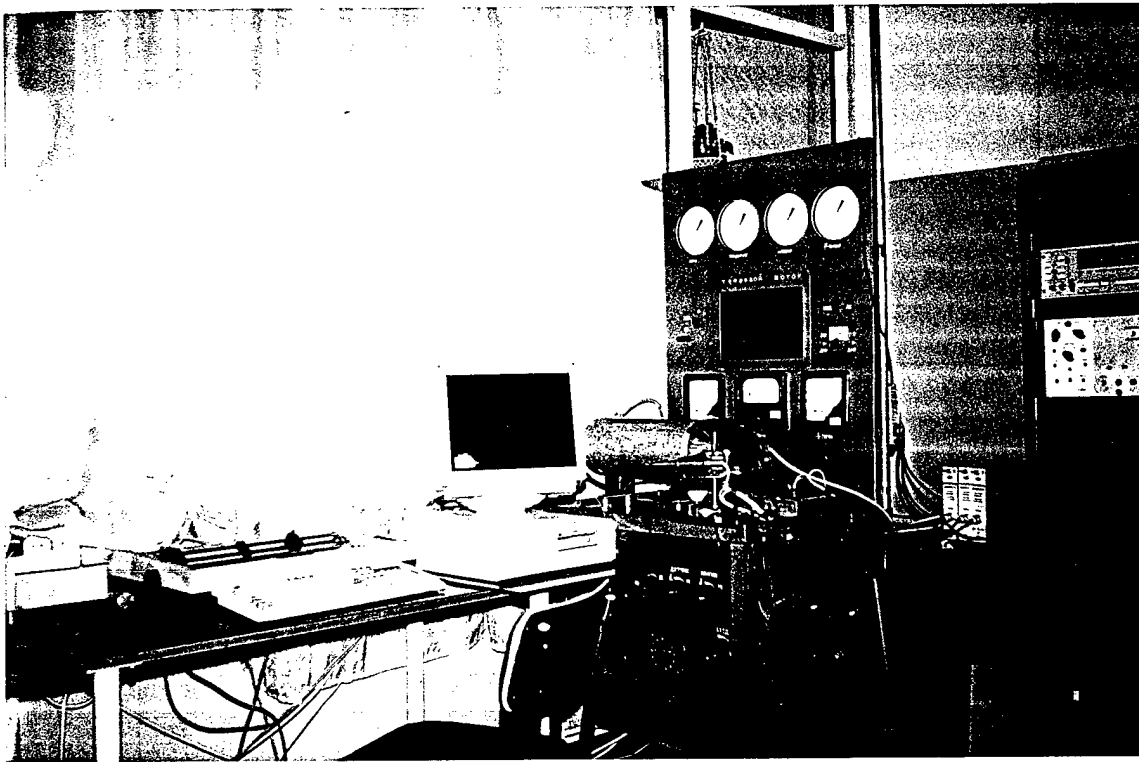
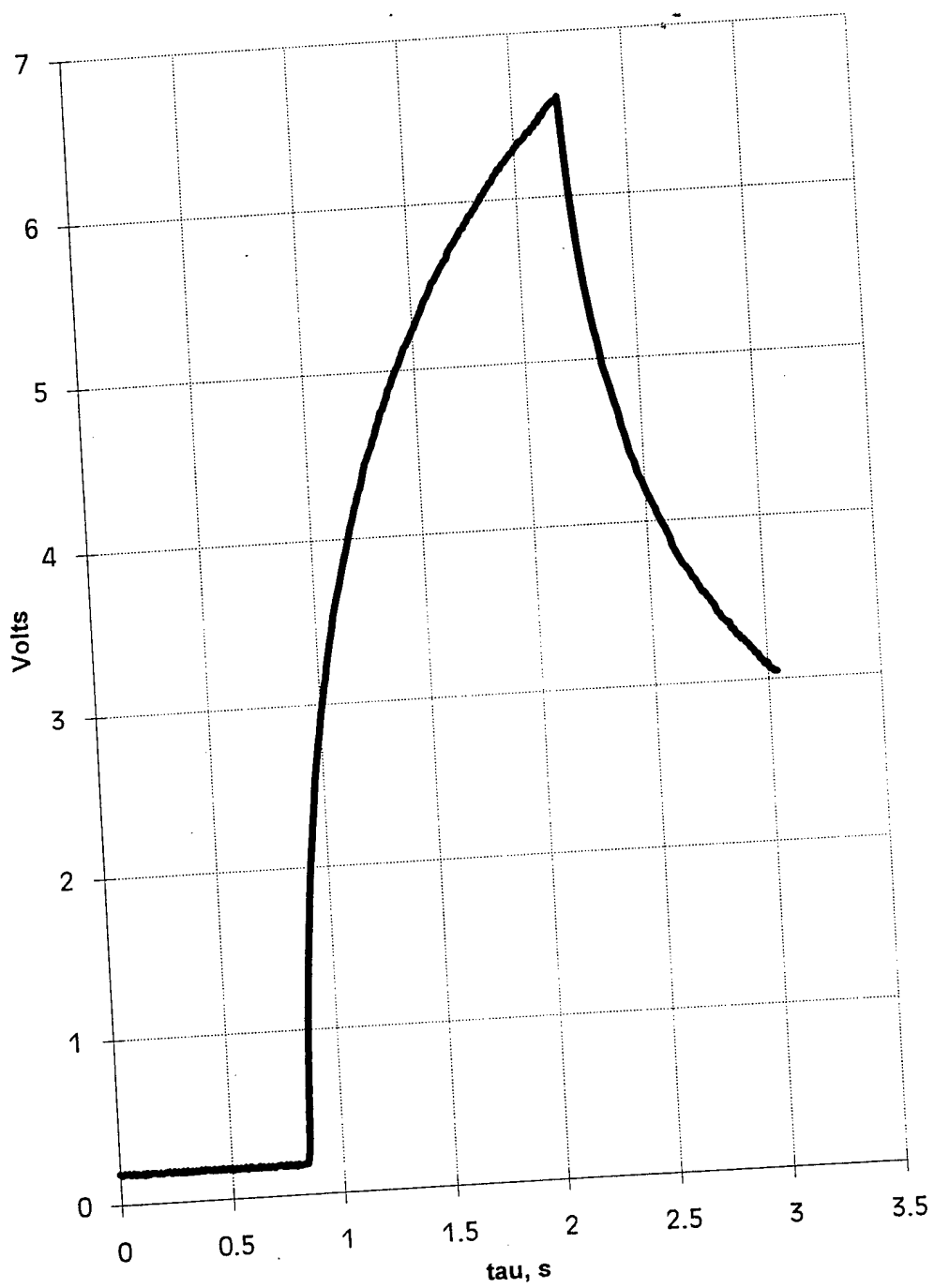


Fig. 12a



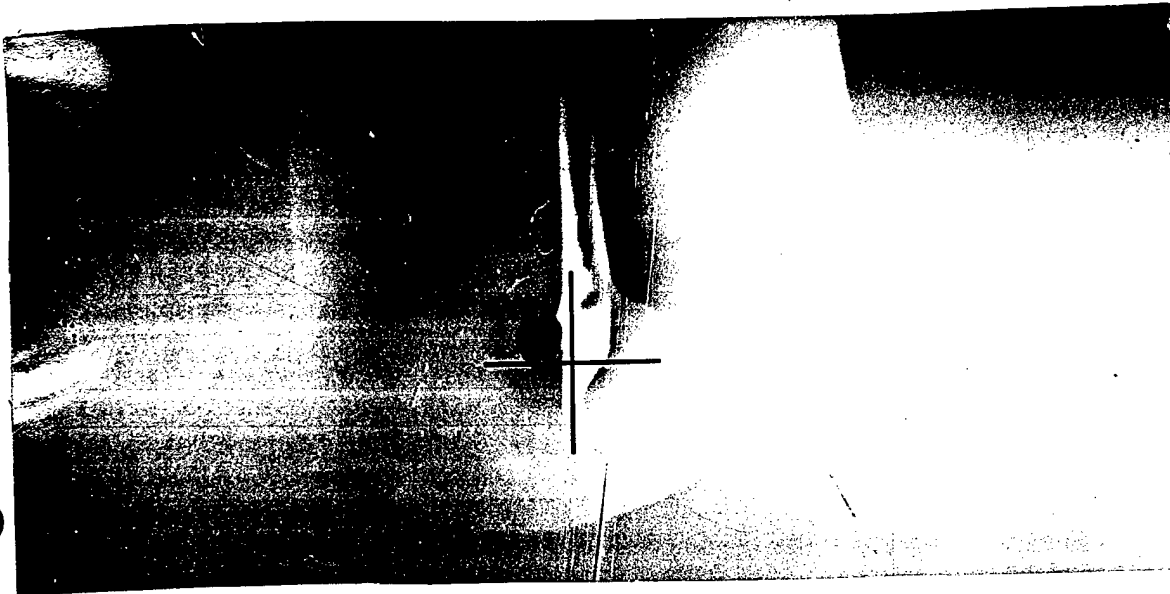
Thermocouple N18

Fig. 12b

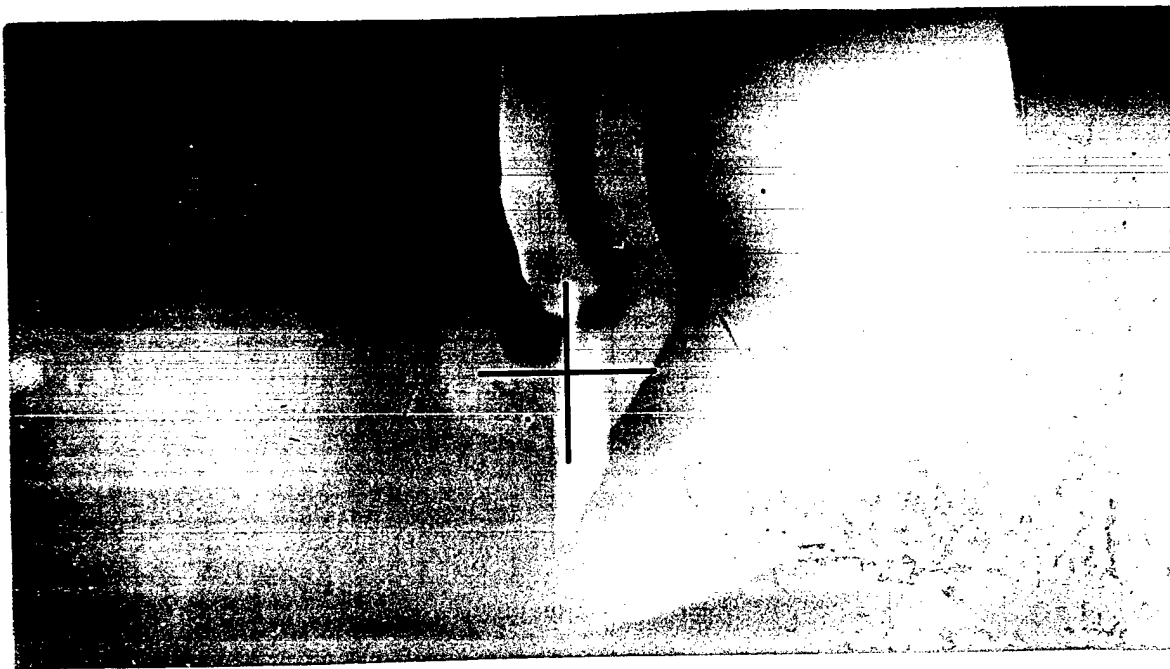
Generator N1

Test N14

$$\alpha = 10^\circ$$

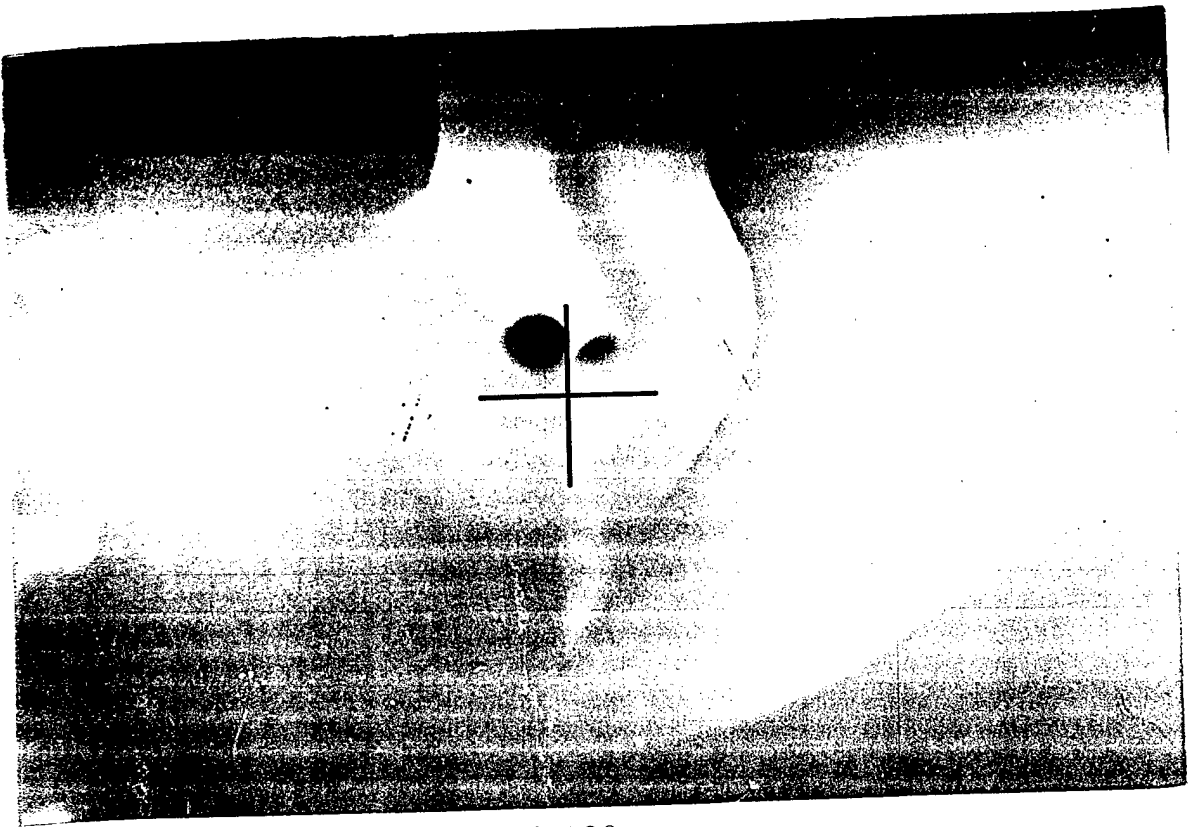


X=20 mm

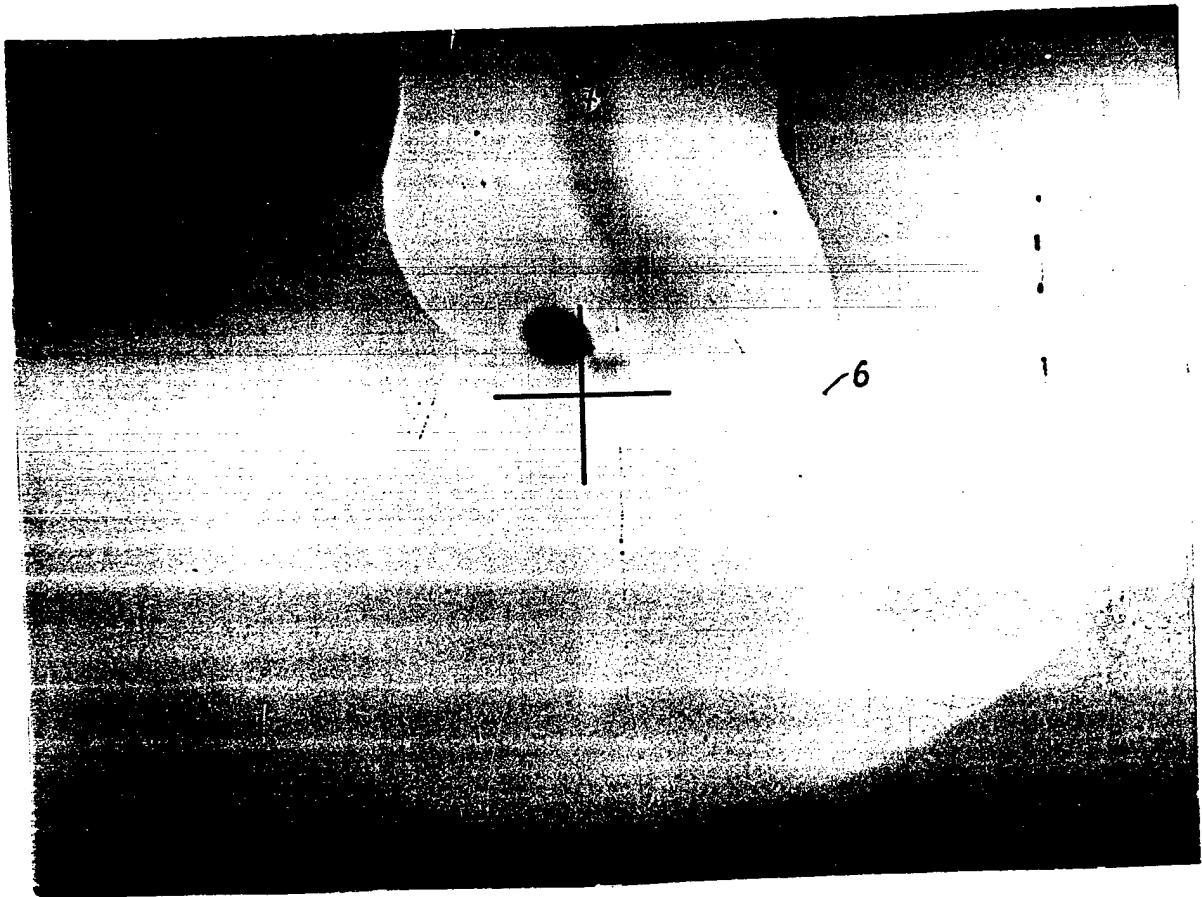


X=60 mm

Fig. 13a



X=100 mm



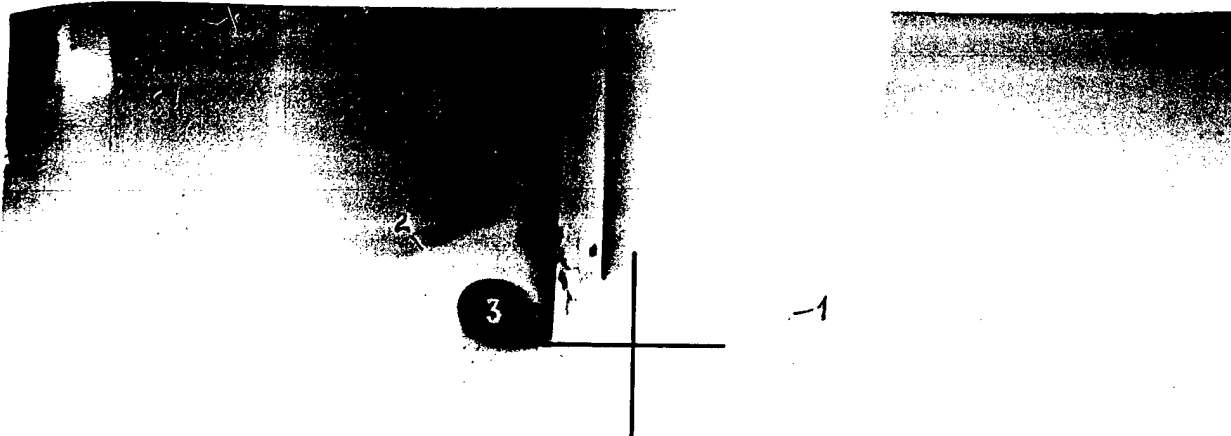
X=135 mm

Fig. 13b

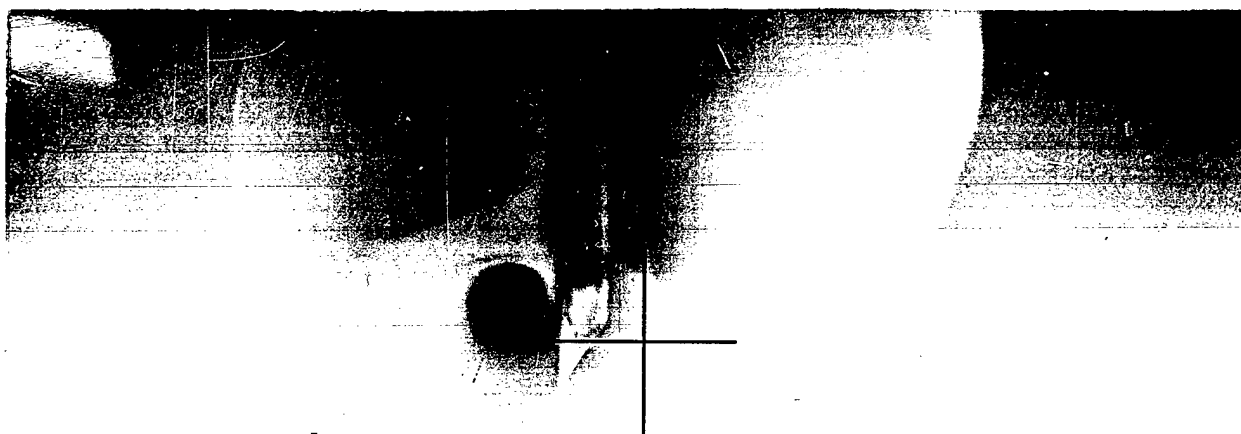
Generator N1

Test N15

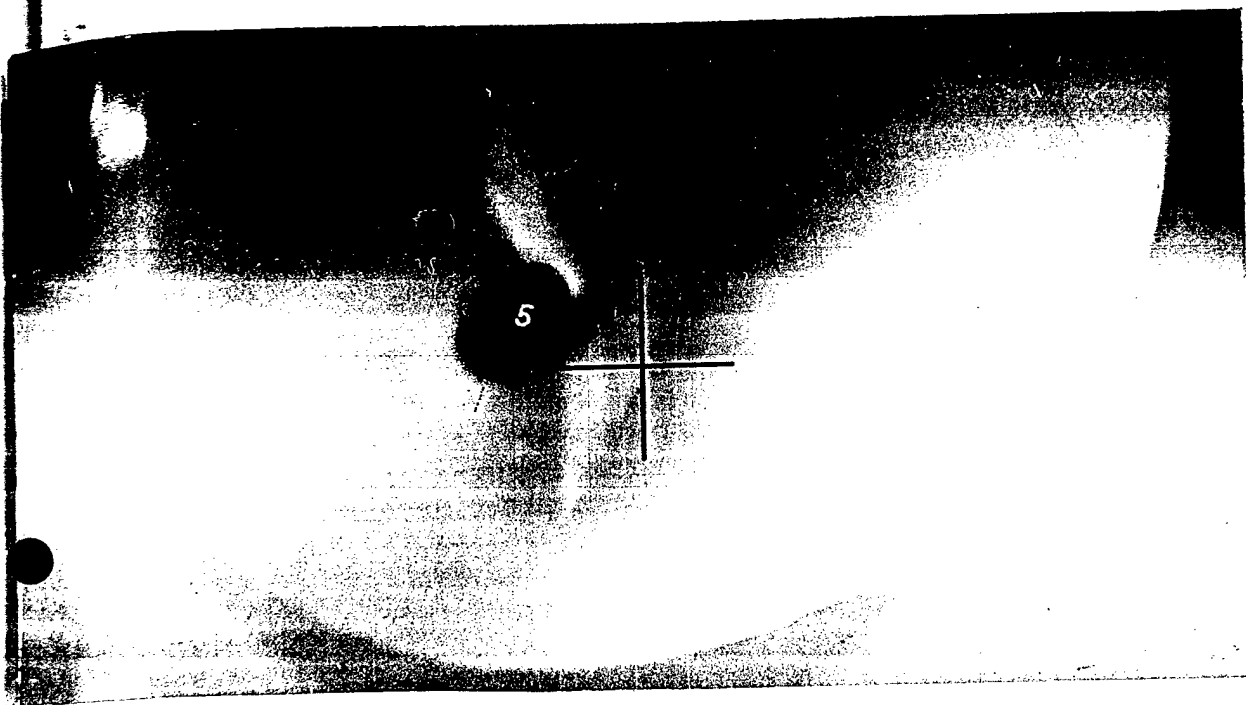
$$\alpha = 20^\circ$$



$X = 2$  mm



$X = 20$  mm



X=60 mm



X=100 mm

Fig. 14b

Generator N1

$$\alpha = 20^\circ$$

X = 2 mm

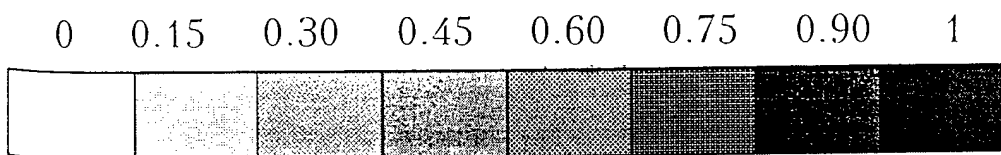
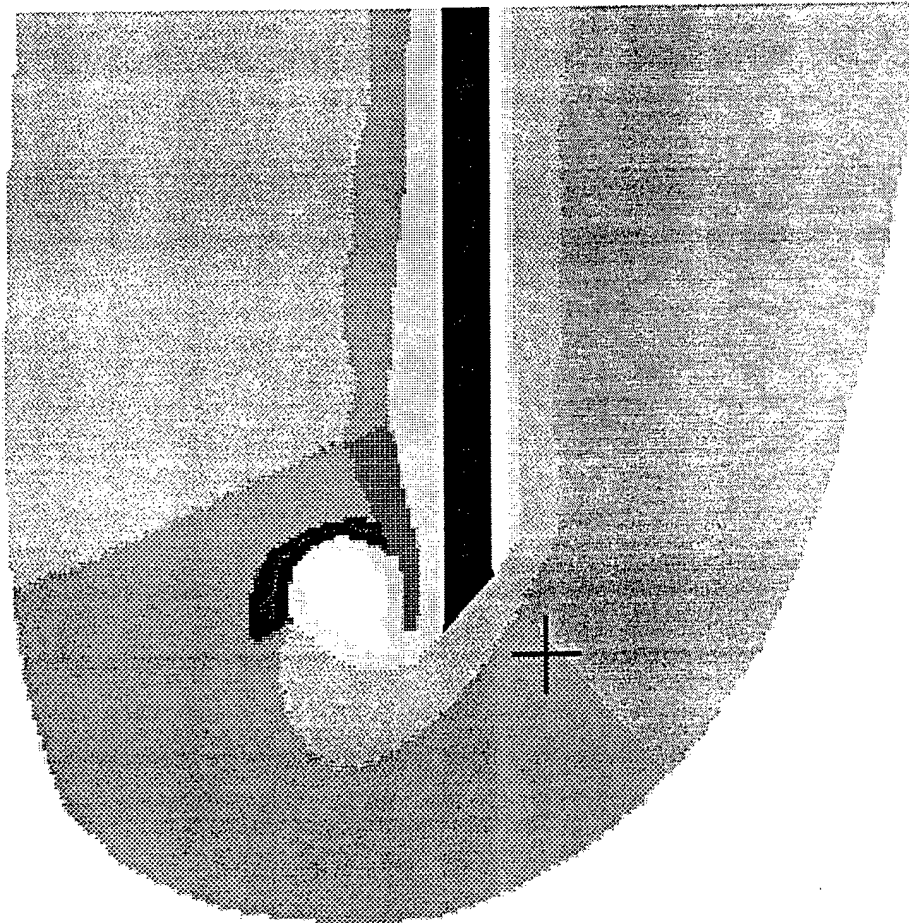


Fig. 15a

$X=20\text{mm}$

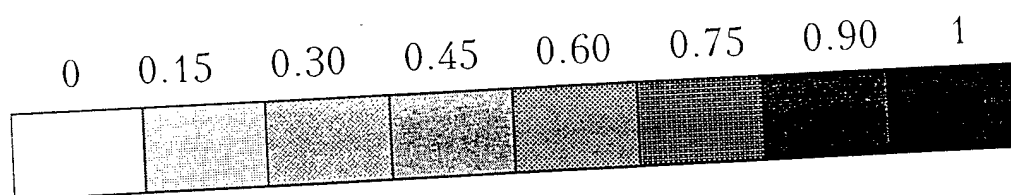
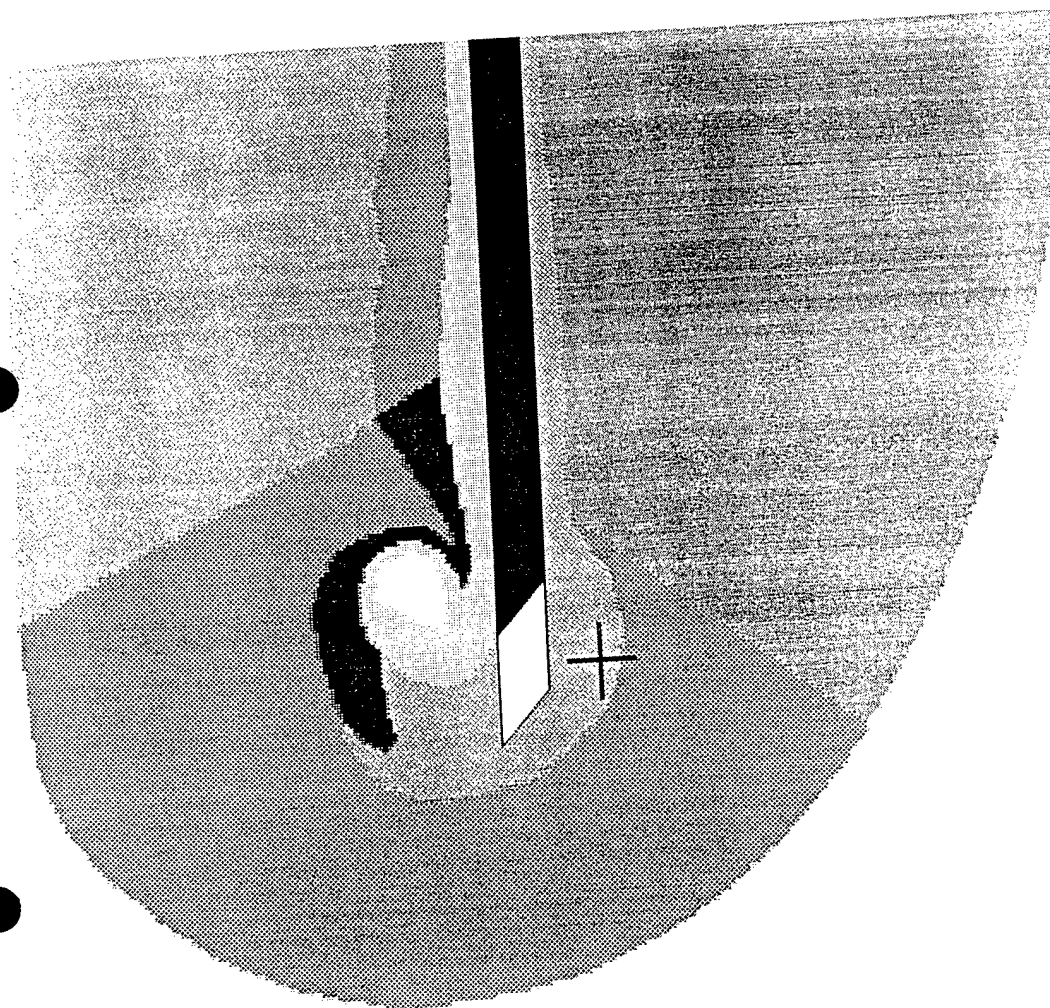


Fig. 15b

X=60mm

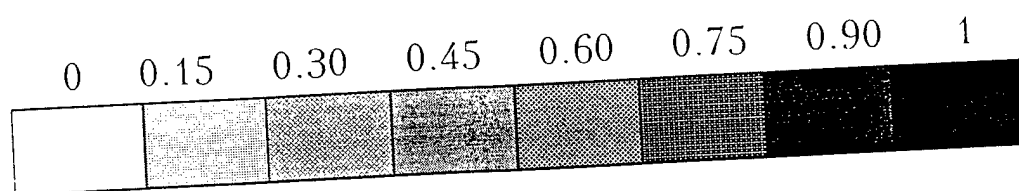
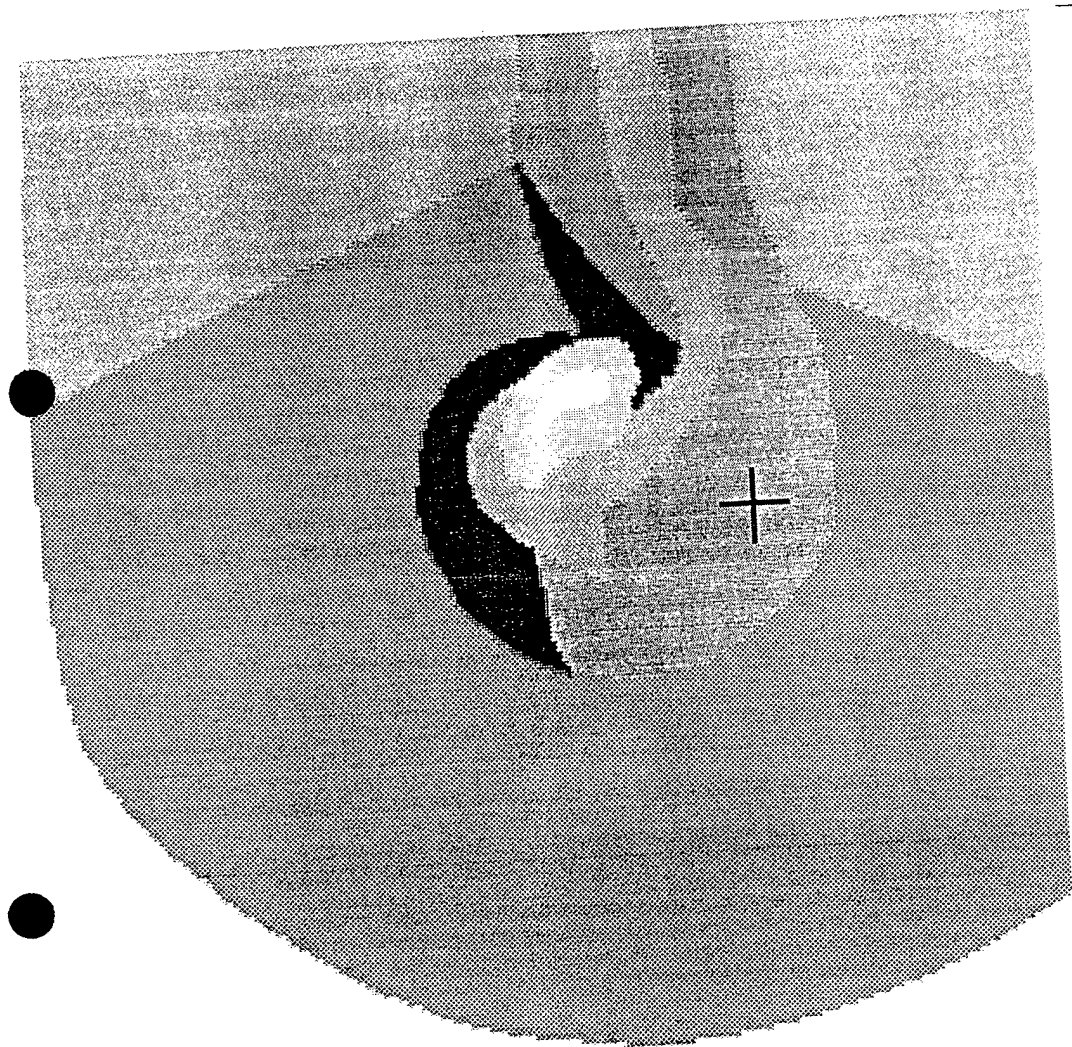


Fig. 15c

$X=100\text{mm}$

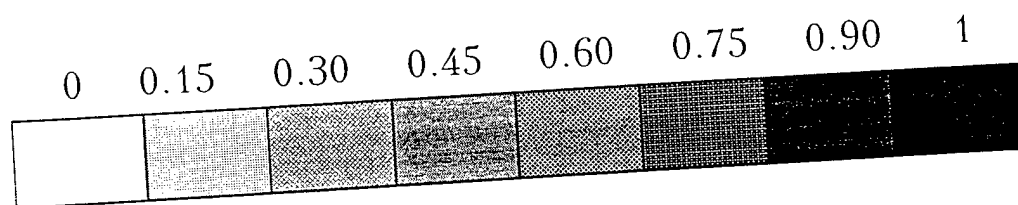
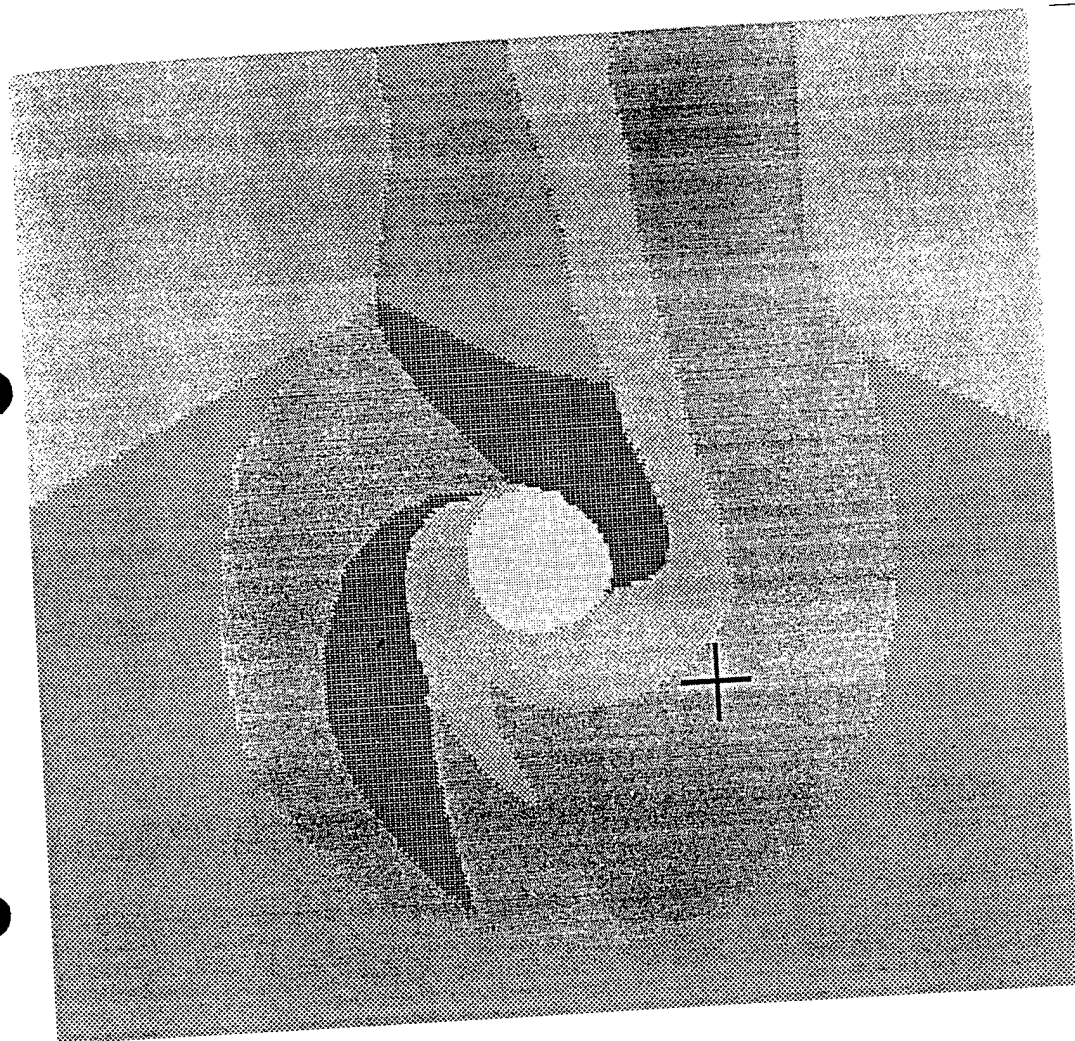
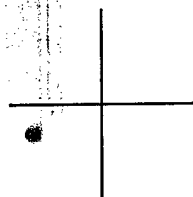


Fig. 15d

Generator N2

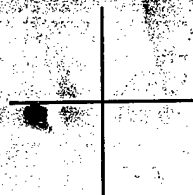
$$\alpha = 10^\circ$$



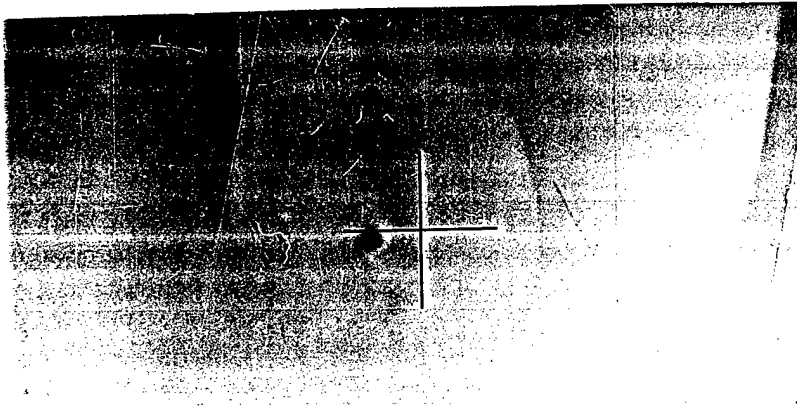
X=2 mm



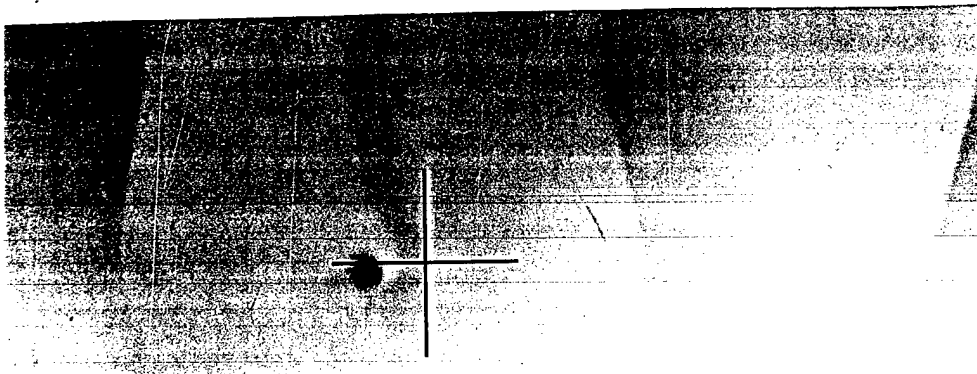
X=20 mm



X=60 mm



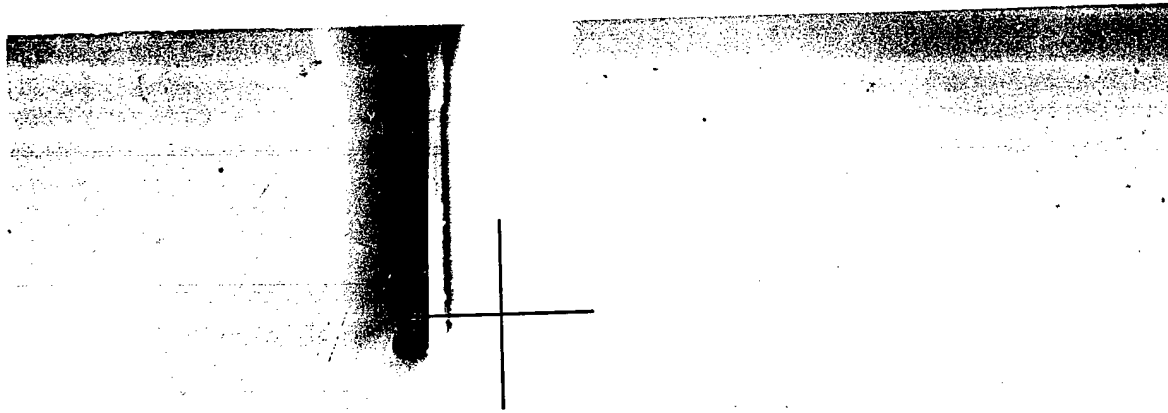
X=100 mm



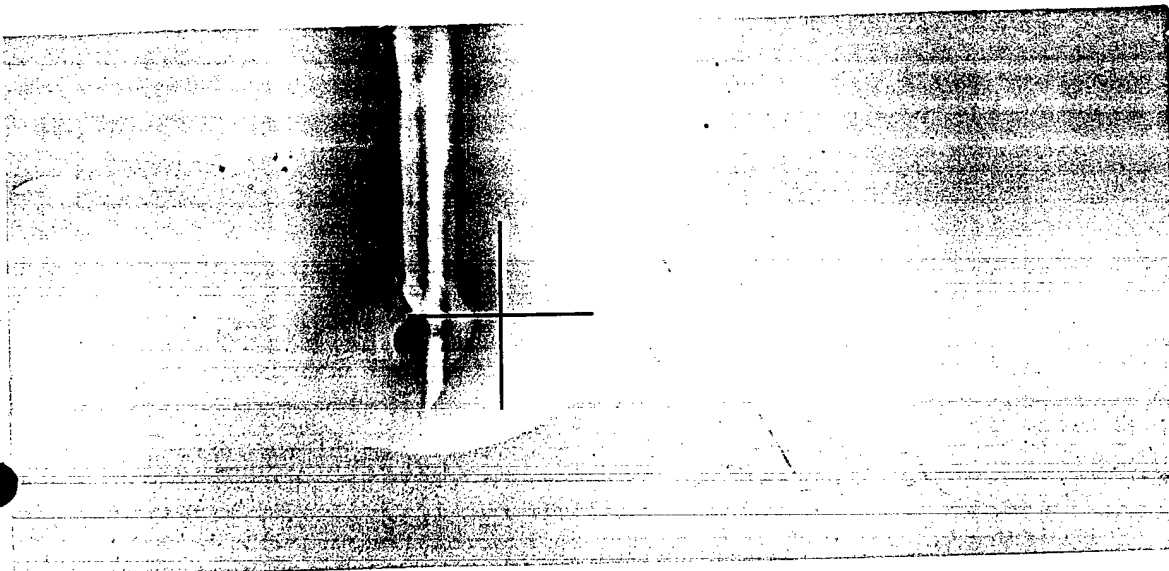
X=135 mm

Fig. 16b

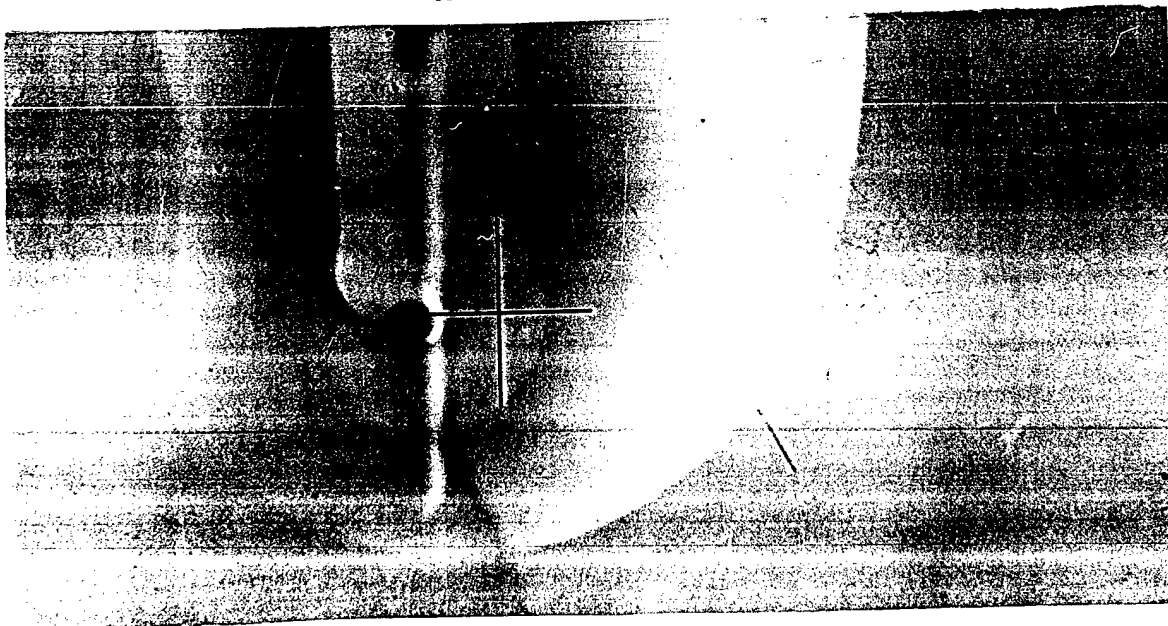
$$\alpha = 20^\circ$$



X=2 mm

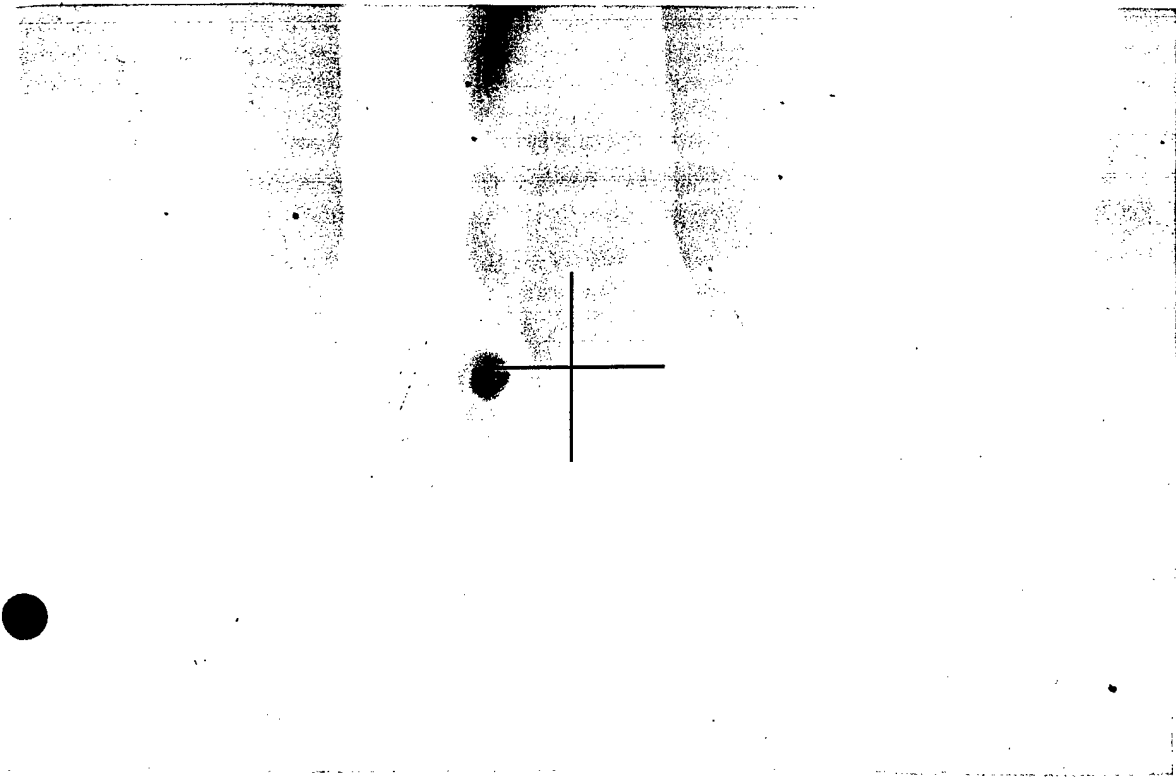


X=20 mm



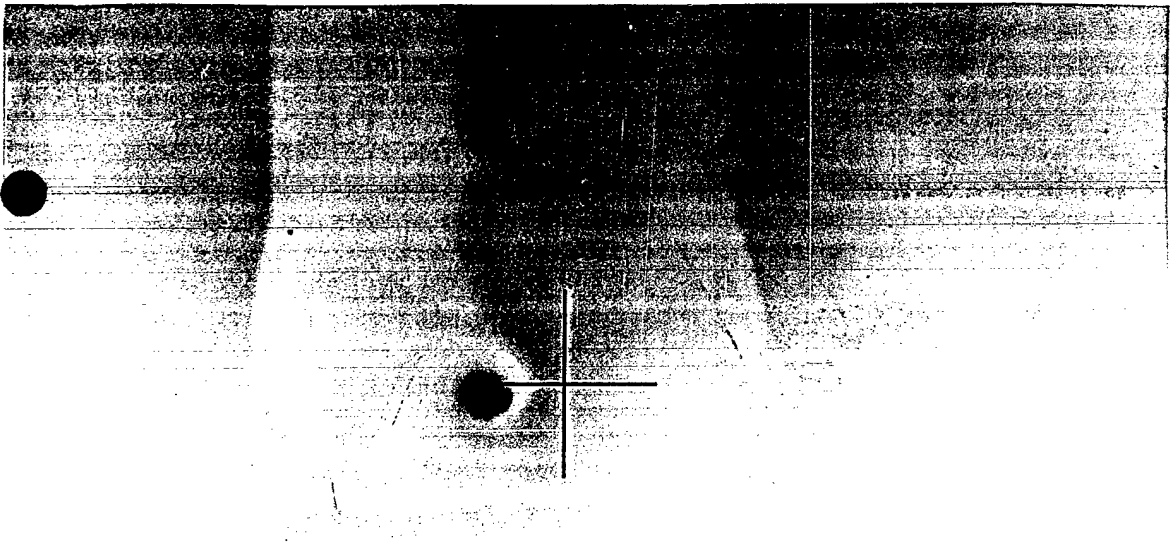
X=60 mm

Fig. 17a



A black and white micrograph showing a textured surface. A small, dark, circular feature is located in the lower-left quadrant. A black crosshair is drawn over this feature, with the vertical line extending above and below it, and the horizontal line extending to the left and right. The background is a light gray with some darker, irregular patches.

X=100 mm

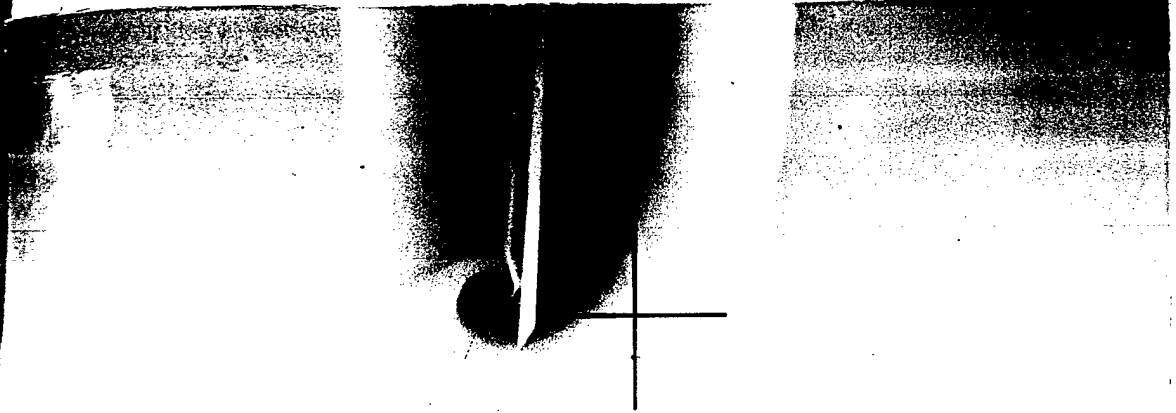


A black and white micrograph showing a textured surface, similar to the one above. A small, dark, circular feature is located in the lower-left quadrant. A black crosshair is drawn over this feature, with the vertical line extending above and below it, and the horizontal line extending to the left and right. The background is a light gray with some darker, irregular patches.

X=135 mm

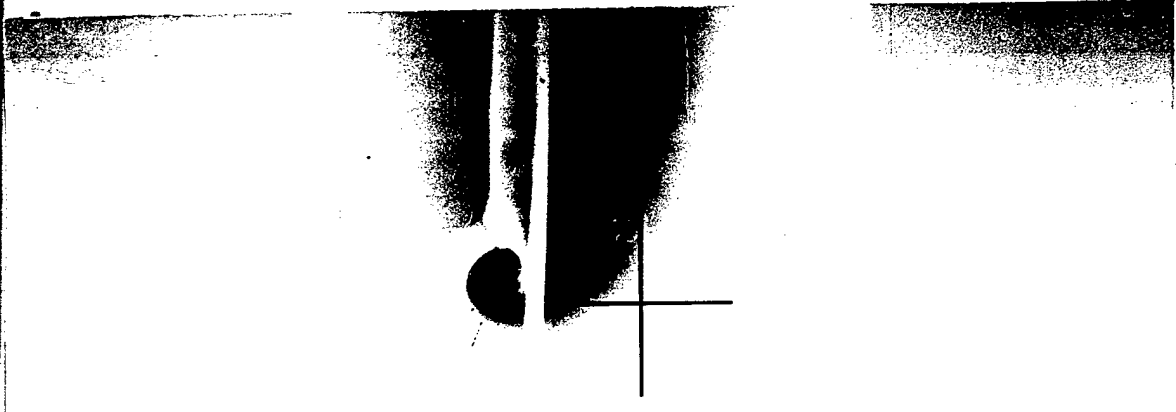
Fig. 17b

$\alpha=30^\circ$



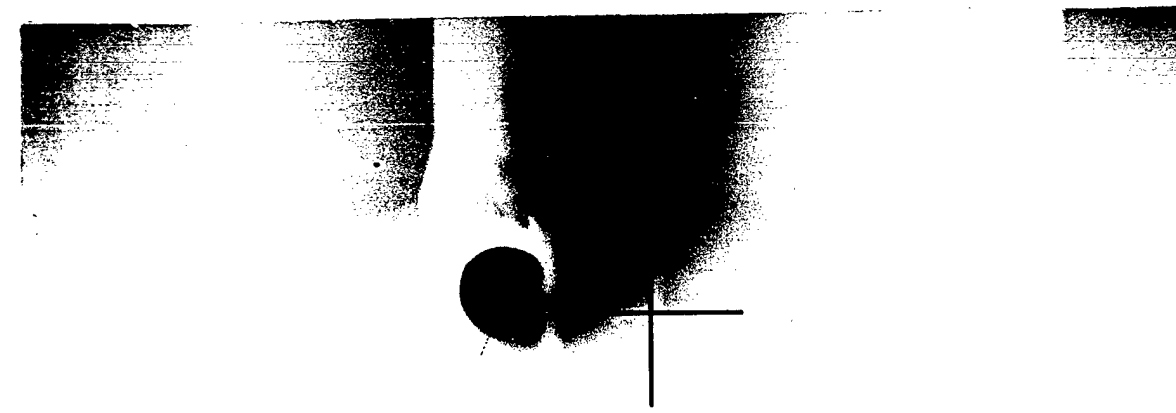
X=7 mm

A high-contrast micrograph showing a dark, V-shaped crack opening. A horizontal crosshair line is positioned just above the crack tip. The background is light and grainy.



X=20 mm

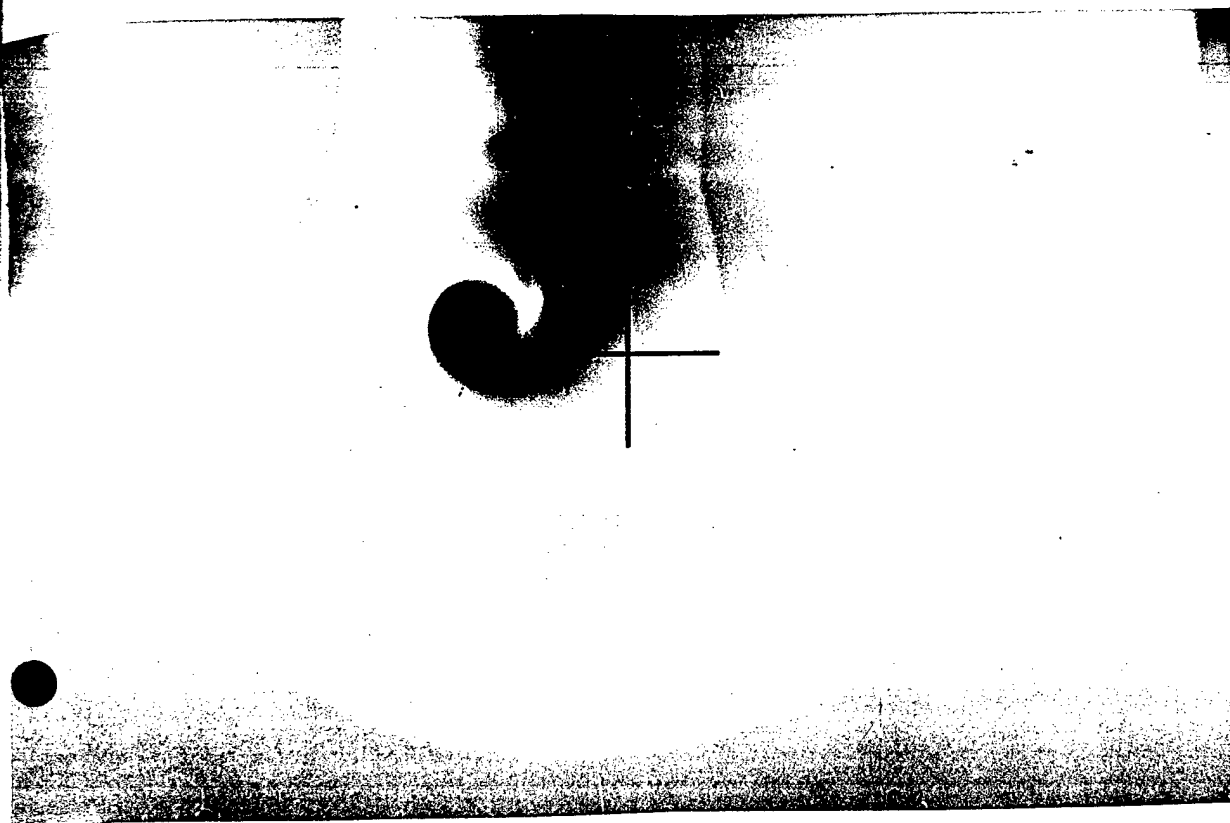
A high-contrast micrograph showing a dark, V-shaped crack opening. A horizontal crosshair line is positioned just above the crack tip. The background is light and grainy.



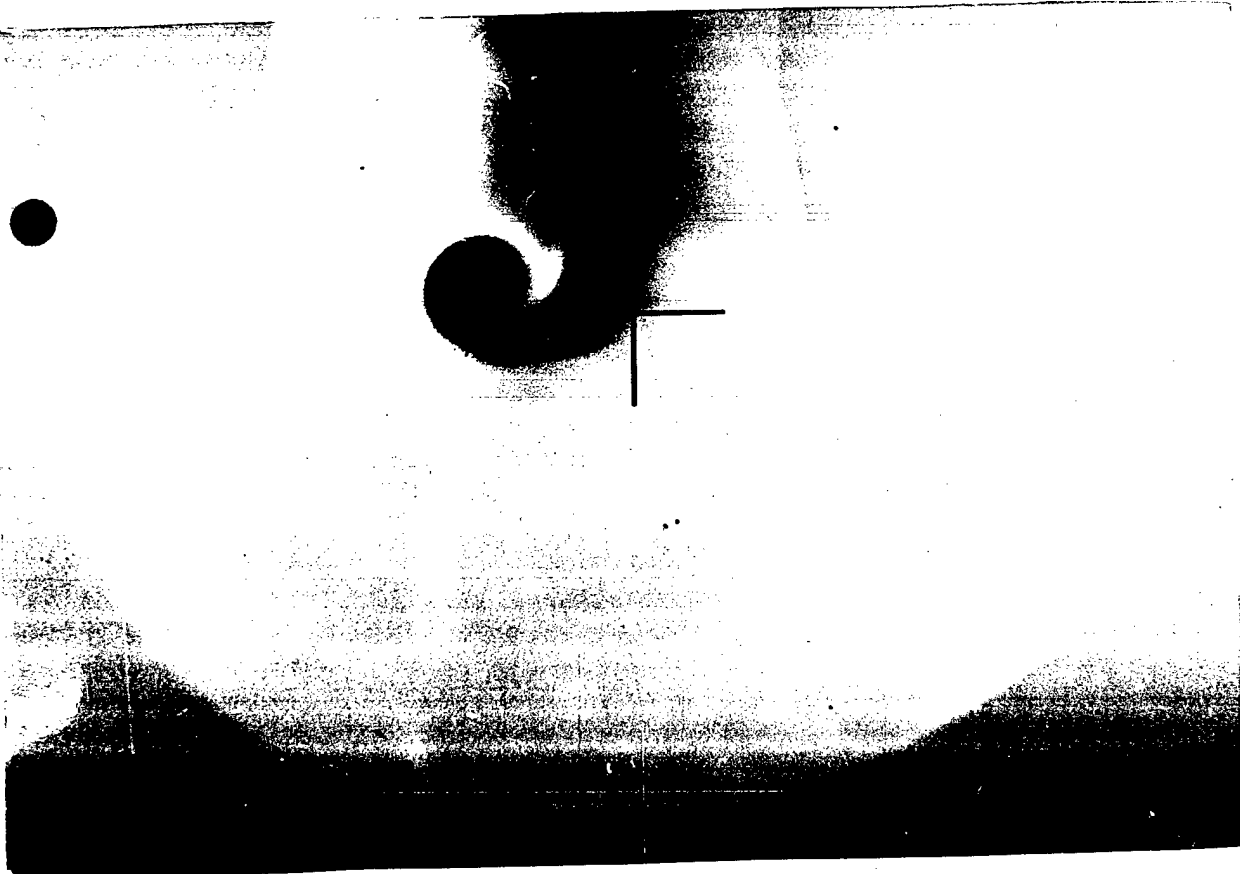
X=60 mm

A high-contrast micrograph showing a dark, V-shaped crack opening. A horizontal crosshair line is positioned just above the crack tip. The background is light and grainy.

Fig. 18a



X=100 mm



X=135 mm

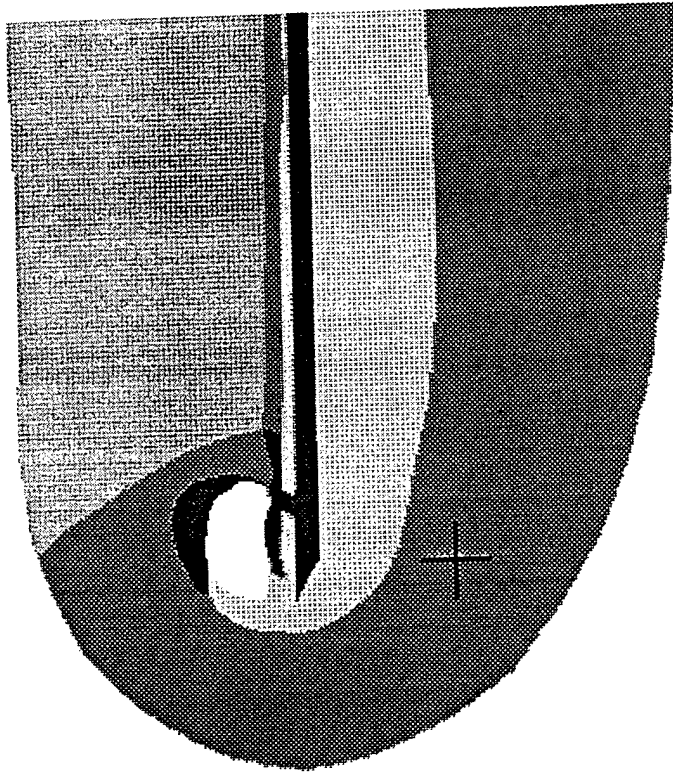
Fig. 18b

Generatr N2

Test N18

$\alpha = 30^\circ$

X=7mm



0 0.15 0.30 0.45 0.60 0.75 0.90 1

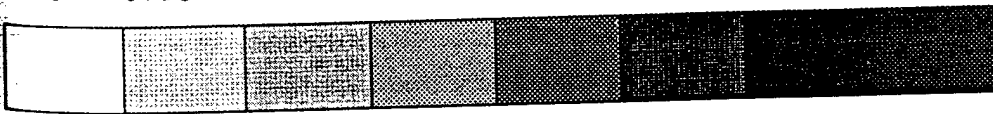


Fig. 19a

X=20mm

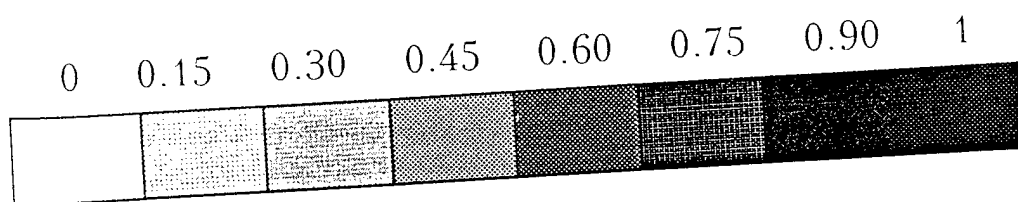
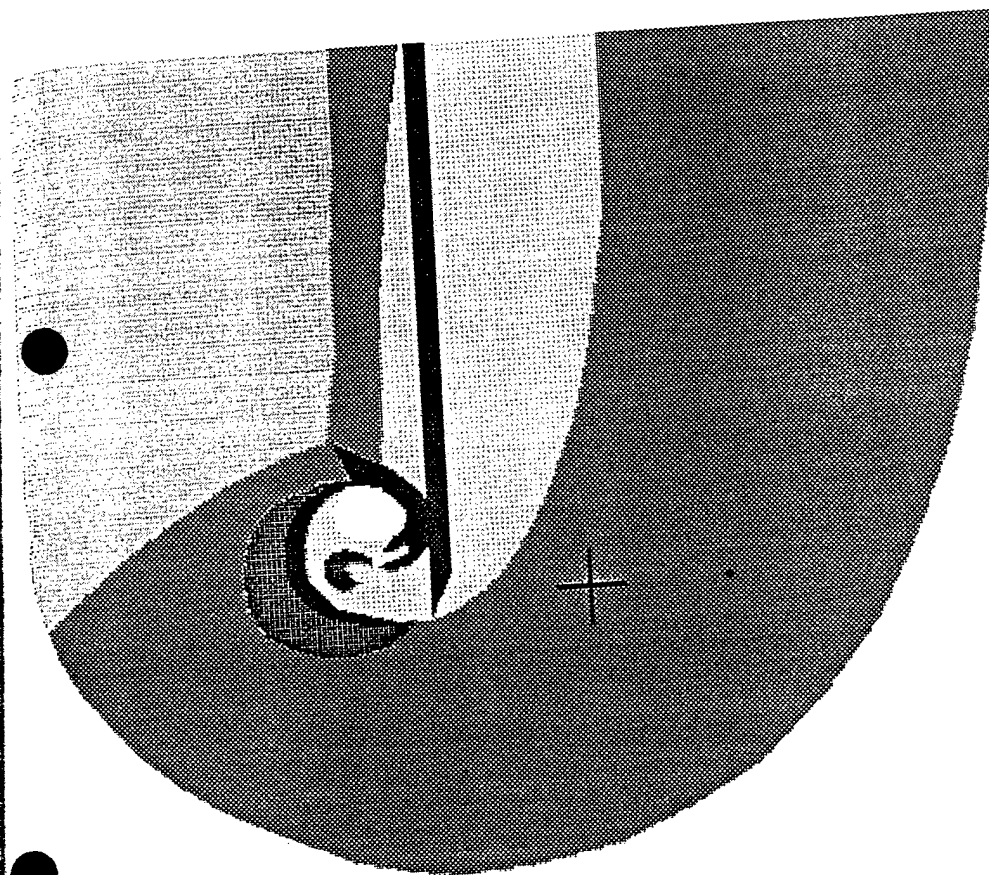


Fig. 19b

X=60mm

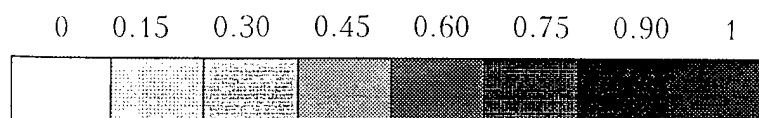
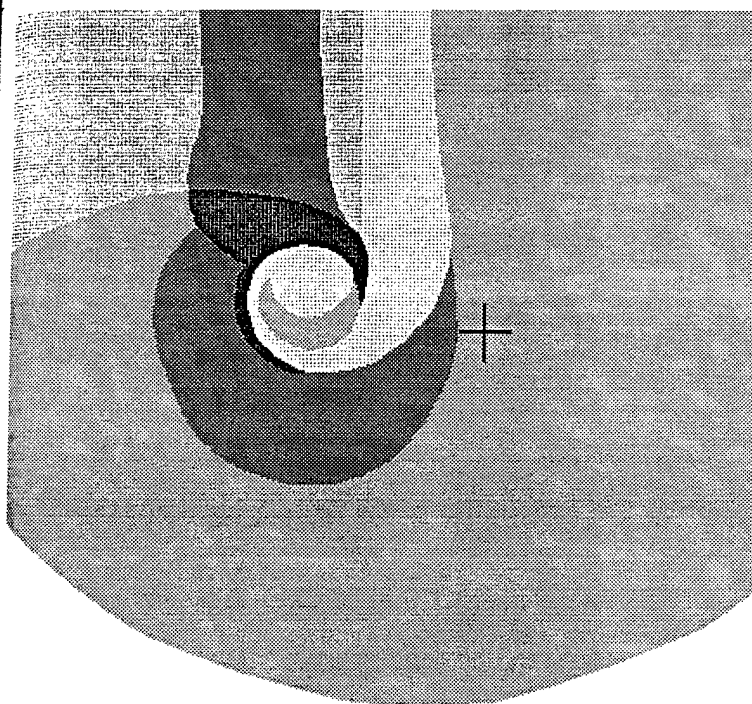


Fig. 19c

X=100mm

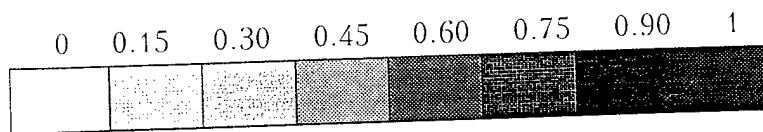
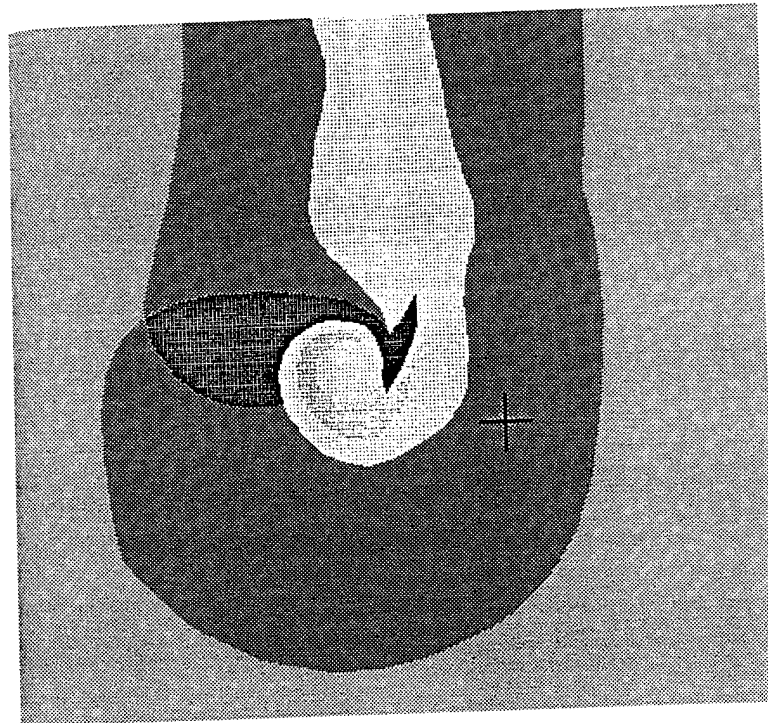


Fig. 19d

X=135mm

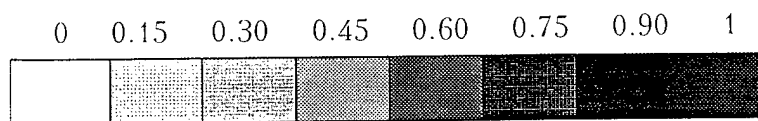
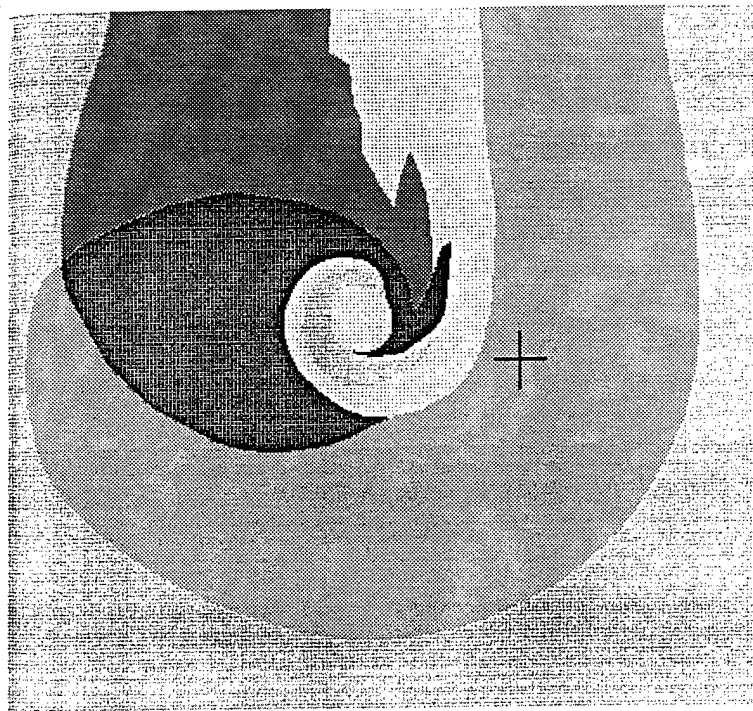
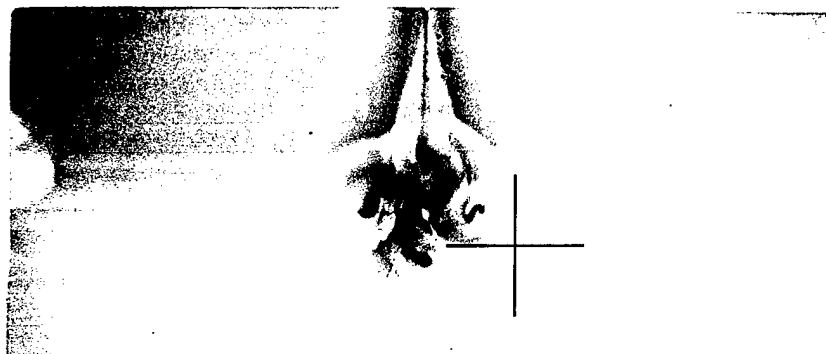


Fig. 19c

Generator N3

Test N17

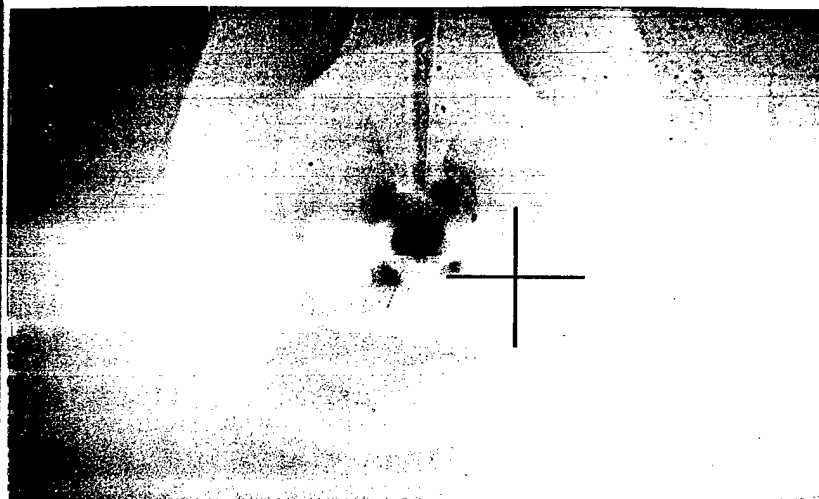
$\alpha=30^\circ$



X=20 mm

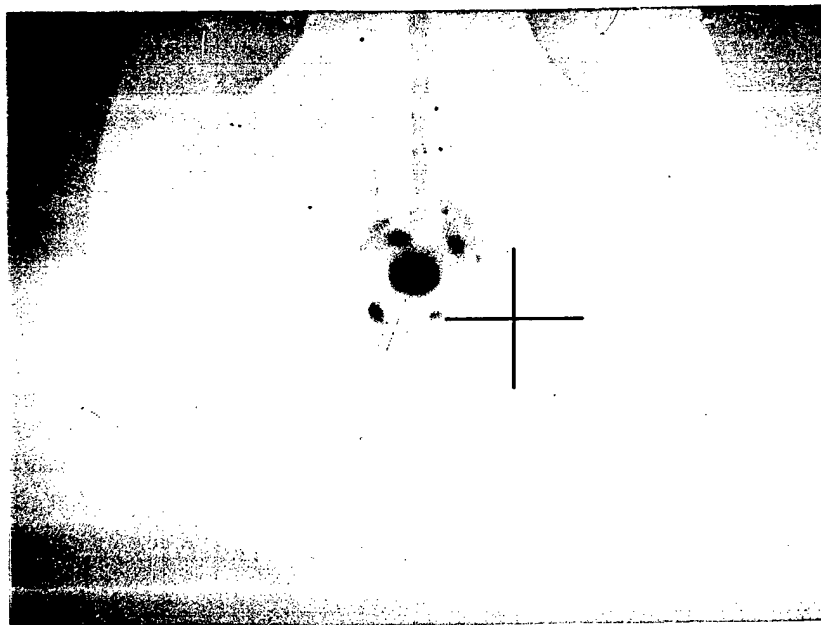


X=60 mm

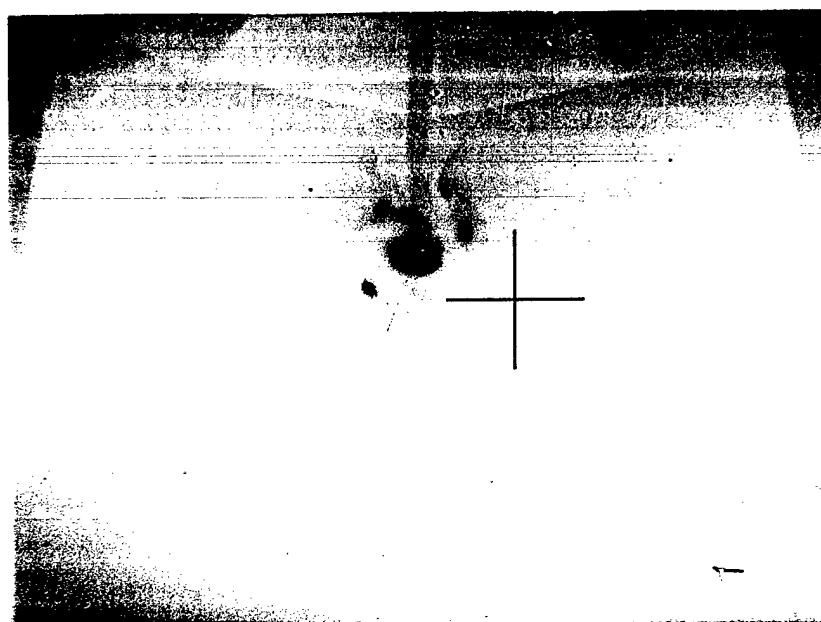


X=100 mm

Fig. 20a



X=135 mm



X=160 mm

Fig. 20b

Test N17

Generator N3

$\alpha=30^\circ$

X=20 mm

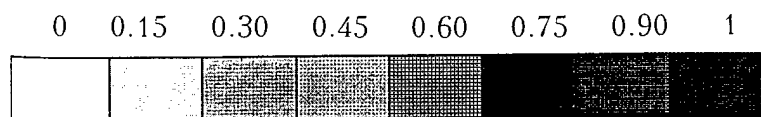
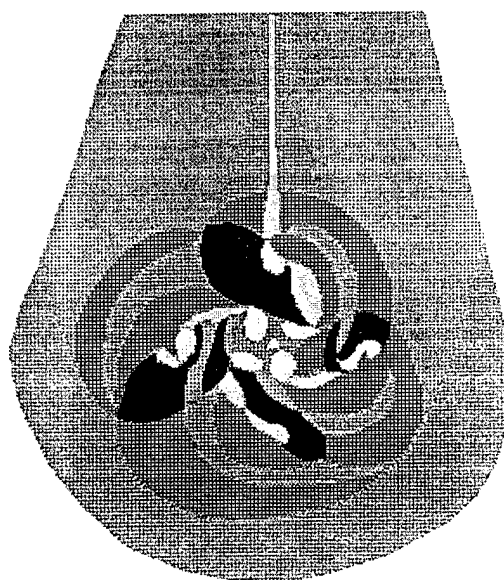


Fig. 21a

X=60 mm

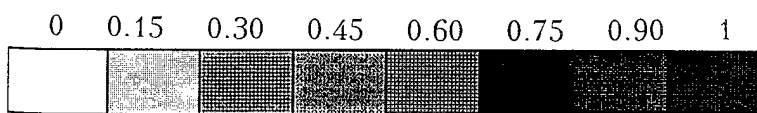
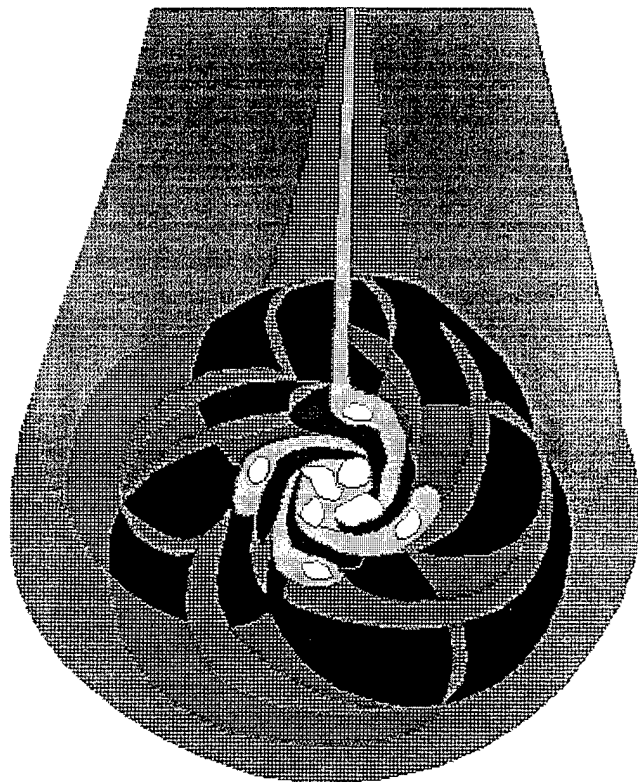


Fig. 21b

X=135mm

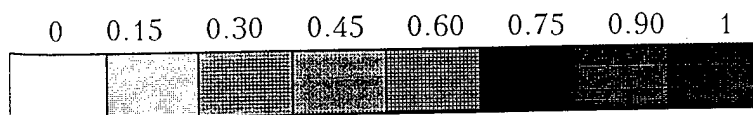
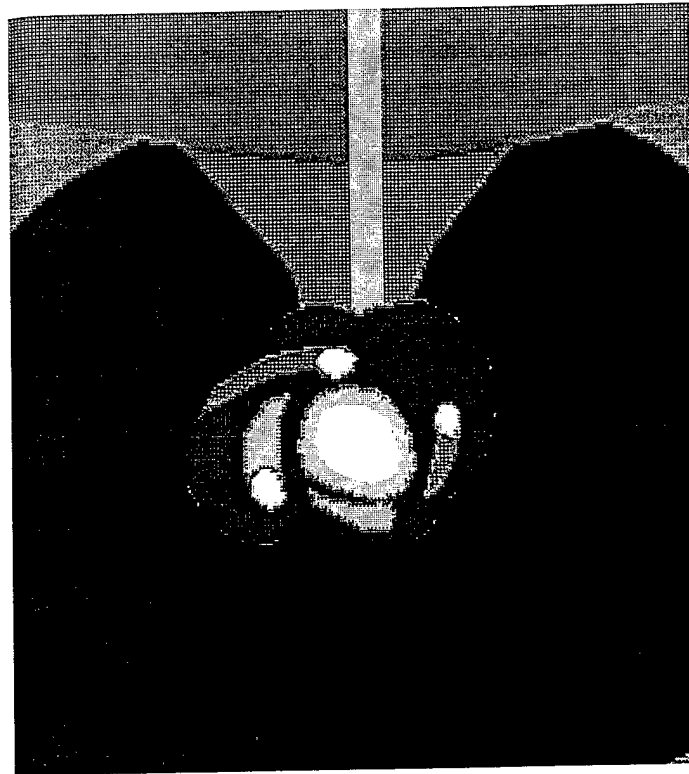


Fig. 21c

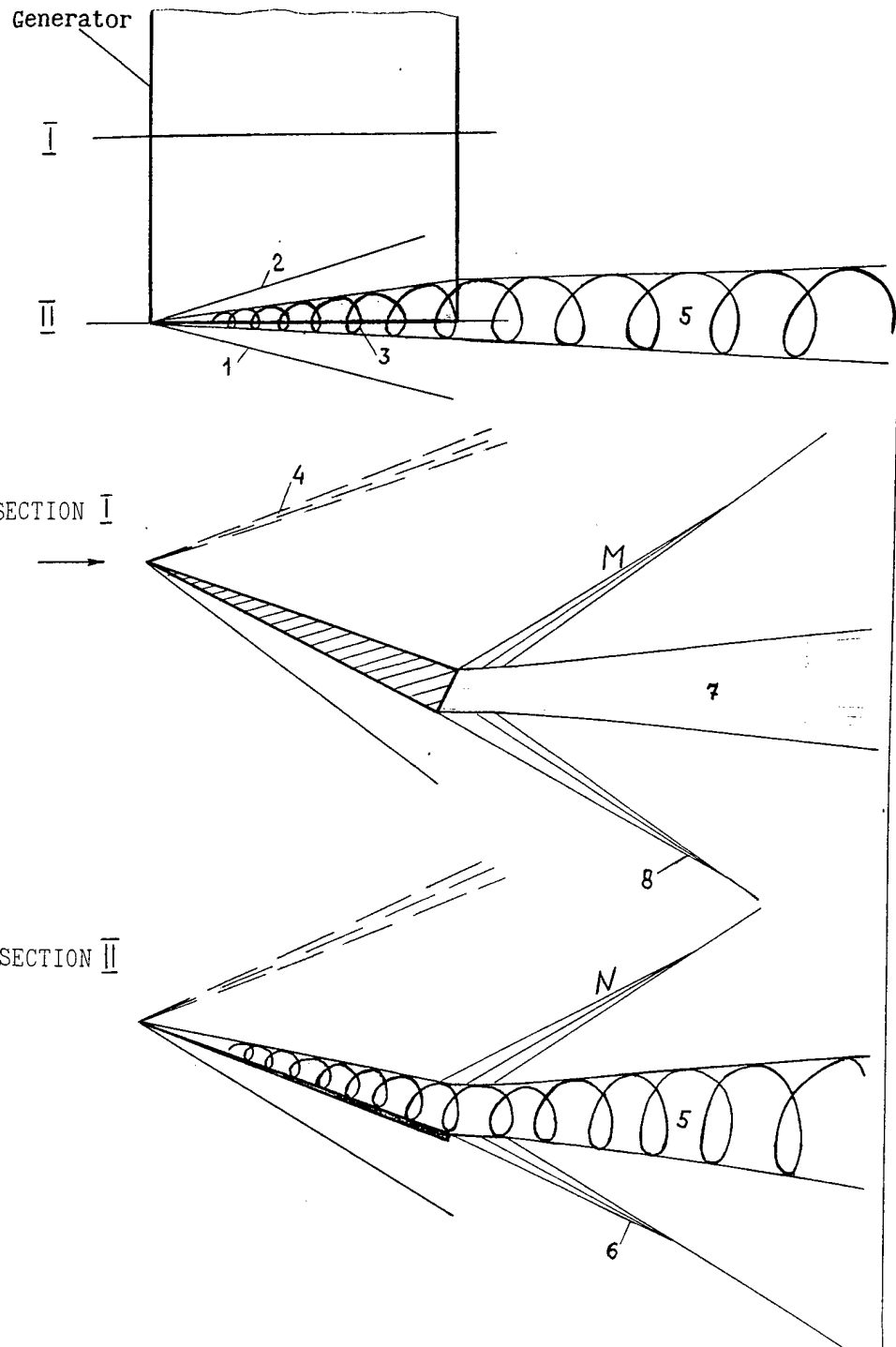


Fig. 22

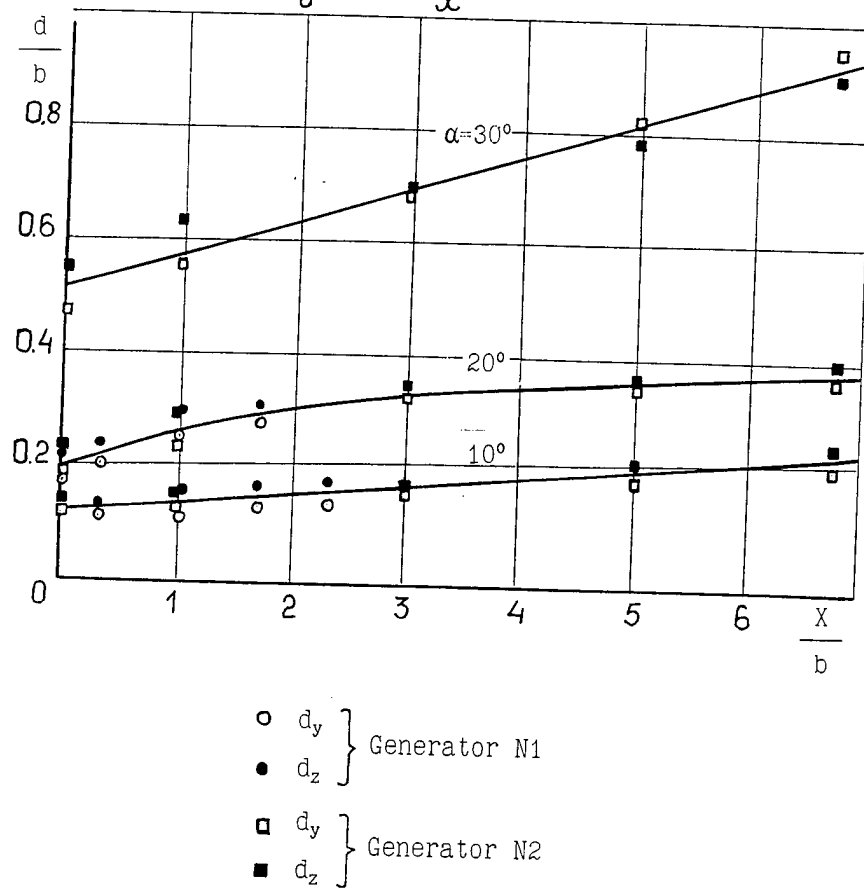
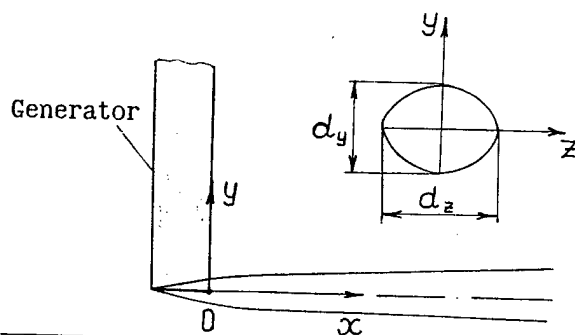
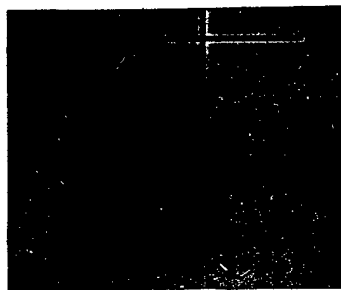


Fig. 23

Test N15

Generator N1

$\alpha = 20^\circ$



X=100 mm



X=60 mm



X=20 mm



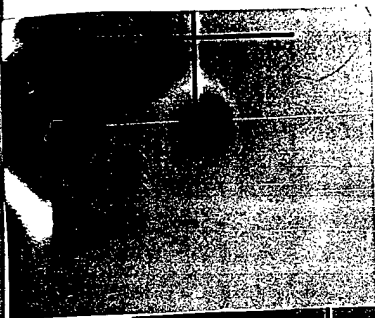
X=2 mm

Fig. 24a

Test N24

Generator N2

$\alpha = 20^\circ$



X=135 mm



X=100 mm



X=60 mm



X=20 mm



X=2 mm

Fig. 24b

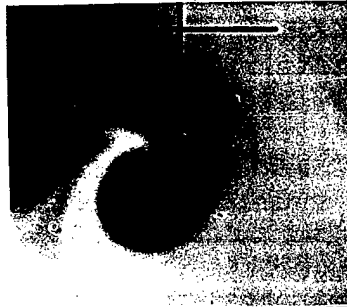
Test N18

Generator N2

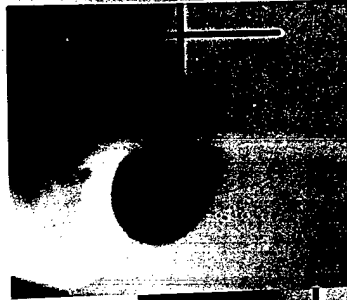
$\alpha = 30^\circ$



X=135 mm



X=100 mm



X=60 mm



X=20 mm



X=7 mm

Fig. 24c

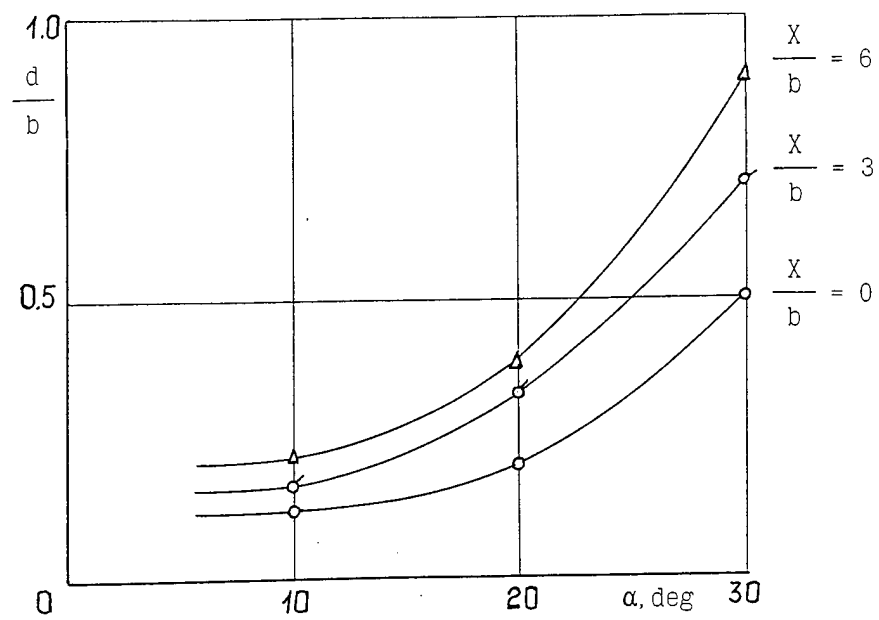


Fig. 25

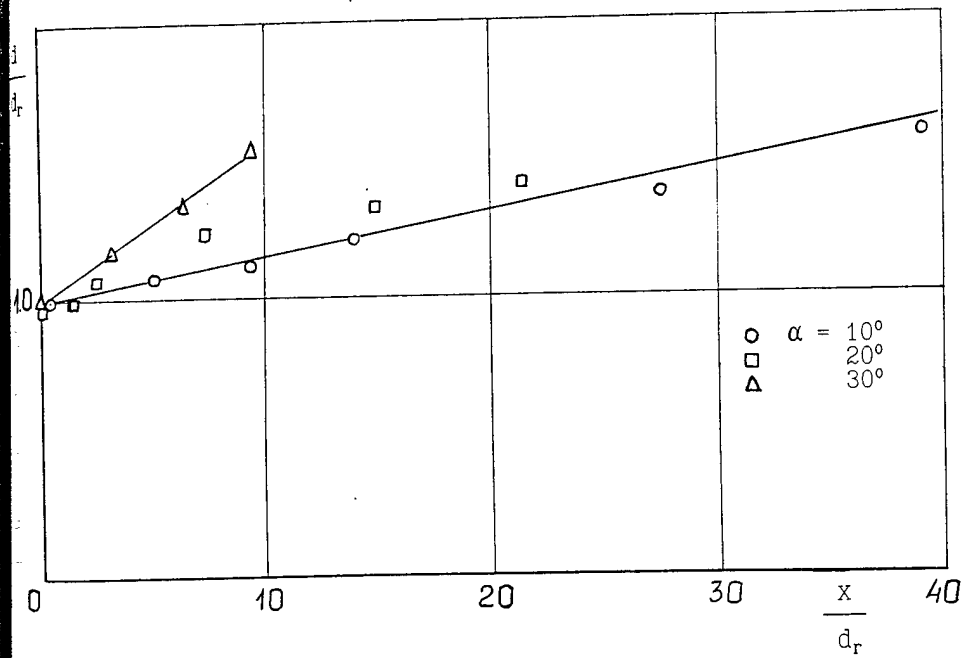
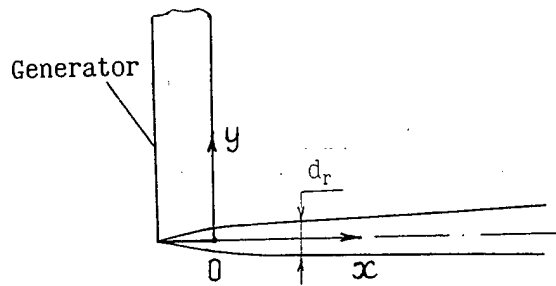


Fig. 26

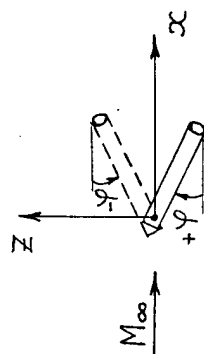
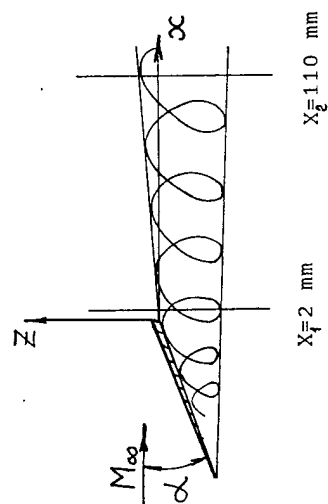
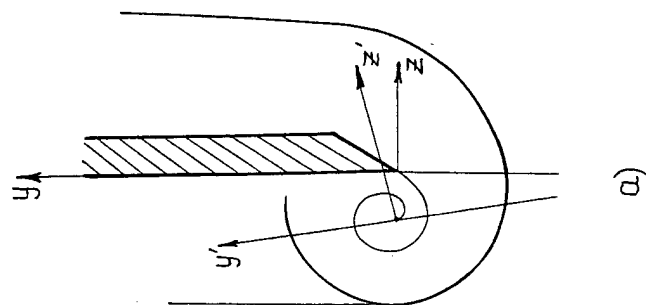


Fig. 27

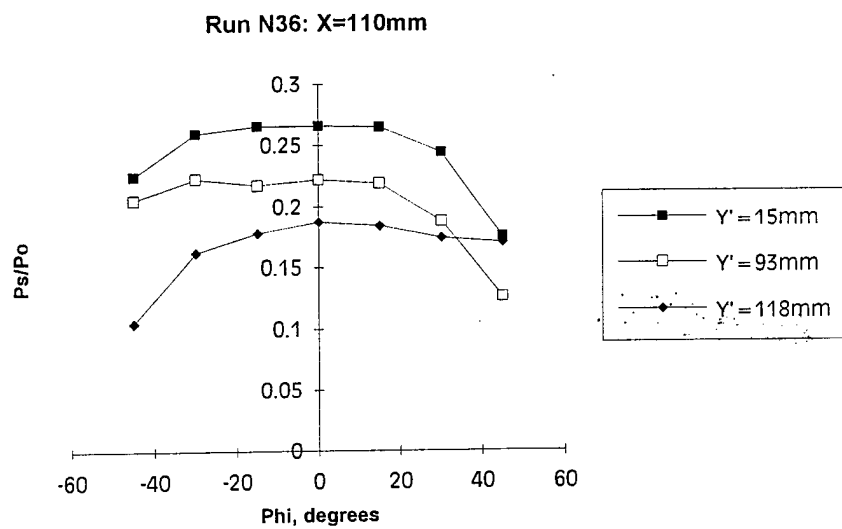
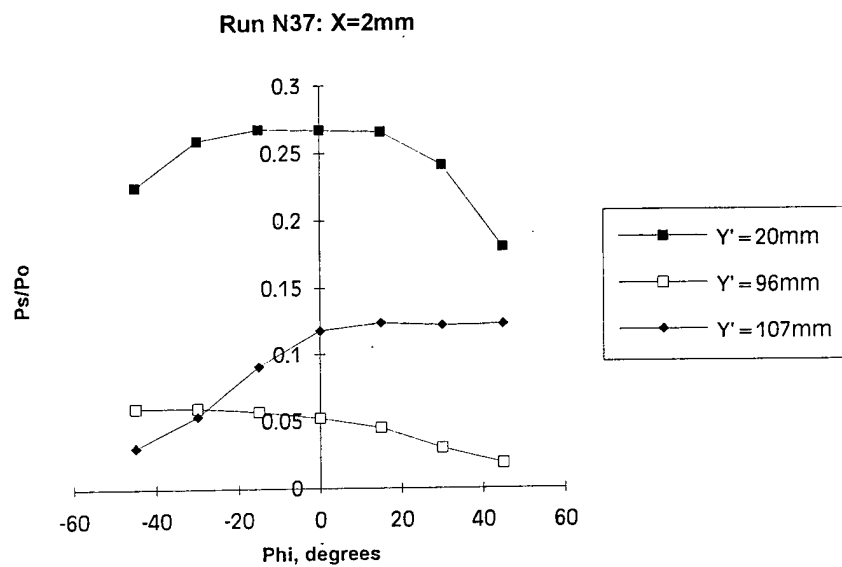
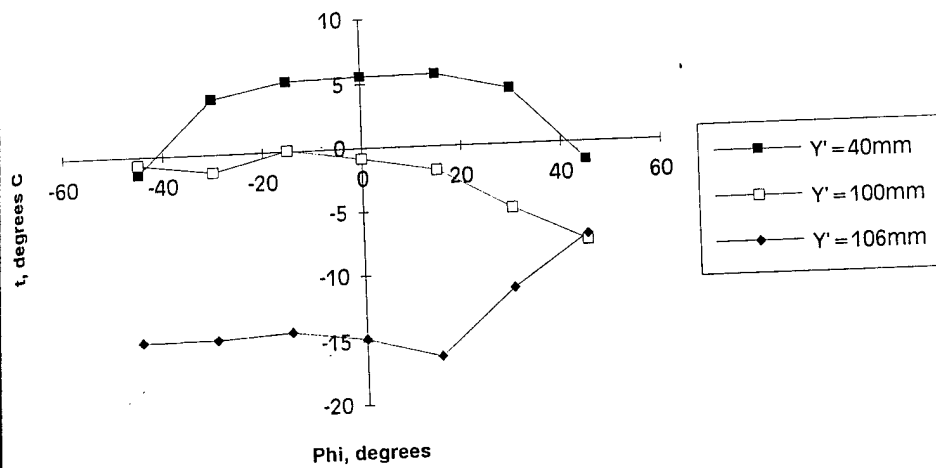


Fig. 28

Run N38: X=2mm



Run N41: X=110mm

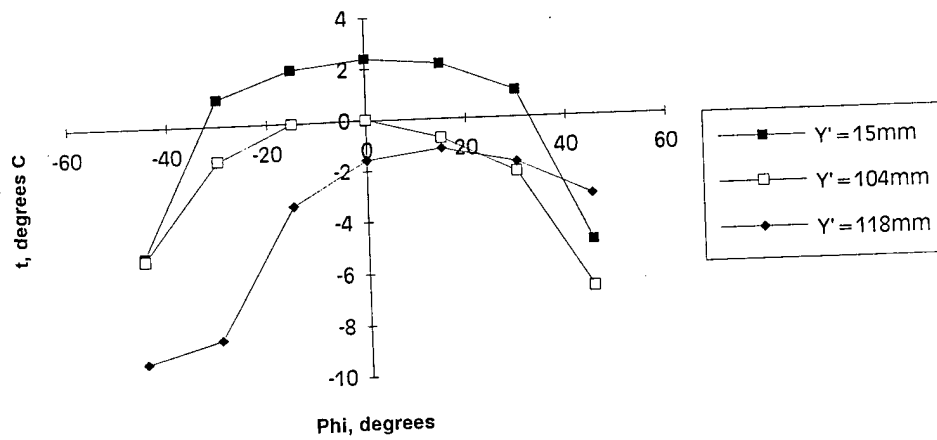


Fig. 29

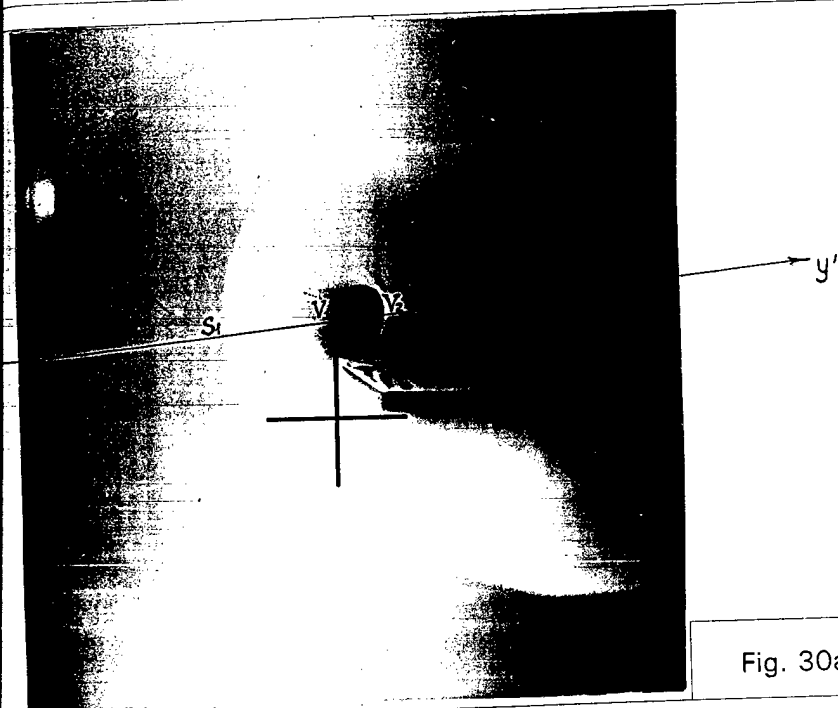
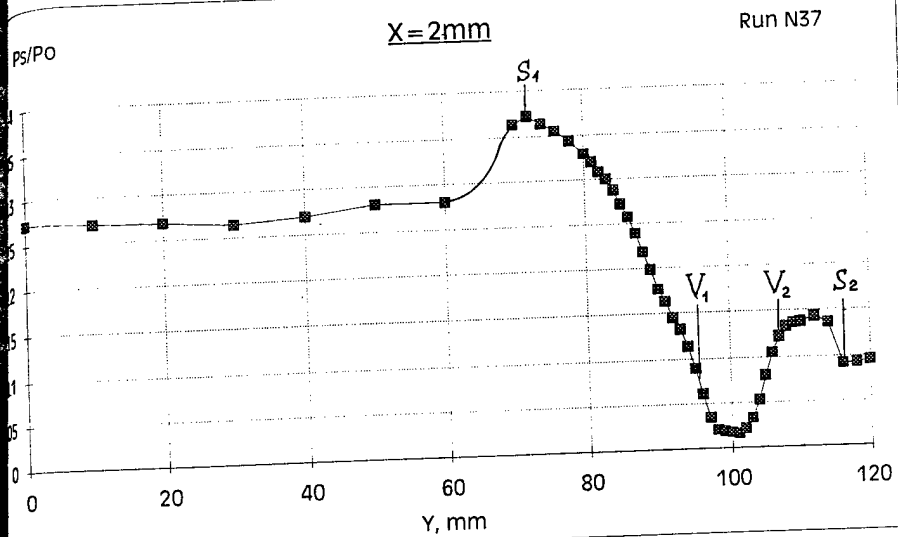
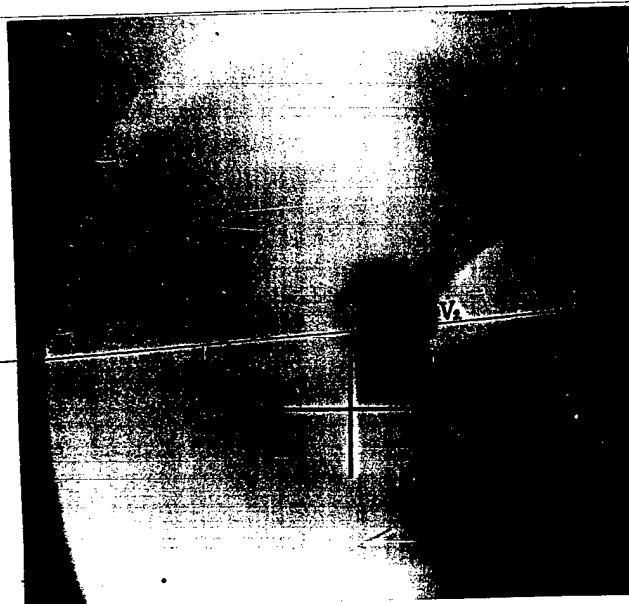
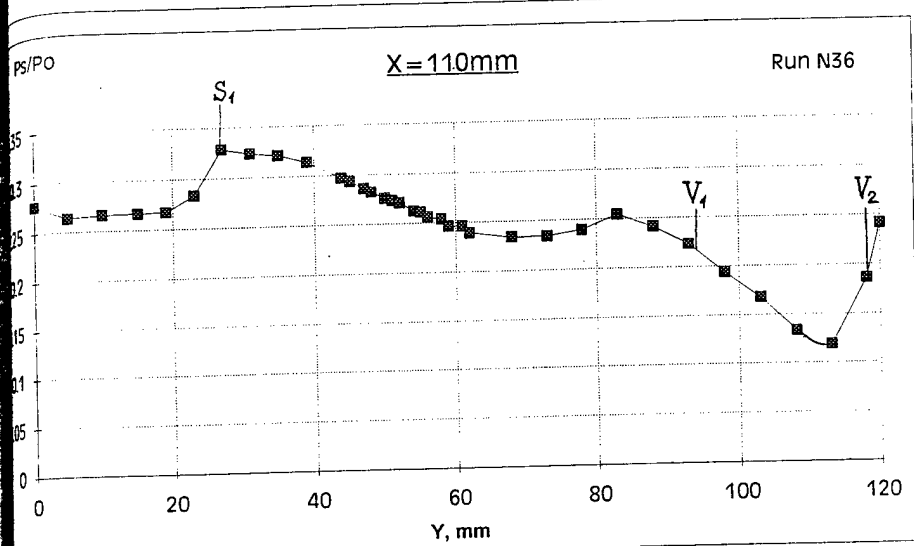


Fig. 30a



Stagnation pressure after generator N1  
 $\alpha = 20^\circ$

Fig. 30b

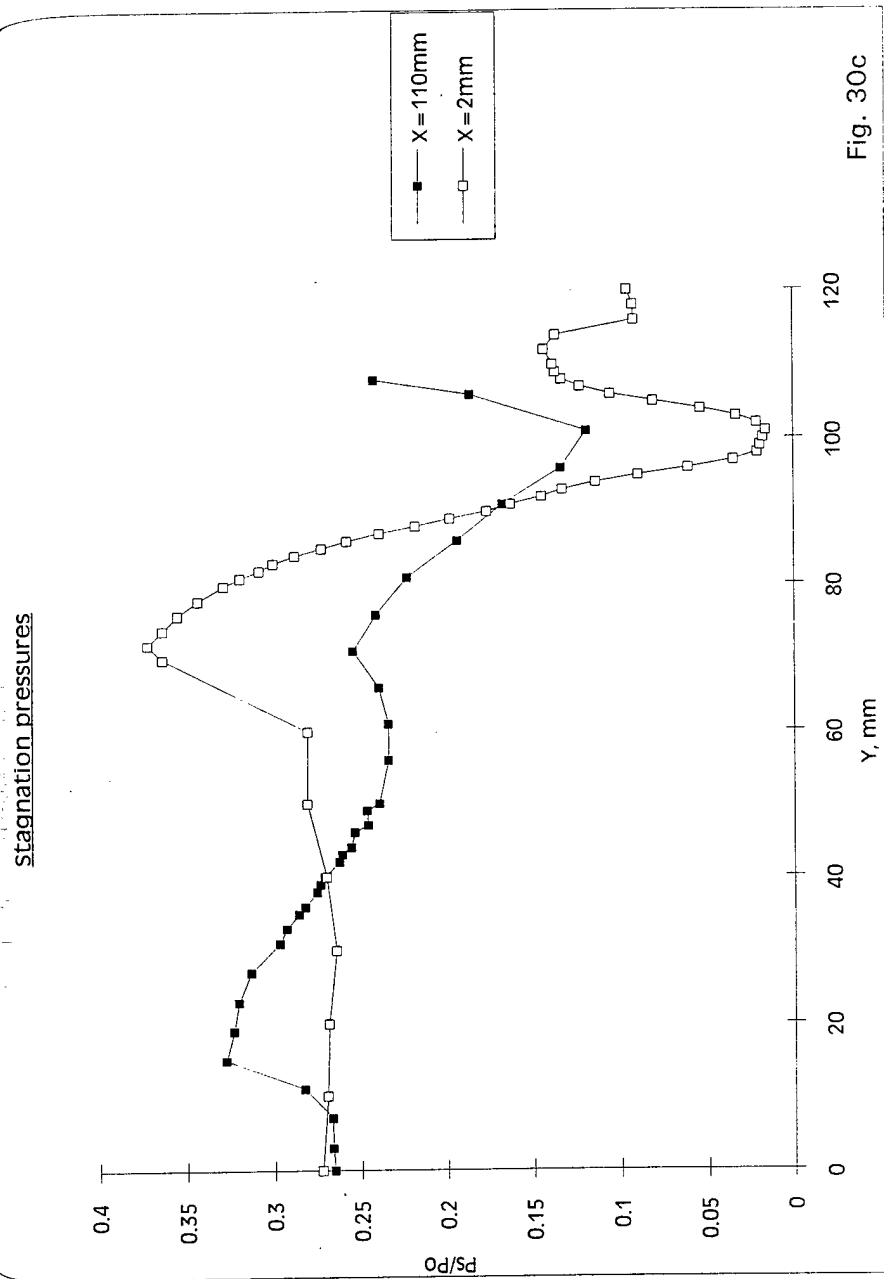
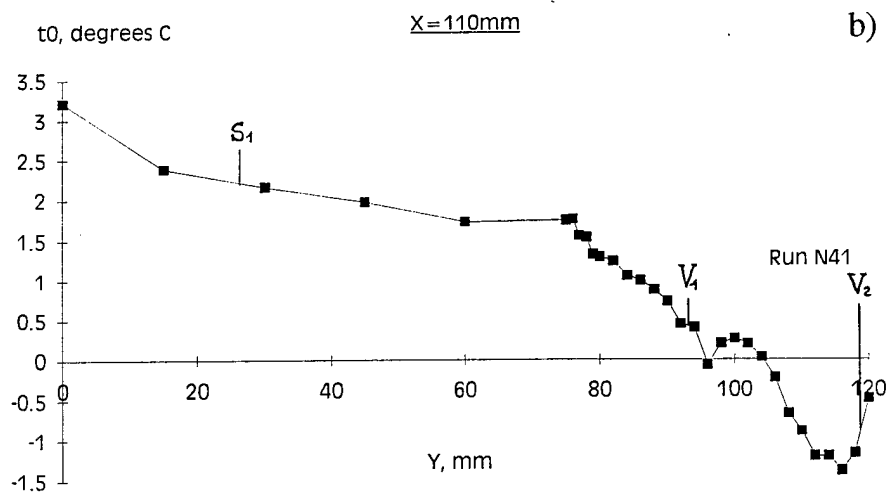
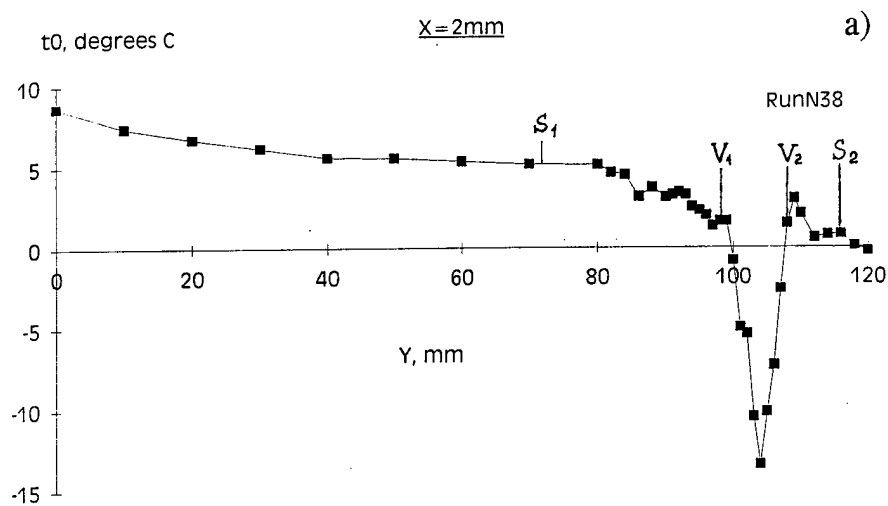


Fig. 30c



Stagnation temperature  
after generator N1,  
 $\alpha = 20^\circ$

Fig. 31

Run N38, 41

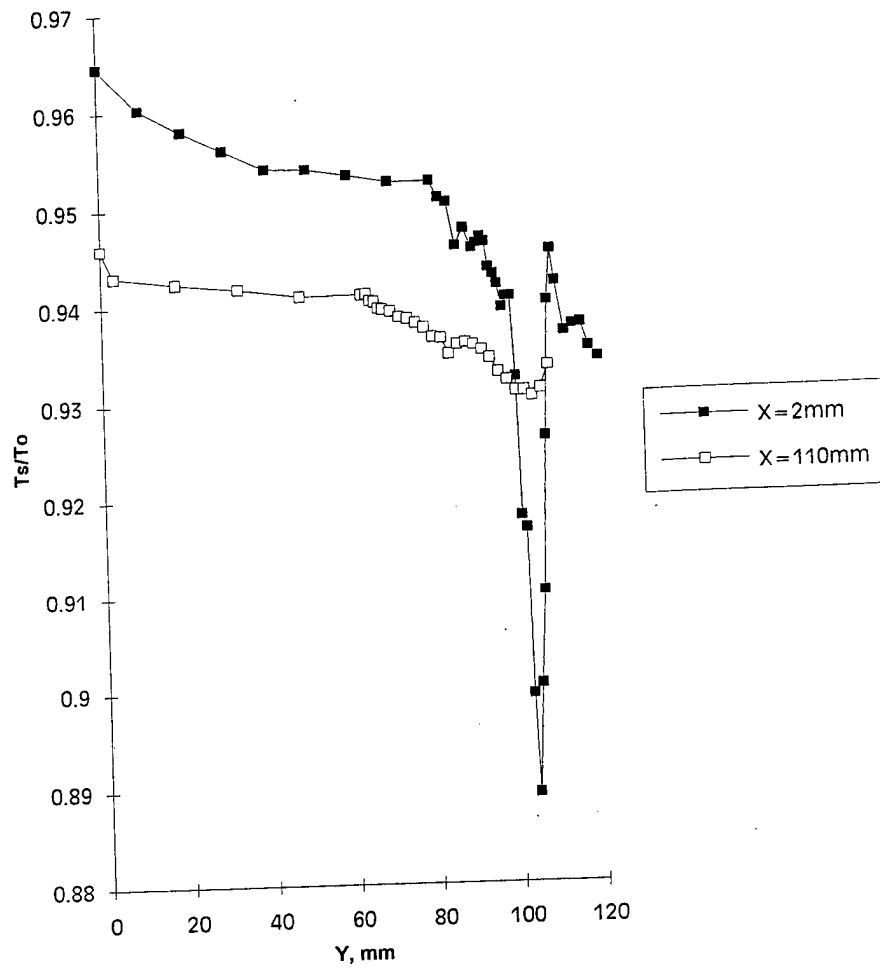
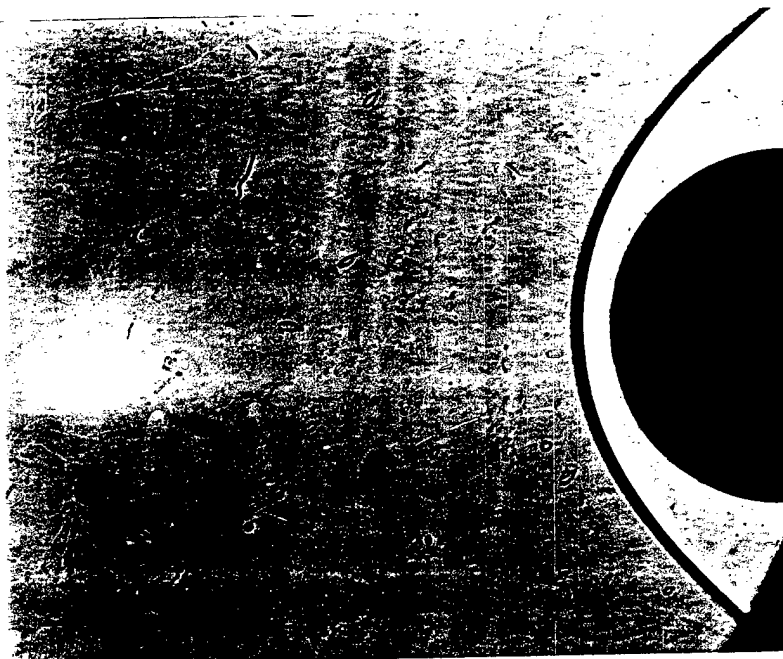


Fig. 32

a)



Generator N2

b)

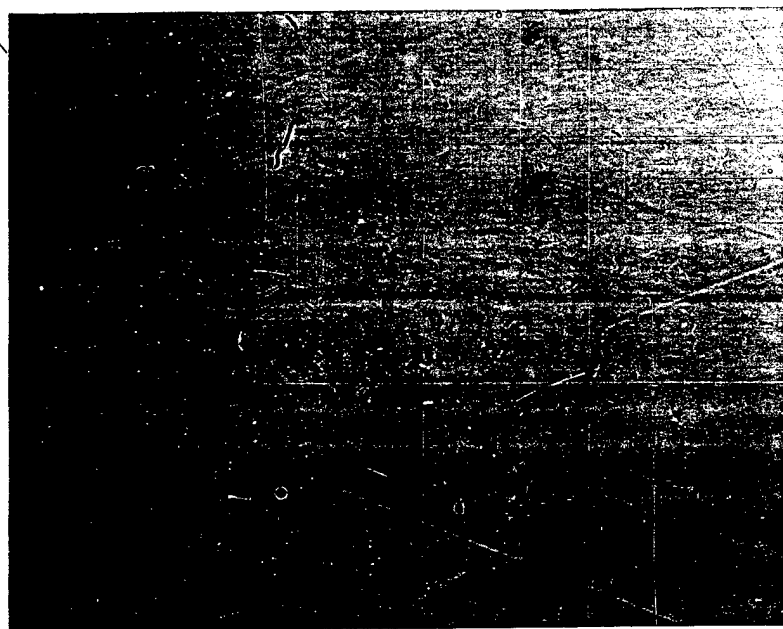
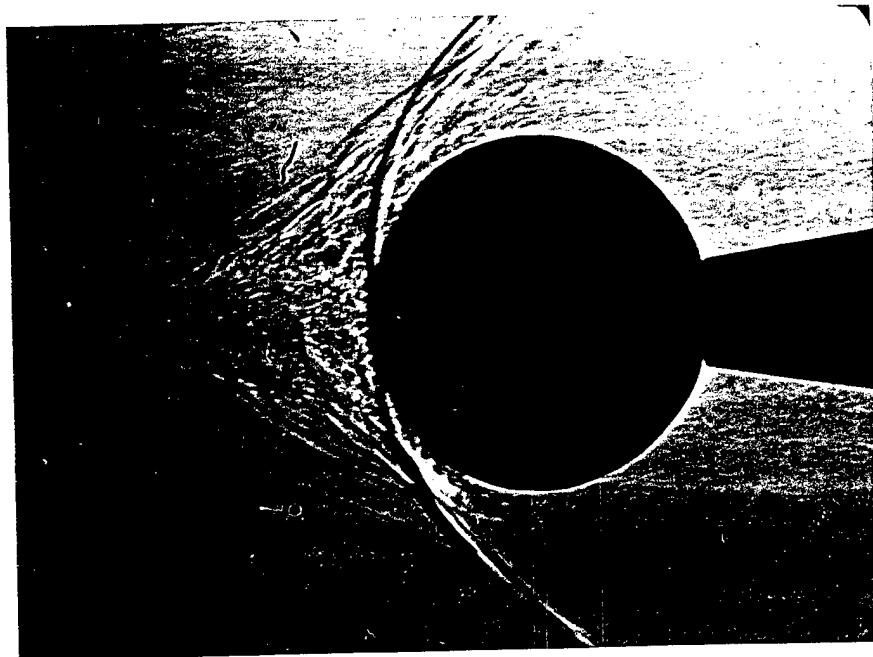


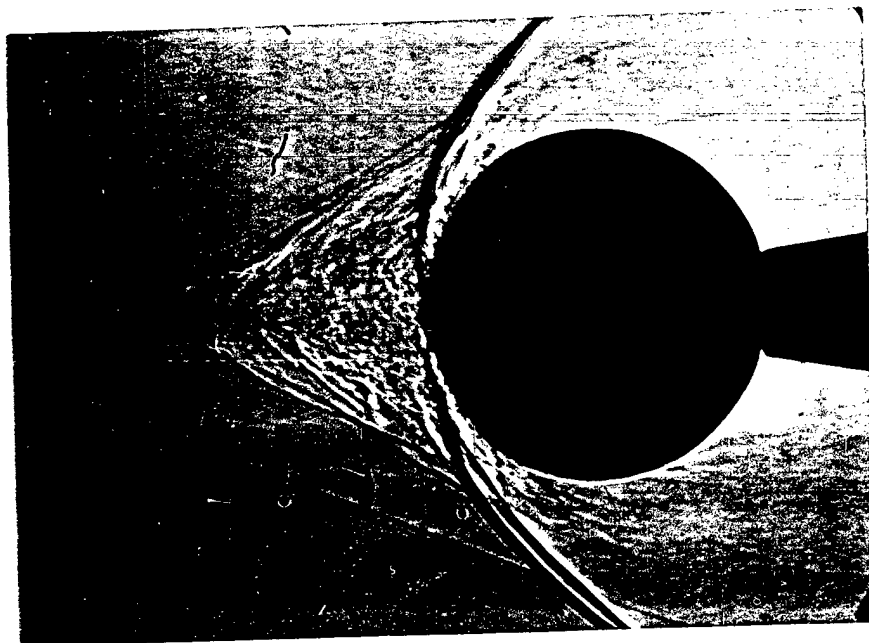
Fig. 33

Generator N2  
 $\alpha=10^\circ$

Test N22

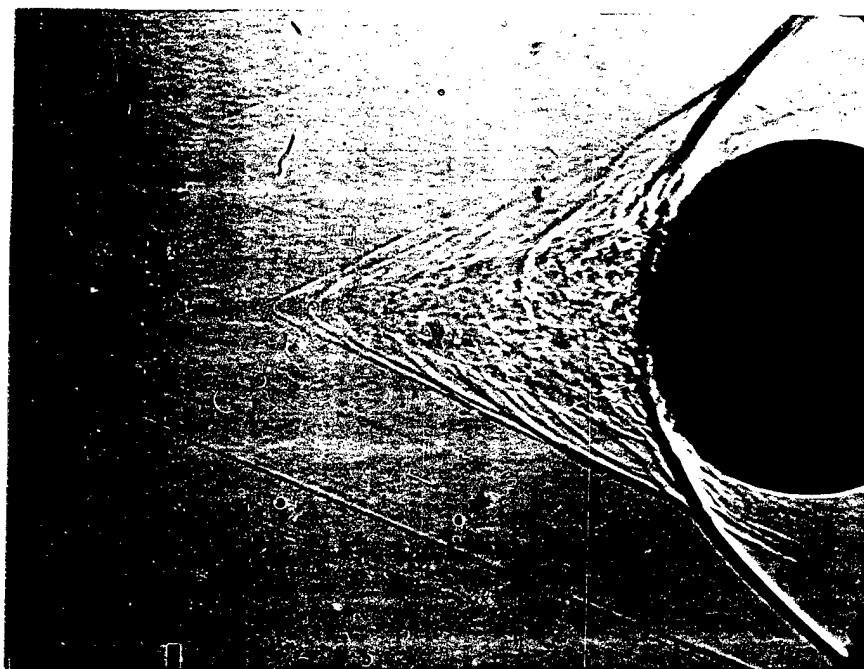


$\bar{X}_s = 0.95$

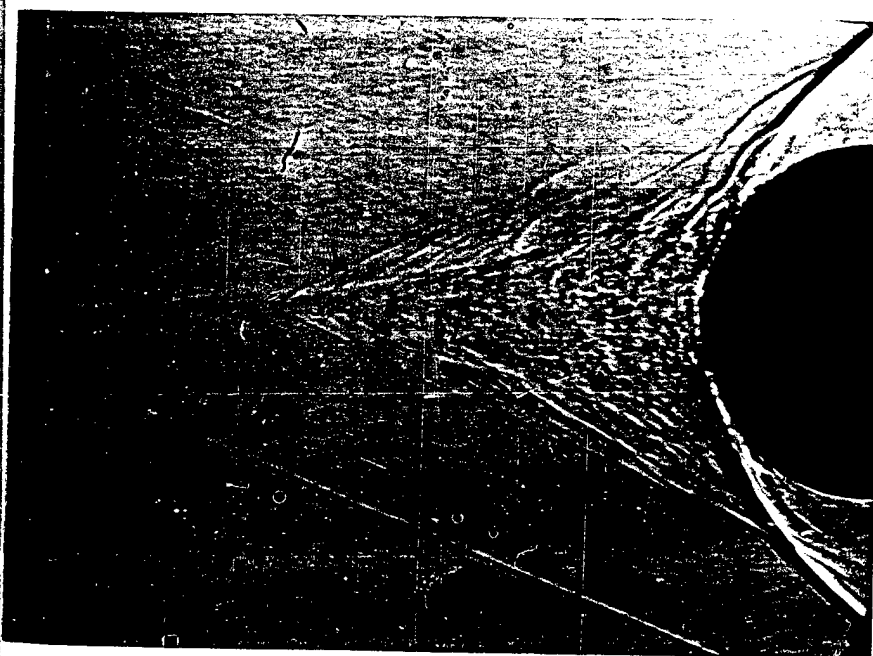


$\bar{X}_s = 1.17$

Fig. 34a



$\bar{X}_s = 1.80$

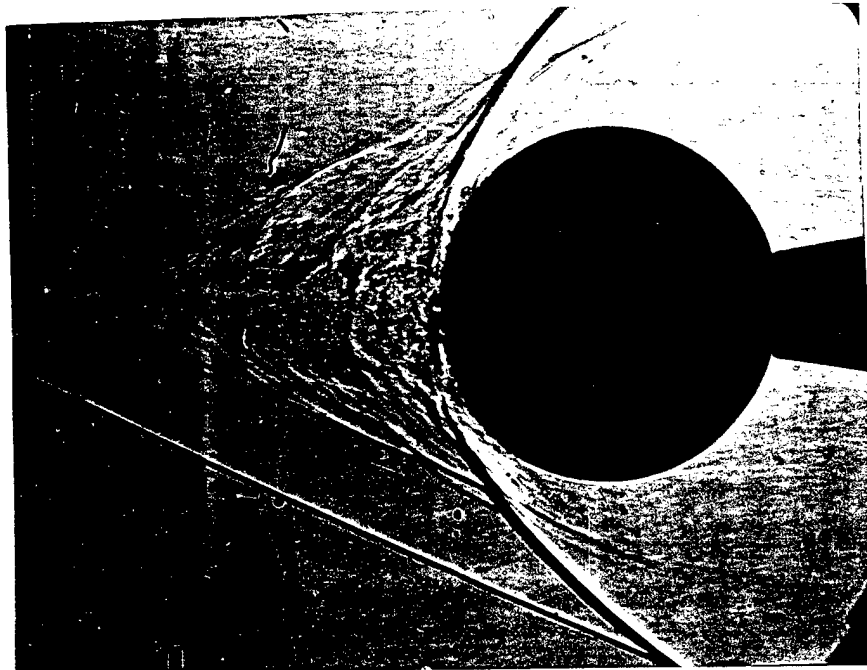


$\bar{X}_s = 1.97$

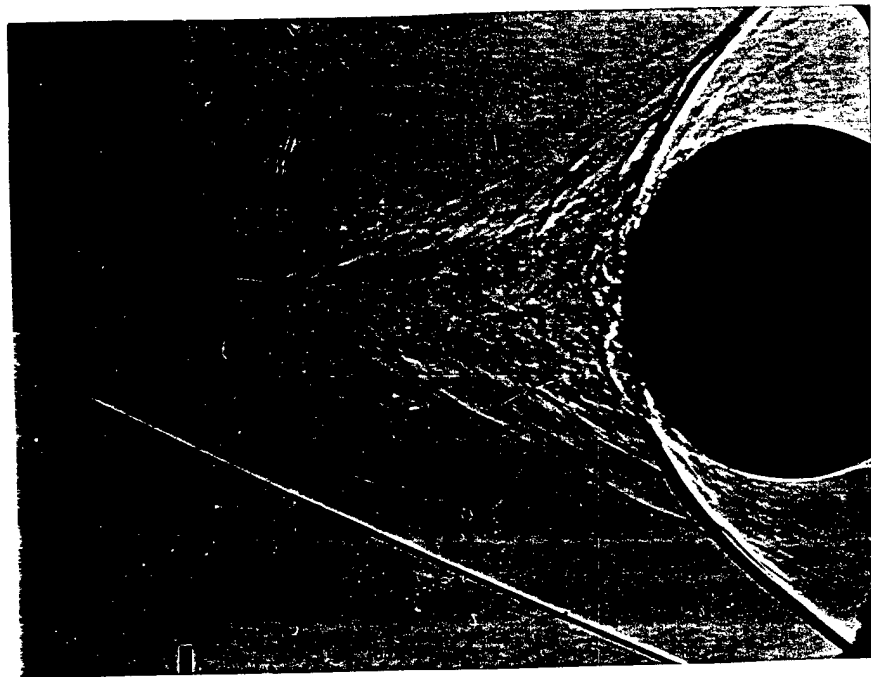
Fig. 34c

Generator N2  
 $\alpha=20^\circ$

Test N20

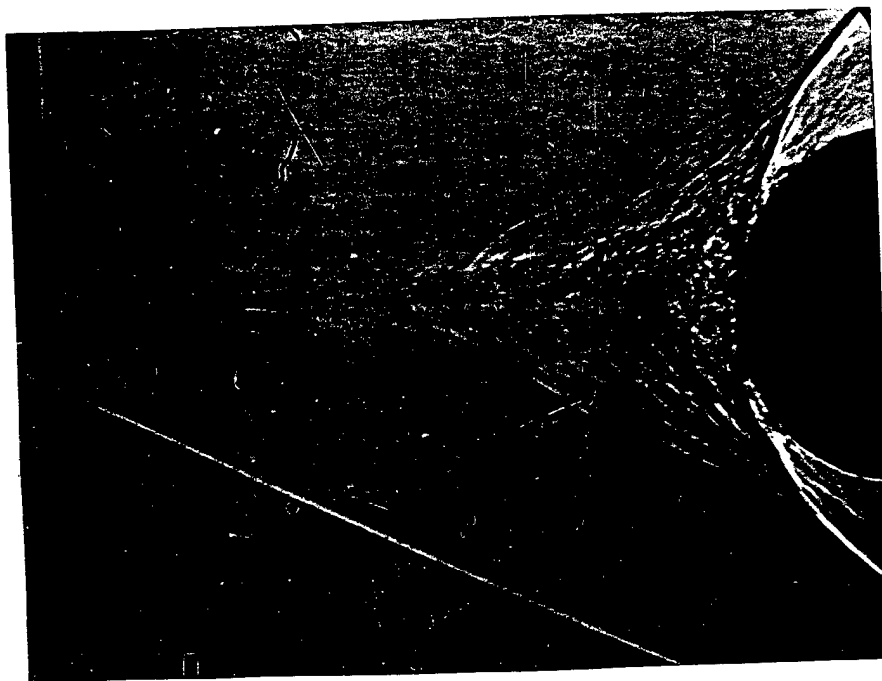


$\bar{X}_S = 1.17$



$\bar{X}_S = 1.72$

Fig. 35a



$\bar{X}_s = 2.03$

Fig. 35b

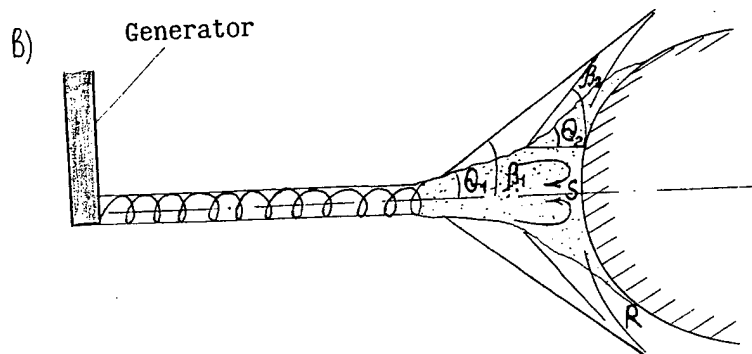
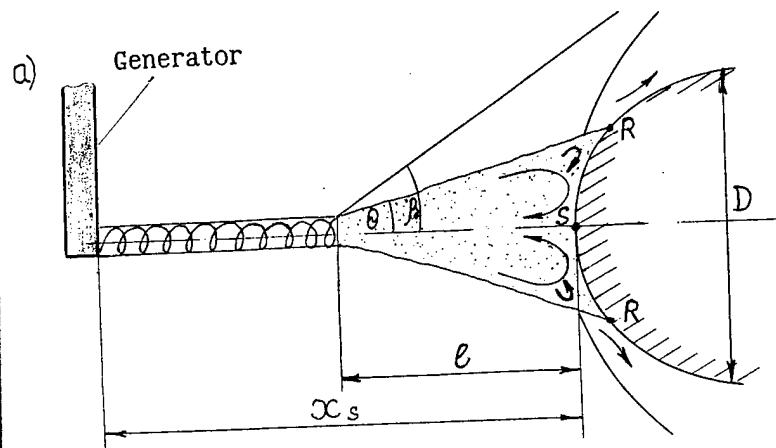


Fig. 36

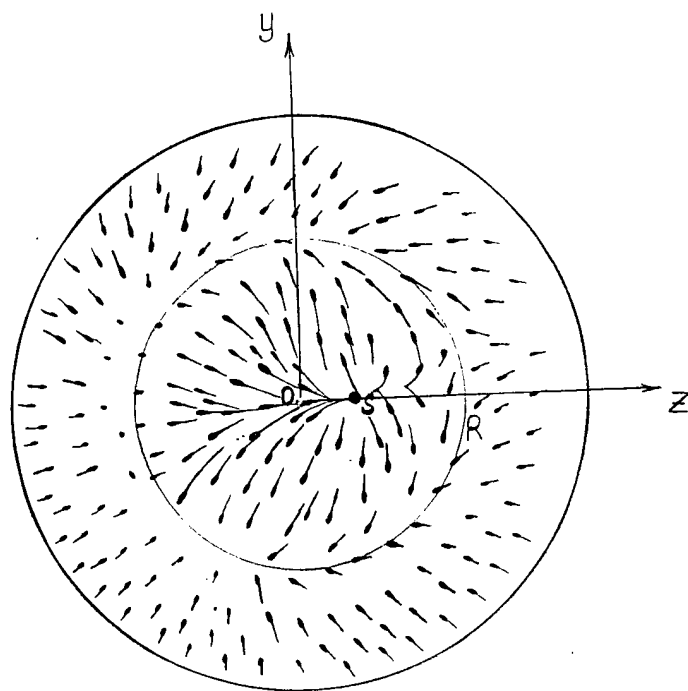
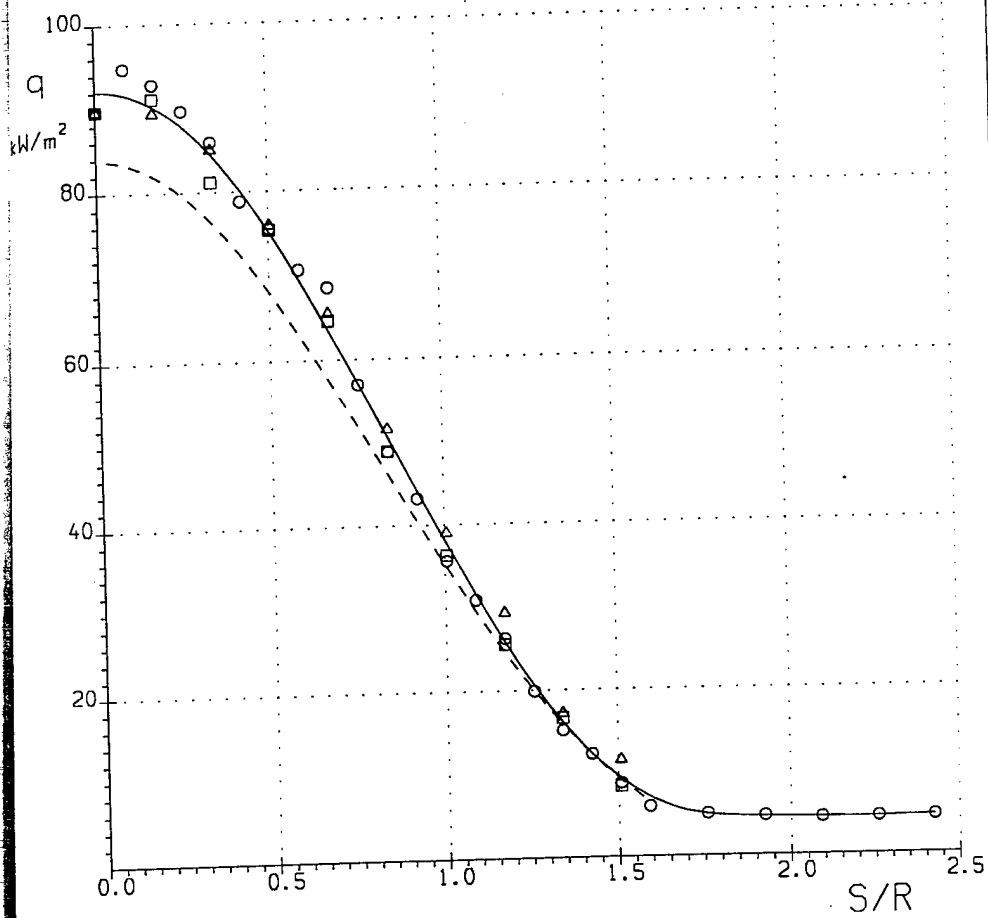
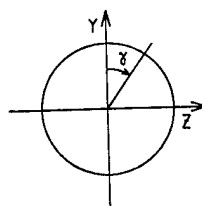


Fig. 37



- $\square$   $\gamma = 0^\circ$
- $\circ$   $\gamma = 90^\circ$
- $\triangle$   $\gamma = 180^\circ$
- experiment
- - - theory

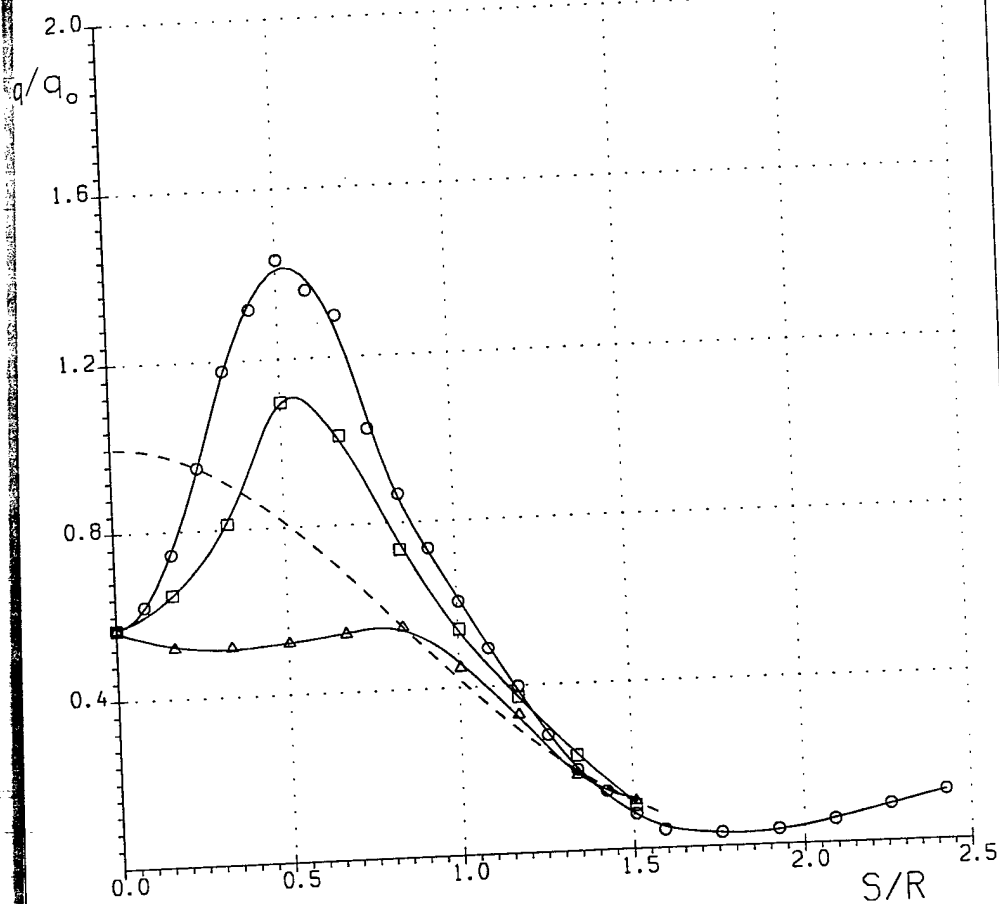


Sphere  $T_H = 290 \text{ K}$

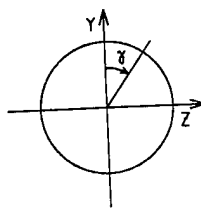
Run 28

Fig. 38

$$\alpha = 10^\circ$$



- $\square$   $\gamma = 0^\circ$
- $\circ$   $\gamma = 90^\circ$
- $\triangle$   $\gamma = 180^\circ$
- theory

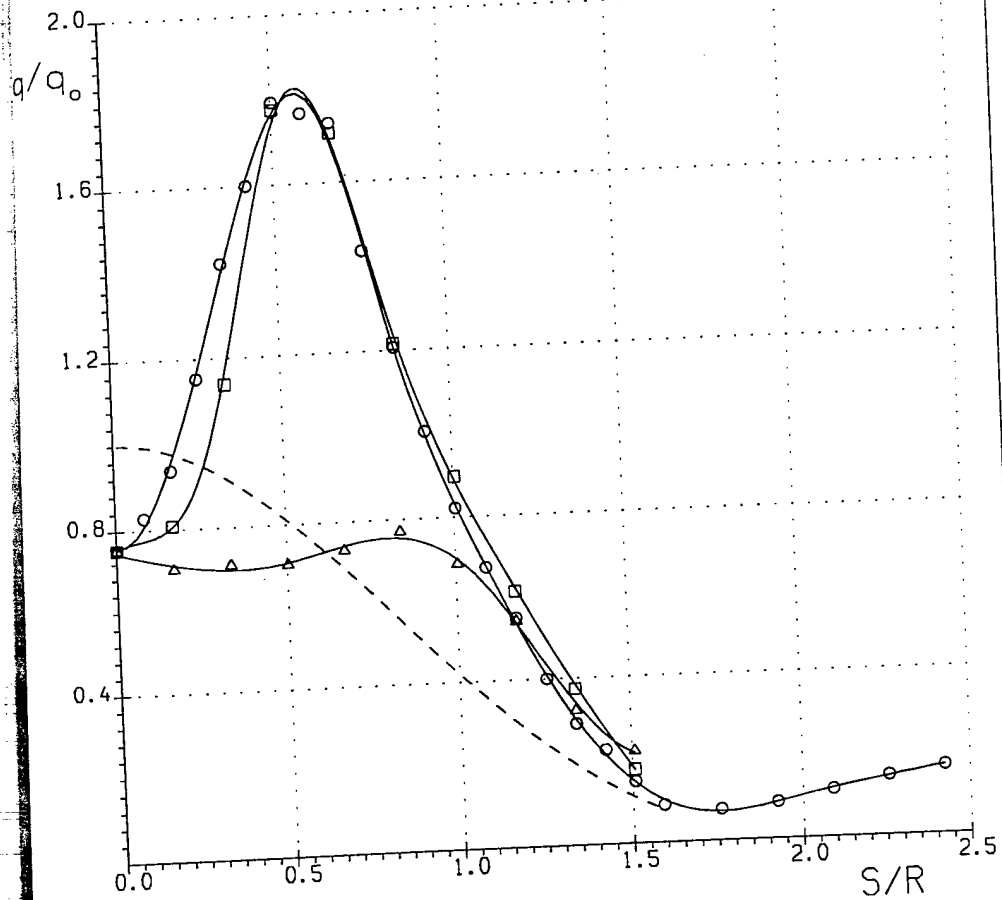


Sphere with generator No. 2,  $X_5/D=1.17$

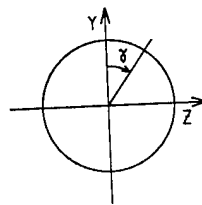
Run 30

Fig. 39a

$\alpha = 20^\circ$



- $\gamma = 0^\circ$
- $\gamma = 90^\circ$
- △—  $\gamma = 180^\circ$
- - - theory

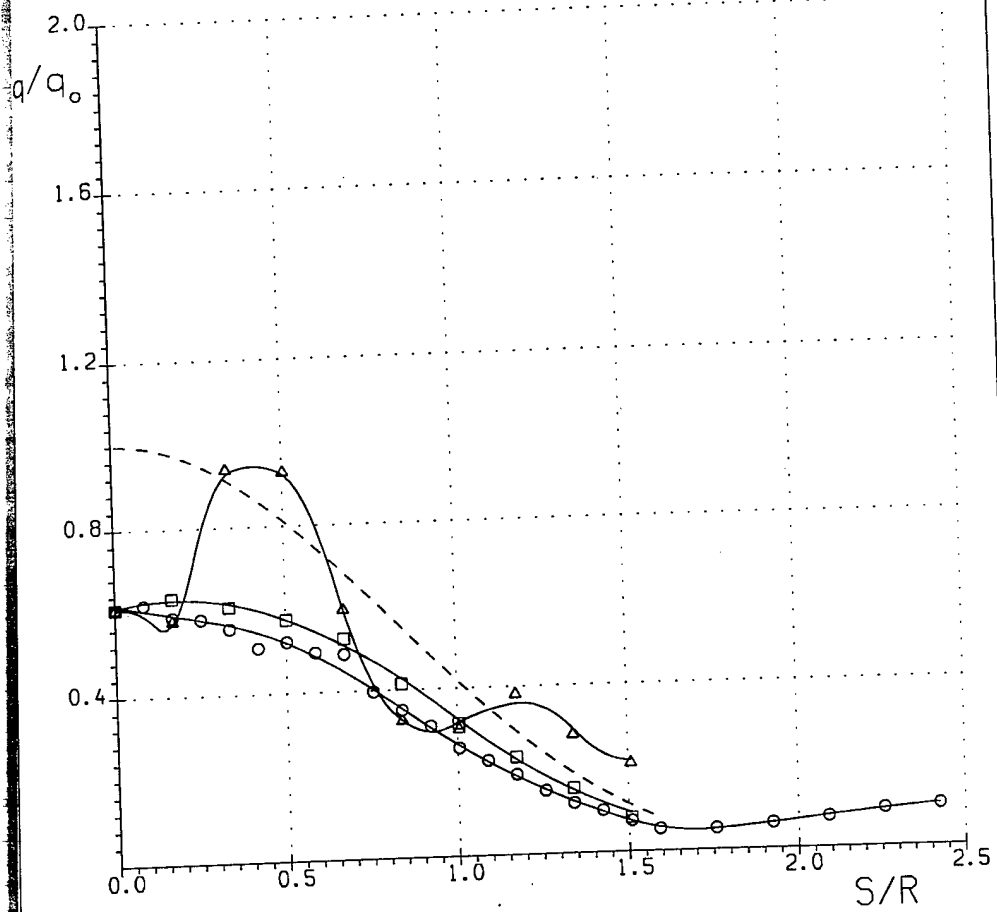


Sphere with generator No.2,  $X_5/D=1.17$

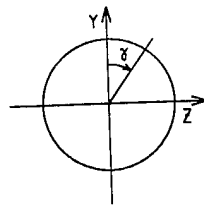
Run 29

Fig. 39b

$\alpha = 30^\circ$



- $\square$   $\gamma = 0^\circ$
- $\circ$   $\gamma = 90^\circ$
- $\triangle$   $\gamma = 180^\circ$
- theory

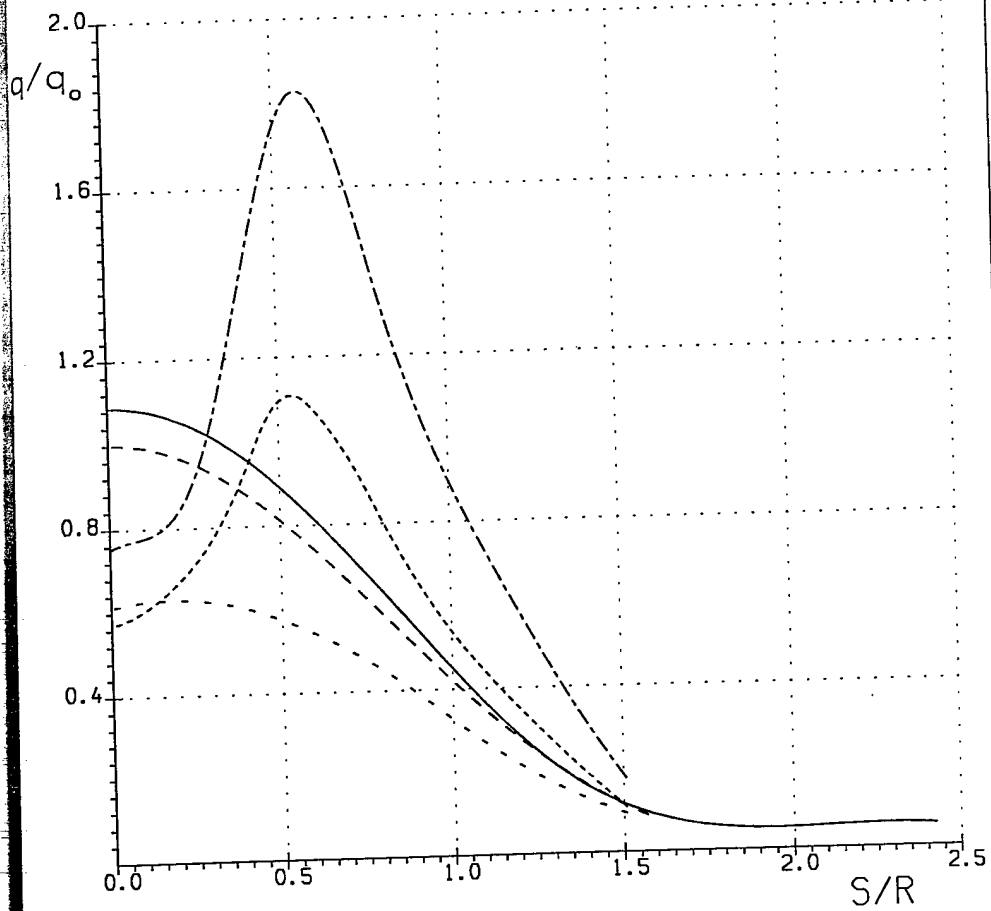


Sphere with generator No. 2.  $x_s/D = 1.17$

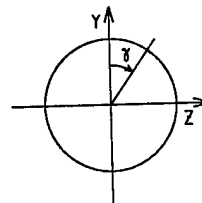
Run 43

Fig. 39c

$$\gamma = 0^\circ$$



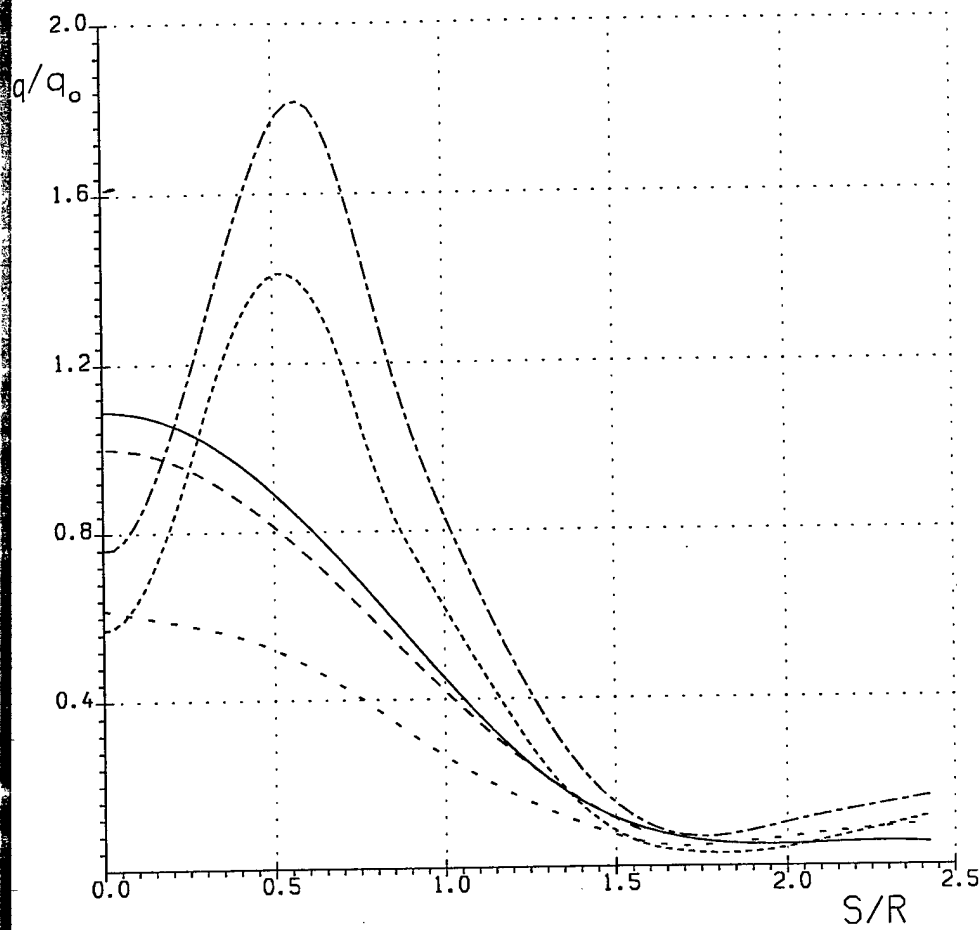
- without generator
- - -  $\alpha=10^\circ$
- . -  $\alpha=20^\circ$
- ...  $\alpha=30^\circ$
- - - theory



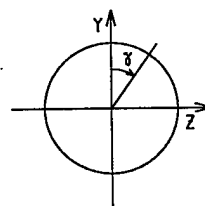
Sphere with generator No. 2,  $X_5/D=1.17$

Fig. 40a

$\gamma = 90^\circ$



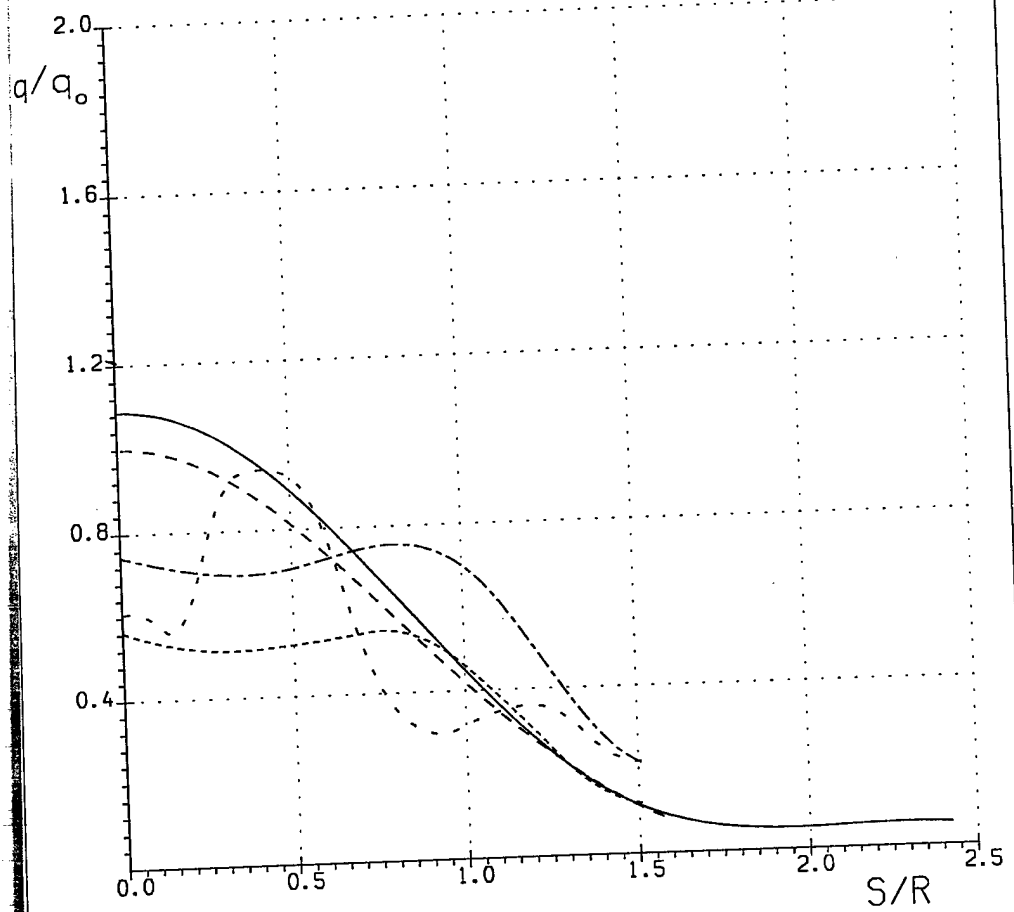
- without generator
- - -  $\alpha=10^\circ$
- - -  $\alpha=20^\circ$
- . -  $\alpha=30^\circ$
- - - theory



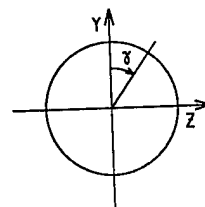
Sphere with generator No.2,  $X_s/D=1.17$

Fig. 40b

$$\gamma = 180^\circ$$



- without generator
- - -  $\alpha=10^\circ$
- . -  $\alpha=20^\circ$
- . . .  $\alpha=30^\circ$
- - - theory



Sphere with generator No.2,  $x_5/D=1.17$

Fig. 40c

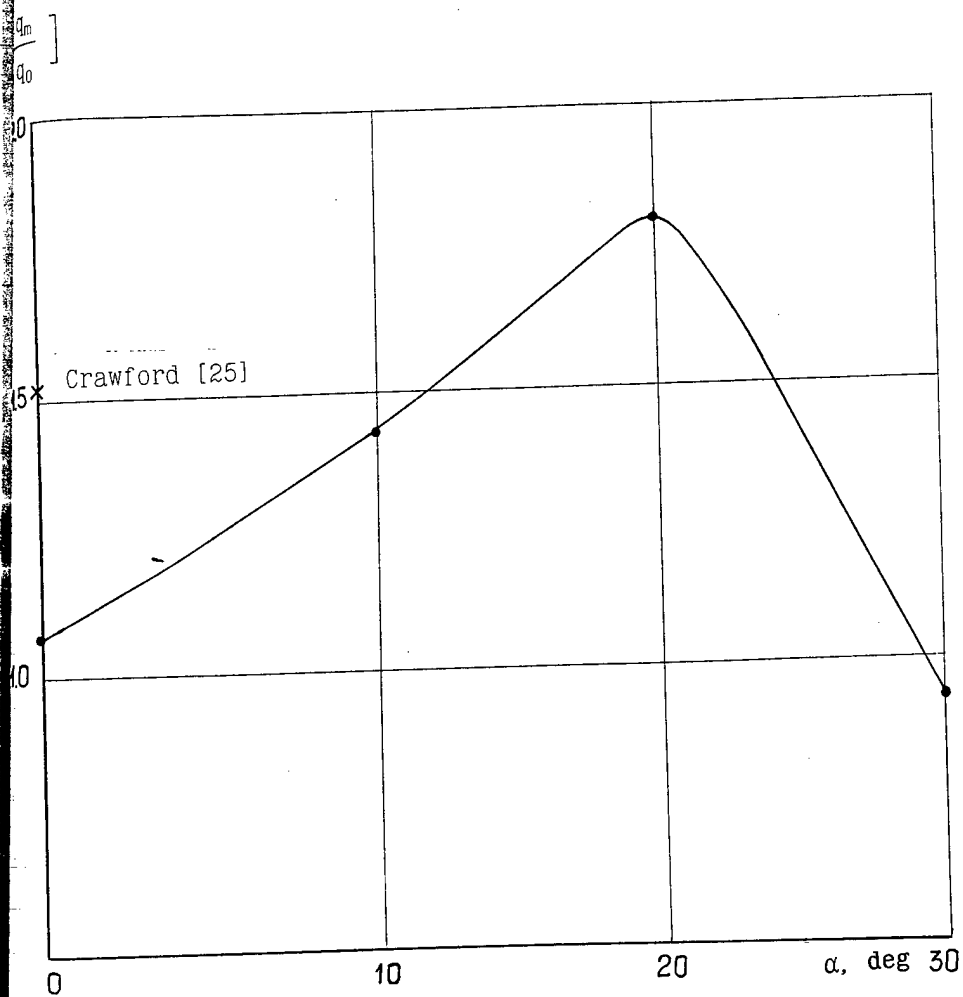


Fig.41

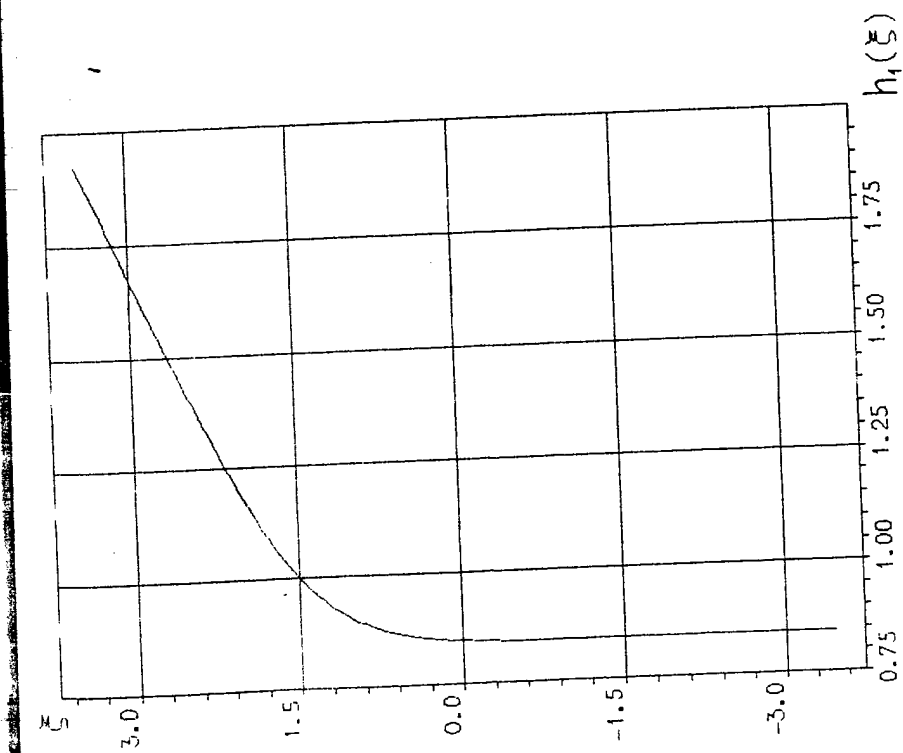


Fig.42

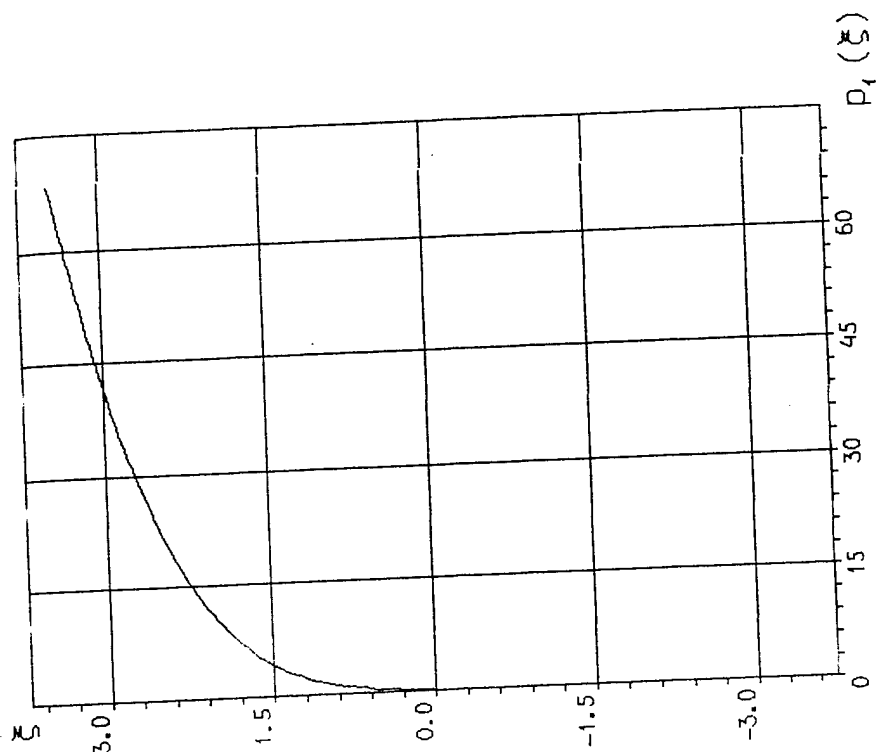


Fig.43

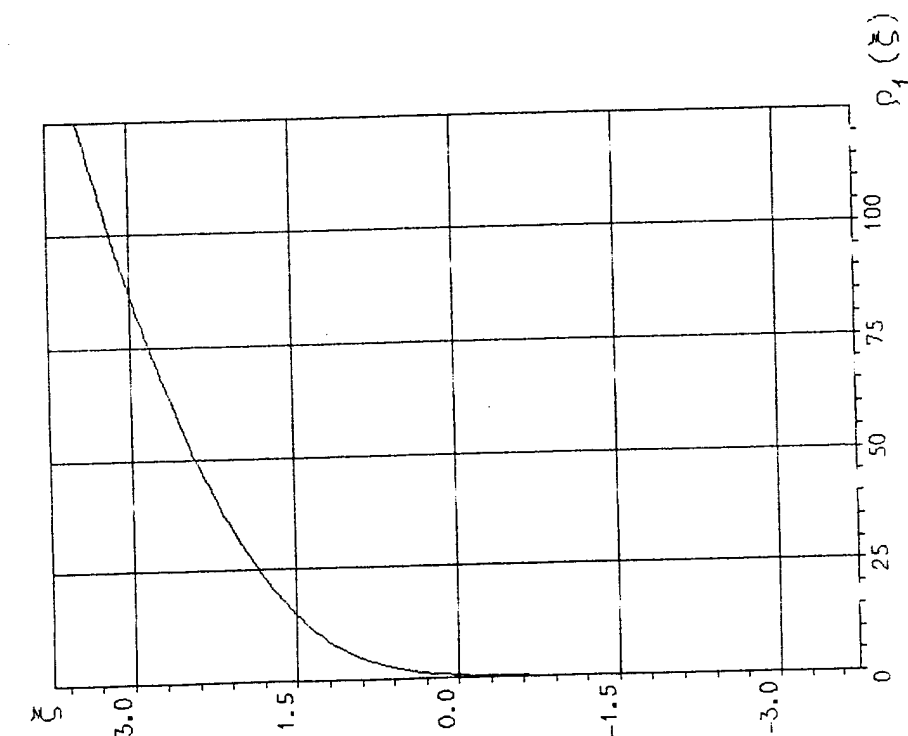


Fig. 44

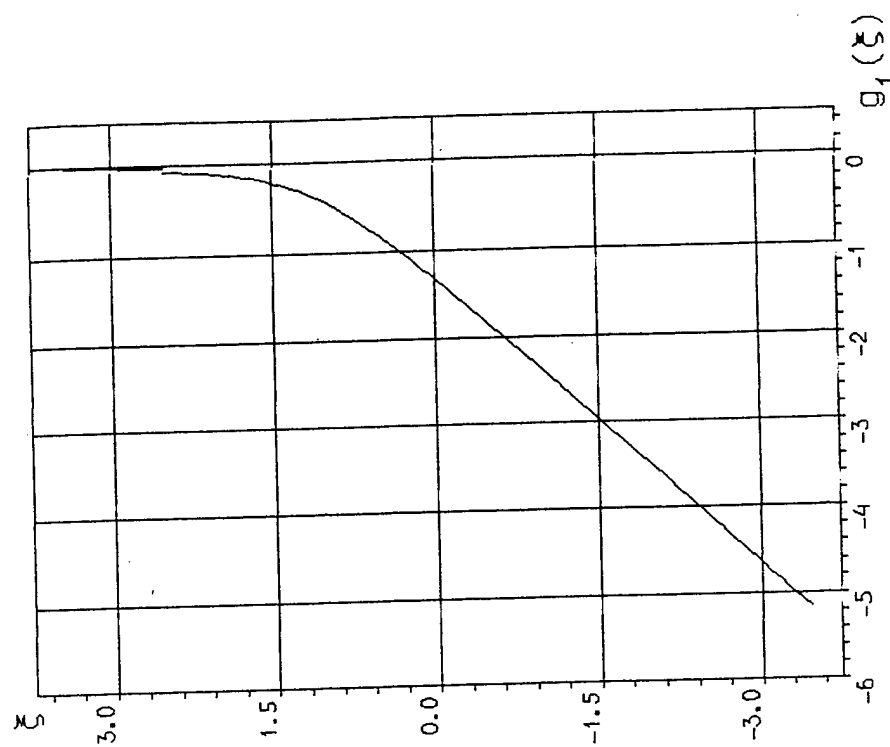


Fig. 45

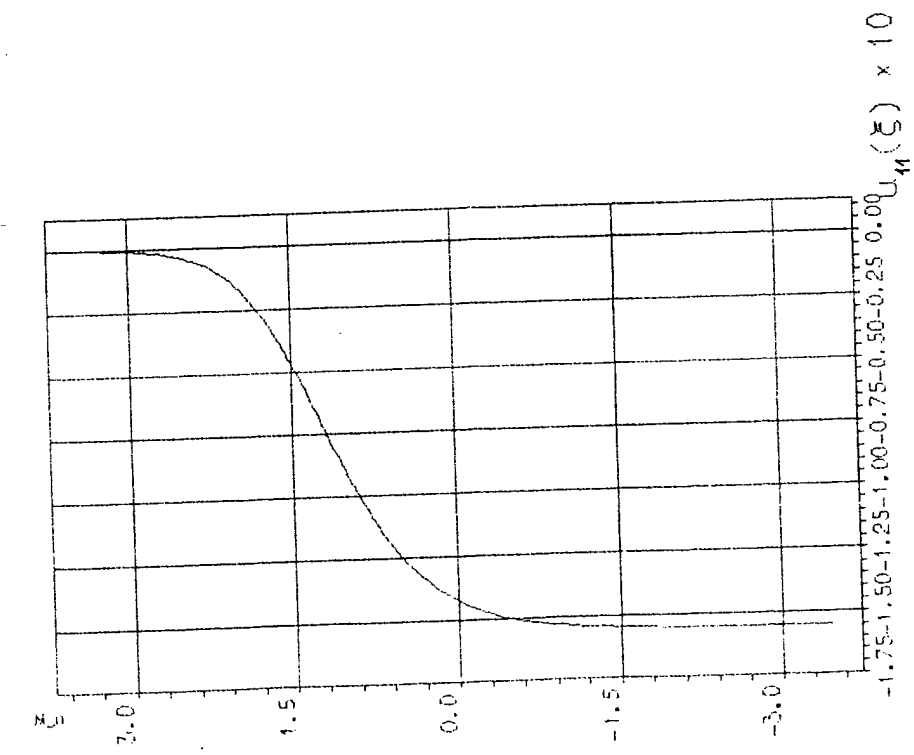


Fig.46

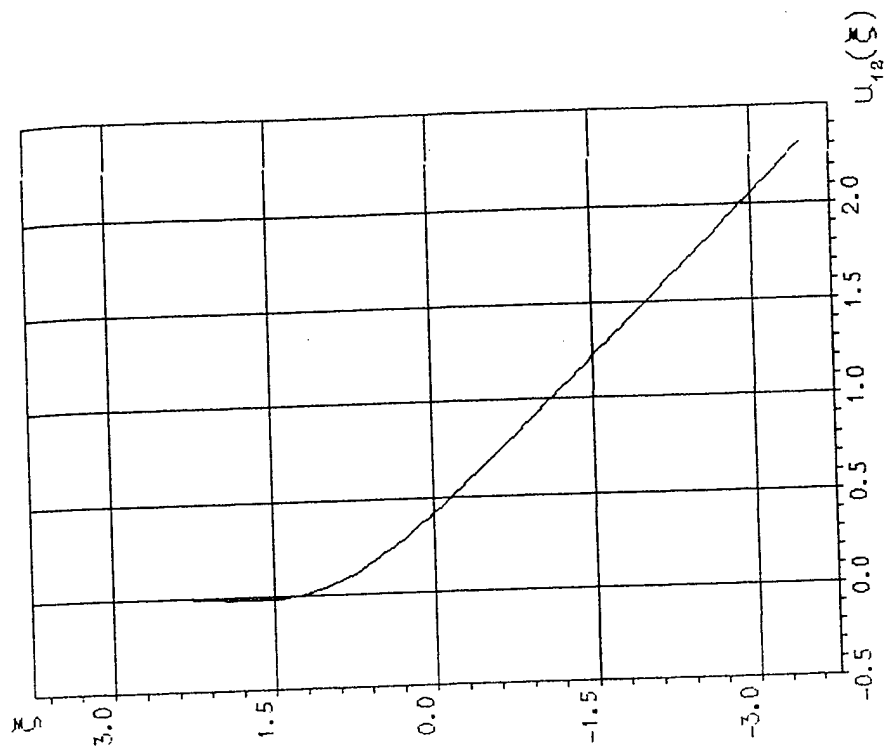


Fig.47

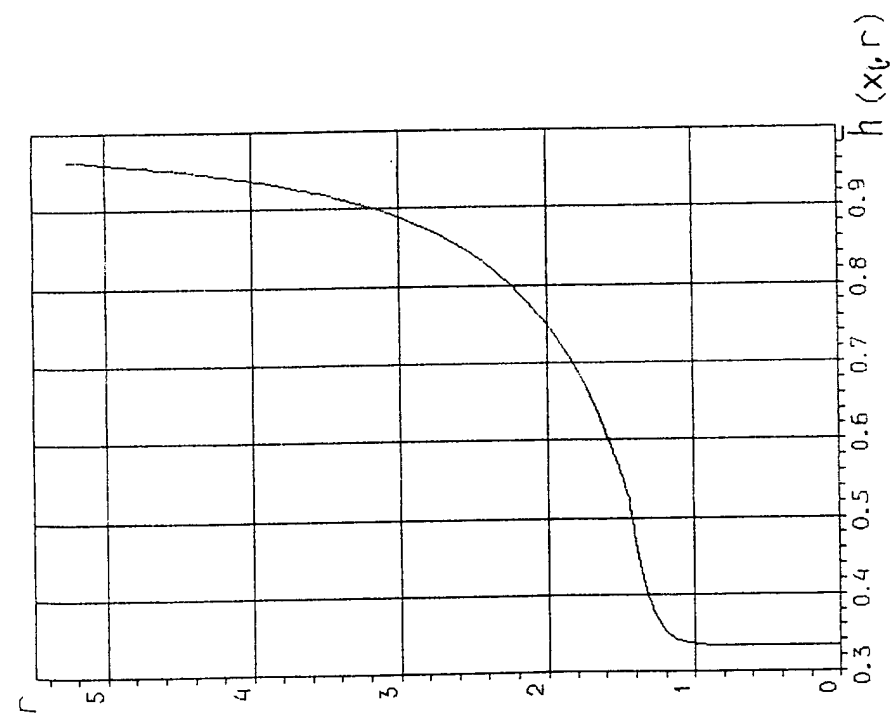


Fig.48

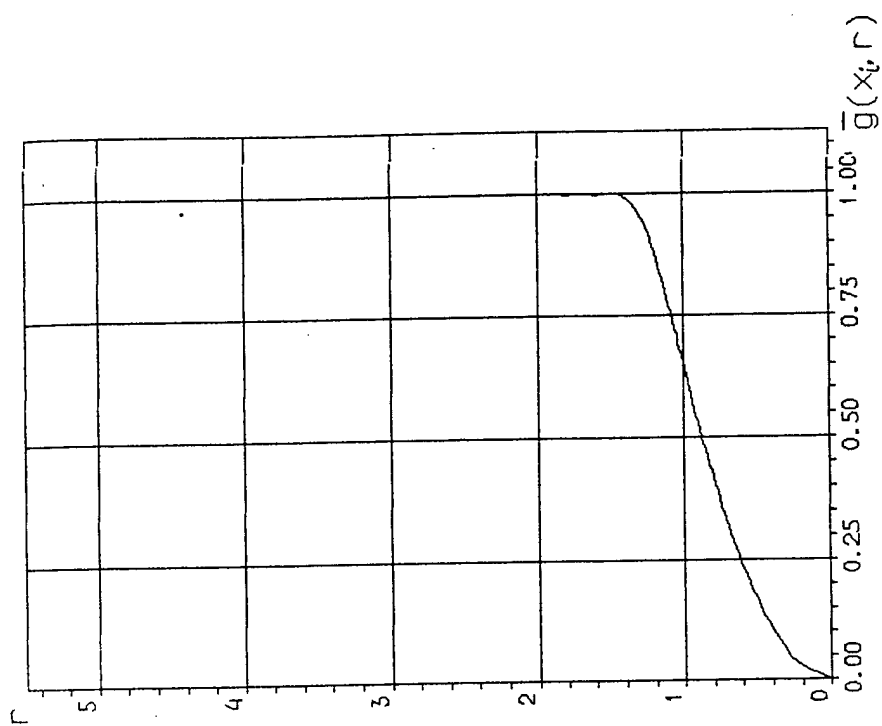


Fig.49

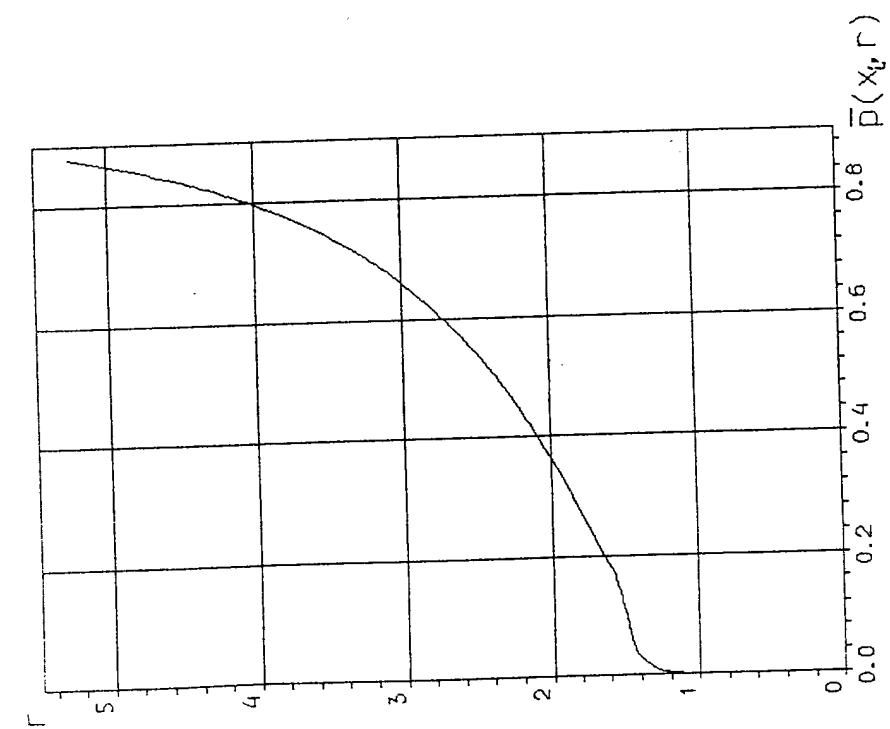


Fig.50

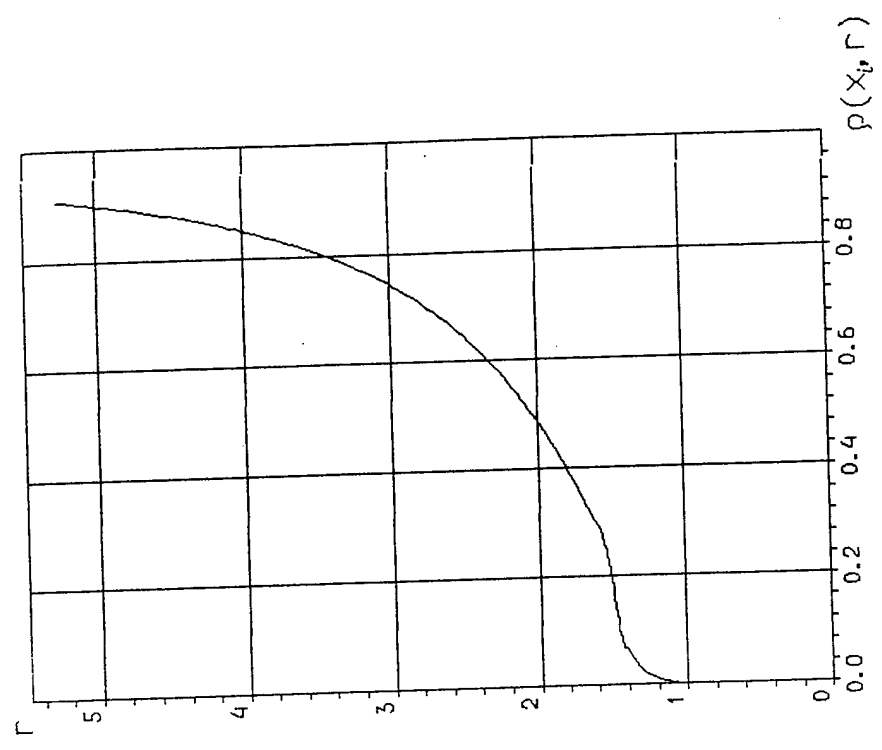


Fig.51

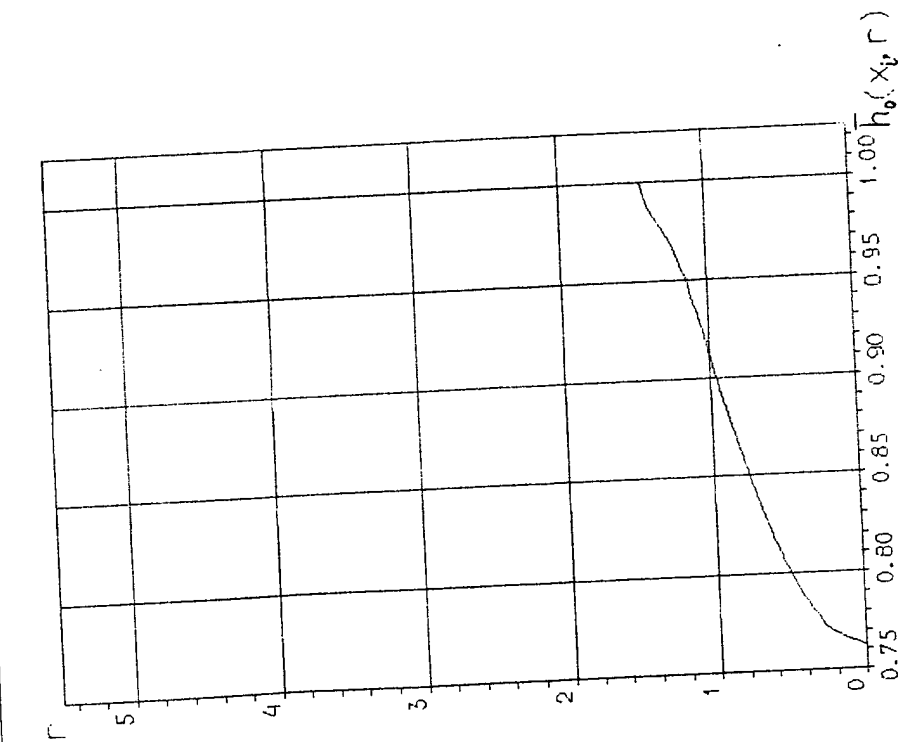


Fig. 52

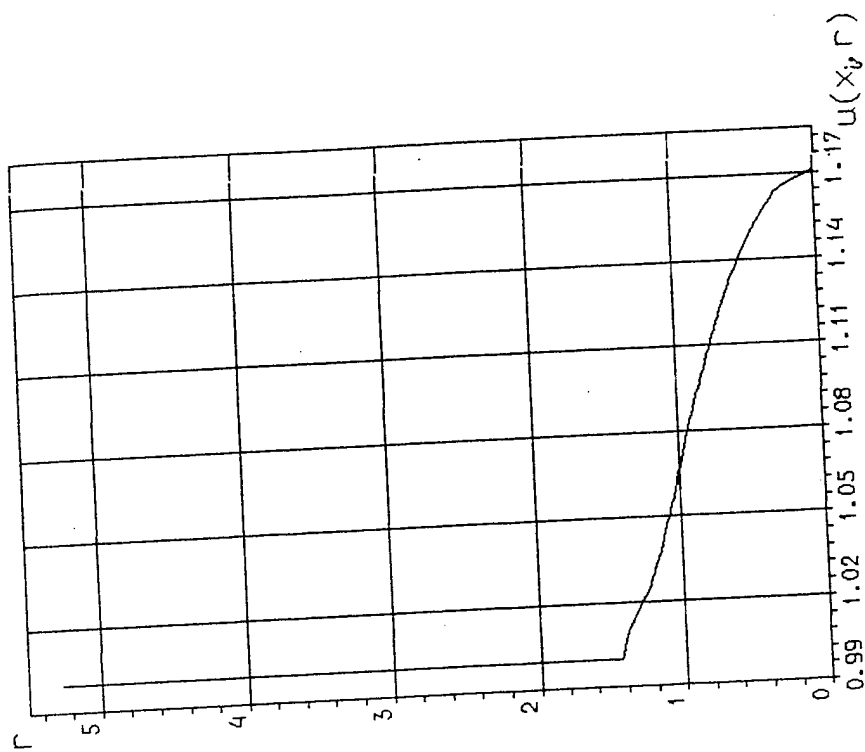


Fig. 53

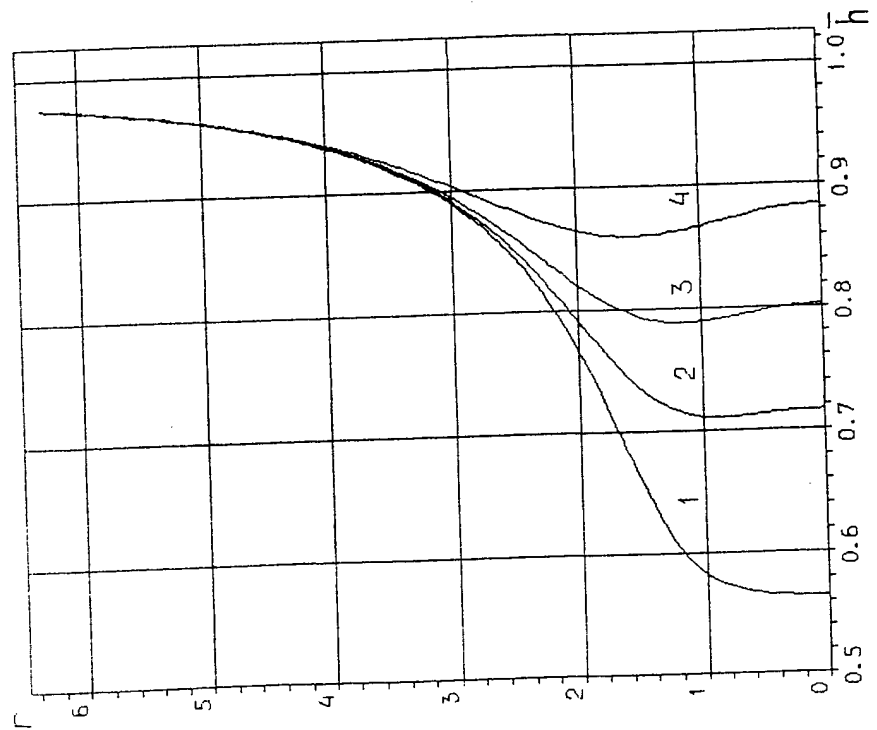
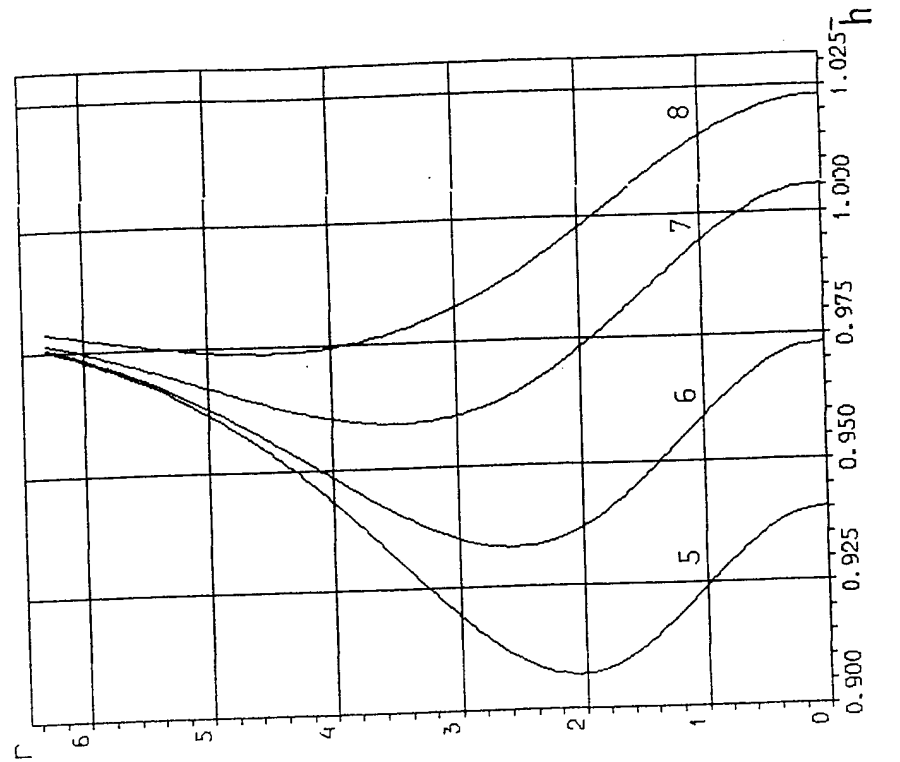


Fig.54

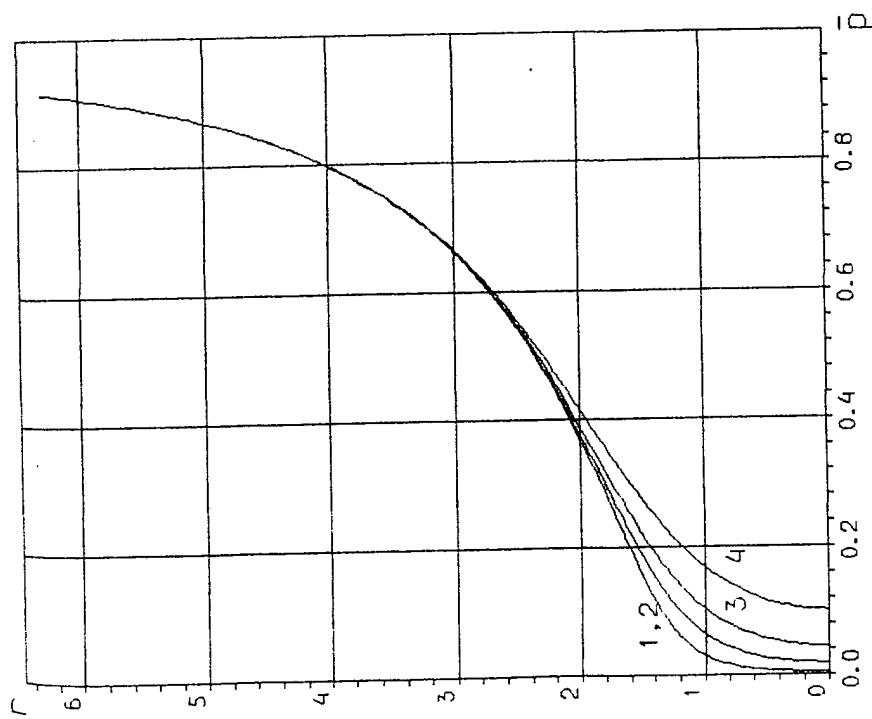
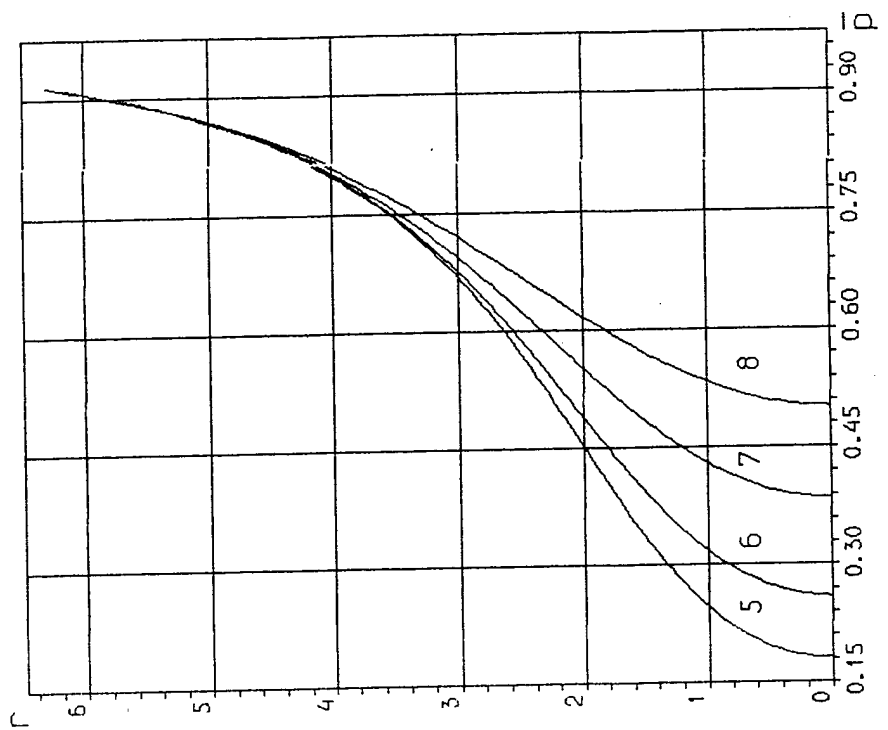


Fig.55

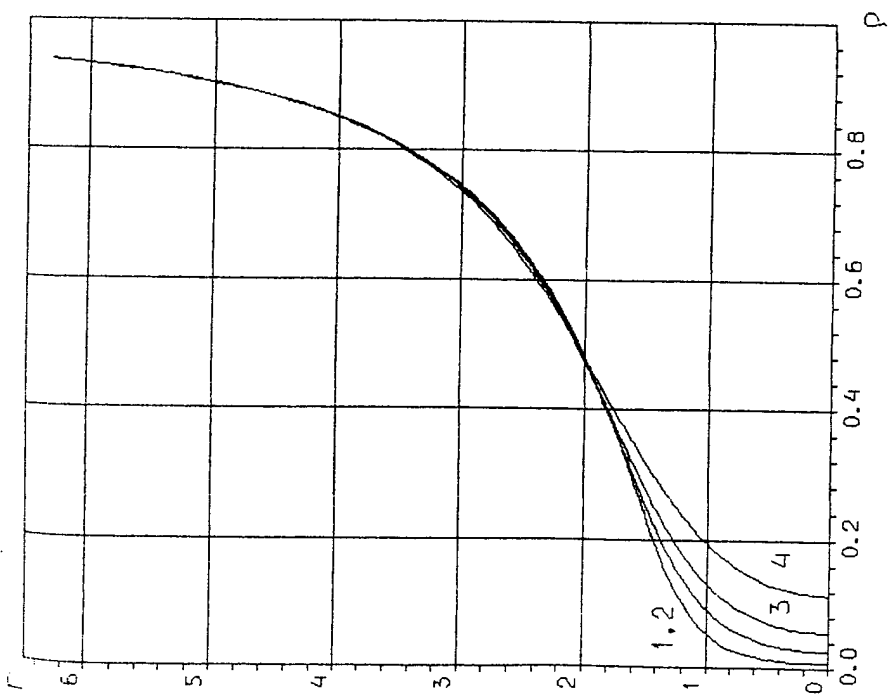
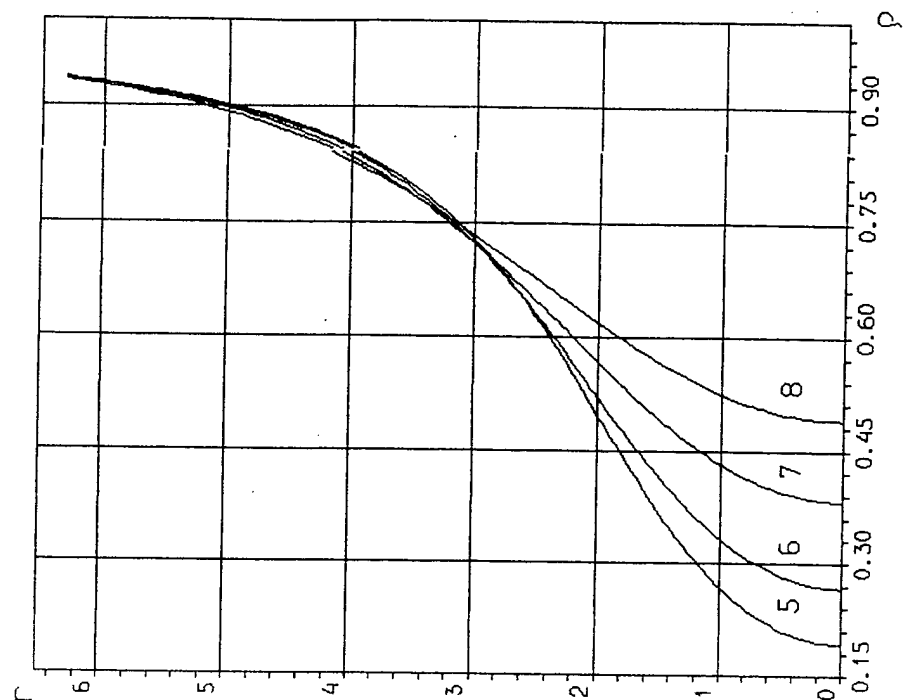


Fig. 56

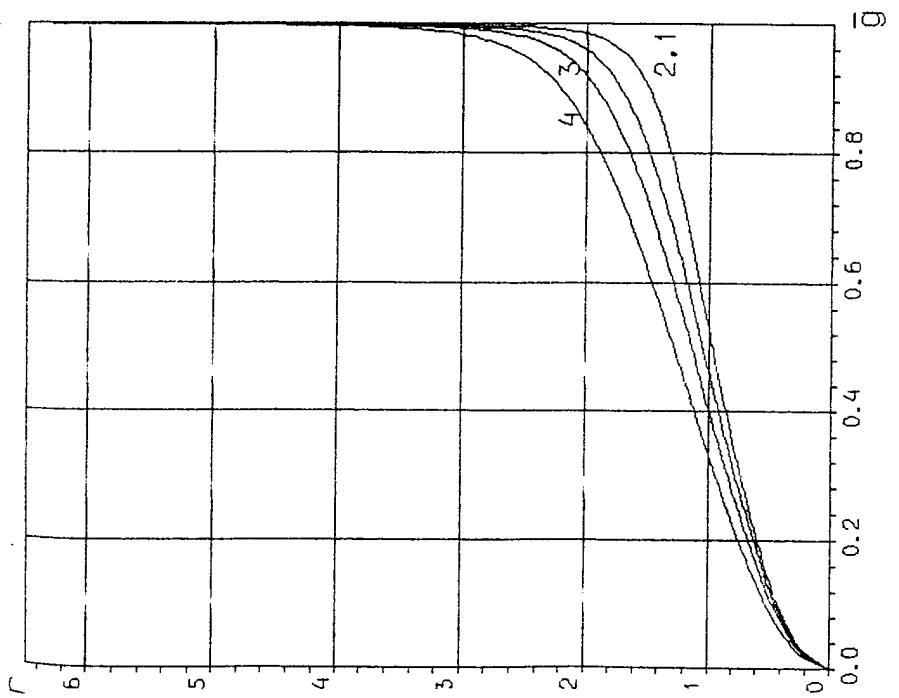
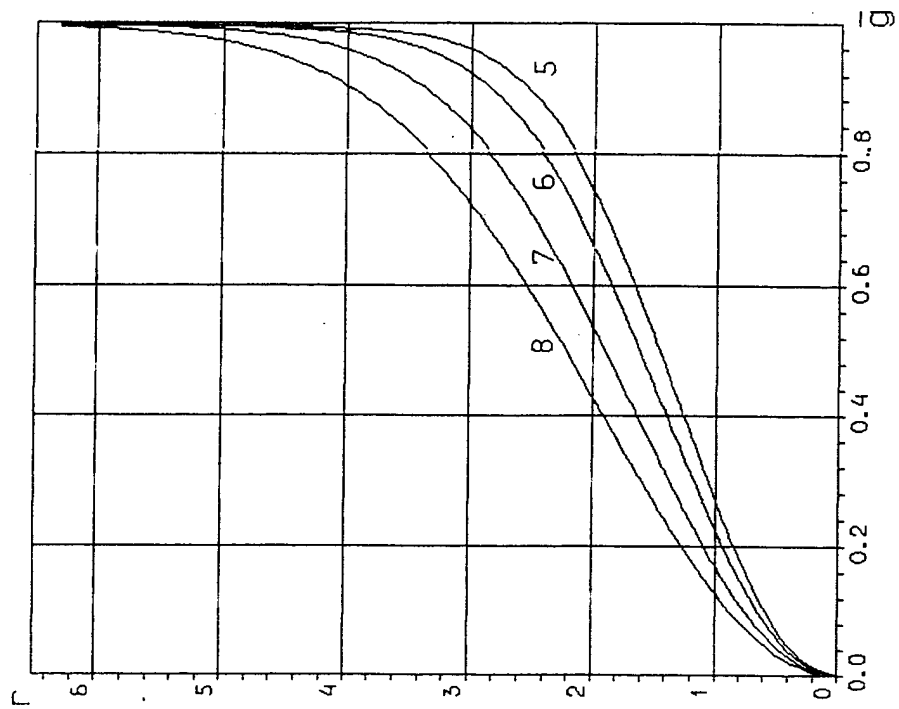


Fig.57

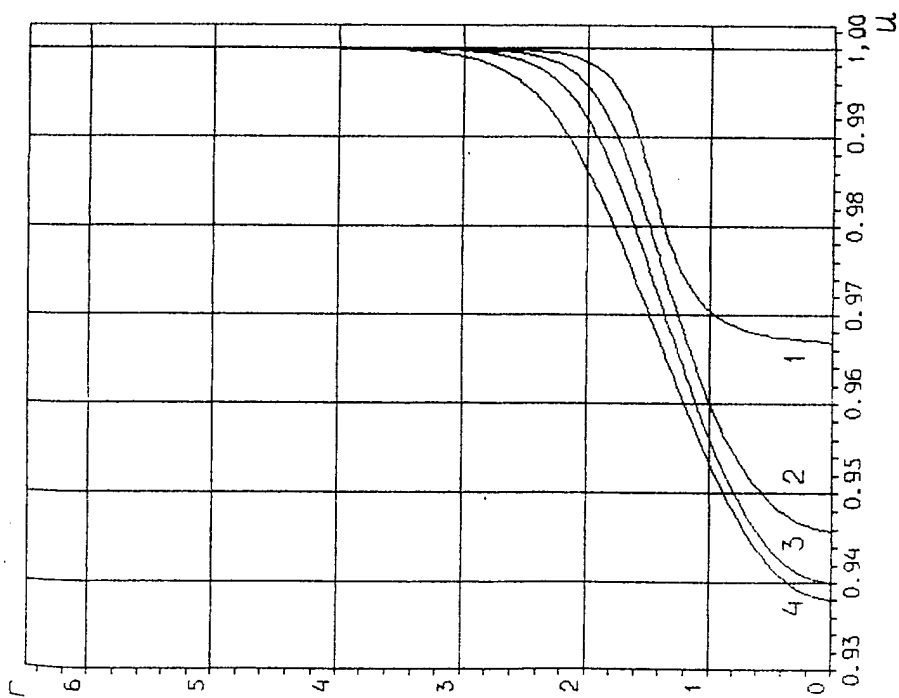
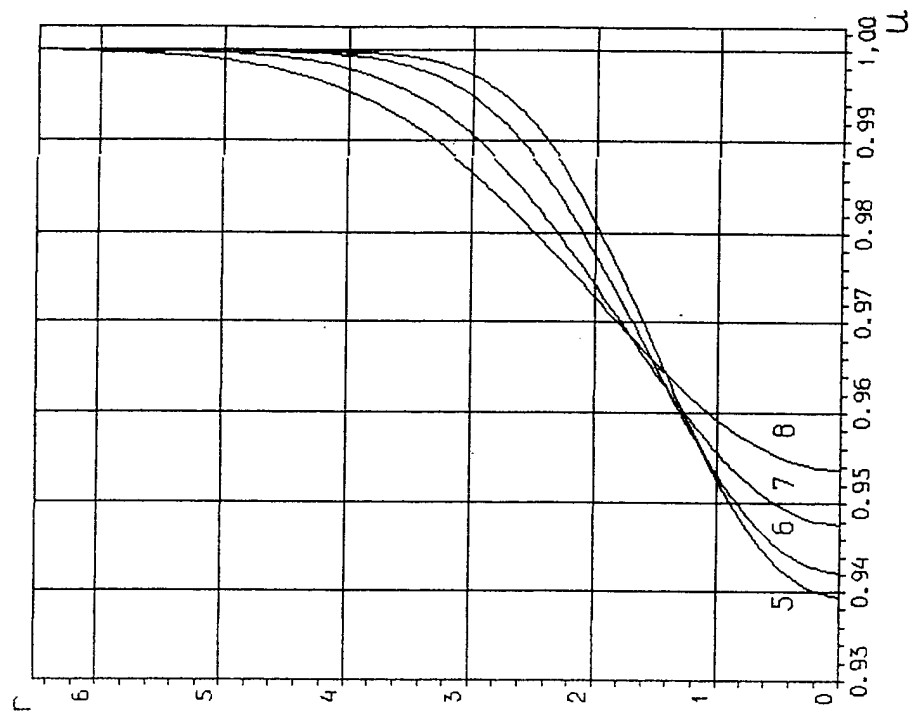


Fig.58

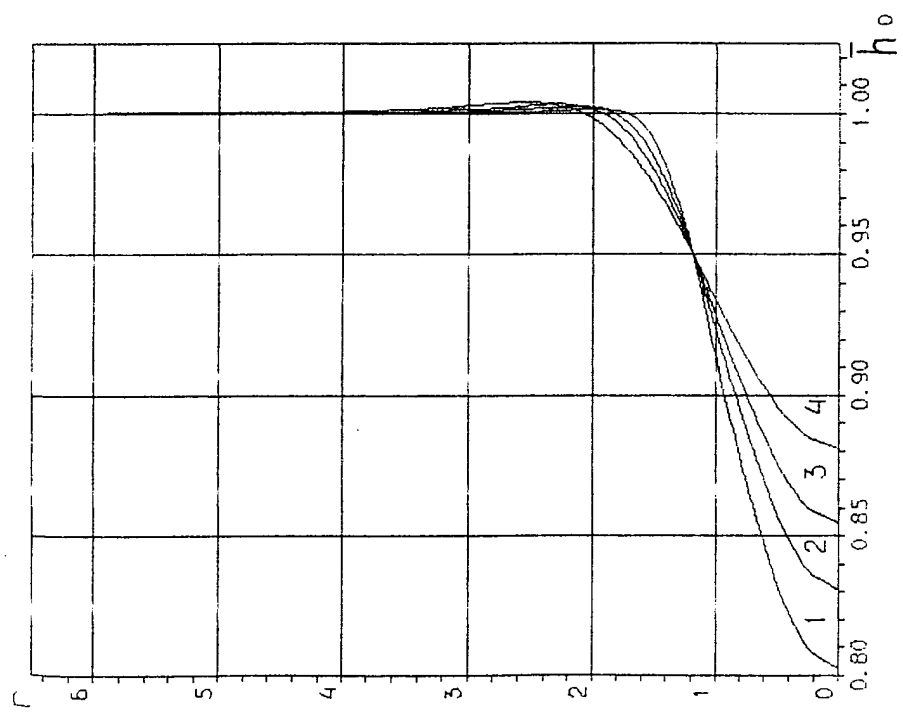
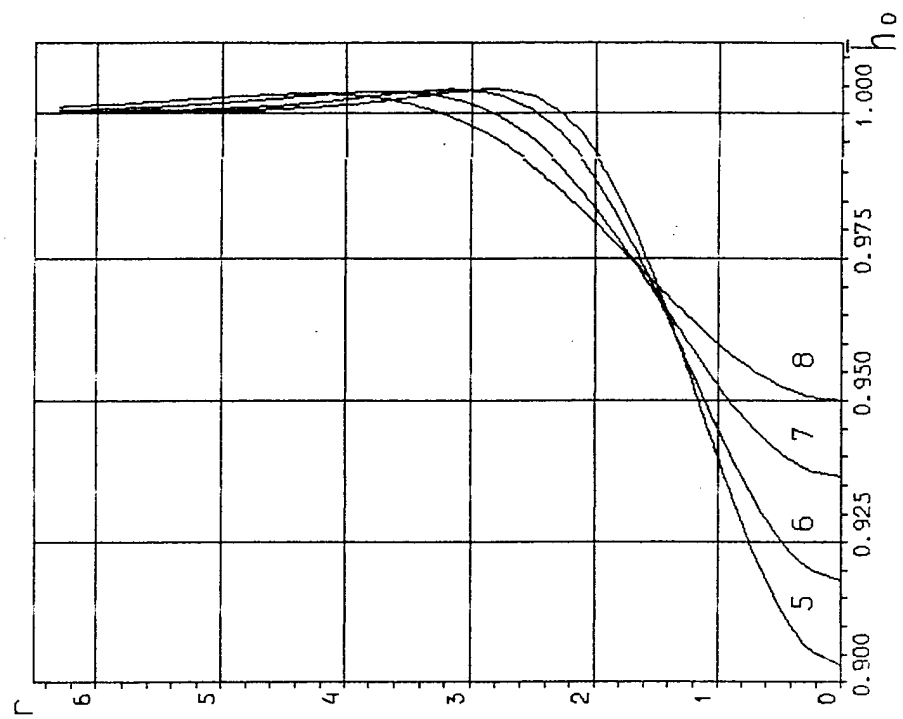


Fig. 59

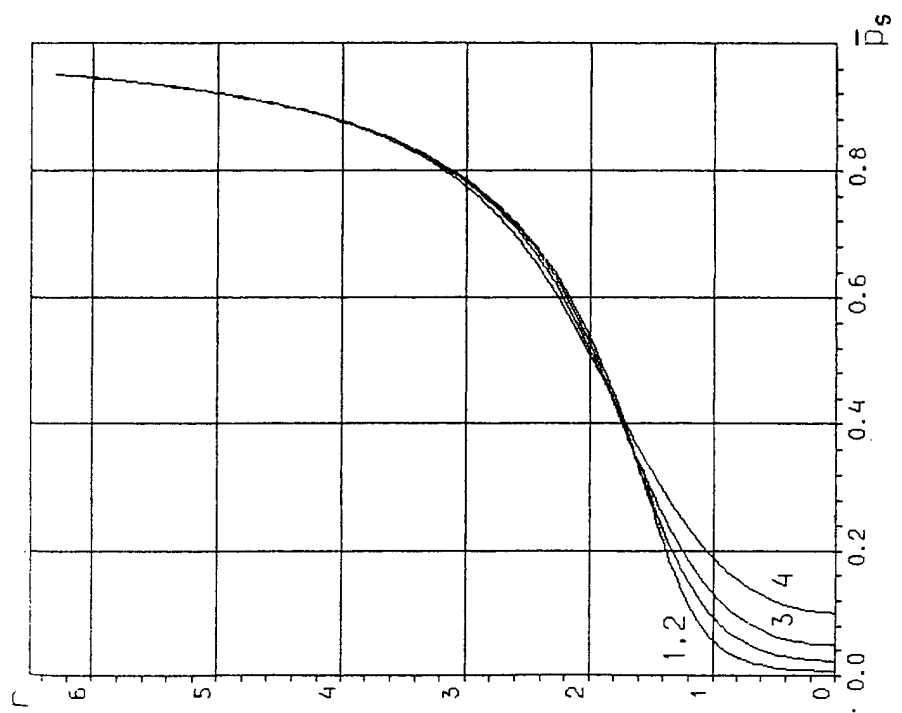
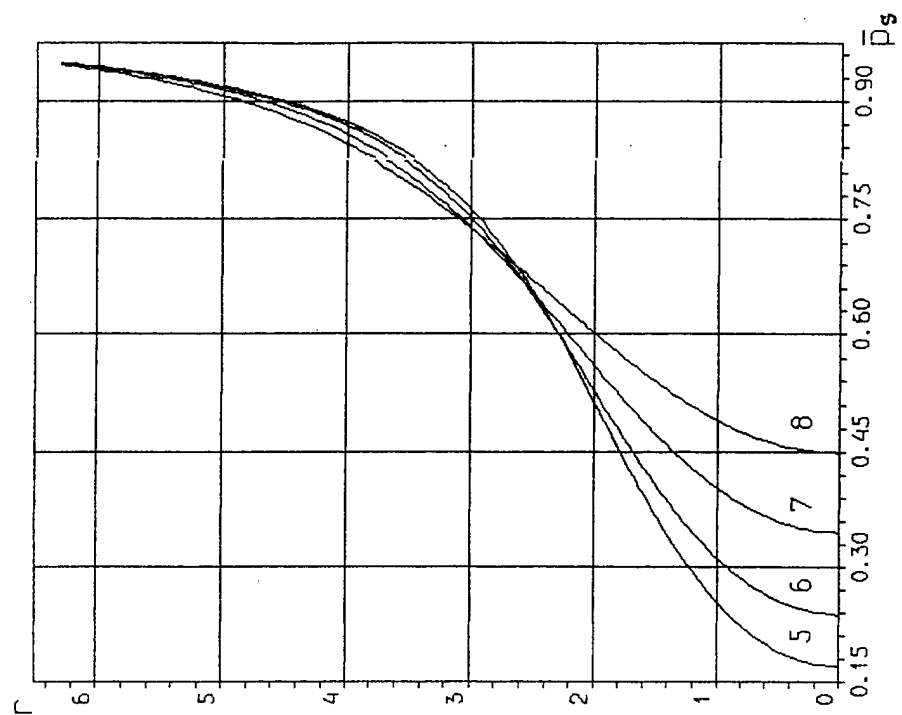


Fig.60

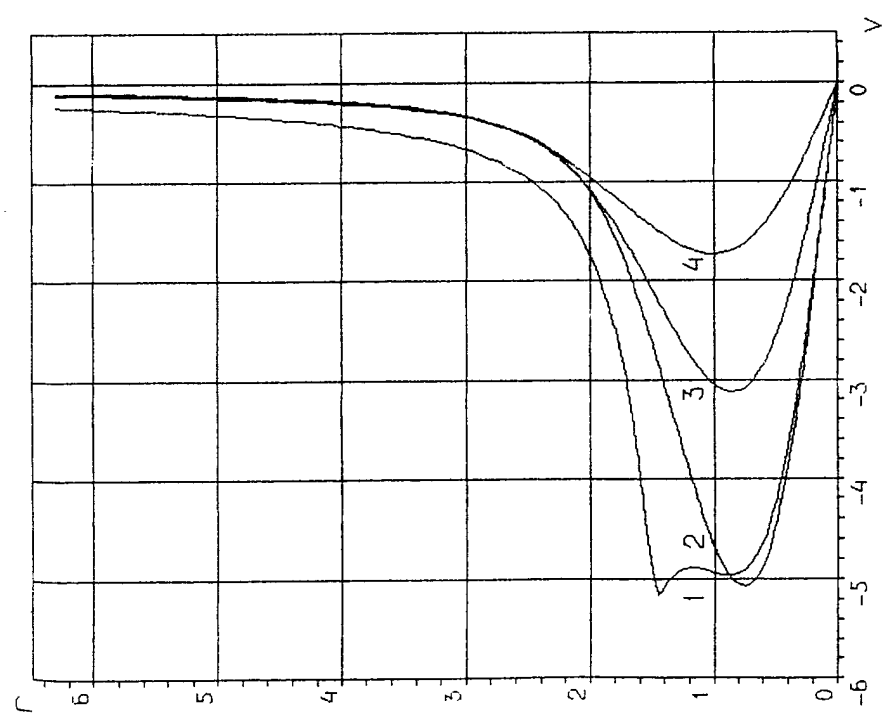
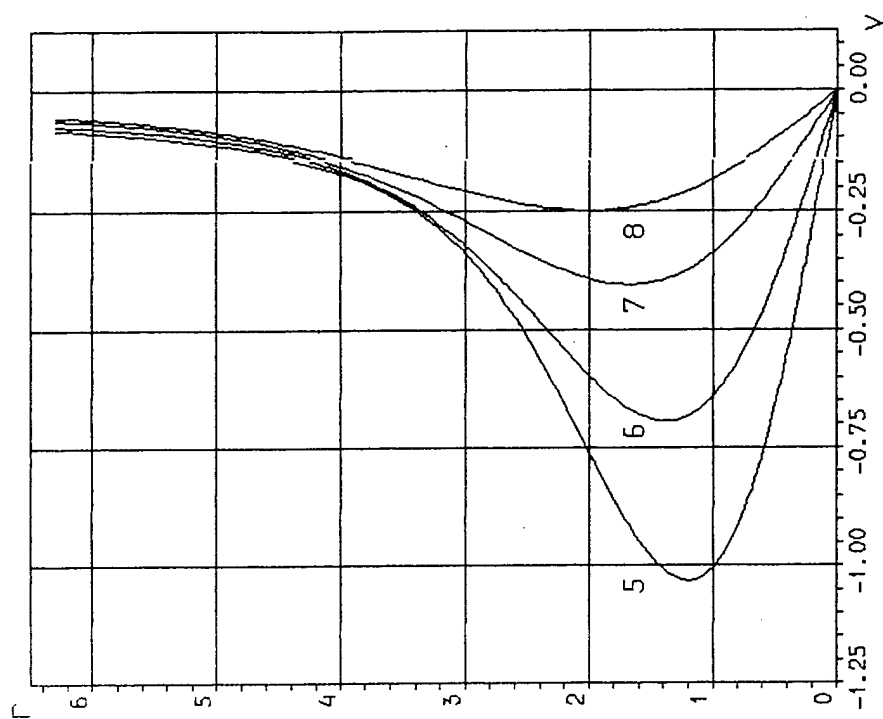


Fig.61

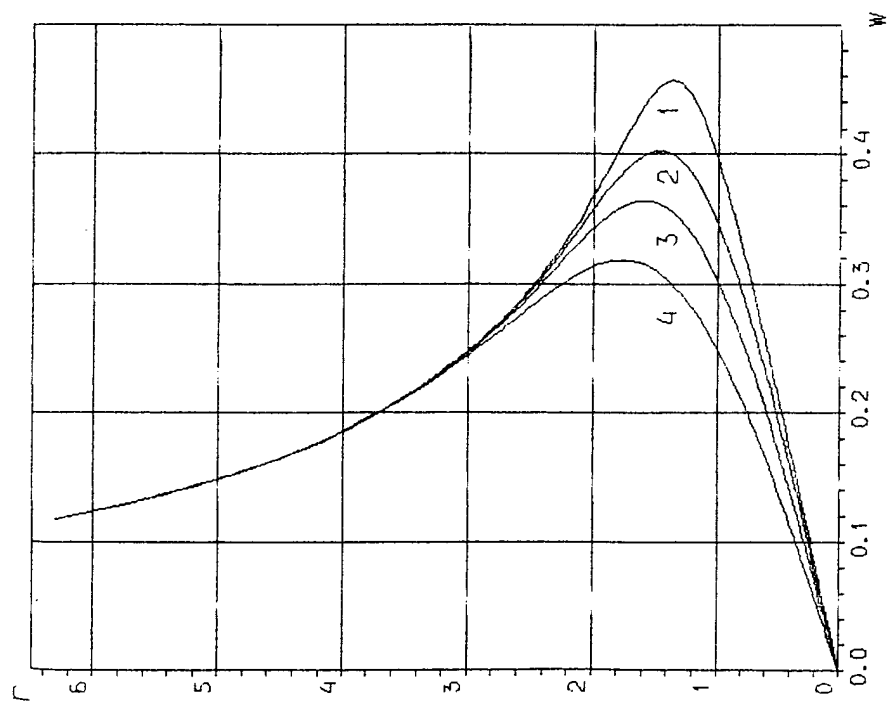
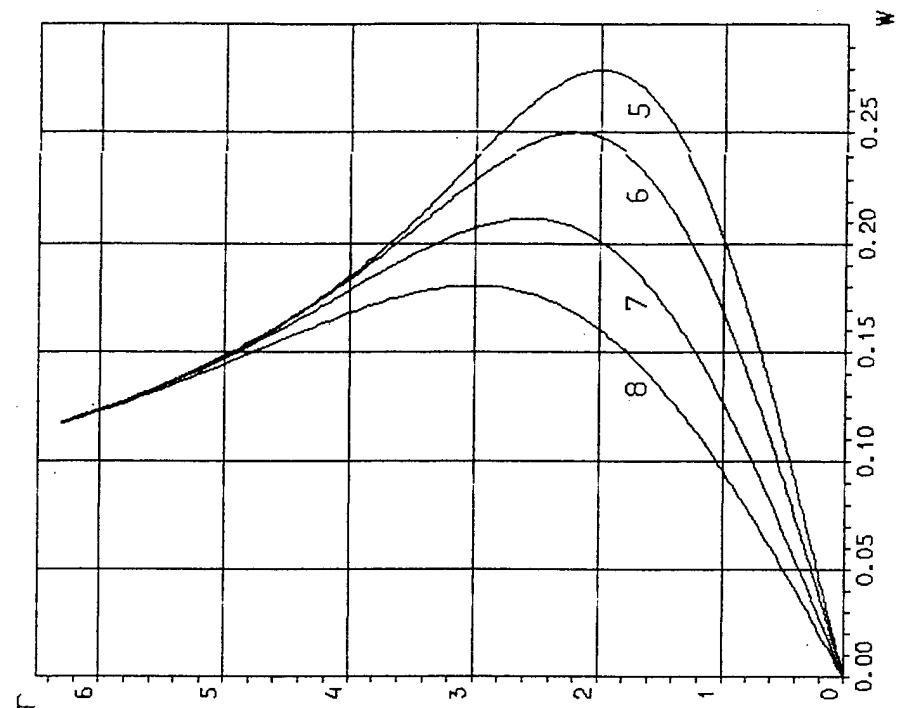


Fig. 62

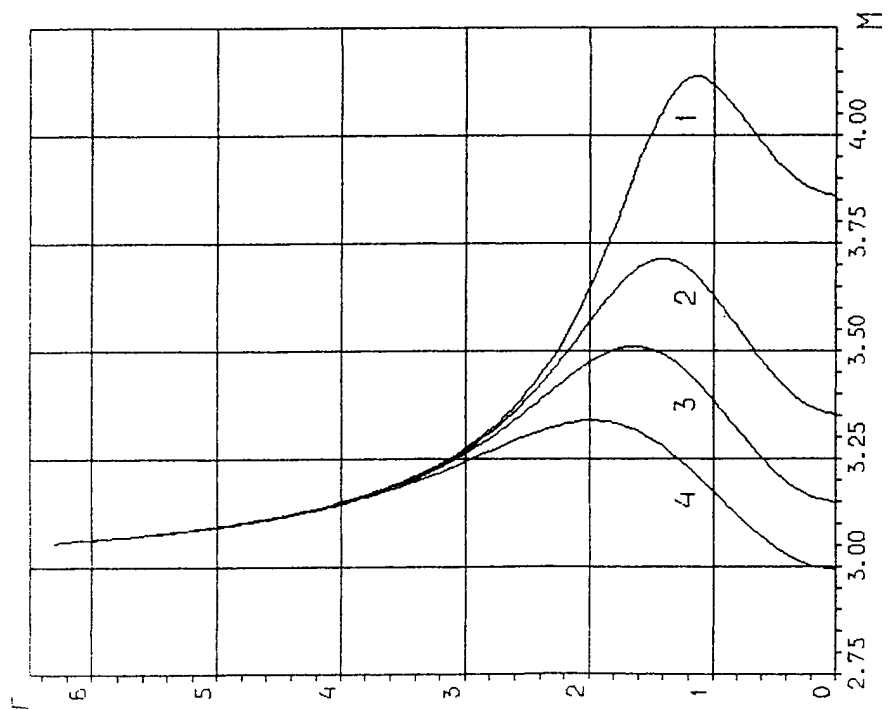
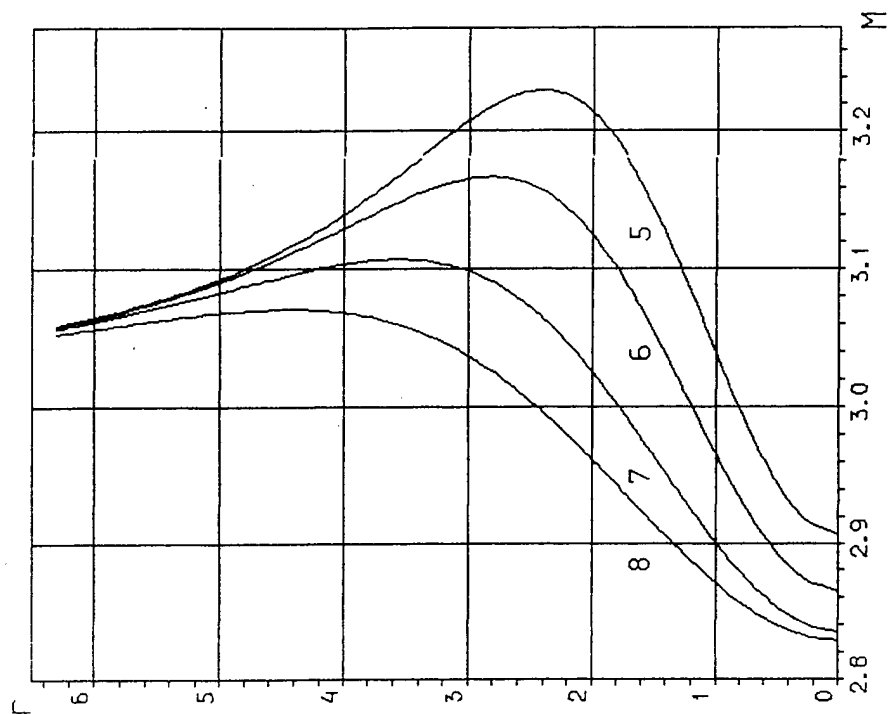


Fig.63

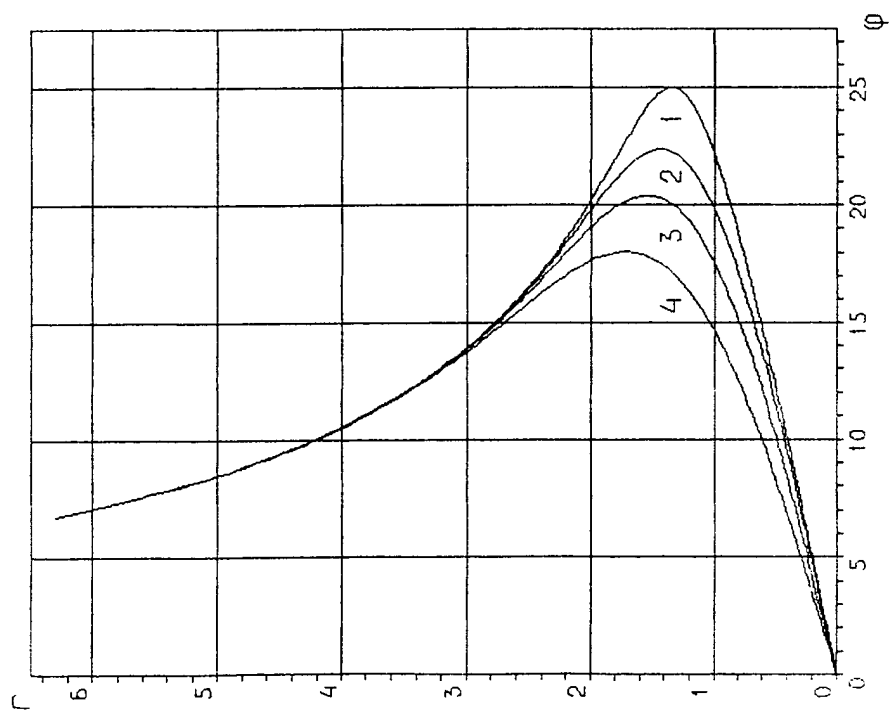
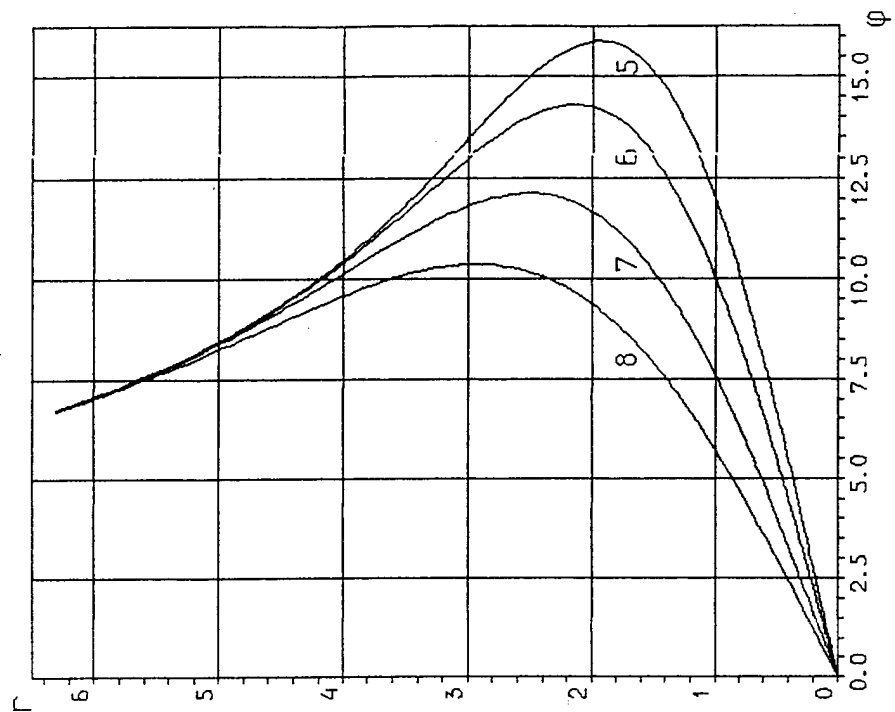


Fig. 64

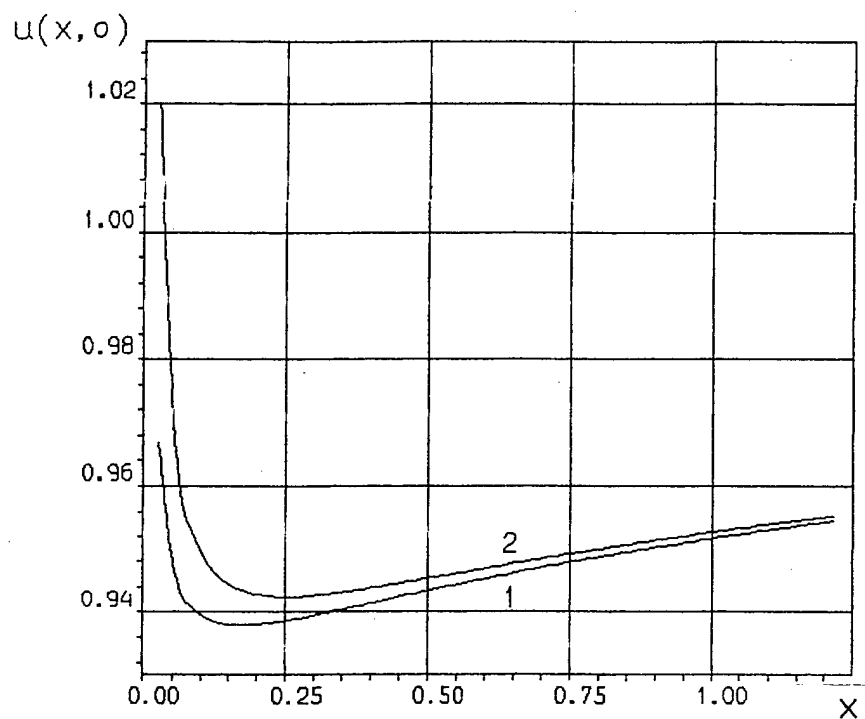


Fig.65

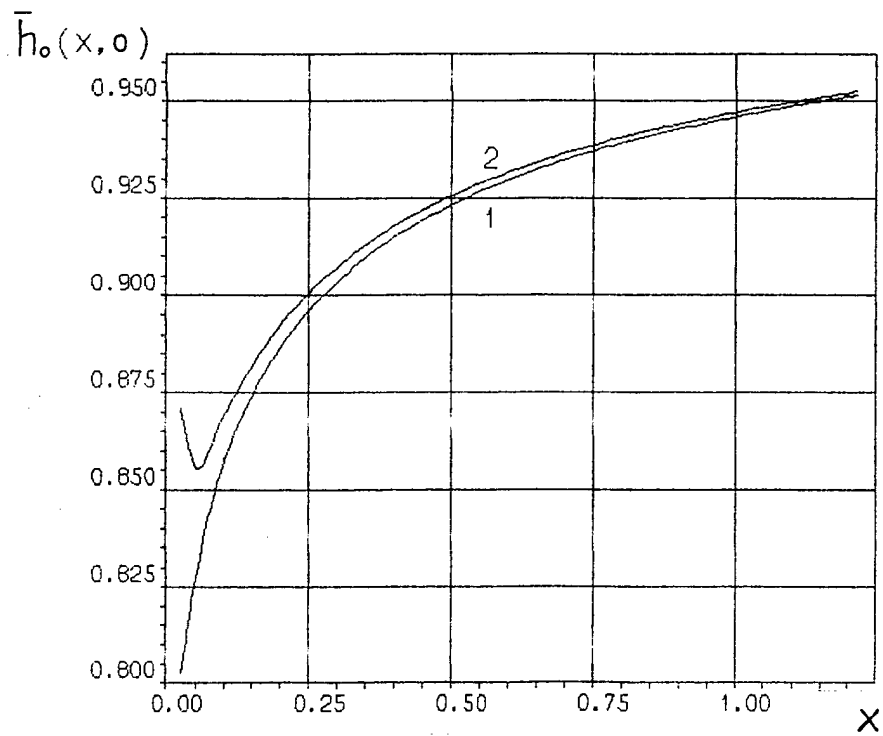


Fig.66

$\bar{p}_s(x, 0)$

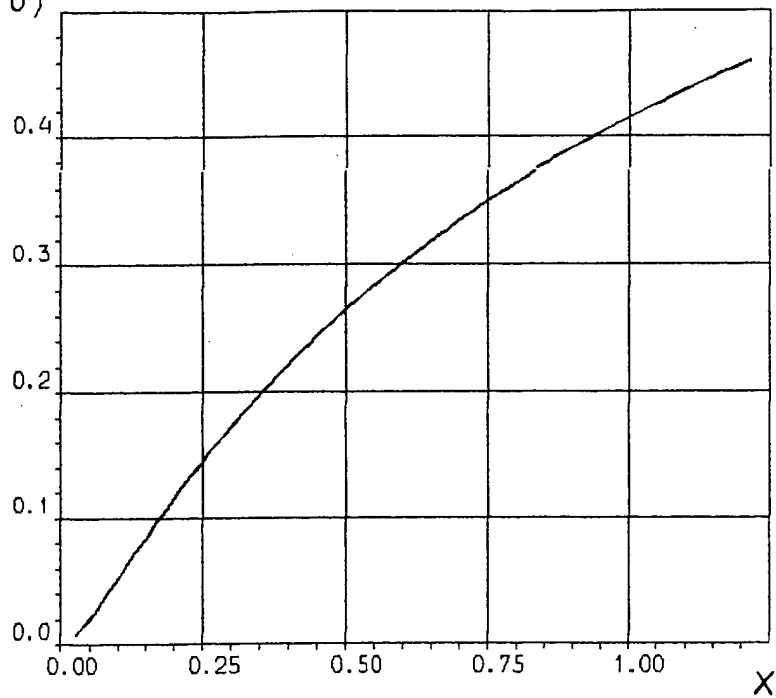


Fig.67

$M(x, 0)$

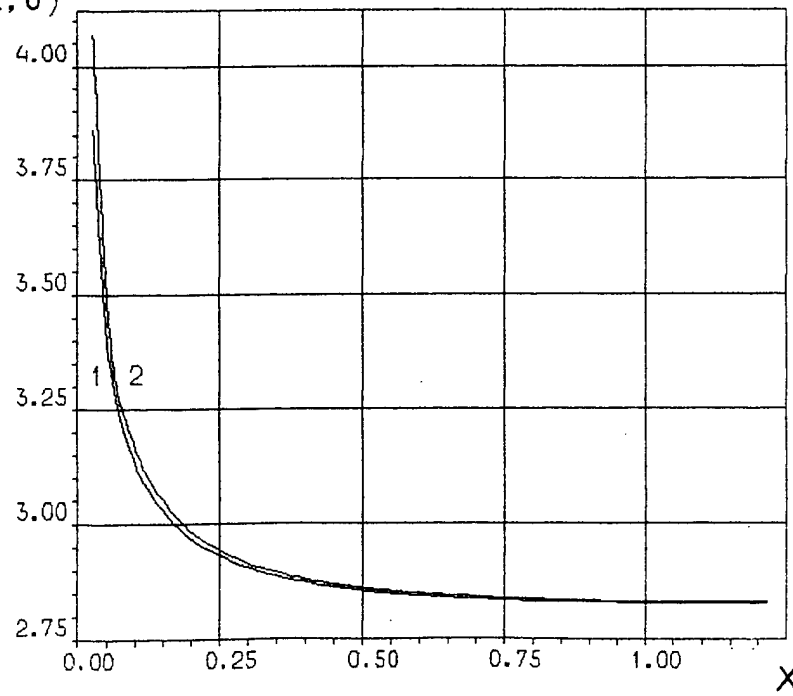


Fig.68

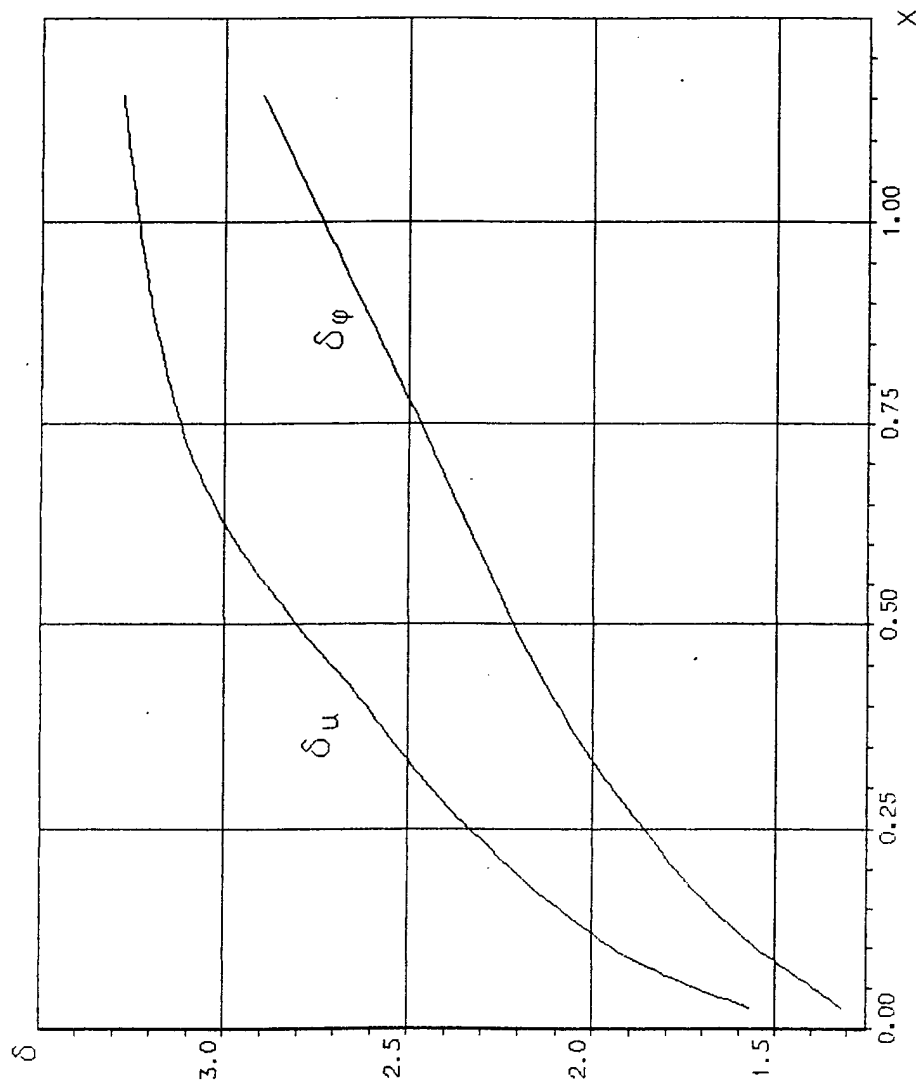
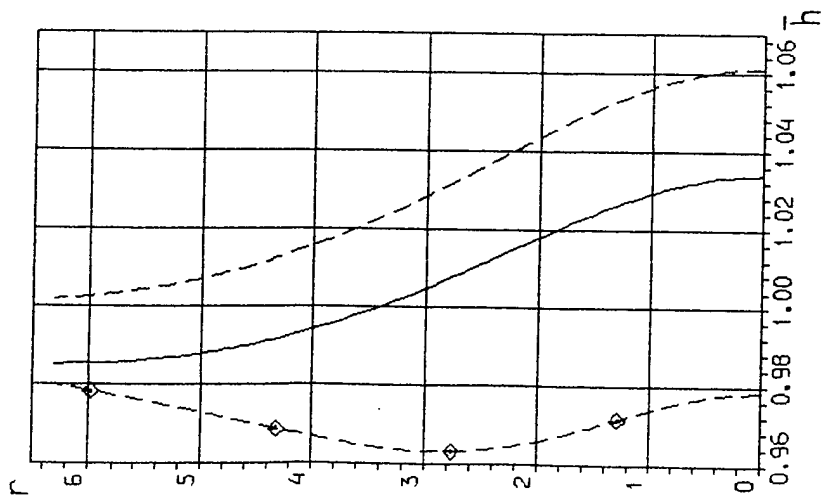
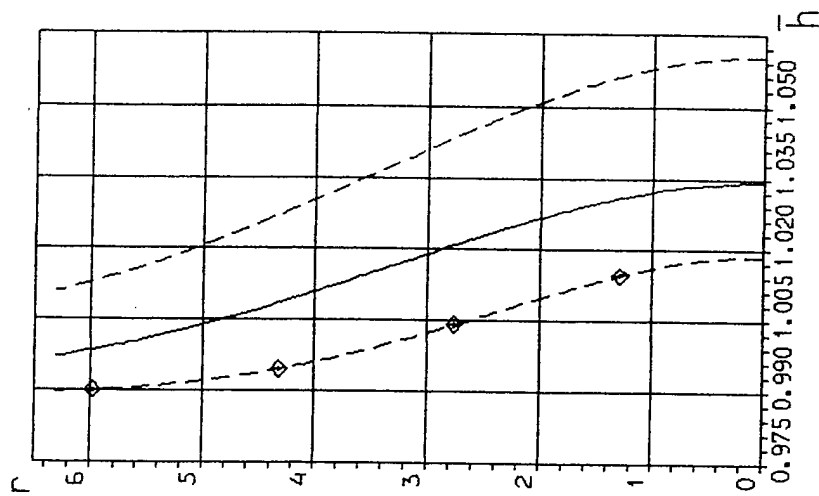


Fig. 69

$X=2.05$



$X=4.05$



$X=8.05$

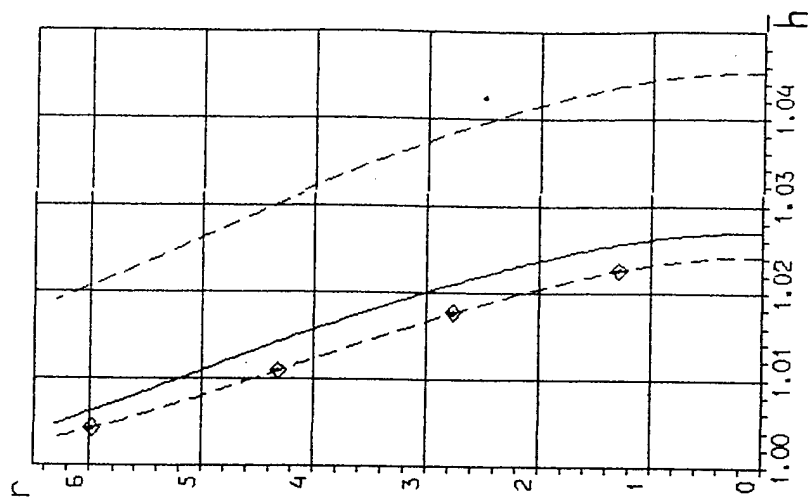


FIG. 70

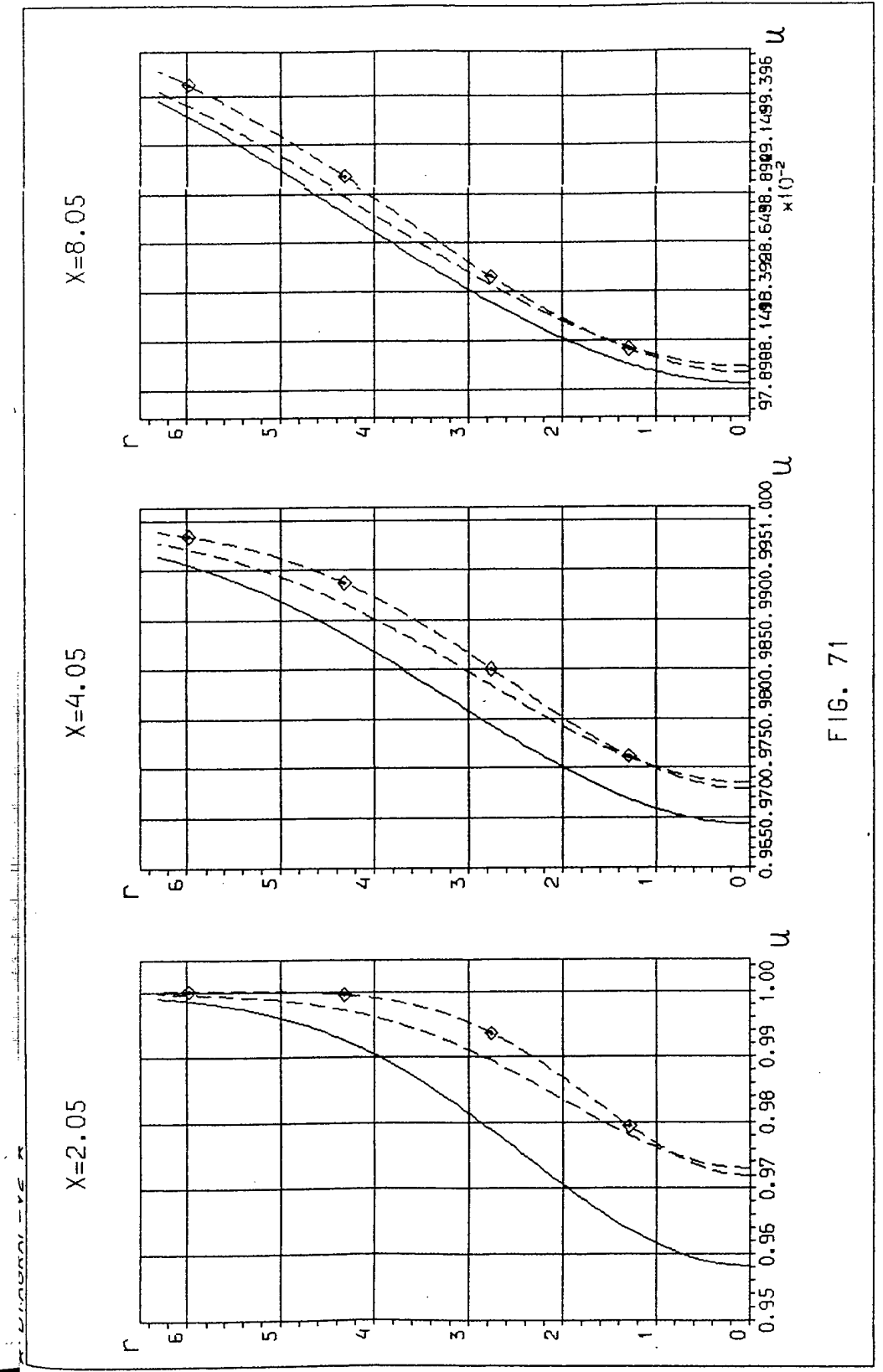
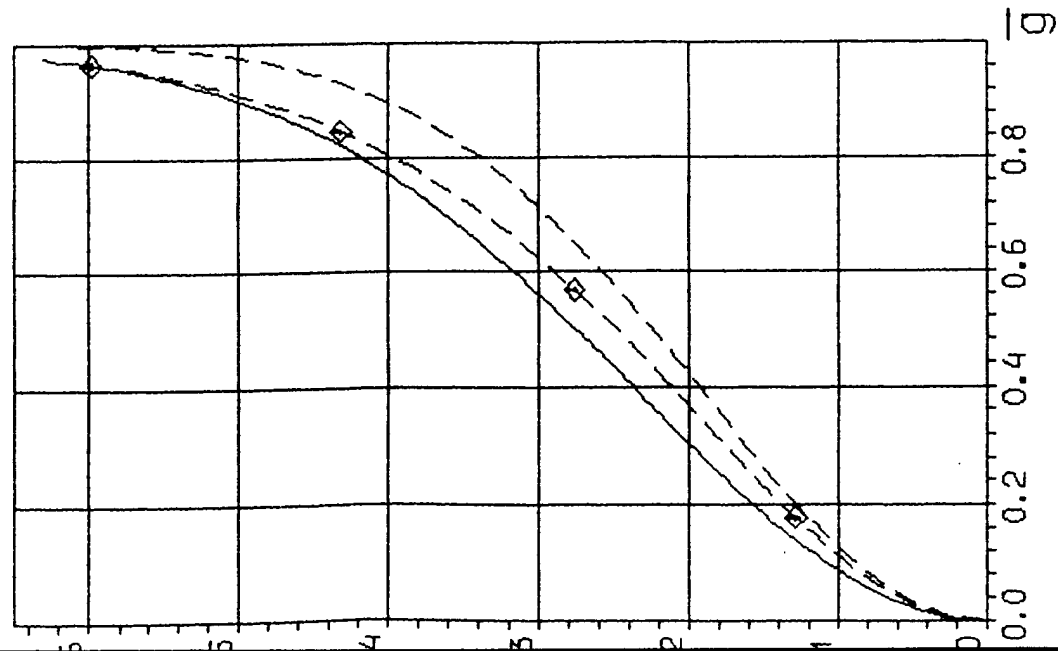
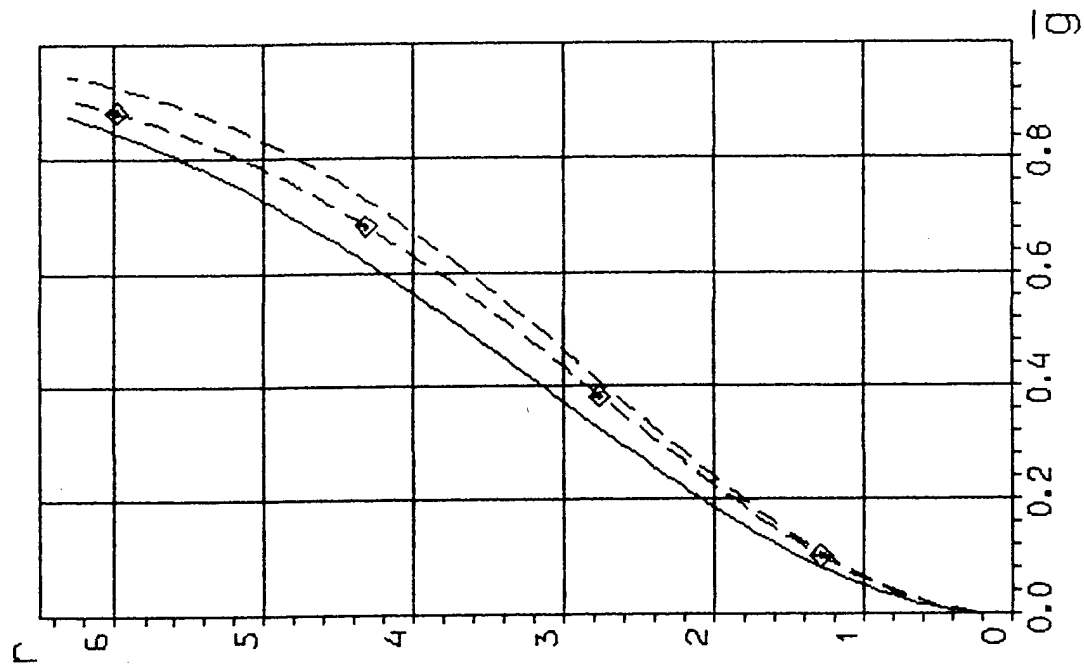


FIG. 71

X=2.05



X=4.05



X=8.05

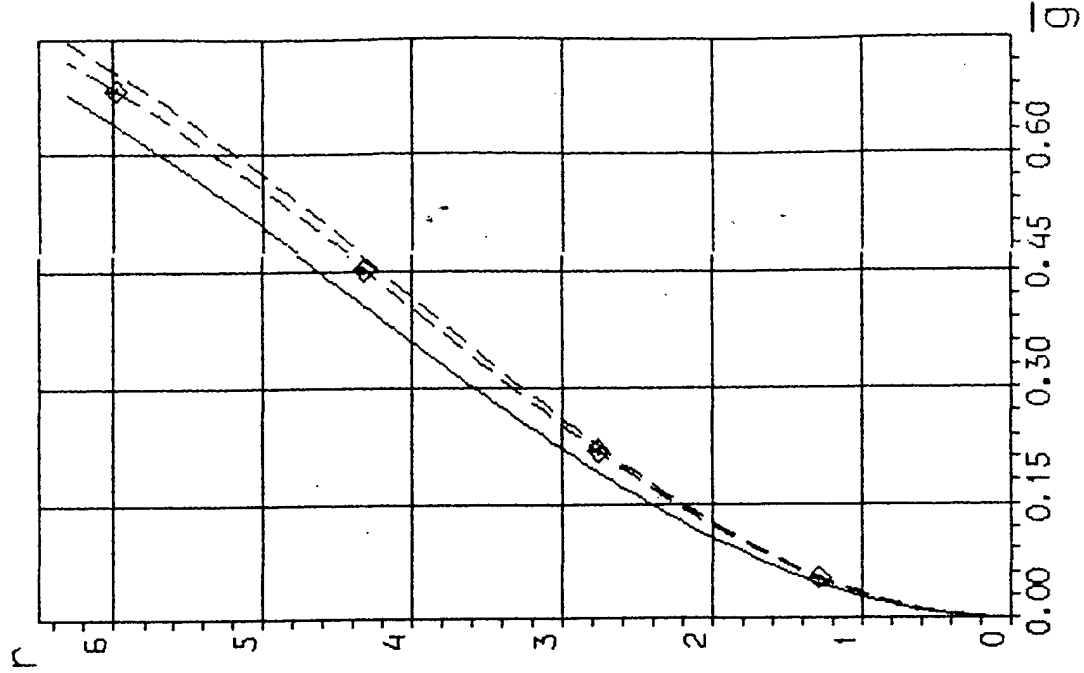
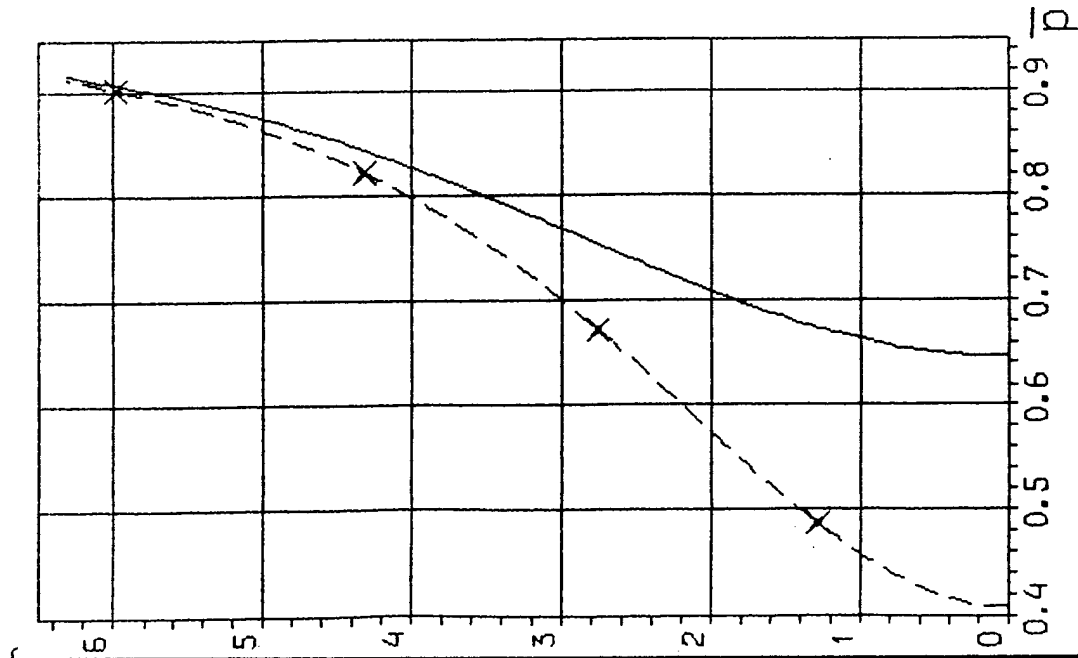
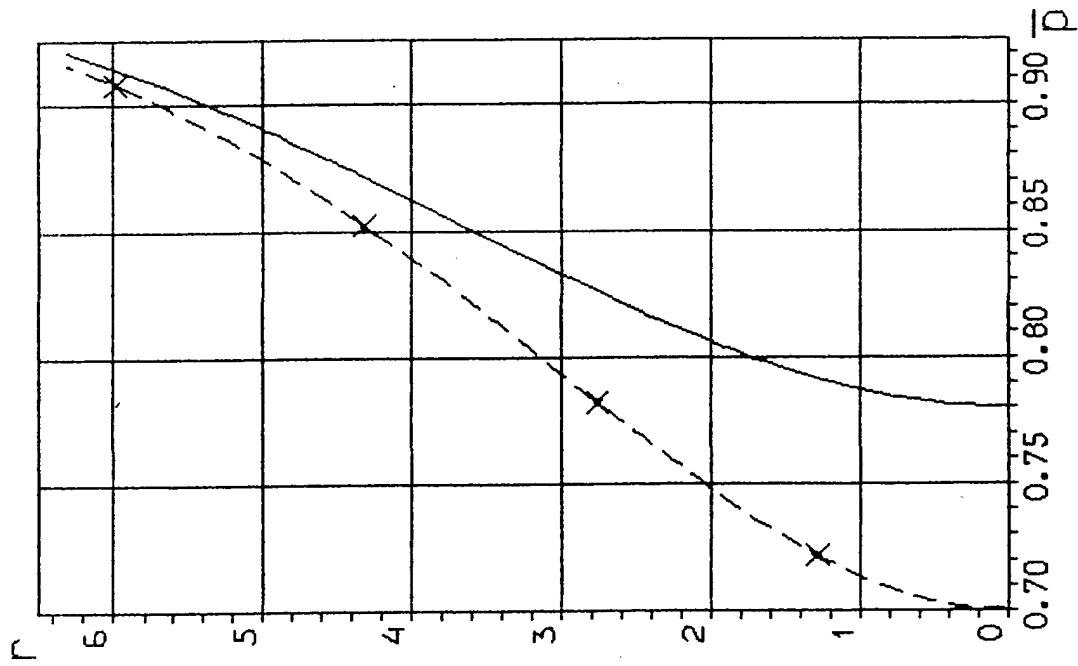


FIG. 72

$X=2.05$



$X=4.05$



$X=8.05$

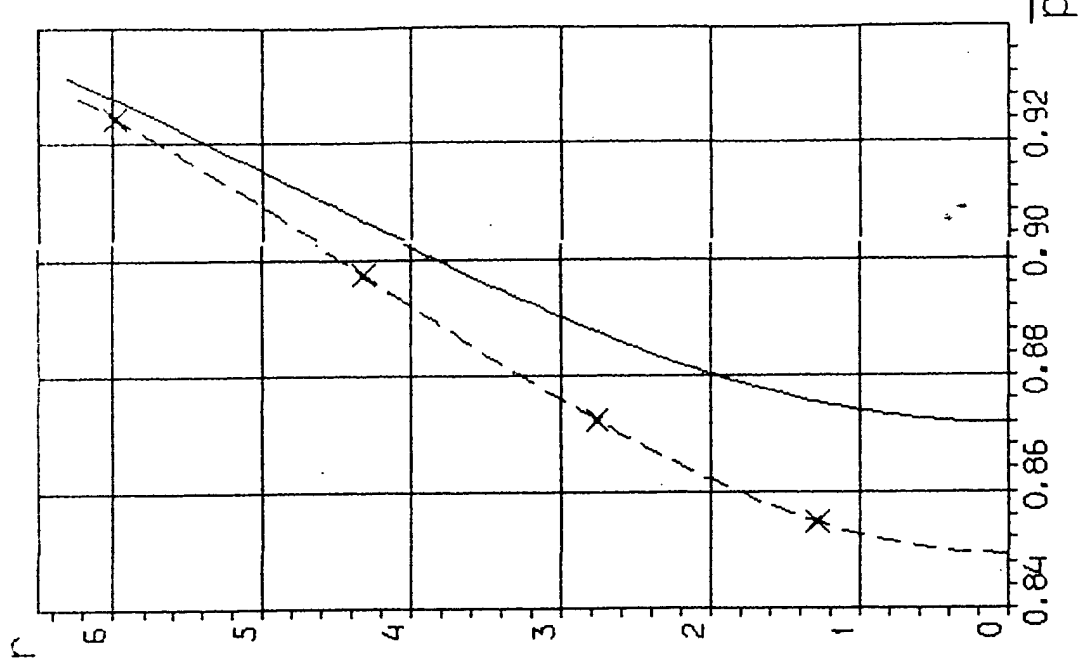


FIG. 73

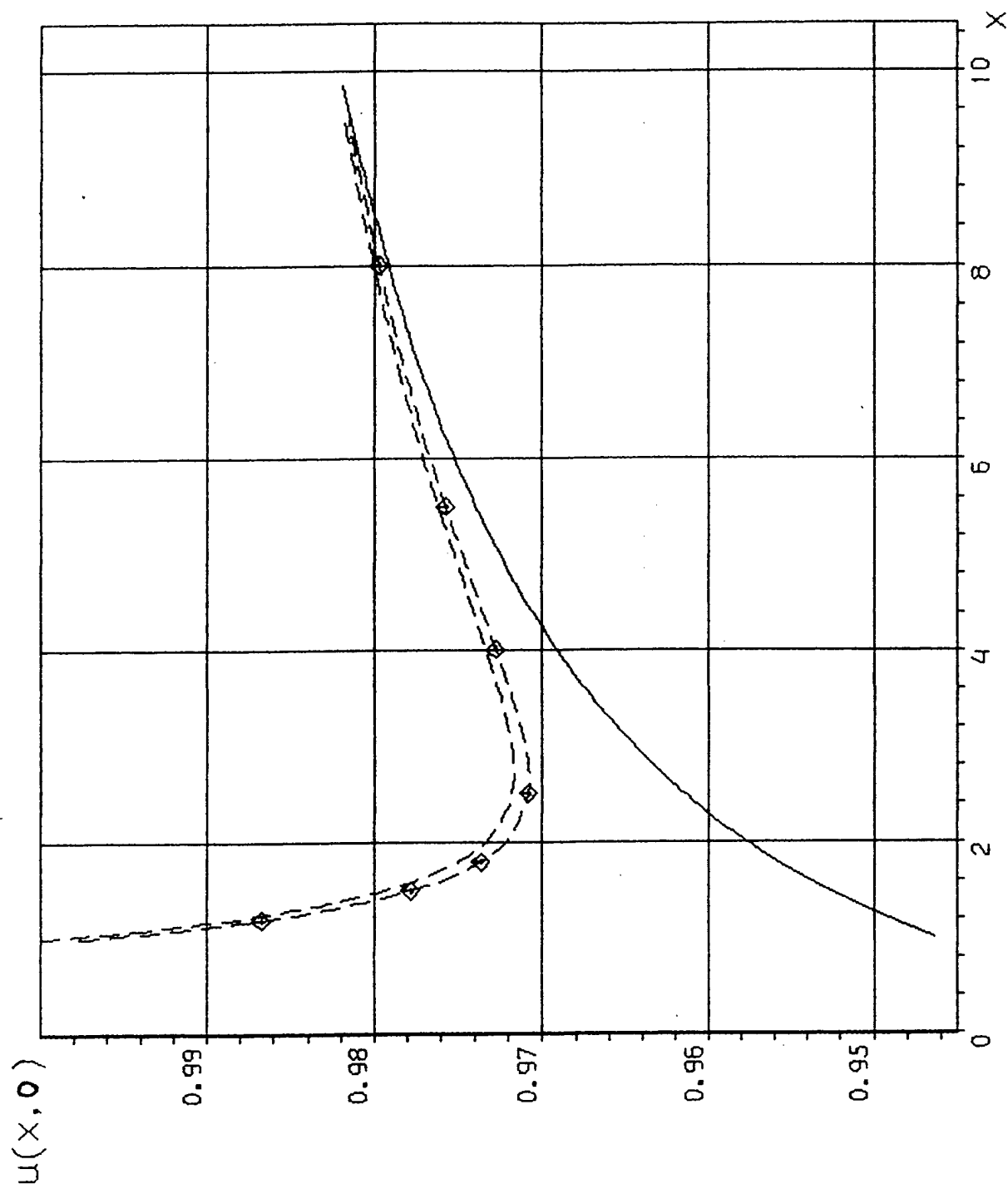


FIG. 74

WINDMILL - VE X

$\bar{h}(x,0)$

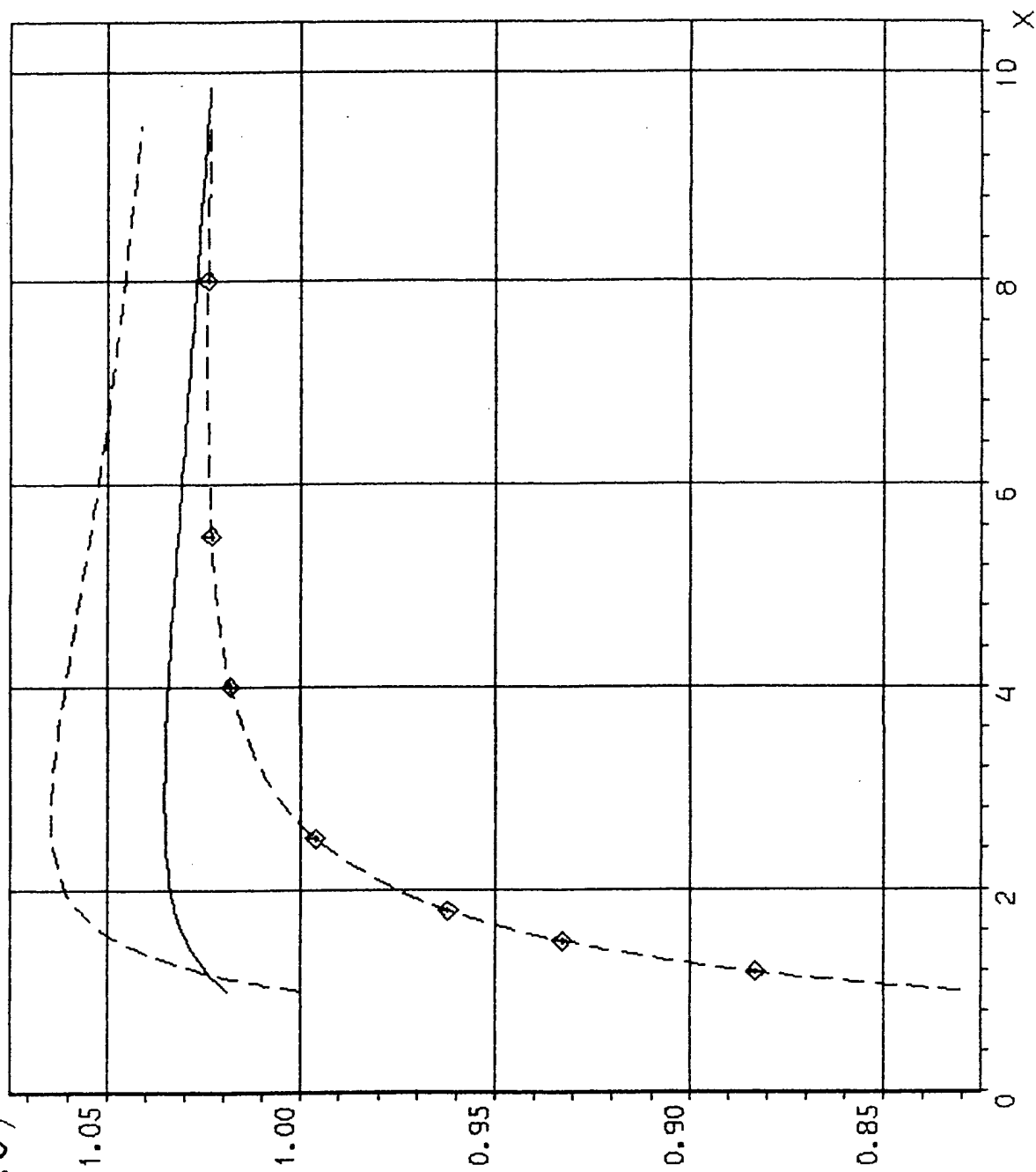


FIG. 75

UNIVERSITY OF TEXAS

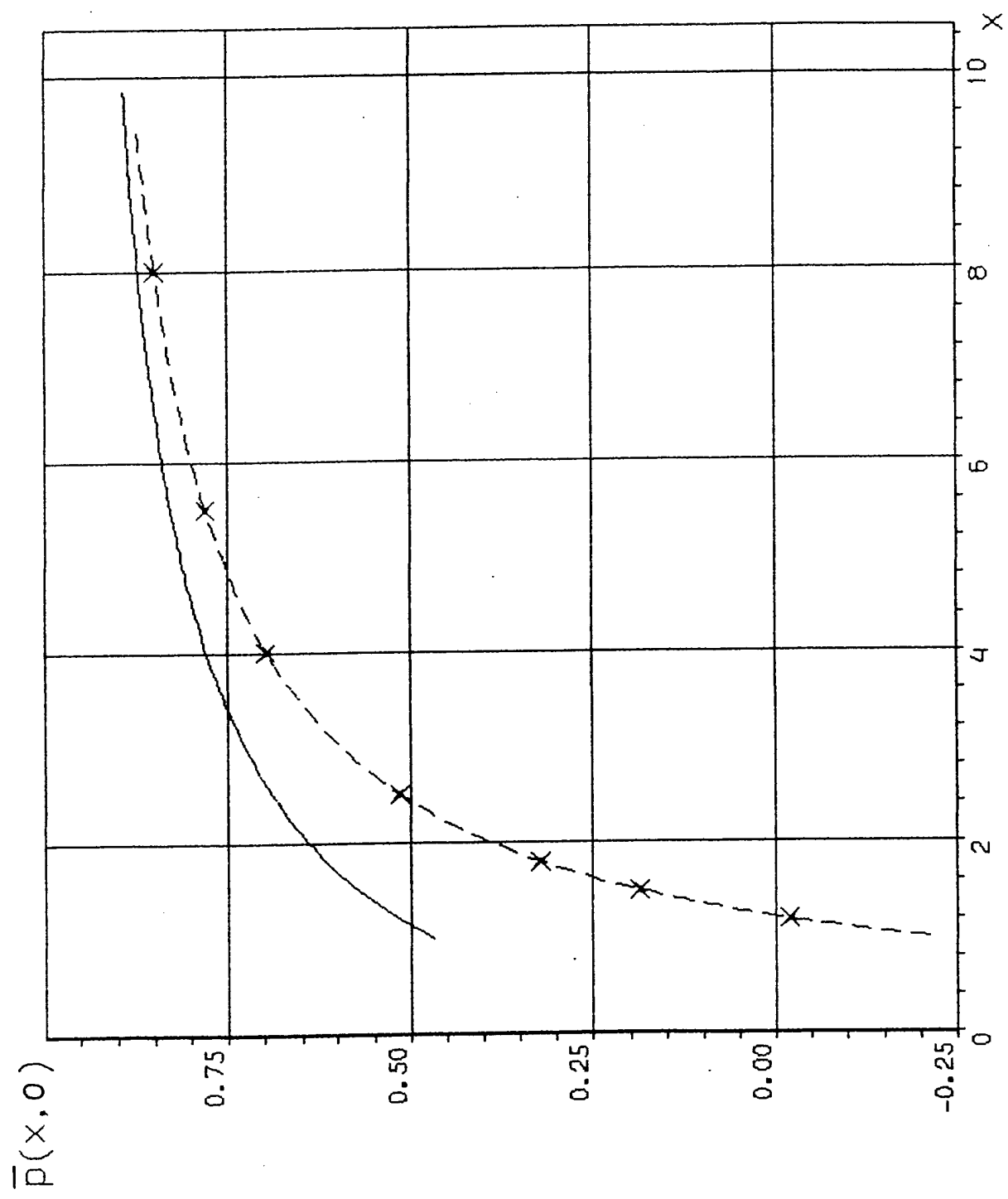


FIG. 76

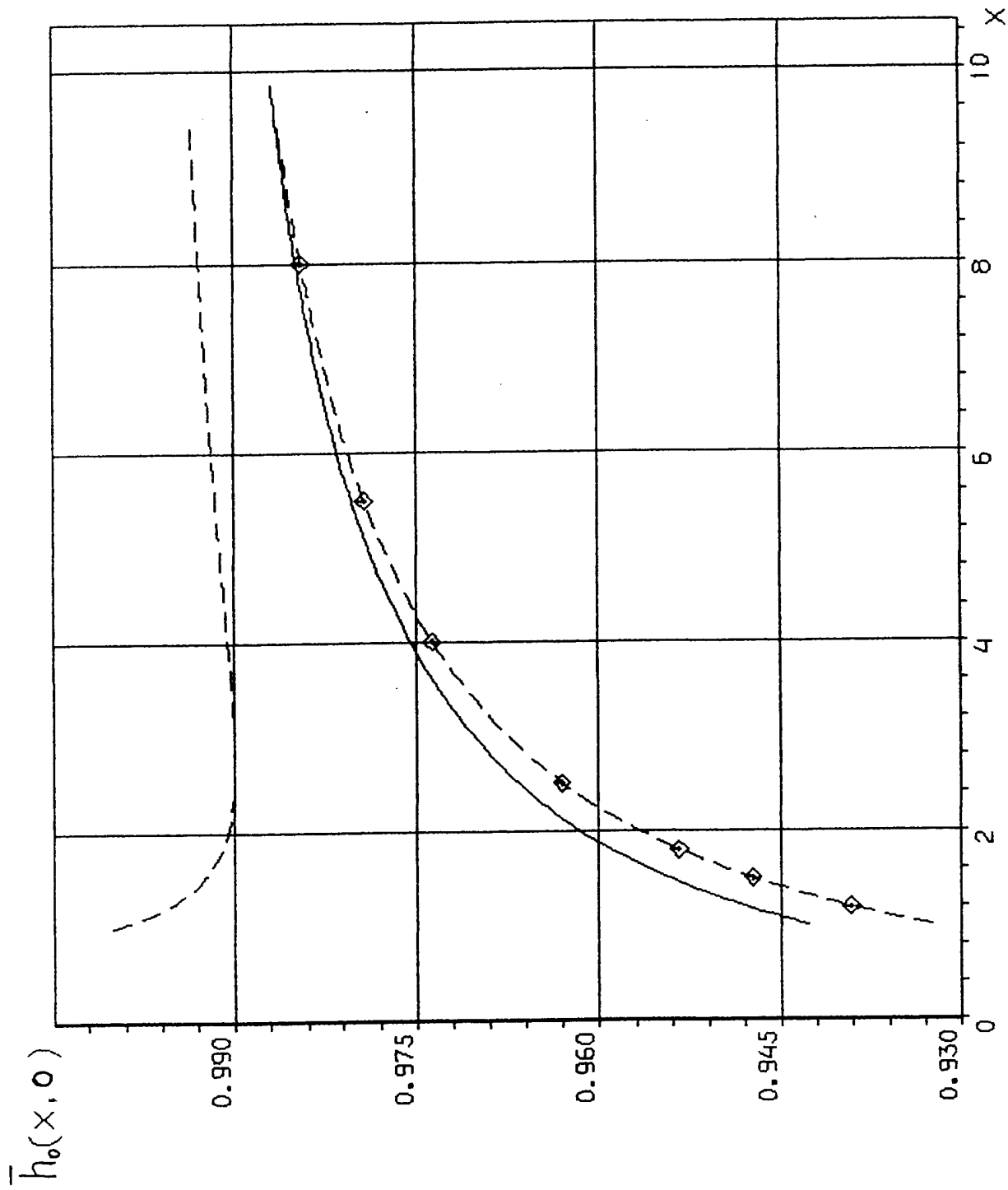


FIG. 77

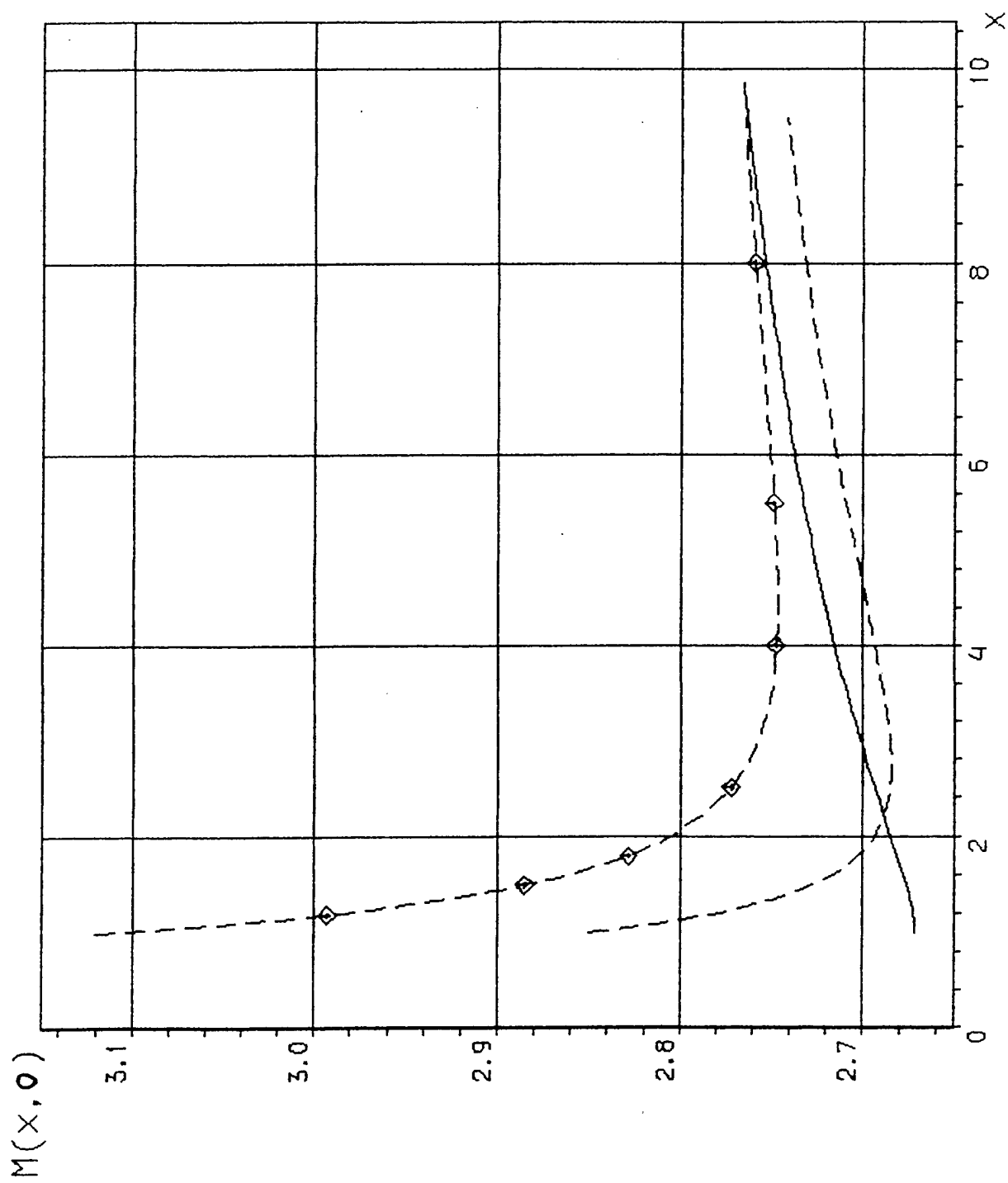


FIG. 78

$X=1.1$

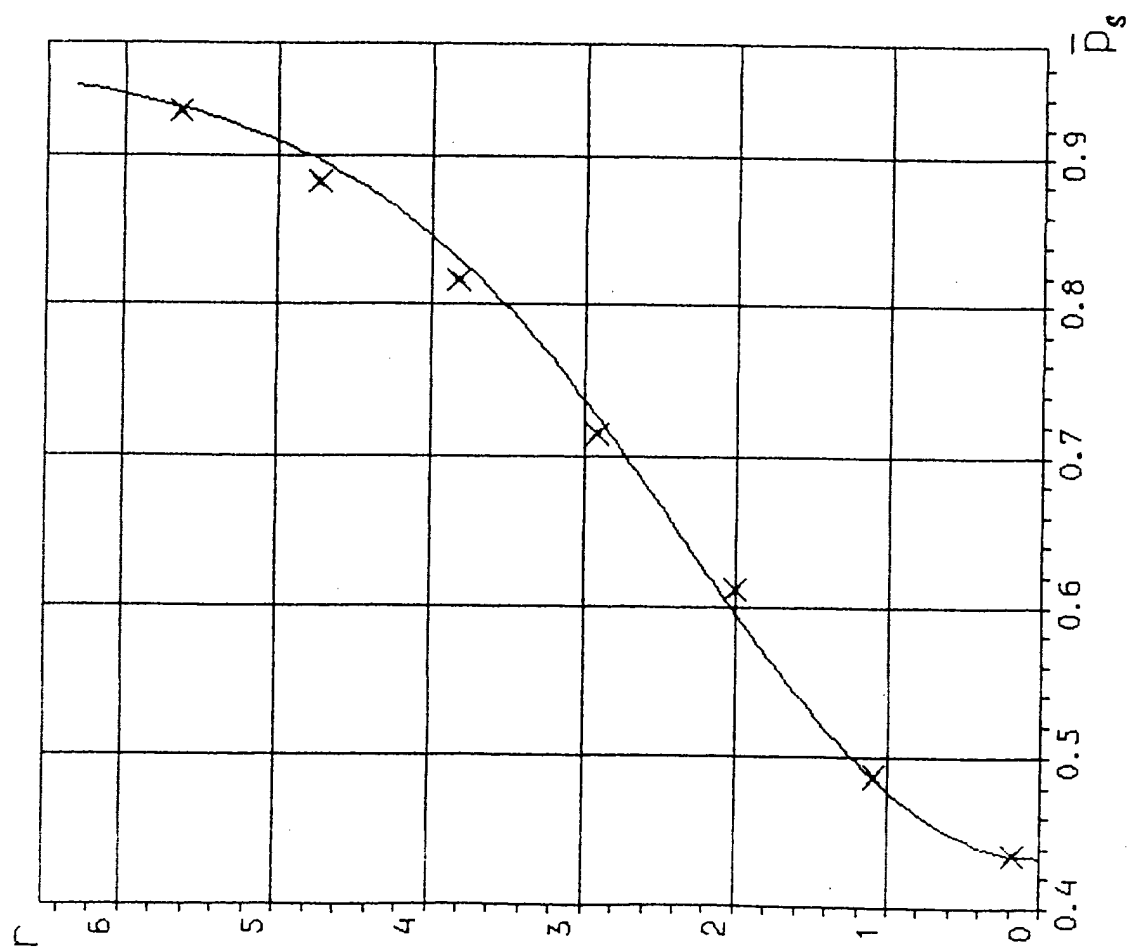


Fig.79

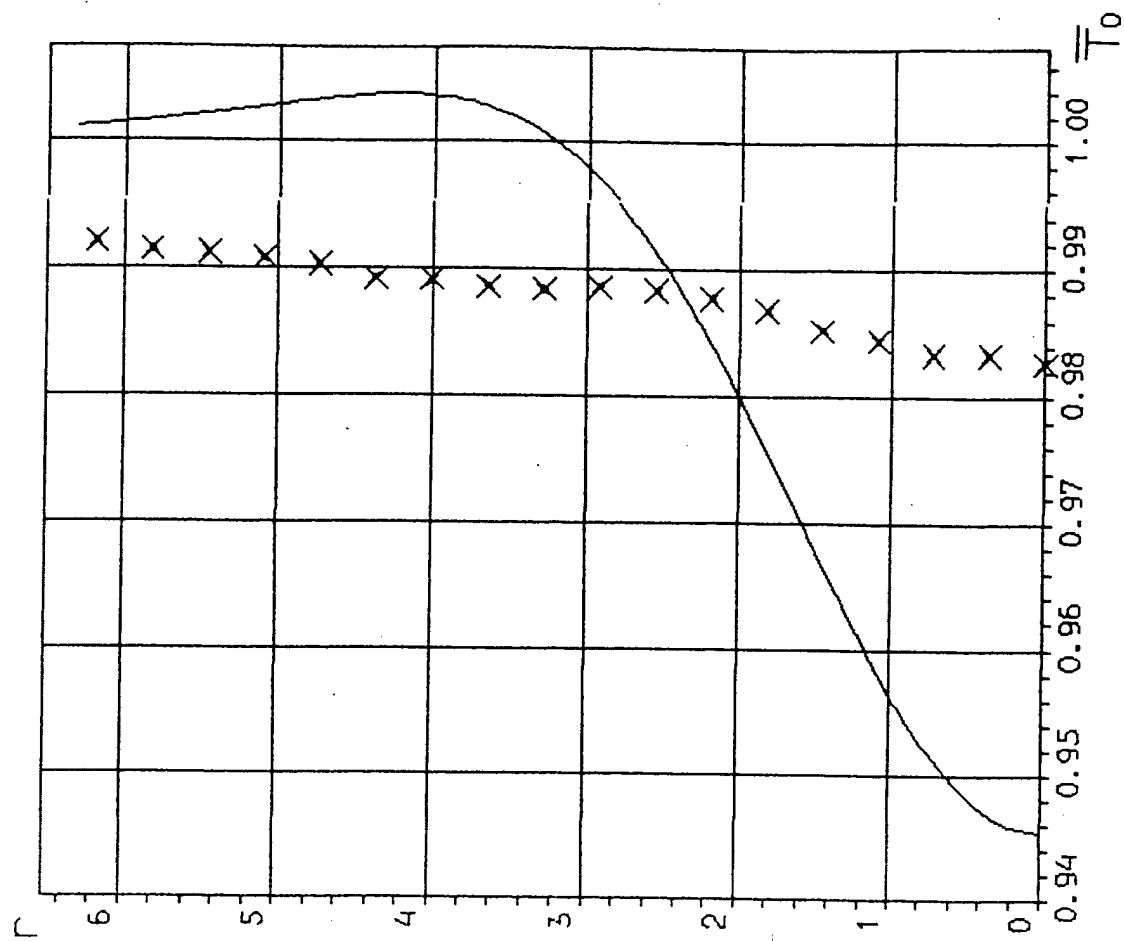


Fig.80

$X=0.115$

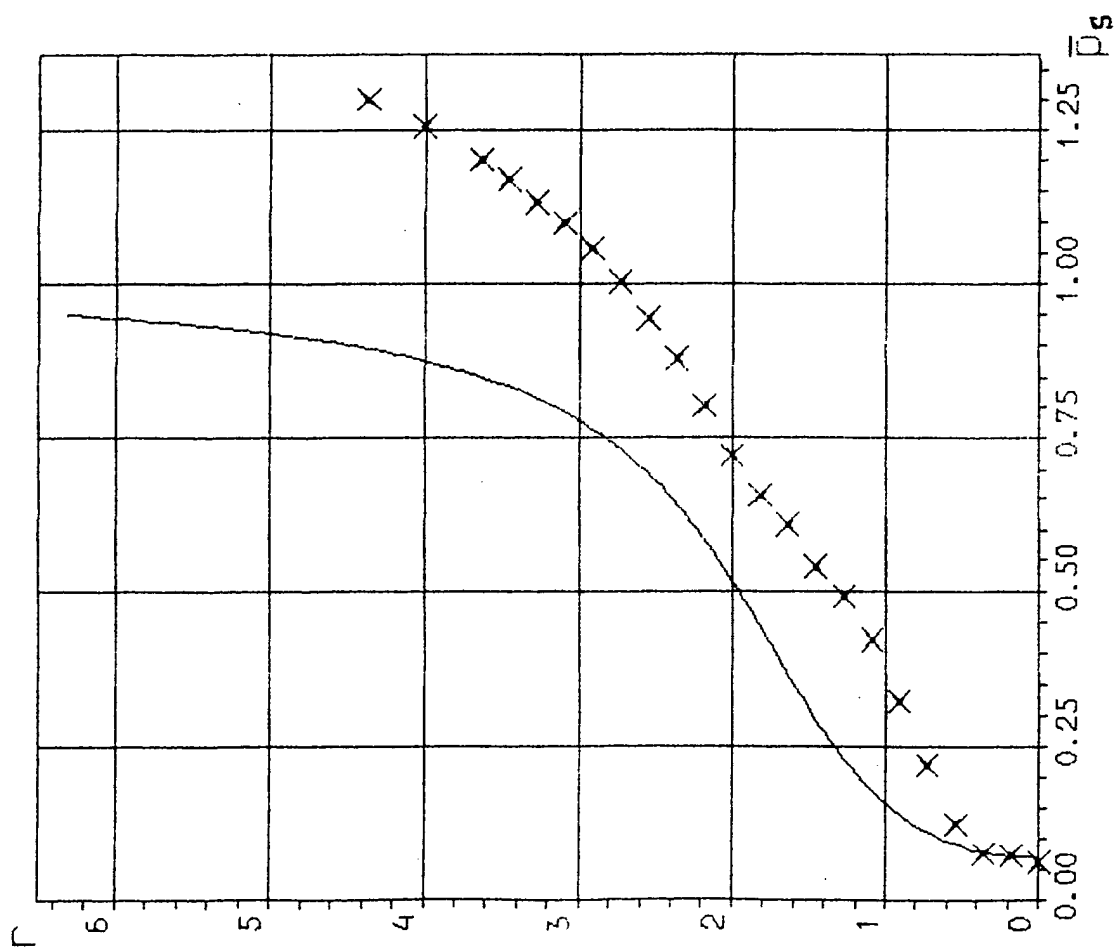


Fig.81

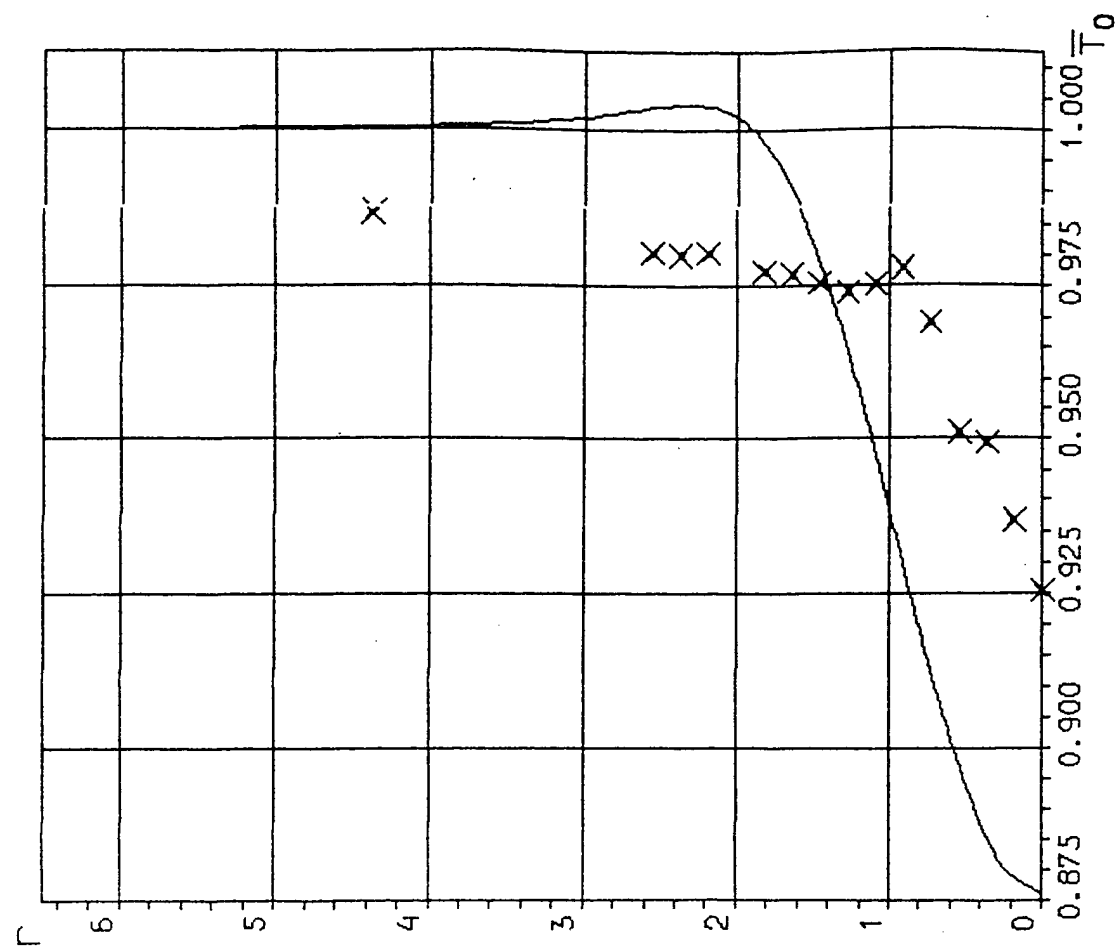


Fig.82